Development of Optical Fibre Curvature Sensors for Subsea Instrumentation

Nikolitsa Papachristou

A dissertation submitted for the degree of Doctor of Philosophy

Heriot-Watt University

School of Engineering and Physical Sciences

FEBRUARY 2019

The copyright in this thesis is owned by the author. Any quotation from the thesis or use of any of the information contained in it must acknowledge this thesis as the source of the quotation or information.

To my family,

ACKNOWLEDGEMENTS

First and foremost, I would like thank my supervisor *Dr. William N. MacPherson.* His constant support and enthusiasm always motivated me to overcome my scientific problems. I also want to thank him for his patience and kindness during the most difficult moments of my research. I am extremely grateful for his guidance, rooted in many years' worth of knowledge and experience, which has allowed me to develop as a researcher.

A special thanks goes to my second supervisor *Dr. Robert R.J. Maier* for accepting me into the Applied Optics and Photonics group at Heriot-Watt University. The opportunity to work with him during my Erasmus Placements project led me to apply for my PhD studies at Heriot-Watt University.

Thanks are also due to *Dr. Jonathan A. Morton* and *Dr. Richard M. Carter* for their support and help during challenging times in the lab, as well as to all the *Applied Optics and Photonics* and the *LAkHsMI* group members, which always made me feel welcome in their small community.

I would also like to thank my friends that spent three wonderful years with me in Edinburgh: *Evangelos Kalamaras and Meltiani Belekoukia* who opened their home and accommodated me during the last months of my PhD; *Dr. Dimitrios Polyzos* that kept me company at the "usual bench" while I was seeking inspiration to write my PhD thesis; and *Georgia Anastasiadi* for her company at our labs.

Enormous thanks goes to my friends back in Greece: *Mariza Varvarigou, Aggeliki Sotiropoulou, George Moriatis, Sophia Mantikou and Maria Vourlioti.* Their company during my vacations back home as well as their daily messages were endearing and kept me going with my work. I always felt their positive energy and support across the globe.

Finally, special thanks goes to my *family: Petros Papachristou, Maria Tsaroumi, Athanasia Papachristou, Evangelos Sinodinos (also known as "the small imposter") and Lucie.* Their unconditional love and support was and will always be my inner strength.

ACADEMIC REGISTRY

Research Thesis Submission

Name*:*	NIKOLITSA PAPACHRISTOU		
School:	SCHOOL OF ENGINEERING AND PHYSICAL SCIENCES (EPS)		
Version: *(i.e. First, Resubmission, Final)*	FINAL	Degree Sought:	PHD

Declaration

In accordance with the appropriate regulations I hereby submit my thesis and I declare that:

1) the thesis embodies the results of my own work and has been composed by myself
2) where appropriate, I have made acknowledgement of the work of others and have made reference to work carried out in collaboration with other persons
3) the thesis is the correct version of the thesis for submission and is the same version as any electronic versions submitted*.
4) my thesis for the award referred to, deposited in the Heriot-Watt University Library, should be made available for loan or photocopying and be available via the Institutional Repository, subject to such conditions as the Librarian may require
5) I understand that as a student of the University I am required to abide by the Regulations of the University and to conform to its discipline.
6) I confirm that the thesis has been verified against plagiarism via an approved plagiarism detection application e.g. Turnitin.

** Please note that it is the responsibility of the candidate to ensure that the correct version of the thesis is submitted.*

Signature of Candidate*:*	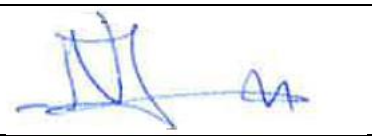	Date:	04/02/2019

Submission

Submitted By *(name in capitals):*	
Signature of Individual Submitting:	
Date Submitted:	

For Completion in the Student Service Centre (SSC)

Received in the SSC by *(name in capitals):*			
Method of Submission *(Handed in to SSC; posted through internal/external mail):*			
*E-thesis Submitted (**mandatory for final theses)***			
Signature:		Date:	

ABSTRACT

The experimental results presented in this thesis were part of a bigger research project (LAkHsMI) funded by the European Union (Horizon 2020). The overall project's aim is to monitor sea flow speeds for different applications with electrical and optical fibre sensors. Here, the fabrication of the sensors which exploit Fibre Bragg Grating (FBG) using conventional, as well as novel optical fibres is presented.

Two different curvature sensors were produced for the purposes of the project. The first one was fabricated using four single mode fibres (SMFs) bundled together, while the second used one Multicore fibre (MCF) with four optical cores. The structure of both permitted their curvature to be determined in two dimensions. The first type of optical fibre curvature sensor was also used for the fabrication of a FBG Attitude sensor, where the orientation of a platform in two planes could be determined with accuracy of ±2°.

The main priority of the studies presented here was the fabrication and performance of the MCF curvature sensors. The transmittance and reflectance (using inscribed FBGs) of the light into the MCF is explored, where an interface device between the MCF to SMF is required. Two different cases are reported, the first uses a silica inscribed waveguide fan-out device, while the second uses a tapered MCF fan-out device. In the first case the temperature sensitivity of the silica waveguide fan-out device is detected. This sensitivity can be diminished with the use of the tapered MCF fan-out device and discussed. Moreover, in the second case coupling of light from one core of the MCF to all four cores is required. Hence, inscription of different FBGs into the cores of the MCF was achieved so that the overlap of the FBGs spectra would be avoided.

The challenges that arose during the fabrication and performance of these sensors are reported. Moreover, their temperature sensitivity as well as the strengths and weaknesses over several aspects are reported. Finally, a comparison between the curvature sensors is included and states which sensor can be used for subsea flow measurements and which has the potentials for further development.

CONTENTS

ACRONYMS

ADCP	Accoustic Doppler Current Profiler
EU	European Union
FBG	Fibre Bragg Grating
FWHM	Full Width at Half Maximum
IR	InfraRed
LAkHsMI	LArge scale HydrodynaMic Imaging
LPG	Long Period Grating
MCF	MultiCore Fibre
MM	MultiMode Fibre
POF	Polymer Optical Fiber
SMF	Single Mode Fibre
TDM	Time Division Multiplexing
UV	UltraViolet
WDM	Wavelength Division Multiplexing

COMMON VARIABLES

C	Coupling Coefficient
d	Core separation
l	Cantilever length
n	Refractive index
T	Temperature
$V-number$	Normalised frequency parameter
z	FBGs position
ε	Strain
Λ_{FBG}	FBG pitch
$\lambda_{reflected}$ **or** λ_{FBG}	FBG Reflected wavelength peak

Chapter 1. Introduction

This chapter covers the motivation as well as the aims and objectives of the European Union funded LAkHsMI (LArge scale HydrodynaMic Imaging) project under which the research reported in this thesis was developed. The primary objective of LAkHsMI is the collection of subsea flow measurements using novel flow sensors. Existing approaches and limitations are discussed and a general outline of the thesis is presented.

1.1. Motivation

The primary objective of LAkHsMI is the fabrication and calibration of a flow sensor for environmental monitoring of hydrodynamic environments. Throughout the fabrication of this sensor, several challenges arose regarding the deployment of the sensors in the sea, and in particular the connection and packaging of a sensor network. Hence, this was addressed by exploring different types of optical fibre flow sensors to determine those most suitable.

Hydrodynamic imaging has been extensively studied in the last three decades [1]. The term was initially defined by Hassan (1989), who studied Blind Cave Fish (Anoptichthys jordani) [2]. Despite the fact that these fish are blind, they have the ability to avoid collisions with stationary objects. The mechanism that makes them aware of their surroundings, is strongly correlated with the flow field around them [3]. Their sensory receptors are able to detect variations of the flow stream around them. By this mechanism, these fish are able to determine the presence of obstacles and image the flow surrounding them [3] with the principle having since been employed biomimetically [4].

Flow velocity and direction measurements of streams and wakes in oceans, seas or even lakes and canals have significance for many applications and for a number Hydrodynamic imaging is essential; with oceanography being the most important. Examples include, the fabrication and installation of marine renewable energy devices [5], harbour awareness [6], and ferry traffic [7]. Moreover information about seabed scouring is critical in design and stabilisation of offshore structures (Figure 1-1). Distinctive examples include wind or wave energy farms [8] and installed of subsea power cables and pipelines [9]. Currently, information is mainly obtained from satellites [10] or point measurement devices placed on ships, buoys or anchors [11].

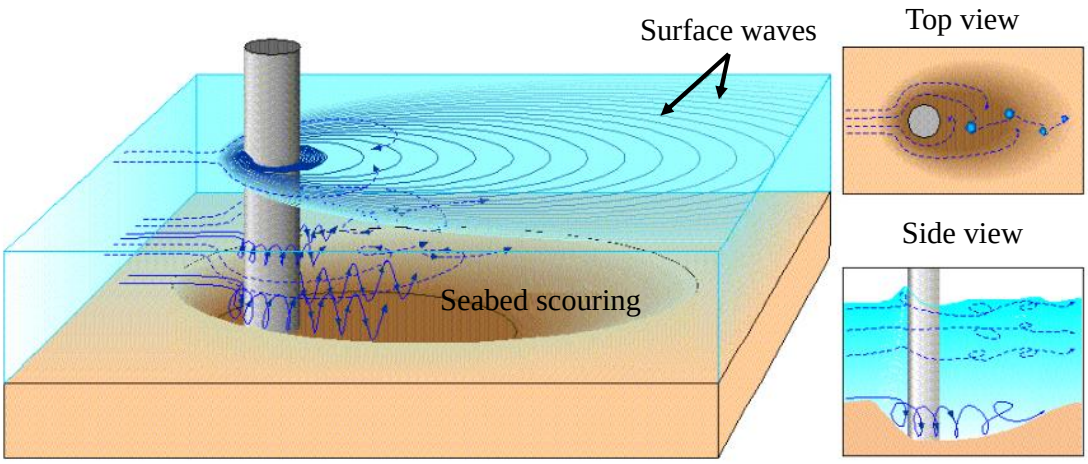

Figure 1-1. Wave vortices and seabed scouring around a cylindrical element (image modified from [12]).

1.2. Conventional flow measurement techniques and their limitations

Several techniques have been reported for tidal flow measurements. Each has specific strengths and weaknesses which makes them appropriate either for low or high flow velocity measurements. In Northern Europe the average tidal current speed is between 2 m/sec with the highest being 5 m/sec (this range is useful for renewable energy applications) [13]. The most common flow velocity methods are the float, dilution gauging, trajectory, electromagnetic and various current meters [14].

According to the *float method*, the flow velocity can be calculated by tracking the travel distance and time of a low density object in a stream, this method can be used only for low and straight streams (e.g. currents that are usually produced in flow canals) [15]. Flow range of a range of 0 - 1 m/sec with accuracy 0.2 m/sec [15]. However, developments in particle tracking algorithms could see improvements in this technique.

The *dilution gauging method* requires diffusion of a chemical tracer with flow velocity obtained by measuring the concentration of the tracer with respect to time. Automated measurements can be provided from electrical conductivity meters or ion electrodes. This method can be used in turbulent flows but environmental water contamination must be considered [16]. This method commonly measures the discharge of a flow (m^3/sec) and is considered as a low accuracy method with percentage probable error varying up to 21% [17].

Flow measurements with the *trajectory method* entail diversion of the stream into a pipe, which necessitates skilled personnel and can be invasive. The rate of the flow in the pipeline is calculated using equations that describe the pressure discharge of a water jet. The velocity measurements comprise difficult calculations [18] and similarly to the dilution gauging method the measurements are expressed as discharge of the flow (m^3/sec) [19]. The California pipe method and the trajectory method (reported by Greeve [18]) are the most common of them with error varying up to 10% [18].

The *electromagnetic method* is based on Faraday's law (for electromagnetic induction) and provides continuous and accurate results of a point velocity in a flow stream. Moreover, it can be used in low and high flow rates. However, diversion of the flow in pipes is needed in a similar manner to the trajectory method [20]. Measurements provided with this method have a range of 0 - 4 m/sec [21] and high accuracy (0.05 m/sec) [22].

Current flow meters can be used in high flow streams and large depths. Point velocity measurements can be taken from well-established devices, such as turbine or propeller flow meters, tilt flow meters or inclinometers. *Turbine and rotor flow meters* have a wide range of velocity measurements (0.01 – 6.0 m/sec) [21] with high accuracy (~0.02 m/sec) [23]. This range depends on the cross sectional area of the pipe where the propeller is installed. *Tilt flow* meters or *inclinometers*, commonly have a cantilever geometry. Their working principle is based on measurements of the dragging force produced on them due to the flow [24]. There are cases where these measurements are enhanced by attaching a spherical material on top of the cantilever. It has been reported that an inclinometer can measure flow speeds up to 0.6 m/sec with high accuracy (~ 0.05 m/sec) [25].

The *Acoustic Doppler Current Profiler* (ADCPs) is the most sophisticated flow meter currently in use. ADCPs use Doppler shift to determine the flow velocity by correlating the frequency of a transmitted sound wave to the echoes from particles in the stream with three or four acoustic beams (at least three are required in order to triangulate the 3-D velocity direction [26]). ADCPs have superseded flow current meters due to the fact that they can provide measurements as a function of depth. An additional advantage of ADCPs is their high accuracy, it is reported that this accuracy can reach ± 0.015 m/sec [27], while the velocity range is between 2.5 to 5 m/sec [28]. Furthermore, ADCPs can give

information about the velocity of a flow stream in three directions [29]. However, ADCPs have two main disadvantages, they are expensive and there is uncertainty in measurements taken in the boundary layer close to the seabed. The standard deviation of the velocity measurements 1 meter above the sea bottom (upper layer) was reported to be 0.065 m/sec [30]. However, the standard deviation for the bottom layer (up to 1 m from the sea bottom) was 0.143 m/sec [30] i.e. more than twice the error. Figure 1-2 (a), (b) and (c) show a schematic diagram of the three above mentioned flow meters.

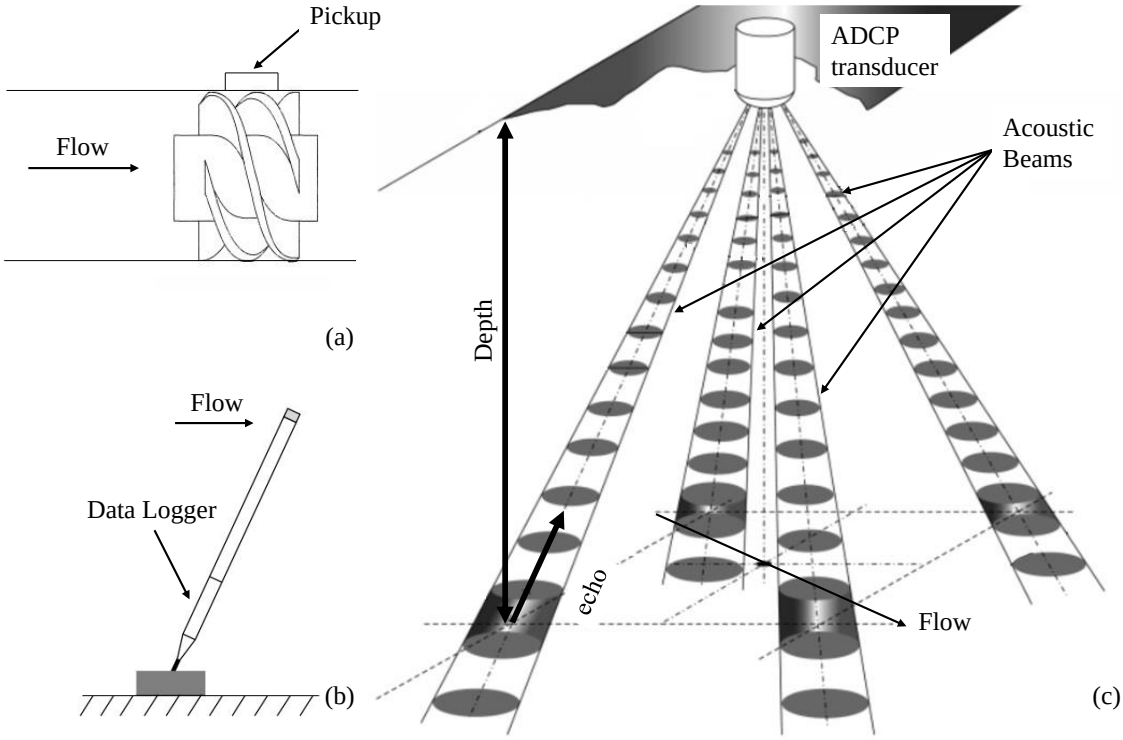

Figure 1-2. (a) Turbine flow meter, (b) Tilt flow meter (image modified from [24]) (c) Acoustic Doppler Current Profiler (image modified from [26]).

1.3. Bioinspired sensing

Throughout history, human beings have learned from and imitated nature, by fabricating different technological inventions for our convenience. Examples of biomimicry include the fields of biophysics, biochemistry and bioengineering [31]. In these areas, combining biological with physical, chemical or engineering principles is explored [32], where the behaviour of biological organisms is incorporated into technological inventions.

Similarly, this work was inspired by the biophysics of the fish lateral line organ. The lateral line is a sensing system, with which fishes are able to: detect prey or avoid

predators [33]; communicate and navigate in groups [34]; identify hydrodynamic environments and; extract energy from the flow [35]. Thus, by mimicking fishes' lateral line system, Lakshmi aims to show that it is possible to extract information about the flow stream of a fluid.

Within fish the flow stream is detected by receptors, which are hair cells extended by hair bundles [35]. These cells are protected by the extracellular cupula and both together constitute the neuromasts. There are two different types of neuromasts in the lateral line system of a fish, the superficial and the canal neuromast. Figure 1-3 (a) shows a full and (b) a magnified image of a Mexican cave fish (*Astyanax mexicanus*) and specifically the neuromasts. Moreover, Figure 1-3 includes a schematic diagram of fish's skin (c) where the superficial (d) and canal (e) neuromasts are shown. The superficial neuromasts are located on the skin of the fish and deflections of the neuromast arise directly from the flow. Subsequently, the displacement of the hair bundles is transduced to electrical potentials. Conversely canal neuromasts are positioned underneath the fish skin and they are sensitive to environmental pressure changes [36].

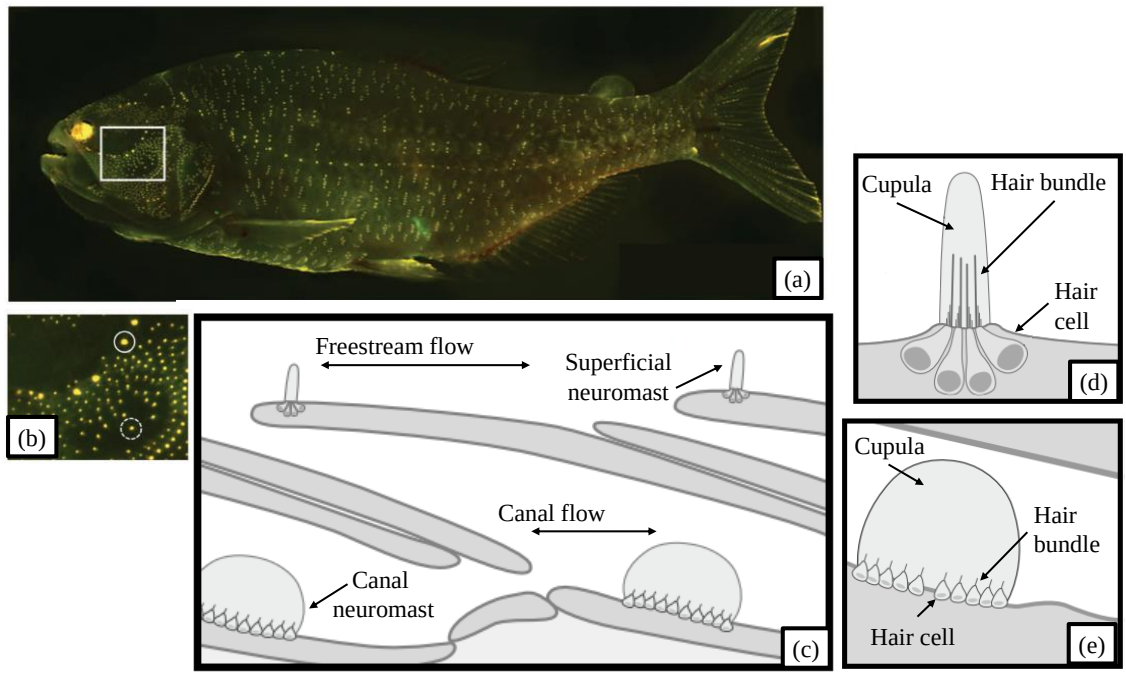

Figure 1-3. (a) Full and (b) magnified image, of a blind Mexican cave fish where the fluorescent staining is the superficial (dashed circle) and canal (solid circle) neuromasts (images taken from [36]) and cross sections schematic diagrams of the fish's skin (c), superficial neuromast (d), canal neuromast, respectively (e) (images modified from [35]).

1.4. Optical fibre flow sensors

Optical fibre sensors have potential to surpass existing flow sensors due to the inherent advantages characterising optical fibres [37]: (a) Their small volume and flexibility allow them to be embedded or cast into other materials or to access remote areas. (b) Optical fibre sensors are a scalable technology. They can be connected (multiplexed) thus creating an array with minimal physical connectivity requirements. Therefore, by collecting several point measurements of the flow at the seabed, hydrodynamic imaging can be achieved. Finally, (c) an optical fibre is a dielectric material which transfers signals optically without the need for electrical components. Therefore, optical fibre sensors are slow to fail due to water ingress.

1.4.1. Sensors technology

The fabrication of the optical fibre flow sensors presented in this thesis, is inspired by the biological structure of the fishes' lateral line neuromasts. A schematic diagram of the general concept of the flow sensor is shown in Figure 1-4. Their geometry (cantilever geometry) is similar to the superficial neuromast (Figure 1-3 (d)). However, the same sensors can be embedded into membranes and create a canal neuromast (Figure 1-3 (e)).

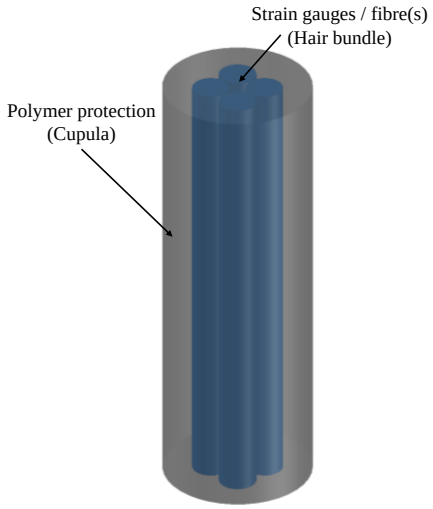

Figure 1-4. Schematic diagram of the flow sensors' geometry.

Two different types of sensors were explored, a Multicore fibre (MCF) curvature sensor (Figure 1-5 (a)) and a 'four single mode fibres or stem' flow sensor (Figure 1-5 (b)). In both cases the deflection of the sensor is transduced to strain changes and measured through an optical signal transmitted within the optical fibres. In the case of the MCF curvature sensor the fibre itself corresponds to the hair bundle, while in the second

case sensor the fibres 'stem' acts as the hair bundle. Finally, the cupula can be associated with the polymer protection. This sensor configuration provides has an additional benefit, the direction of the flow can be determined alongside with the flow measurements.

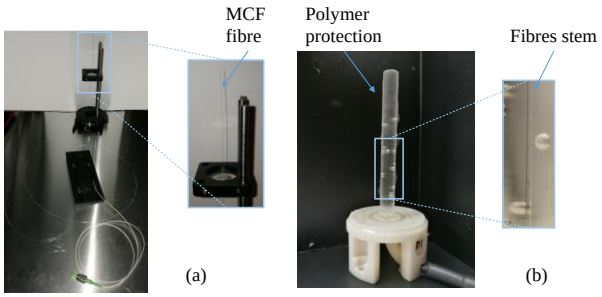

Figure 1-5. Fabricated sensors during LAkHsMI project (a) MCF curvature sensor, (b) 'four single mode fibres flow' sensor.

1.4.2. Final arrangement of the sensors system for subsea measurements

The decision of the sensor's geometry (stem or cantilever geometry) was taken in reference to several considerations. The optical fibre flow sensors, fall into the "current flow meter" (1.2) category and the operational principle is similar to the tilt meter which can provide measurements with high accuracy. The sensors are designed to measure the flow speed close to the bottom of the sea (~ 0.02 - 1 m from the seabed). This is a regime where the ADCPs have their highest error in flow measurements. Despite the fact that they can be characterised as single point measurements, they can be easily connected to each other in arrays, since they are fabricated from optical fibres. The same sensors are "adaptable" and can be rearranged in order to measure flow speed at different depths. Finally different protection materials (polymer protection Figure 1-5 (b)) can be explored in order to optimise their use in different flow speed ranges through variation in the stiffness. Figure 1-6, shows an initial trial ready for deployment in Oban (UK) coastline.

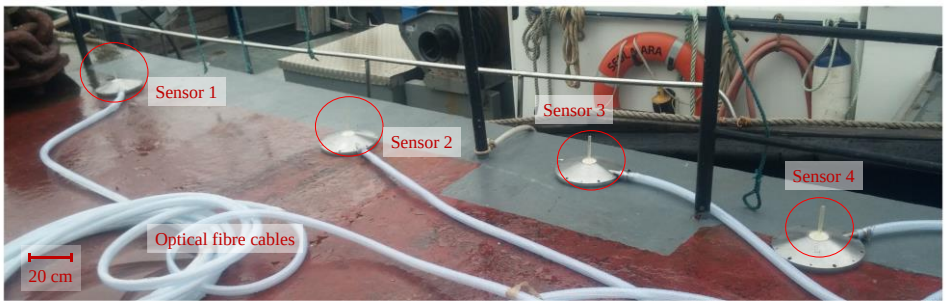

Figure 1-6. Initial flow optical fibre sensors used for measurements at Oban coastline foe LAkHsMI project.

An additional aim for LAkHsMI is to provide information about the flow direction at a number of locations as well as the velocity. Optical fibre flow sensors can provide measurements by fixing the sensors on a sensing platform (see Figure 1-7). The platform's orientation in regard to the seabed is required for directional measurements. This led to the development of an attitude sensor which could be enclosed in the platform. This sensor has the same technology with the flow sensors for experimental convenience.

Another objective of LAkHsMI's is to provide real time measurements of subsea temperatures. This is for two main reasons: (a) Subsea temperature measurements for research purposes. For example, temperature variations of streams can affect the flora and fauna of the oceans and seas [38], or understanding environmental impact such as ice shelves melting [39]. The second reason is due to practical limitations (b): The optical fibre flow sensors may be temperature sensitive. Therefore, measurements obtained from them require temperature compensation.

Final sensor unit deployment is shown in Figure 1-7, where four flow sensors and three temperature sensors are mounted on the outside of the deployment platform and can be used for direct measurement of the sea flow and temperature, while the attitude sensor and optical components are packed inside the main body. This sensor deployment (Figure 1-7) is considered to provide four point flow measurements each associated with one of the four 20 cm sensing elements. Nevertheless, by connecting identical platforms together an array can be created.

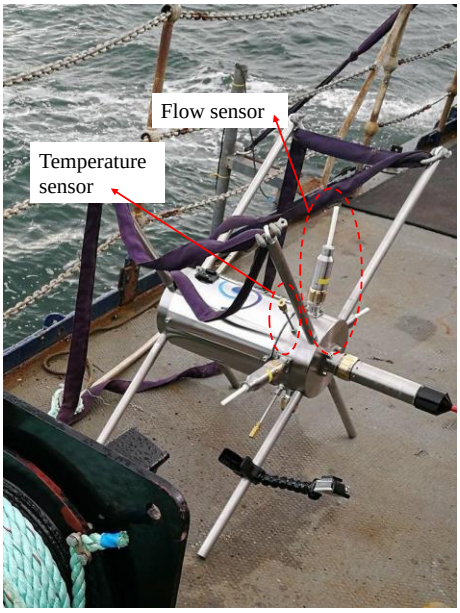

Figure 1-7. Final arrangement of sensors system unit, the picture was taken before deployment at the Orkney Islands (Stromness, UK).

1.5. LAkHsMI background and partners

LAkHsMI is a European Union's Horizon 2020 funded research project, under grant agreement No: 635568, and consists of 6 project partners, where three are scientific research groups based at three European universities, while the others are companies: (1) Tallinn University of Technology (TUT), Estonia, (2) University of Groningen (RUG), Netherlands, (3) Heriot-Watt University (HWU), United Kingdom, (4) Hydro Bond Engineering Ltd., United Kingdom, (5) Aquatera Ltd. Orkney Islands, United Kingdom and (6) Eliko TAK., Estonia. Each partner's geographical location as well as the project logo is shown in Figure 1-8.

The primary aim of LAkHsMI's project is the fabrication of Sensors for LArge scale HydrodynaMic Imaging. Heriot-Watt University's objective in this project, is to fabricate and test optical fibre sensors capable of measuring the following subsea environmental parameters: (a) flow velocity and direction, (b) temperature, and (c) pressure.

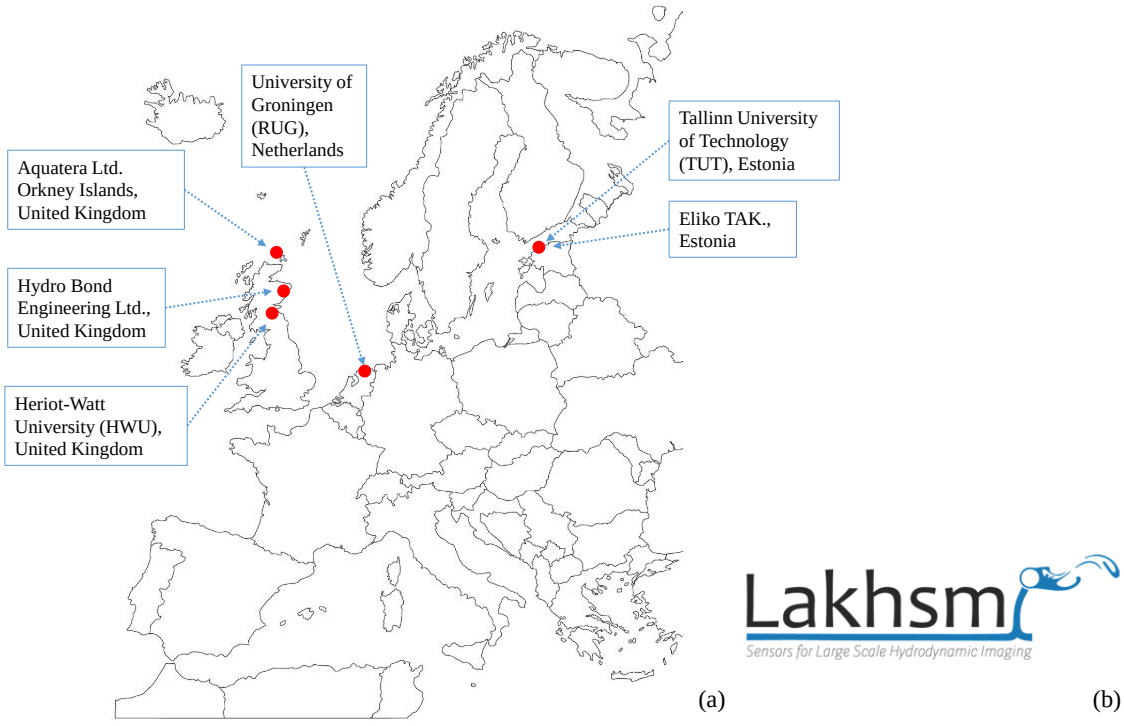

Figure 1-8. (a) Geographical location of project's partners across Europe and (b) project logo.

1.6. My contribution at LAkHsMI project

As a PhD student at Heriot Watt University my contribution at LAkHsMI project was focused on the fabrication and performance tests of the optical fibre sensors. Three

different types of optical fibre sensors were explored: temperature, attitude and flow sensors. Additionally, the flow sensors that I was mainly focused on (MCF curvature sensors (Figure 1-5 (a)), were considered as the "next generation" flow sensors for the project. Hence, I concentrated on recognising their weaknesses and improving their performance. Finally, I was partly responsible on the packaging of the sensors for deployment. As well as connecting them in order to create an array.

The sensors produced for LAkHsMI's project field trials can provide measurements temperature and flow measurements as well as flow direction at different points of the seabed. The sensors unit as well as the application that can be used are considered of a great novelty.

1.7. Thesis outline

This thesis is organised based on the experimental work produced for LAkHsMI project at Heriot-Watt University. Here, an introduction and a literature review chapter are designated (Chapter 1 and 2). These are required for the experimental results (Chapters 3, 4 and 5) to be comprehended. The optical fibre sensors reviewed in the thesis were either actually used on field trials or explored for potential use. A final overview of all fabricated sensors for LAkHsMI sensors is provided at the conclusions Chapter (Chapter 6).

Chapter 1 is an introduction chapter which includes the motivation for the work reported in this thesis. The final aim of this work was to produce flow sensors for hydrodynamic imaging and subsea measurements. Therefore, a brief review of conventional flow measurements and technique is given. Moreover, the inspiration of the flow sensor's structure (bioinspired) is reviewed. Finally, the background of LAkHsMI project and the partners are reported.

Chapter 2 includes an extended literature review on sensors. The general concept of relevant types of sensors is reported. The chapter is focused on optical sensors with the optical fibre sensors being the primary category of review. Fibre Bragg Grating (FBG) sensors are thoroughly studied, since these type of sensors are going to be developed in the experimental chapters. Moreover, the temperature and the strain sensitivity of the FBG sensors are explored. I will also consider FBG curvature sensors, which are basically strain sensors. In the final paragraphs, the theory on coupling of light from one fibre to

another is reported. This theory is useful for understanding the fabrication of the final MCF curvature sensor.

Chapter 3 is an experimental chapter where the fabrication and calibration of FBG temperature and attitude sensors are explored. Both sensors were used in field trails for LAkHsMI project experiments.

Chapter 4 explores the fabrication and the performance of a MCF curvature sensor. The multi-core nature of the fibre makes it ideal for measurements of curvature of the fibre. However, it requires an interface component in order to couple light from the MCF cores to conventional optical fibres which can be connected to spectrometers or interrogators. The commercially available interface devices are called fan-outs [40], and one of these was used for the fabrication of the sensor reported in this chapter. Studies show that this sensor is sensitive to environmental temperature variations.

Chapter 5 explores the prospect of eliminating the fan-out device by producing a tapered region along the MCF. At this region coupling of light from one core of the MCF to all four cores can be achieved. Theoretical as well as experimental studies were performed for optimising the tapering parameters. Consequently, by splicing one core of the fibre to a single mode fibre (SMF) light transmittance can be achieved. This sensor appeared to be less sensitive to temperature variations.

Chapter 6 includes an overview of all optical fibre sensors that were fabricated at Heriot – Watt University for the LAkHsMI project. A comparison between three main optical fibre curvature sensors produced for the project is reported. Finally, in this chapter options for future work and development of the sensors are discussed.

1.8. References

[1] S. P. Windsor, S. E. Norris, S. M. Cameron, G. D. Mallinson, and J. C. Montgomery, "The flow fields involved in hydrodynamic imaging by blind Mexican cave fish Part II: gliding parallel to a wall," *The Journal of Experimental Biology*, vol. 213, no. 22, pp. 3832-3842, 2010.

[2] E. S. Hassan, "Hydrodynamic Imaging of the Surroundings by the Lateral Line of the Blind Cave Fish Anoptichthys jordani," *Springer New York*, pp. 217-227, 1989.

[3] D. S., "The functioning and significance of the lateral line organs," Biological Reviews, vol. 38, no. 1, pp. 51-105, 1963.

[4] Y. Yingchen, N. Nguyen, N. Chen, M. Lockwood, C. Tucker, H. Hu, H. Bleckmann, C. Liu and D. Jones., "Artificial lateral line with biomimetic neuromasts to emulate fish sensing," *Bioinspiration & Biomimetics*, vol. 5, no. 1, p. 016001, 2010.

[5] G. Emmanouil, G. Galanis, C. Kalogeri, G. Zodiatis, and G. Kallos, "10-year high resolution study of wind, sea waves and wave energy assessment in the Greek offshore areas,"Renewable Energy, vol. 90, pp. 399-419, 2016.

[6] L. Dengler and B. Uslu, "Effects of Harbor Modification on Crescent City, California's Tsunami Vulnerability," *Pure and Applied Geophysics*, vol. 168, no. 6, pp. 1175-1185, 2011.

[7] T. Soomere, "Fast Ferry Traffic as a Qualitatively New Forcing Factor of Environmental Processes in Non-Tidal Sea Areas: A Case Study in Tallinn Bay, Baltic Sea," *Environmental Fluid Mechanics*, vol. 5, no. 4, pp. 293-323, 2005.

[8] C. T. Stansberg, R. Baarholm, T. Kristiansen, E. W. M. Hansen, and G. Rortveit, "Extreme Wave Amplification And Impact Loads On Offshore Structures," *in Proc. Offshore Technology Conference*, 2013.

[9] F.P. Gao, B. Yang, Y.X. Wu, and S.M. Yan, "Steady current induced seabed scour around a vibrating pipeline," *Applied Ocean Research*, vol. 28, no. 5, pp. 291-298, 2006.

[10] Q. Zheng, L. Li, X. Guo, Y. Ge, D. Zhu, and C. Li, "SAR imaging and hydrodynamic analysis of ocean bottom topographic waves," *Journal of Geophysical Research*, vol. 111, no. C9, 2006.

[11] A. Erm and T. Soomere, "The impact of fast ferry traffic on underwater optics and sediment resuspension," *Oceanologia*, vol. 48, pp. 283-301, 2006.

[12] *Earth Word-Scour.* (Access date: 05.10.2018) Available: www.usgs.gov/news/earthword-scour

[13] M. Grabbe, E. Lalander, S. Lundin, and M. Leijon, "A review of the tidal current energy resource in Norway," *Renewable and Sustainable Energy Reviews*, vol. 13, no. 8, pp. 1898-1909, 2009.

[14] P. Dobriyal, R. Badola, C. Tuboi, and S. A. Hussain, "A review of methods for monitoring streamflow for sustainable water resource management," *Applied Water Science*, vol. 7, no. 6, pp. 2617-2628, 2017.

[15] A. Hauet, J.-D. Creutin, and P. Belleudy, "Sensitivity study of large-scale particle image velocimetry measurement of river discharge using numerical simulation," *Journal of Hydrology*, vol. 349, no. 1, pp. 178-190, 2008.

[16] C. Comina, M. Lasagna, D. A. De Luca, and L. Sambuelli, "Geophysical methods to support correct water sampling locations for salt dilution gauging," *Hydrology and Earth System Sciences*, vol. 18, no. 8, pp. 3195-3203, 2014.

[17] T. J. Day, "On the precision of salt dilution gauging," *Journal of Hydrology*, vol. 31, no. 3, pp. 293-306,1976.

[18] F. W. Greve, *Measurement of pipe flow by the coordinate method*. Lafayette, Ind.: Purdue University, 1928.

[19] W. F. Vlotman, "Discharge measurement structures," *Delft Hydraulics Laboratory*, 1989.

[20] H. Ryckborst and R. O. Christie, "Feasibility of electromagnetic streamflow measurements using the earth's field " *Hydrological Sciences Bulletin*, vol. 22, no. 2, pp. 241-255, 1977.

[21] R. W. Herschy, "Streamflow Measurement, Third Edition," *Taylor & Francis*, 2008.

[22] C. S. Li Ke, "Electromagnetic Flow Meters Achieve High Accuracy in Industrial Applications," *AnalogDialogue*, vol. 48, 2014.

[23] *Comparing Flowmeters*. (Access date: 05.10.2018). Available: www.engineeringtoolbox.com/flowmeter-selection-d_526.html

[24] N. S. Lowell, D. R. Walsh, and J. W. Pohlman, "A Comparison of Tilt Current Meters and an Acoustic Doppler Current Meter in Vineyard Sound, Massachusetts," *IEEE/OES 11th Current, Waves and Turbulence Measurement*, 2015.

[25] R. Marchant *et al.*, "A Buoyant Tethered Sphere for Marine Current Estimation," (in English), *Ieee Journal of Oceanic Engineering*, vol. 39, no. 1, pp. 2-9, Jan 2014.

[26] M. Muste, K. Yu, and M. Spasojevic, "Practical aspects of ADCP data use for quantification of mean river flow characteristics; Part I: moving-vessel measurements," *Flow Measurement and Instrumentation*, vol. 15, no. 1, pp. 1-16, 2004.

[27] S. Jimenez-Gonzalez, R. Mayerle, and J. J. Egozcue, "On the accuracy of acoustic Doppler current profilers for in-situ measurements. A proposed approach and estimations for measurements in tidal channels," *in Proc. IEEE/OES Seventh Working Conference on Current Measurement Technology, 2003.*, 2003, pp. 197-201.

[28] Nortek. *Ocean currents/current profiler*. (Access date: 05.10.2018) Available: www.nortekgroup.com/products/ocean-currents

[29] R. Kostaschuk, J. Best, P. Villard, J. Peakall, and M. Franklin, "Measuring flow velocity and sediment transport with an acoustic Doppler current profiler," *Geomorphology*, vol. 68, no. 1-2, pp. 25-37, 2005.

[30] S. Jiménez-González, R. Mayerle, and J. J. Egozcue, "A proposed approach for the determination of the accuracy of acoustic profilers for field conditions," *PROMORPH* 2006, pp. 409-420.

[31] J. Kang and C. B. Purnell, "Implications for Undergraduate Education of Two Interdisciplinary Biological Sciences: Biochemistry and Biophysics," *CBE—Life Sciences Education*, vol. 10, no. 2, pp. 111-112, 2011.

[32] R. Doursat, H. Sayama, and O. Michel, "A review of morphogenetic engineering," *Natural Computing*, vol. 12, no. 4, pp. 517-535, 2013.

[33] D. K. Bassett, A. G. Carton, and J. C. Montgomery, "Saltatory search in a lateral line predator," *Journal of Fish Biology,* vol. 70, no. 4, pp. 1148-1160, Apr 2007.

[34] B. L. Partridge and T. J. Pitcher, "The sensory basis of fish schools: Relative roles of lateral line and vision," *Journal of Comparative Physiology A,* vol. 135, no. 4, pp. 315-325, 1980.

[35] S. M. van Netten and M. J. McHenry, "The Biophysics of the Fish Lateral Line," *The Lateral Line System. Springer Handbook of Auditory Research* vol. 48, pp. 99-119, 2013.

[36] S. P. Windsor and M. J. McHenry, "The influence of viscous hydrodynamics on the fish lateral-line system," *Integrative and Comparative Biology,* vol. 49, no. 6, pp. 691-701, 2009.

[37] D. A. Jackson and J. D. C. Jones, "Fibre Optic Sensors," *Optica Acta: International Journal of Optics,* vol. 33, no. 12, pp. 1469-1503, 1986.

[38] A. Clarke, R. B. Aronson, J. A. Crame, J.-M. Gili, and D. B. Blake, "Evolution and diversity of the benthic fauna of the Southern Ocean continental shelf," *Antarctic Science,* vol. 16, no. 4, pp. 559-568, 2004.

[39] P. R. Holland, A. Jenkins, and D. M. Holland, "The Response of Ice Shelf Basal Melting to Variations in Ocean Temperature," *Journal of Climate,* vol. 21, no. 11, pp. 2558-2572, 2008.

[40] R. R. Thomson H. T. Bookey, N. D. Psaila, A. Fender, S. Campbell, W. N. MacPherson, J. S. Barton, D. T. Reid, and A. K. Kar. "Ultrafast-laser inscription of a three dimensional fan-out device for multicore fiber coupling applications," *Optics Express,* vol. 15, no. 18, pp. 11691-11697, 2007.

Chapter 2. Literature Review

Here an overview of sensors and their impact on a broad range of scientific fields is presented. Optical sensors constitute a subcategory of sensors which take advantage of the properties of light to extract information about their environmental surroundings. Optical fibre sensors are also reviewed here, with the Fibre Bragg Grating (FBG) sensors thoroughly explored including their use in various applications.

Then concentrates on the fabrication of a curvature sensor using FBGs in a fibre with multiple cores. The mechanical properties of the sensor as well as the optical response of the FBGs are reviewed. Finally, different ways of monitoring the sensor's reflection spectra are discussed.

2.1. Overview

Sensors are devices which detect changes of one or more parameters of their surrounding environment and convert them into a useful signal (transducer). Numerous sensors have been developed to date, many of these have been exploited to provide benefits to everyday life. Examples include: Fire alarms, where gas, smoke or temperature changes are detected and can trigger an alarm. Motion sensors, increasingly used for electrical energy preservation and environmental sustainability, as well as safety and security applications. Recent developments include wearable sensors and internet enabled sensors which are connected to or embedded inside smartphone devices or personal computers. The increased availability of small, high performance sensors offers the prospect of new applications, for example health awareness and monitoring [1, 2].

Despite the wide range of commercially available sensors, there is still interest in developing new sensors or advancing those already existing. This aims to improve some aspect of the sensor for example higher sensitivity, quicker response, less complex interface, and smaller (or larger) volume depending upon their intended applications. Figure 2-1 shows a range of sensors in the global market for years 2015 and 2020, by application. According to Statista Ltd [3] the sensors market size reached 95.3 billion U.S. Dollars in 2015. Image sensors are top-listed in the market share (Figure 2-1), this is due to the fact that sensors in this category occupy a wide range of applications with great importance. Characteristic examples include environmental monitoring and healthcare imaging.

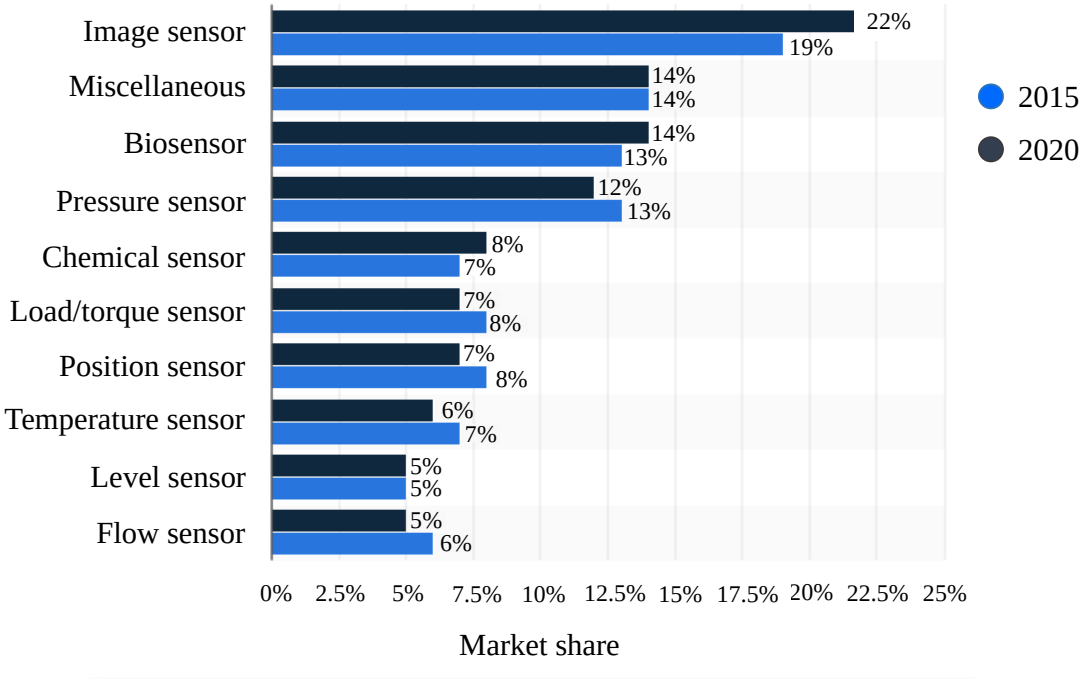

Figure 2-1. Breakdown of the global sensors market, by application [3].

There are two different ways to categorise sensors: sensing principles or applications. Based on sensing principle the most important groups of sensors are: (a) mechanical and magnetic sensors which use the materials' properties to detect environmental changes [4, 5], (b) acoustic, wave or vibration sensors, with seismometers being of particular importance [6], (c) chemical sensors, with the pH sensor being commonly referenced in literature [7], (d) electrical sensors, with the thermocouples being a distinctive example [8], (e) image sensors with numerous examples in commonplace technological devices such as fingerprint detectors in smartphones [9] and (f) optical sensors which use changes in an optical signal as a detecting technique [10, 11]. A recent addition to this list is bioinspired sensors, which mimic sensing techniques and geometries of sensors in nature [12, 13].

Secondly, sensors can be categorised according to their applications range as: (a) environmental monitoring sensors, with the water or food contamination , being a primary objective [14], (b) biosensors, which are used for the detection of viruses or illnesses in biological and medical applications [15], (c) structural health monitoring sensors for safety awareness, including applications in airframe and bridge health monitoring [16], (d) navigation system sensors (inertia), with the fabrication of various types of gyroscopes [17], and (e) other sensors that are used for detection of changes o various physical parameters such as temperature, pressure, strain, rotation, and flow [18, 19].

2.2. Review of optical sensors

Sensors in this category use the properties of light to detect or measure changes in their environmental surroundings. Their wide range of applications is attributed to their advantages which are reviewed here [20].

2.2.1. Advantages and disadvantages of optical sensors

Due to the fact that an optical signal is used for detection, optical sensors have unique advantages which can be highly competitive with other types of sensors. Optical signals are characterised with high measurement accuracy and resolution resulting in sensors with exceptional sensitivity. An example of which are optical interferometers which have been used for atomic force microscopy [21] and are capable of submicron resolution. Additionally, optical sensors provide quick response measurements and can be cost effective [22].

Despite the fact that electrical sensors are well developed and established, optical sensors have also seen growth mainly because of their ability to overcome problems with traditional electrical sensors (e.g. where metal parts are in-compatible with the sensing environment). Distinctive examples are the optical sensors used during MRI scanning [23] to monitor patients vital sings. Other advantages include optical sensor's low weight and inherent safety (e.g. spark removal). Several aerospace applications have been reported such as for gas leak detections [24] or structural health monitoring [25] or the optical fibre sensor, proposed by Ramsden, for monitoring gas concentrations in a space craft cabins [26]. Finally, optical sensors favour distributed sensing; their ability to be connected to each other facilitate deployment with multiple, simultaneous measurements [27].

Nonetheless, there is one main disadvantage. Sensors that are fabricated to measure one specific physical parameter can be affected by other environmental changes. This feature is commonly termed as cross-sensitivity (also an issue with electrical sensors). The most distinctive examples include pressure [24] or strain sensors [28] which can be affected by environmental temperature changes. However, several compensation techniques have been developed for these cases [29],commonly by measuring each parameter independently. Additional issues include the fabrication cost and the lack of

user familiarity with this technology. Finally, optical losses due to scattering or absorption of the optical signal have to be considered.

2.2.2. Sensing techniques and characteristic examples of optical sensors

The general properties of an optical signal are intensity, wavelength (or wavelength range), phase and polarization. When this signal interacts with matter or another optical signal these properties can change through various phenomena such as absorption, reflection, diffraction, refraction, or interference. Researchers have taken advantage of these phenomena in order to establish unique optical sensing techniques and various optical sensors designs [30].

An example of this is gas sensing, were information can be extracted out of the *absorbance* spectra of an optical signal, propagated through a gas sample [31]. The majority of these sensors are used for environmental monitoring. However, gas sensors are of great importance for safety purposes. Characteristic examples include sensors used for avoidance of explosions [32] as well as toxic gas leakages. These sensors have a wide range of accuracies which depend on the sensing method and gas to be detected. An example, for water vapour the minimum detectable concentration (70ppt) has been achieved with second harmonic wavelength modulation spectroscopy [31].

Additionally, when light is *absorbed* by a molecule it can be excited and after that relaxed, through several mechanisms. The most studied mechanism is fluorescence *emission*, where multiple sensors have been fabricated with numerous applications in biosensing [33]. Sensors in this category are commonly used to measure the fluorescence intensity [34] or the lifetime [35] which are characteristic to a material. Schematic diagrams of both, gas optical sensors and fluorescent emission sensors are shown in Figure 2-2 (a) and (b).

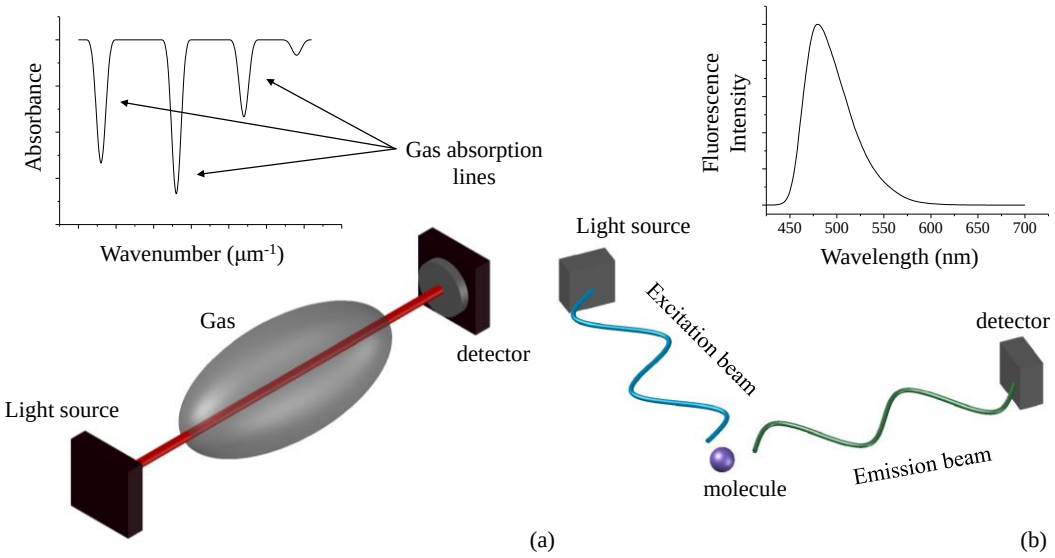

Figure 2-2. Schematic diagram of (a) an optical gas absorption sensor, (b) fluorescent emission biosensor.

One commonly optical sensor in literature is the surface plasmon resonance sensor [36], with applications for detection of chemical or biological molecules [37]. Plasmon resonance sensors use both *refraction* and *absorption* properties of light for molecular detection. Figure 2-3 (a) shows a schematic diagram of these sensors, which have been used for detection of molecules such as analytes, proteins, DNA and RNA.

The phenomena of *diffraction* or *refraction* have also been used for the development of refractive index sensors. Examples include waveguide sensors [38], grating sensors and light coupling sensors [39]. Figure 2-3 (b) shows a schematic diagram of a waveguide coupler sensor. In this case the intensity of the light after the coupling is affected by the refractive index of the environment where the waveguides are close with each other.

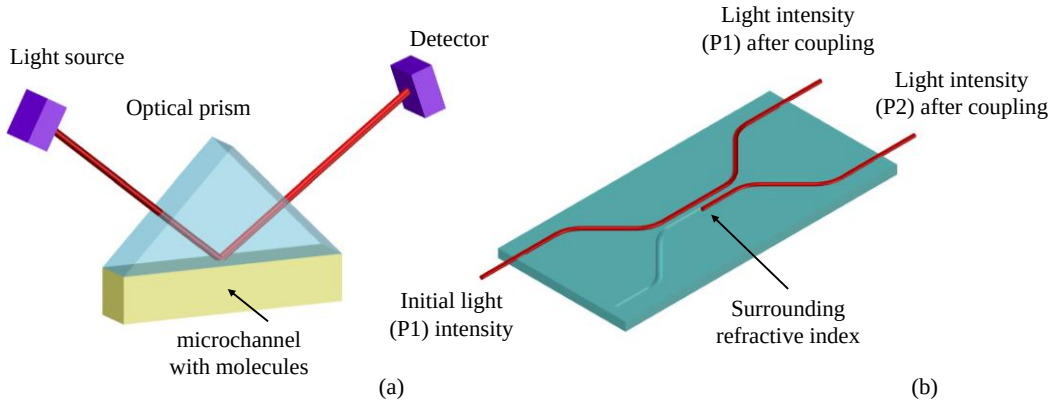

Figure 2-3. Schematic diagrams of (a) a surface plasmon resonance sensor and (b) waveguide coupler sensor.

Polarization shifts can occur when a polarized optical beam gets reflected, absorbed or passes through birefringent materials [40]. Various polarisation sensors have been reported in literature with navigation [41] and imaging sensors being key examples [42]. An example of navigation sensor mimics the function of the eye of an ant [43]. The sensor monitors the polarization of Rayleigh scattered light from the sky above the observer (zenith) and correlates it with scattered light coming from the sun, hence navigation can be achieved. The second is an imaging sensor which uses a CCD (charged coupled device) camera capable of monitoring the optical properties of the reflected light which is partially polarized.

Finally, *interferometric* sensors constitute a large group of optical sensors, where the phase or intensity shifts of an optical signal are monitored. Interference occurs when two or more beams interact. Several examples of interferometric sensors have been reported in the literature, the best known type is the Michelson interferometer (schematic diagram in Figure 2-4 (a)) [44]. The first Michelson-Morley-Miller interferometric "sensor" was fabricated for the detection of the aether [45]. While in 2016 an advanced version the same setup was used for the detection of gravitational waves (Nobel Prize in Physics (2017), Rainer Weiss, Barry Barish and Kim Thorne) [46]. An aerial image of the Laser Interferometer Gravitational-Wave Observatory is shown in Figure 2-4 (b).

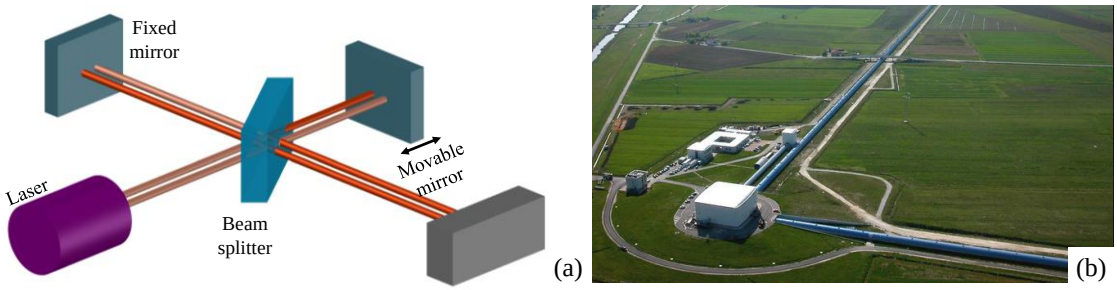

Figure 2-4. (a) Schematic diagram of the Michelson interferometer (b) aerial view of the Laser Interferometer Gravitational-Wave Observatory (LIGO- figure taken from [47]).

Other examples of resonators include the Mach - Zehnder (schematic diagram shown in Figure 2-5 (a)) [48] and the ring laser resonator [49]. W. M. Macek and D. T. Davis used the ring laser resonator technique in order to fabricate the first optical gyroscope in 1963 [50] and Figure 2-5 (b) shows a schematic diagram of this type of sensor. Recent advances include, fiber optic gyroscopes (FOGs) [51] or interferometric fibre optic gyroscopes (IFOGs) [52]. These gyroscopes are commercially available (commonly with bias offset ± 2°/h [53]) and commonly used in aircraft navigation. Many of these optical

techniques can be deployed using optical fibres and the next section includes a detailed review of optical fibre sensors.

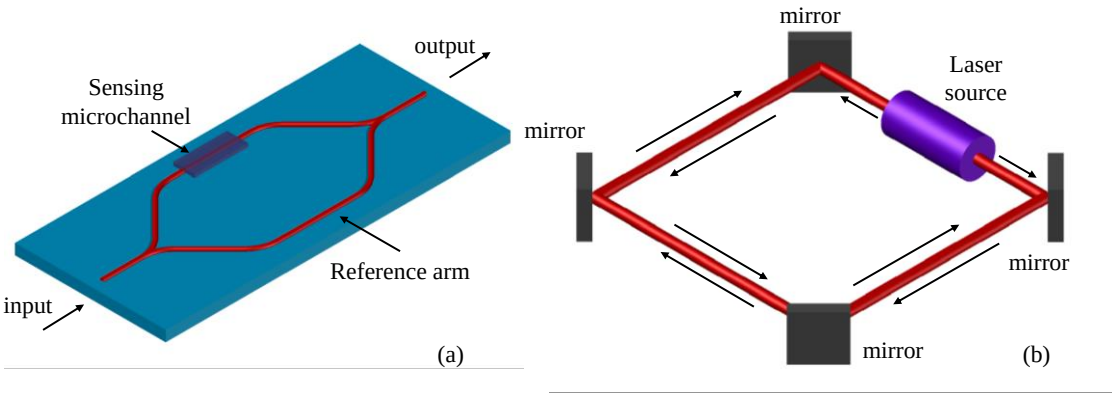

Figure 2-5. Schematic diagram of (a) a Mach Zehnder waveguide interferometric sensor and (b) a ring laser resonator, used for the first gyroscope fabrication

2.3. Optical fibre sensors

Being a subcategory of optical sensors, fibre sensors are characterised with many of the same strengths and weaknesses reported in paragraph 2.2.1. However, due to the nature of optical fibres, some additional advantages arise. They are compatible with optical communication technologies and benefit from the development of commercially available components. Thus optical fibre sensors can be fabricated using commercial of-the-shelf-technology components. Their fabrication materials and their small volume, makes them robust and resilient to high temperatures (~900°C), hence they are excellent candidates for harsh environment applications. Optical fibres provide optical signal transmittance over large lengths with low losses (0.2 dB per km at communication wavelengths) and can be efficiently multiplexed [54, 55]. Finally, they are flexible, allowing deployment of sensitive optical techniques outside the lab.

2.3.1. Optical fibres

An optical fibre is a cylindrical optical waveguide into which light can be coupled and guided. Optical fibres consist a light guiding core and a cladding region, where the refractive index of the core region is higher than the cladding. This confines the light to mainly propagate in the core [56].

The fabrication of optical fibres is a well-established procedure, where glass (doped or pure fused silica) or plastic (PMMA) cylindrical rods known as preforms and canes are drawn down in size while they are heated [57]. Variations of the refractive index in the

core or cladding regions can be achieved by diffusing various dopants into the preform before the drawing procedure. The most common dopant is germanium dioxide (GeO_2) which is deposited in the core region and increases the refractive index [58]. Similarly, Aluminium oxide (Al_2O_3) can be used in the core region. Alternatively, reduction of the refractive index can be achieved by doping the cladding region with fluorine or boron trioxide (B_2O_3) [59].

Commonly, optical fibres can be categorized in two different types, multimode (MMFs) and single mode optical fibres (SMFs). The modes are the possible solutions of Maxwell's electromagnetic waves equations using the boundary conditions for the case of cylindrical waveguides (e.g. optical fibres). MMF can support more than one transverse mode of light propagation. MMF often have greater than 50 μm core diameter and their refractive index profile can be either stepped or graded. Light propagation in graded index fibres sees less dispersion than step index MMF [60]. Figure 2-6 shows the refractive index profiles and a schematic diagram of both above mentioned fibre types.

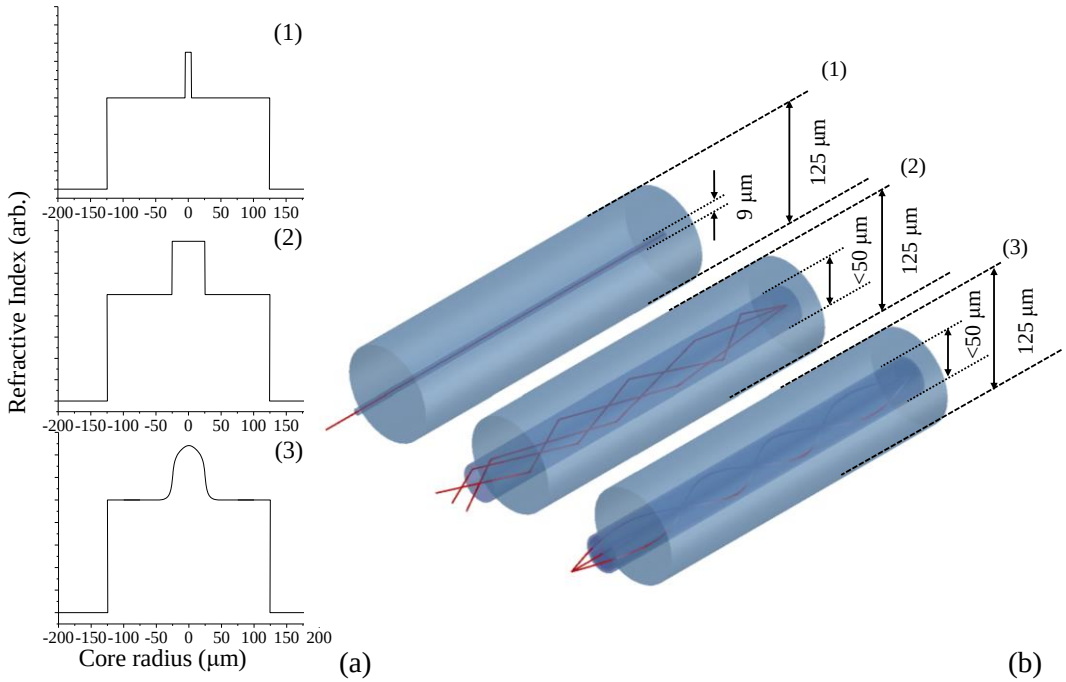

Figure 2-6. (a) Refractive index profiles and (b) schematic diagrams of the optical fibres with light guided rays for the different types of optical fibres, (1) Single mode fibre, (2) step-index multimode fibre and (3) gradient index multimode fibre.

Apart from the core diameter, single mode fibres can be differentiated from multimode fibres through the normalized frequency parameter. This parameter is also called the '*V* number' and can be calculated through the following equation:

$$V = \frac{2\pi\alpha}{\lambda}\sqrt{n_{core}^2 - n_{clad.}^2} = \frac{2\pi\alpha}{\lambda}NA \qquad \text{Equation 2.1}$$

where α and n_{core} are the radius and the refractive index of the core respectively, λ is wavelength of the optical signal coupled in the fibre, n_{clad} the cladding's refractive index and NA is the numerical aperture of the fibre. The V number can be used to predict the transmittance modes and a fibre is considered to be single mode when $V < 2.4048$.

SMFs usually have 8-9 μm core diameter for light propagation with wavelength in the conventional telecommunication band (~1530-1565). Their refractive index profile allow only one mode of light propagation with strong coupling in the core by liming the core radius and or the refractive index contrast in accordance with Equations 2.1. Hence they outmatch the MMFs when considering inter-modal dispersion [61].

In recent years other types of optical fibres have been designed and used in several scientific fields, with several operating with significantly different guidance principles. Polarization-maintaining optical fibres (PM-fibres), fibres with multiple cores (multicore fibres) and fibres with hollow cores (Photonic crystal fibres), are characteristic examples. In recent years the super continuum generation in photonic crystal fibres is one of the most studied phenomenon and has led to new light sources and applications [62]. Characteristic cross sections of a PM-fibre (a), a multicore fibre (b) and a photonic crystal fibre (c) are shown in Figure 2-7.

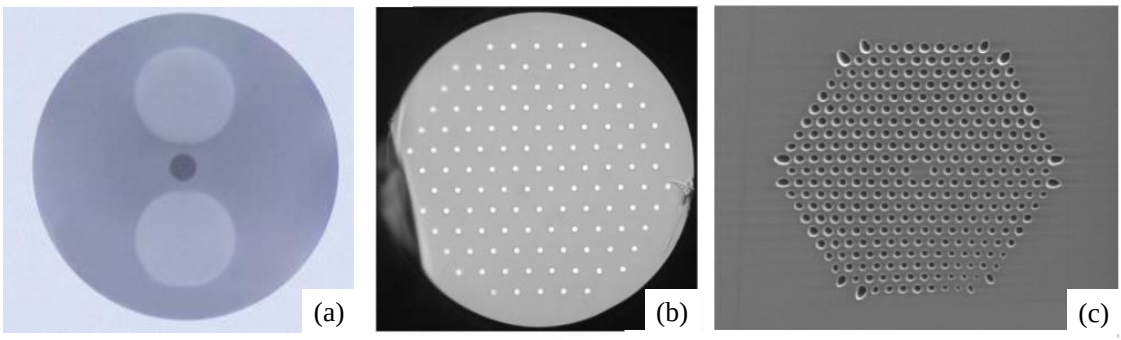

Figure 2-7. Optical fibre cross sections, of characteristic examples used in research of (a) a PM-fibre (PANDA, image modified from [63]), (b) a multicore fibre (121-cores) (figure taken from [64]) and (c) a hollow core photonic crystal fibre (figure taken from [65]).

2.3.2. Types of optical fibre sensors and characteristic examples

There are two categories of optical fibre sensors, extrinsic and intrinsic. *Extrinsic* sensors use the optical fibre as a means to propagate signals to and from the sensor

element, but the light leaves the optical fibre to make the measurement. *Intrinsic* optical fibre sensors are formed when the fibre itself is a primary sensing element.

Intrinsic optical fibre sensors may monitor changes in intensity, wavelength, phase or polarization of the guided light in order to draw a conclusion on local environmental changes. Characteristic examples include evanescent field or wave sensing, interferometry, distributed sensing, and fibre Bragg grating sensors [11].

There is a small portion of light that is guided outside the core of an optical fibre and this referred to as the *evanescent wave* or cladding modes (Figure 2-8) [66]. The intensity of this optical wave can be affected by the changes of the environmental refractive index (*n*). Based on this principle, several optical fibre sensors geometries have been demonstrated which take advantage of this phenomenon [67]. Characteristic examples include the tapered fibre sensors, where Kishan Rijal *et. al.* fabricated a biconical tapered fibre sensor for the detection of Escherichia coli pathogen [68, 69], as well as the directional couplers sensors where the detection of analytes has been reported [70]. Schematic diagrams of these sensors are shown in Figure 2-9.

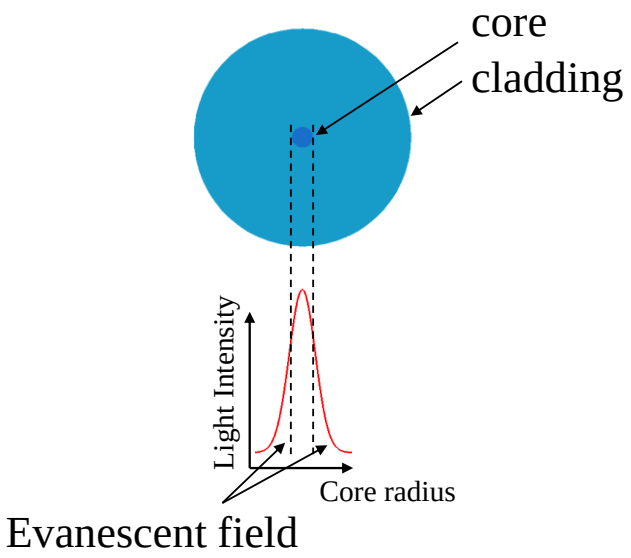

Figure 2-8. Evanescent wave transmitted in an optical fibre.

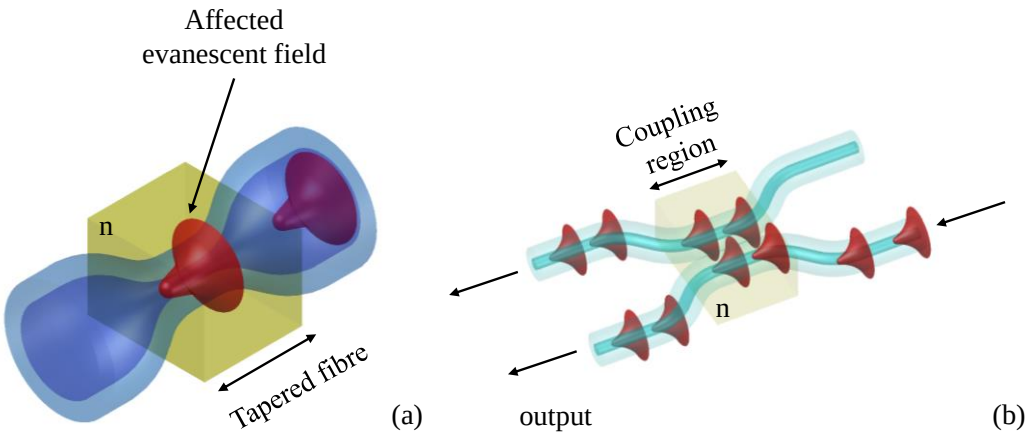

Figure 2-9. Characteristic examples of evanescent field optical fibre sensors (a) tapered and (b) coupler.

In the majority of cases *interferometric* optical fibre sensors measure the *phase shifts* between a signal and a reference arm in order to draw conclusions about environmental changes. Various geometries have been reported in literature such as the Mach-Zehnder fibre interferometer [71] and tapered fibres where the core and cladding modes are used for interference measurements [72]. However, one of the most studied example of this category for fibre sensing is the Fabry-Perot optical fibre sensor, where a reflecting surface is usually positioned at the end of the fibre, a cavity can then be formed. Changes on the length of this cavity can produce phase shifts on the interfered optical signal [73]. Figure 2-10 (a) and (b) shows a schematic diagram and an actual image of a Fabry-Perot optical fibre sensor respectively. Fabry-Perot optical fibre sensors are commonly used for temperature and pressure measurements. In these cases, the sensors cavity lengths vary due to thermal expansion/contraction and force application respectively [74]. As a result, these sensors can be used for temperature and flow measurements.

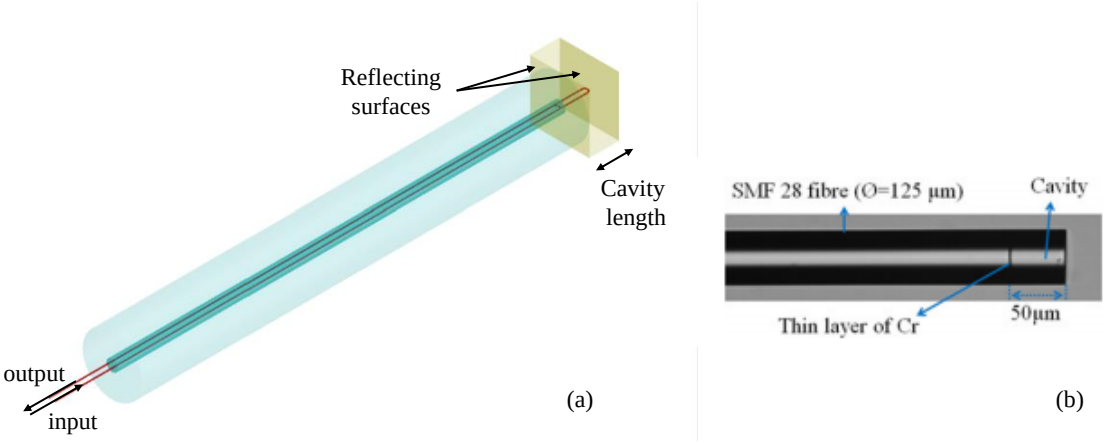

Figure 2-10. (a) Schematic diagram and (b) actual image (taken from [73]) of a Fabry-Perot optical fibre sensor.

Distributed sensors take advantage of the scattering phenomena that naturally occurs when light propagates through a medium. The scattering phenomena are produced due to the refractive index variations of the propagating material due to density and composition fluctuations [75]. Hence, Rayleigh, Brillouin and Raman scatterings can be caused from imperfections or impurities in an optical fibre, which can be affected by environmental changes (Figure 2-11 (a)) [76]. Distributed sensors are commonly fabricated to monitor temperature, strain and vibration variations along the length of the optical fibres. It has been reported that by using the Brillouin scattering technique, a 2° C temperature resolution can be achieved over a 2 km fibre length. While strain sensors can reach a few micro-meters resolution over one-meter [77]. Figure 2-11 (b) shows a deployed fibre sensor on a railway which is used for structural health monitoring. Another common form of distributed sensor is the optical time-domain reflectometer (OTDR), used for measuring the back scattering produced in an optical fibre and often deployed to diagnose faults in telecommunication systems [76].

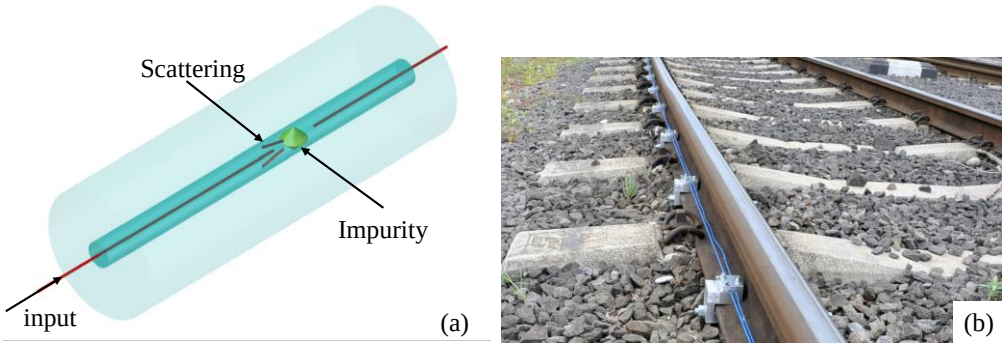

Figure 2-11. (a) Schematic diagram a Scattering distributed fibre sensor (b) Image of a deployed sensor of this type on a railway (taken from [78]).

Fibre optic *polarization* sensors monitor changes in the birefringence values by measuring the intensity of the transmitted light [79]. Polarization-maintaining fibres are used frequently for the fabrication of pressure sensors. A characteristic example is the polarization maintaining photonic crystal fibre pressure sensor, where the Sagnac interference effect produced in fibre is monitored to detect pressure variations [80].

However, *Fibre Bragg Grating* (FBG) sensors are probably the most studied optical fibre sensors due to their sensitivity, performance, and multiplexing ability. Temperature and strain measurements are the most common applications for FBGs sensors [81] and these are reviewed in the following sections.

2.4. Fibre Bragg Gratings

K. O. Hill was the first to demonstrate inscription of Fibre Bragg Gratings in 1978, at the Canadian Communications Research Centre (CRC), Ottawa, Canada [82]. Since then, many research groups have focused on the fabrication and applications of FBGs. As a result, numerous FBGs sensors have been demonstrated with many now commercially available.

2.4.1. Principles of Fibre Bragg Gratings

A FBG is a periodic perturbation of the refractive index in the optical fibre core and can be characterised as a narrow band filter or reflector. When broadband light is coupled in an optical fibre containing an inscribed Bragg grating in the core a narrow band of the spectrum is reflected back, while the rest is transmitted. The wavelength peak position of this band ($\lambda_{reflected}$) depends on the period of the grating (pitch, Λ_{FBG}), and the effective refractive index (n_{eff}), according to the following equation [83]:

$$\lambda_{reflected} = 2n_{eff}\Lambda_{FBG} \qquad \text{Equation 2.2}$$

Figure 2-12, shows a schematic diagram of a single mode fibre with an inscribed Bragg grating and the incident, reflected and transmitted spectra.

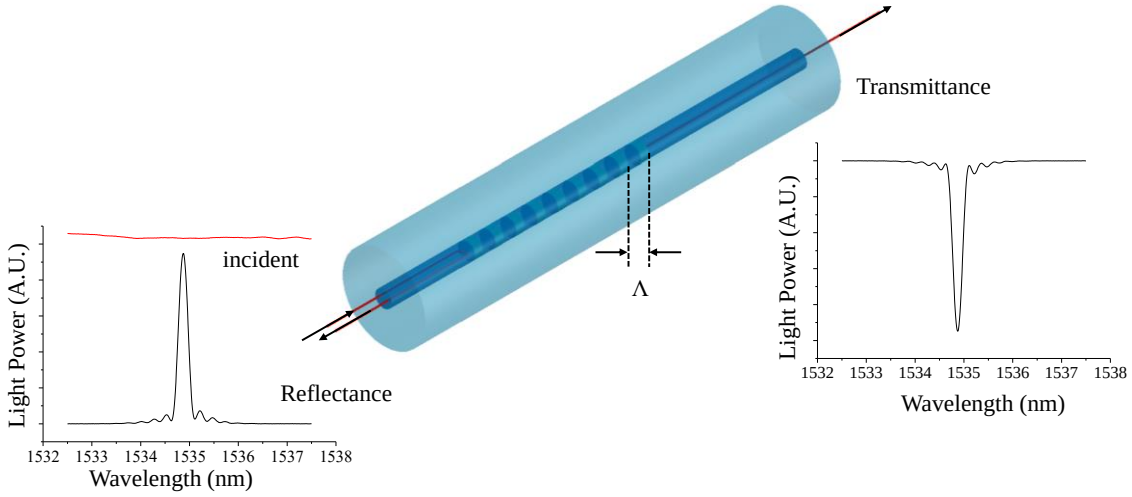

Figure 2-12. Single mode fibre with inscribed FBG and the incident, reflected (left) and transmitted (right) spectra (in this example, grating was in-house inscribed with the experimental set up described in Chapter 4).

The bandwidth of the reflected spectrum depends on the length and the uniformity of the inscribed grating. FBGs with over 90% reflectivity have been reported in the

literature [84, 85]. A mathematical expression for the reflectivity of an ideal FBG can be derived through coupled mode theory (Equation 2.3), where the modulation of the refractive index (Δn), the length of the FBG (l) and the propagation constant (K) of the fibre are required for the calculation [86].

$$R = tanh^2\left(\frac{\pi\,\Delta n\,l}{\lambda_{reflected}}\left(1-\left(\frac{2\,\pi\,K}{\lambda_{reflected}}\right)^{-2}\right)\right) \qquad \text{Equation 2.3}$$

The most common ways of interrogating FBGs are by collection the reflectance or the transmittance spectra using an optical spectrum analyser (OSA). OSAs emit and collect broadband light (usually in the range of 1510 nm – 1590 nm) from fibre coupled devices or even in free space. The prisms or gratings positioned in the device are sending the light to the detector and regarding to the incident angle (wavelength of the refracted light) the intensity of the spectrum can be recreated. Here, in this thesis a commercially available interrogator will be used for monitoring the FBGs (Micron optics), which use the same principle.

2.4.2. Types of Fibre Bragg Gratings

Several types of FBGs have been fabricated and categorised. The primary criteria to categorise FBGs, are their fabrication procedures. Hence, each type has different response, mainly in temperature variations, as well as temperature stability.

The different types of FBGs are: (a) Standard or type I gratings, (b) Type IA gratings, which are regenerated gratings inscribed in hydrogenated fibres (hydrogenation increases the fibre's photosensitivity in the UV region, see section 2.5.1) and have the lowest temperature coefficient [87]. (c) Type IIA gratings, which are referred in literature as negative index grating [88], and (d) Type II gratings, which are produced from lasers with intensity higher than the silica damage threshold [89].

2.4.3. Different structures of Fibre Gratings (FG)

Different structures of FBGs have been fabricated over the years to address a range of applications including spectrum filtering [90], optical feedback for fibre lasers [91], and as sensing elements. The most studied FBGs structures are the uniform, the long period, the sampled, the chirped and the tilted [92] (schematic diagrams in figure 2-13).

Each structure of FG has specific characteristics. In the case of long period gratings (LPGs) the reflected mode is coupled to the propagating cladding modes. The period of the LPGs is commonly between 100 to 1000 micrometres and their most common application is wavelength filtering [93]. However recently they have also been reported for biosensing applications [94].

Sampled gratings reflect different wavelengths with specific separation on the spectrum. These gratings are mainly used as distributed reflectors for the fabrication of tunable lasers [95].

Chirped gratings (where the grating period varies) provide wider reflected spectrum in regards to uniform gratings and they are commonly several centimetres long. This is because at longer FBG periods, longer wavelengths are reflected (see Equation 2.2). These gratings are commonly used to reduce dispersion of broadened laser pulses [96].

Finally, in the case of the tilted gratings the reflected modes can be coupled to backward core and claddings propagating modes, since the inscribed "reflectors" have an angle. Hence, the tilted gratings are frequently used as refractive index sensors [97]. Figure 2-13, shows schematic diagrams of different structures of FGs.

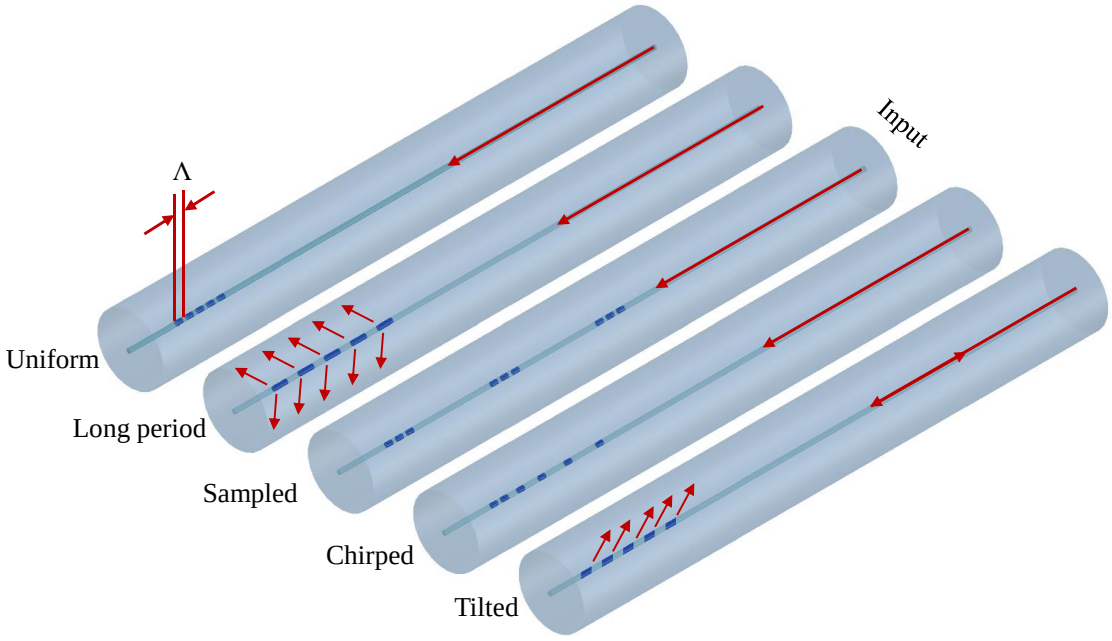

Figure 2-13. Schematic diagrams of different FBGs structures.

2.5. Fibre Bragg Gratings Fabrication

The periodic modulation of the refractive index in the core of an optical fibre is commonly achieved by exposing it to UltraViolet radiation (UV, $\lambda = 100\,nm - 400\,nm$). The change on the refractive index is attributed to the defects of the germanosilicate glass in the core of the fibre which absorb in the UV region. These defects are usually produced during the drawing procedure [92]. This natural photosensitivity can be enhanced by dopant selection (Boron or Germanium) and/or hydrogenation. Various high power lasers have been reported in the literature which can produce suitable UV radiation. One of the most common lasers is the excimer Krypton - Fluorine KrF, which emits directly in the UV region (248 nm) [98]. Additionally, the use of argon ion and copper vapour lasers has been reported. In this case, crystals with non-linear properties are used to frequency double the laser emission to a more suitable wavelength [99].

The selection of the most suitable laser for the inscription of the FBGs depends on the fabrication technique. However, lasers that emit directly in the UV region of the optical spectrum are preferred as they will be more reliable with less components, making for a simpler more cost effective fabrication system.

2.5.1. Photosensitivity of fused silica

The inscribed gratings in the core of the fibre are considered "permanent" after the UV exposure. However, FBGs can be erased by high temperatures, since proper amount of energy can be given to the germanosilicate molecules in order to return to the ground state. Therefore, thermal annealing techniques have been reported necessary in order to stabilise the FBGs thermal response. It has been reported that the stability of the FBGs remains unaffected at temperatures up to 900° C [100].

In 1993, P. J. Lemaire *et. al.* were the first to demonstrate that the inscription of FBGs into fused silica core can be enhanced by pre-loading the fibres with hydrogen [101]. The generation of hydroxyl groups (OH^-) in the core of the fibre results in an increase of the fibre's photosensitivity. Fundamentally, on a standard germanium doped telecommunication fibre, a refractive index modulation of $\Delta n \sim 3 \times 10^{-5}$ can be produced. However, on hydrogenated fibres the refractive index modulation is increased to $\Delta n \sim 3 \times 10^{-3}$, i.e. two orders of magnitude higher, which means that the inscribed FBGs are stronger with higher reflectivity. Fibre hydrogenation can be achieved with

various techniques, however the most common is to load the fibres into pressurized hydrogen atmosphere before the inscription process [102].

2.5.2. Different techniques for the inscription of the FBGs

Four different experimental set ups have been reported in literature capable of fabricating Bragg gratings. The first three set ups have in common that an interference pattern of the UV radiation must be produced in order to create the periodic modulation of the refractive index into the core of the exposed fibre. However, in the last decade a new technique has been developed where the interference pattern is not necessary by using a point-by-point writing technique. All these four techniques are reviewed in the following sections.

i. Internal inscription of FBGs

The first observation of a FBG was a result of internal inscription of Bragg gratings and was demonstrated by Hill *et. al.* [103]. Here, the interference pattern is produced by the primary beam and the reflected beam from the end of the fibre (Fresnel reflection). Figure 2-14 (a) shows the experimental set up used for the inscription of the first FBG with a single-mode argon ion laser, where the emission wavelength lines of the laser were 488 and 514 nm. The reflectance wavelength of the inscribed gratings produced from this set up is positioned in the visible range of the optical spectrum, close to the laser's emission wavelength lines [104]. The reflectance and transmittance spectra of the first inscribed FBG is shown in Figure 2-14 (b).

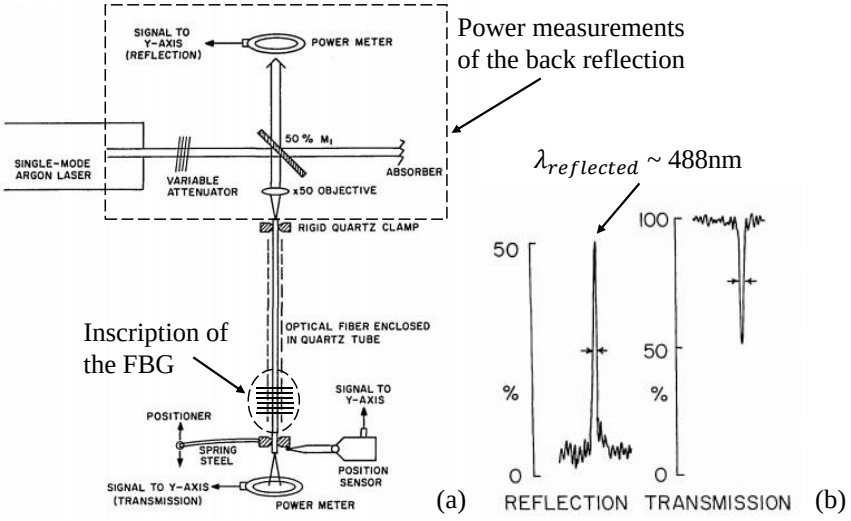

Figure 2-14. (a) Experimental setup and (b) Reflection and transmission spectra of the first inscribed FBG (figures taken from [103]).

ii. Transverse holographic inscription of FBGs

Meltz et.al. introduced the second technique for inscription of FBGs, referred as transverse holographic technique in 1989 [105]. Here the UV interference pattern is created with a beam splitter and two mirrors. A schematic diagram of this experimental set up and the transmission / reflection spectra of the FBG inscribed with this technique are shown in Figure 2-15.

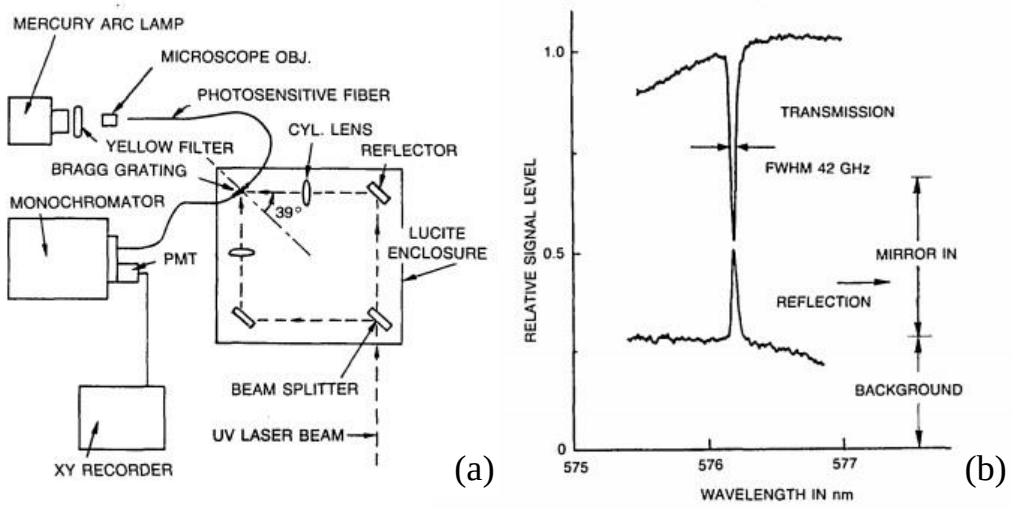

Figure 2-15. (a) Schematic diagram of the set up used on transverse holographic technique and (b) Transmission and reflection spectra of the inscribed FBG (figures taken from [105]).

The period of the fabricated grating depends on both the wavelength of the incident beam and the angle between the two beams, according to Equation 2.4. Where λ_{laser}, is the laser's emission wavelength used for inscription and φ is the half-angle of the two beams at interference [92].

$$\Lambda_{FBG} = \frac{\lambda_{laser}}{2 \sin \varphi} \qquad \text{Equation 2.4}$$

The main advantage of the holographic technique is that FBGs with different reflectance wavelength can be fabricated with the same experimental set up. Moreover, a variety of lasers can be used for the inscription, such as Argon or Krypton fluoride lasers (ArF or KrF). However, the alignment of the optical components can be time consuming and sensitive to small vibrations, which can result to a reduction on the strength of the inscribed FBG.

iii. Inscription of FBGs with the phase mask technique

The phase mask is the most common and studied technique for inscription of FBGs and has superseded the other techniques, especially for the case of inscription of uniform FBGs. In comparison to the other techniques, the optical alignment for the phase mask is simplified. Additionally, the alignment of the optical components is less affected by vibrations in comparison to the other two techniques due to the shorter path lengths between key components [92]. Moreover, strong Bragg gratings can be inscribed with a low coherence UV beam. Finally, this approach can produce multiple gratings into different fibres with a single UV exposure (with parallel positioning of the fibres).

Figure 2-16 (a), shows a schematic diagram of the set up that is usually used for FBGs inscription with the phase mask technique. The cylindrical lens is used in order to focus the UV spot to a line, the phase mask produced the UV interference pattern and the fibre is positioned close to the focal point of the lens, in the interference pattern region.

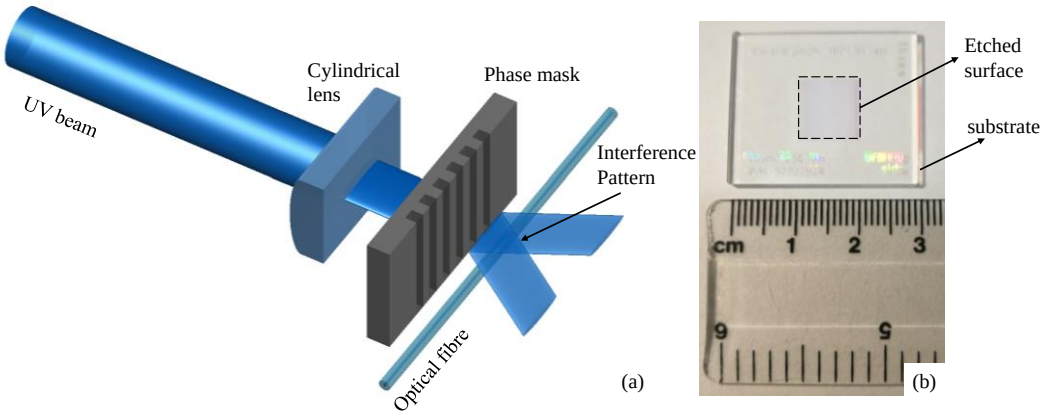

Figure 2-16. (a) Common experimental set up used for inscription of FBGs with the phase mask technique, (b) actual phase mask.

Phase masks are etched fused silica surfaces, which are usually fabricated with photolithographic techniques or with electron beam lithography [106]. Typical silica substrate dimensions are usually some millimetres, a characteristic example of a phase mask is shown in Figure 2-16 (b), where the etched surface is 10×10 mm, the substrate is 30×25 mm and its thickness is 2 mm. Phase masks are transparent to the UV laser beam and they produce diffraction patterns according the angle of the incident beam. The diffraction orders that are commonly used for the inscription are the +1, and -1 (Figure 2-17). The interference pattern is produced by the two diffracted beams. In the case of

+1, -1 diffraction orders the inscribed Bragg grating period (Λ_{FBG}) depends only on the phase mask's period (Λ_{PM}) and not on the wavelength of the UV beam [107]:

$$\Lambda_{FBG} = \frac{\Lambda_{PM}}{2} \qquad \text{Equation 2.5}$$

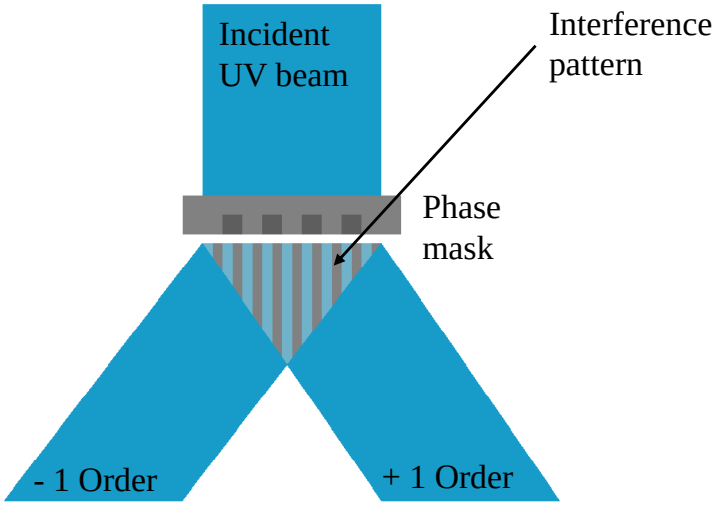

Figure 2-17. Interference pattern produced by phase masks from the - 1, + 1

While the phase mask technique seems only beneficial, there is one limitation: Each phase mask can produce only one specific FBG wavelength and in situations where different FBGs are required then phase masks with different periods have to be used. Slightly different inscription of FBGs with the same phase mask have been reported by either introducing strain on the fibre [108], by positioning it with a small angle in the interference pattern or by introducing an additional lens before the phase mask (Talbot effect). The first case is commonly used for inscription of different FBGs in Polymer optical fibres (POFs) and the maximum Bragg reflectance wavelength difference that was achieved was over 7 nm [109]. While in the second case a shift of ~ 2.5 nm wavelength Bragg grating was reported [110]. Finally, for the last case, it was reported a 1.71 nm wavelength difference on the Bragg gratings inscribed with the additional converging lens [111].

Similarly, the exposure time of the fibre on the UV interference pattern can produce FBGs with slightly different reflectance wavelength [112]. Nevertheless, the exposure time is strongly related with the reflectivity of the FBGs. The highest value of the FBGs' reflectivity can be achieved during several minutes of the UV exposure [113]. The range

of the exposure time depends on the alignment and stability of the inscription set up, the power of the laser and the photosensitivity of the fibre.

iv. Point – by – point inscription of FBGs

The most recently developed technique for FBGs inscription is the so-called point-by-point approach [114]. In this case high power femtosecond pulsed lasers with an emission wavelength usually in the near-Infrared (IR) region of the optical spectrum is used. The point-by-point inscription can be achieved by focusing the laser beam in the core of the optical fibre with a high magnification microscope objective lens (Figure 2-18 (a)) The inscription in this case is achieved due to the non-linear absorption of the laser beam from the optical fibre.

The main advantage of this technique is that gratings with different period (or pitch, Λ) or type [115] can be inscribed using the same experimental set up. However, there are two major difficulties that have to be encountered in this case. The first is the need of precision movement of the fibre, which can be solved, at a cost with high precision translation stages (~ 2 nm resolution). While the second is the distortion of the laser beam due to the cylindrical surface of the fibre which can be countered by coating the fibre or by inserting it in squared structured capillary (Figure 2-18 (b)) [116]. Finally, inscription of FBGs with this technique is considered to be quite slow in comparison to the phase mask technique.

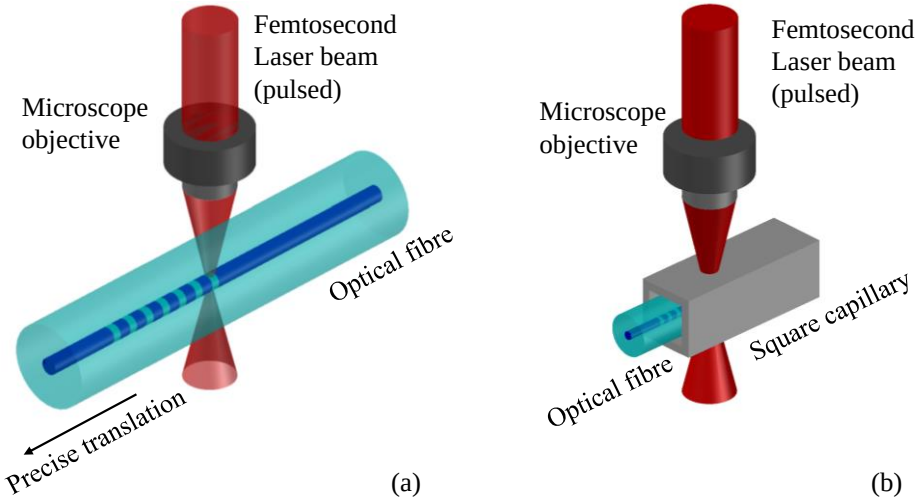

Figure 2-18. (a) Schematic diagram of the commonly used experimental set up for the point by point inscription of FBGs, (b) inscription of the FBG with a square capillary to resolve the beam distortion from the cylindrical geometry of the fibre.

v. Conclusions on FBGs fabricating techniques

Inscription of FBGs was reported with all four experimental setups described in previous cases. However, each technique has different strengths and weaknesses. The main three criteria are: (a) optical alignment difficulties, (b) available FBG reflectance wavelength and structure flexibility and (c) the overall fabrication cost.

The internal inscription experimental set up (*i*) can be considered as a low difficulty optical alignment set up and cost effective. However, this experimental set up cannot provide a great variety of FBGs structures as well as reflectance wavelengths, and as a result is not commonly used.

The transverse holographic technique requires a complicated experimental set up (*ii*) with different optical components, hence the optics alignment is significantly more challenge than for the other interference arrangements. Nonetheless, this set up provides a great variety of FBG structures and reflectance wavelengths and it is considered as cost effective for conventional gratings.

The phase mask technique (*iii*) is characterised as a FBG inscription technique with low optical alignment difficulty. Moreover, the FBGs inscribed with this technique are considered of high quality and strong reflectivity. The experimental set up can produce one specific FBG structure with a standard reflectance wavelength. However, replacement of the phase mask can be achieved relatively easily without misaligning the other optical components. The phase masks are considered to be expensive optical components (~1.000-1.500 GBP). Hence this technique can be regarded as ideal for mass production of identical gratings but poor for bespoke arrangements.

Finally, the point-by-point technique (*iv*) requires the least optical components for the inscription of FBGs, therefore it can be characterised as technique with low optical alignment difficulty. Moreover, with this technique FBGs with different reflectance wavelength can be inscribed. However, the laser used for the inscription (femtosecond pulsed laser) and the mechanical components (translation stage with high precision) have higher costs in regards with the ones used for the other techniques. Therefore, it is considered as cost ineffective but highly flexible.

Table 2-1 includes a visual representation of the strengths and weaknesses of all four inscription techniques for the three aspects. The last two techniques (phase mask and

point-by-point techniques) are the most efficient techniques for inscription of FBGs. However, the phase mask technique is considered as more cost effective with less requirements on optical alignment.

The inscription of the FBGs reported in this thesis, is performed with the phase mask technique.

Table 2-1. Advantages and disadvantages of the four FBG inscription techniques.

low	
medium	
high	

	Internal	Holographic	Phase Mask	Point-by-Point
Optics alignment difficulty				
Inscribed FBGs limitation				
Cost				

2.6. Fibre Bragg Grating sensors

The working principle of a FBG sensor is based upon monitoring the reflection or transmission spectra of the grating. The peak position on the reflectance or transmittance spectrum (Figure 2-12) can shift due to external local environment changes.

According to Equation 2.2, $\lambda_{reflected} = 2n_{eff}\Lambda$ the peak position on the FBG's reflected spectrum depends on the effective refractive index and the grating period. These two parameters are directly affected by both the external strain that is applied on the fibre and the local temperature. Therefore, FBG sensors are commonly used as strain [117] or temperature sensors [118].

Nonetheless, it has been demonstrated in literature that several other physical parameters can be monitored with FBGs with the use of a suitable transducer. Some characteristic examples include refractive index, pressure and vibration, flow or liquid level, tilt, humidity sensing, gas and displacement sensing [119].

2.6.1. Temperature and strain sensitivity of FBGs

The temperature and strain sensitivity of a FBG can be derived from Equation 2.2. The partial derivative with respect to temperature (T) is:

$$\frac{\Delta\lambda_{reflected}}{\Delta T} = 2\, n_{eff}\frac{\partial \Lambda}{\partial T} + 2\, \Lambda\, \frac{\partial n_{eff}}{\partial T} \qquad \text{Equation 2.6}$$

By using again Equation 2.2:

$$\frac{\Delta\lambda_{reflected}}{\Delta T} = \frac{\lambda_{reflected}}{\Lambda}\frac{\partial \Lambda}{\partial T} + \frac{\lambda_{reflected}}{n_{eff}}\, \frac{\partial n_{eff}}{\partial T} \qquad \text{Equation 2.7}$$

and by rearranging Equation 2.7:

$$\frac{\Delta\lambda_{reflected}}{\lambda_{reflected}} = \frac{1}{\Lambda}\frac{\partial \Lambda}{\partial T}\, \Delta T + \frac{1}{n_{eff}}\, \frac{\partial n_{eff}}{\partial T}\, \Delta T \qquad \text{Equation 2.8}$$

or

$$\frac{\Delta\lambda_{reflected}}{\lambda_{reflected}} = (a + \beta)\, \Delta T \qquad \text{Equation 2.9}$$

where, a is the thermal expansion coefficient and is characterised by the material of the optical fibre (usually fused silica). While, β is the thermo – optic coefficient which represents the changes of the refractive index due to local temperature changes.

The strain sensitivity of a FBG can be similarly calculated by the partial derivative of Equation 2.2, with respect to displacement (L):

$$\frac{\Delta\lambda_{reflected}}{\Delta L} = 2\, n_{eff}\frac{\partial \Lambda}{\partial L} + 2\, \Lambda\, \frac{\partial n_{eff}}{\partial L} \qquad \text{Equation 2.10}$$

with the use again of Equation 2.2 and by rearranging:

$$\frac{\Delta\lambda_{reflected}}{\lambda_{reflected}} = \frac{1}{\Lambda}\frac{\partial \Lambda}{\partial L}\, \Delta L + \frac{1}{n_{eff}}\frac{\partial n_{eff}}{\partial L} \qquad \text{Equation 2.11}$$

The first term in the Equation 2.11, represents the physical elongation of the optical fibre and in the case where the Bragg grating lies in the fibre (the most common case) the ratios $\frac{\partial \Lambda}{\partial L}$ and $\frac{\Delta \Lambda}{L}$ are equal. The second term is called photo – elastic coefficient (ρ_e), and represents the refractive index variations of the fibre due to the elongation (strain). Additionally, according to Poisson's ratio of materials, when the optical fibres expands, the photo – elastic coefficient becomes negative. Thus Equation 2.11 becomes:

$$\frac{\Delta\lambda_{reflected}}{\lambda_{reflected}} = (1 - \rho_e)\,\varepsilon_z \qquad \text{Equation 2.12}$$

where ε_z, is strain which is applied on the optical fibre with the core inscribed (and hence the grating) on the z-axis. Finally, the overall temperature and strain sensitivity of a FBG is given by combining equations Equation 2.9 and Equation 2.12:

$$\frac{\Delta\lambda_{reflected}}{\lambda_{reflected}} = (a + \beta)\,\Delta T \; + \; (1 - \rho_e)\,\varepsilon_z \qquad \text{Equation 2.13}$$

With typical parameters (a, β and ρ_e) for a germanium doped silica fibre at the wavelength of 1550 nm the sensitivity of FBGs on temperature and strain variations are [120] [121]:

$$\frac{\Delta\lambda_{reflected}}{\Delta T} = 10 \; pm/℃ \qquad \text{Equation 2.14}$$

$$\frac{\Delta\lambda_{reflected}}{\Delta\varepsilon} = 1.2 \; pm/\mu\varepsilon \qquad \text{Equation 2.15}$$

2.6.2. Fabrication of temperature and strain FBG sensors

According to Equation 2.13, the peak position of the reflected Bragg wavelength depends directly on both the strain and the temperature. Thus, different FBG sensors have been reported in literature, where the temperature and strain are monitored individually [122]. The most common geometry for specific temperature measurement using FBGs is to strain isolate the optical fibre from external forces. This can be achieved by enclosing the fibre with the inscribed grating into rigid tubes and attaching at one end only [123].

Temperature independent strain measurement using an optical fibre is more challenging. The working principle of the FBG strain sensor is based on the fact that fibres can be easily deformed. The reflected wavelength of a Bragg grating inscribed into the core of a fibre increases when it is getting stretched (Figure 2-19). On the contrary, the Bragg wavelength decreases when the fibre is getting compressed. However, local temperature affects the gratings response, therefore concurrent temperature measurements are required and an appropriate compensation needs to be applied.

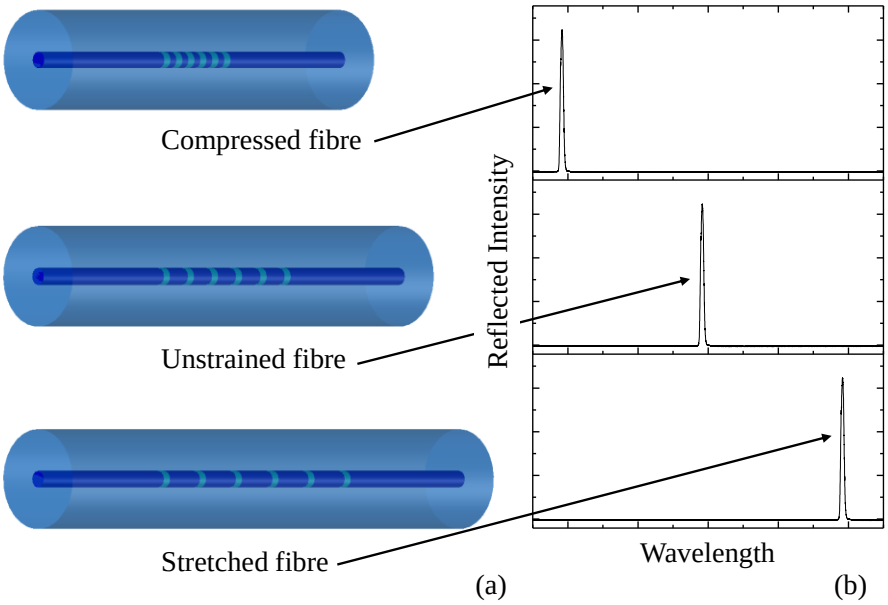

Figure 2-19. (a) A schematic diagram of a compressed, unstrained and stretched fibre and (b) their reflectance spectra.

Temperature compensation of the strain measurements can be achieved by monitoring the local temperature changes with electrical or optical means. In the first case, thermocouples, thermistors or resistance temperature detectors (RTDs) can be used. However, a more compact way for FBG temperature-compensated strain measurements is with optical techniques, hence an all-optical system is used. In this case, two FBGs are commonly used, the first one is affected by both temperature and strain variations while the second one is strain isolated and measures only the local temperature. In one arrangement two FBGs can be inscribed into two different fibres positioned close to each other. Alternatively, two different Bragg gratings inscribed into one fibre can be used for temperature compensated FBG strain measurements [124, 125]. Where compensation was achieved for a strain range of 0-600 με and a temperature range of 10-60 °C with an error of 7.4 %. Figure 2-20 shows a schematic diagram of this kind of FBG strain sensor geometry.

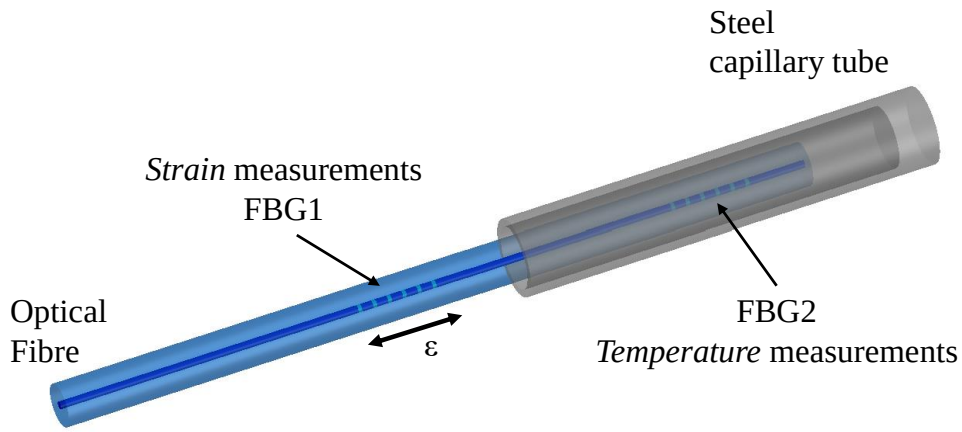

Figure 2-20. Temperature compensated FBG strain sensor, the capillary tube is used for strain-isolating the FBG used for temperature measurements (FBG2).

In the case of a temperature compensated FBG strain sensor with the use of a second FBG, the response from the first FBG (which is affected by strain and temperature (FBG1)) is subtracted from the second (which is affected only by the temperature (FBG2)). In this way, the wavelength shift of the first FBG system provides information only about the strain applied on the fibre.

FBG strain sensors have been used in in a wide variety of applications including physics, engineering and medicine [23]. The most prominent use of FBG strain sensor is for structural health monitoring. The fact that fibres can be used in harsh environments [126] and reach remote and distant areas makes them ideal for embedding them into aircraft engines [127] or bridges [128] for real time monitoring and maintance planning – so called smart structures.

Moreover, the prospect of multiplexing FBG sensors provides the additional advantage, that several strain measurements at different points along the structures can be taken more or less simultaneously (distributed sensing) [129]. Multiplexing of FBG sensors can be achieved either in the time domain (Time Division Multiplexing-TDM [130]) or in the wavelength domain (Wavelength Division Multiplexing-WDM [131]). In the case of the WDM, a commercially available interrogator (Micron optics sm125/130) has a 1510-1590 nm spectral range. Hence, for the "recommended" FBG spacing of ±5 nm between, a 16 FBG sensors multiplexing can be achieved.

2.7. FBG curvature sensors

A compressed or stretched FBG provides information only about the longitudinal deformation of the fibre assuming it lies on the neutral axis of the fibre. However, several

applications necessitate measurements on the curvature of a structure (where the fibre can be embedded) in one or more axis. FBG beam cantilever or curvature sensors [132] have been reported in literature, where the FBGs lie outside of the geometry's neutral axis [133]. Single mode fibres with FBGs that are glued together in triangle [134] or square [135] geometries have been reported and measurements on their curvature have been demonstrated. Figure 2-21 shows a schematic diagram and the cross sections of these FBG curvature sensors.

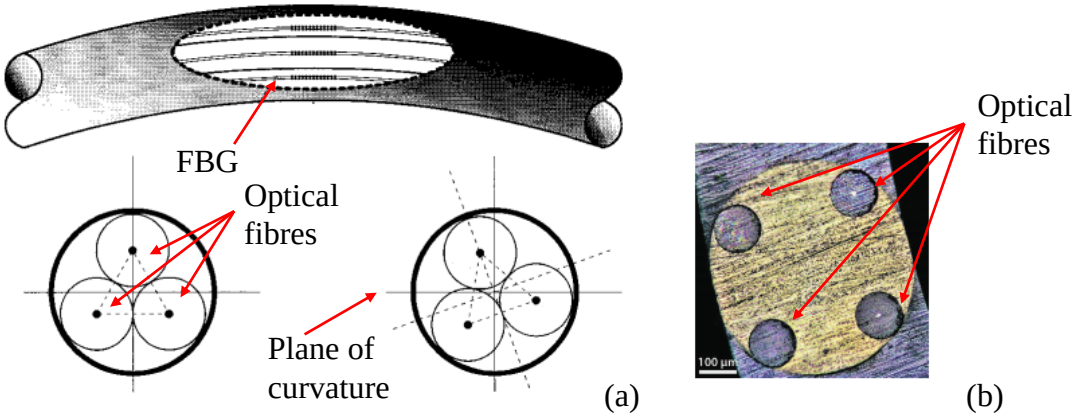

Figure 2-21. Schematic diagram and cross sections of FBG curvature sensors with (a) three and (b) four glued single mode fibres reported in [134] and [135] respectively.

Moreover, novel FBG curvature sensors have been fabricated with the use of multicore fibres (MCFs). These MCF curvature sensors, with FBGs inscribed into their cores have been used as accelerometers [136, 137] or multidirectional flow speed sensors [138]. The cross sections of the MCFs used for the fabrication of these sensors are shown in Figure 2-22. The primary advantage of the MCF curvature sensors in comparison to the glued fibres is that the strain gauges FBGs are surrounded by the same material (cladding, which is usually silica glass). On the contrary, the glued fibres are bonded with adhesive which is less strong and can introduce slippage during the fibres' bending. Thus, errors on the sensor's curvature measurements can result through poor strain transfer, moreover this defect might enhance with age [139].

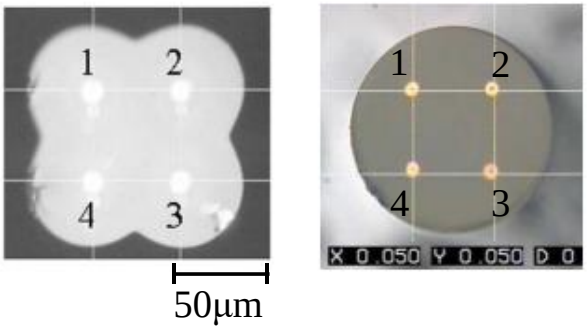

Figure 2-22. Cross sections of the MCFs used for the fabrication of FBG curvature sensors reported at [136, 139] both had core separation of ~50 µm.

2.7.1. Multicore fibre curvature sensor

A MCF can be considered as a cylindrical beam which can be bent in different directions. When a cylindrical beam is bent or strained in one direction, several bisection planes can be characterised as compressive or tensile. In addition there are specific planes, where the strain applied on them is neither compressive nor tensile (i.e. zero). These planes are called neutral, and the axis which lies on them is called neutral axis, see Figure 2-23. The neutral axis coincides with the centroid axis of the beam, when the radius of curvature (R) is large in comparison to the beam's length.

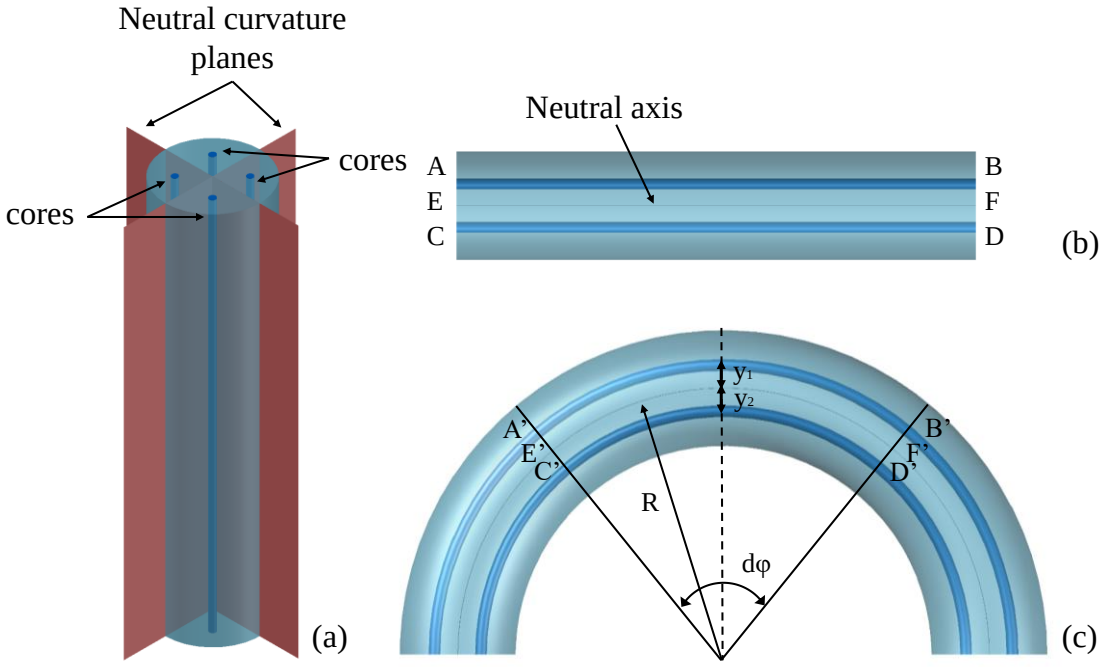

Figure 2-23. (a) 3D view of a circular MCF with two characterististic neutral curvature planes, and 2D view of the fibre (b) when it is straight and (c) bent.

Three different planes can be considered for the determination of the fibre's curvature, the neutral plane and the two planes containing the cores. The strain that is applied, due to the bending of the fibre, along the length of the AB plane is:

$$\varepsilon_{AB} = \frac{A'B' - AB}{AB} \qquad \text{Equation 2.16}$$

However, the lengths AB and $A'B'$ can be determined from the schematic diagrams shown in Figure 2-23 (b) and (c) respectively:

$$AB = EF = CD \qquad \text{Equation 2.17}$$

$$A'B' = (R + y_1)\, d\varphi \qquad \text{Equation 2.18}$$

where,

$$EF = E'F' = R\, d\varphi \qquad \text{Equation 2.19}$$

hence the strain applied on plane AB becomes:

$$\varepsilon_{AB} = \frac{(R + y_1)\, d\varphi - R\, d\varphi}{R\, d\varphi} \qquad \text{Equation 2.20}$$

or,

$$\varepsilon_{AB} = \frac{y_1}{R} \qquad \text{Equation 2.21}$$

Similarly the strain applied on the CD plane is:

$$\varepsilon_{CD} = \frac{y_2}{R} \qquad \text{Equation 2.22}$$

Finally, the differencial strain between the two planes of curvature is:

$$\Delta\varepsilon = \varepsilon_{AB} - \varepsilon_{CD} = \frac{y_1}{R} - \frac{y_2}{R} = \frac{d}{R} \qquad \text{Equation 2.23}$$

where, d is the seperation between the two planes and $1/R = \kappa$ is the curvature of the fibre [140].

2.7.2. Determination of the curvature for a MCF

An MCF can become a curvature sensor by simply creating a cantilever geometry. The curvature of a MCF can be determined with the beam theory which is based on the mechanical properties of materials. The fibre can be considered as a cantilever with one

end fixed and one end free to be deflected. Figure 2-24, shows a schematic diagram of a straightened and a deflected cantilever beam [140].

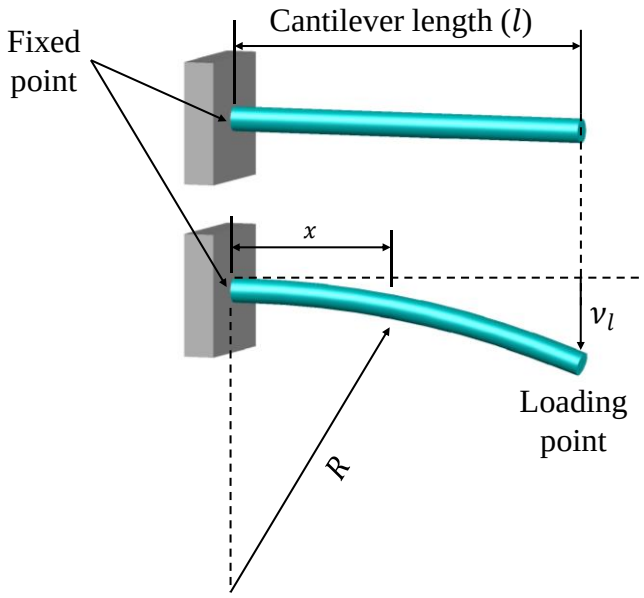

Figure 2-24. Straightened and deflected cantilever beam.

The deflection (v_l) at the loading point of the beam is given by:

$$v_l = \frac{1}{3}\frac{Wl^3}{EI} \qquad \text{Equation 2.24}$$

where, l is the length of the beam at the deflection point (or loading point), W is the weight applied at the loading point, E is the Young's modulus $[N \cdot m]$ of the material and I is the second moment of area $[m^4]$ [140]. Additionally, for small deflections of the cantilever the bending can be considered as elastic, thus:

$$\frac{1}{R} = \frac{M}{EI} \qquad \text{Equation 2.25}$$

where, M is the bending momentum and in this case $M = W\ (l - x)$. Therefore, using Equation 2.24 Equation 2.25 the curvature at any point x of the cantilever beam can determined:

$$\kappa = \frac{1}{R} = \frac{3\ (l - x)}{l^3}\ \ v_l \qquad \text{Equation 2.26}$$

Since optical fibres are fabricated from fused silica, they have well defined mechanical properties. Moreover, they are difficult to deform and benefit from their elasticity. Hence the MCF is more than appropriate for the fabrication of a cantilever sensor.

2.7.3. Response of the inscribed FBGs in a MCF

The structure of the MCF is ideal for the determination of its curvature. Whenever, the four cores lie outside of the neutral planes, two of them will be stretched while the other two will be compressed, during deflection. There are only two extreme cases where two cores can lie on the neutral planes during the deflection of the fibre. In that cases, the cores that lie on the neutral planes are equally stretched or compressed (experience zero strain), while the two opposite cores experience the strongest compression and stretching respectively. Figure 2-25 shows a top view of the MCF when deflected in these two cases.

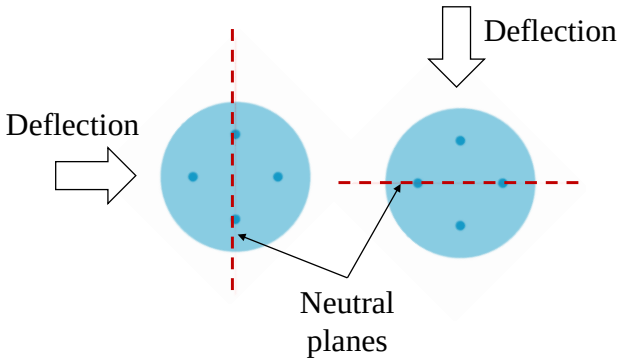

Figure 2-25. Deflection of the MCF in the direction where two cores lie on the neutral planes, while the other two experience the strongest stretching or compression in regards to their position with the neutral planes.

Figure 2-26 shows a schematic diagram a MCF cantilever sensor with inscribed FBGs. By inscribing FBGs into the cores of a MCF and monitoring their response during deflection, information about the curvature of the fibre's curvature can be extracted. The shifts in peak position of the reflected wavelength of the FBGs due to either stretching or compressing of the cores can be converted to strain shift through the Equation 2.15. Additionally, the curvature of the fibre can be calculated with Equation 2.23 from the FBGs response, which can be correlated with the mechanical determination from Equation 2.26. All the above mentioned equations are included in Table 2-2.

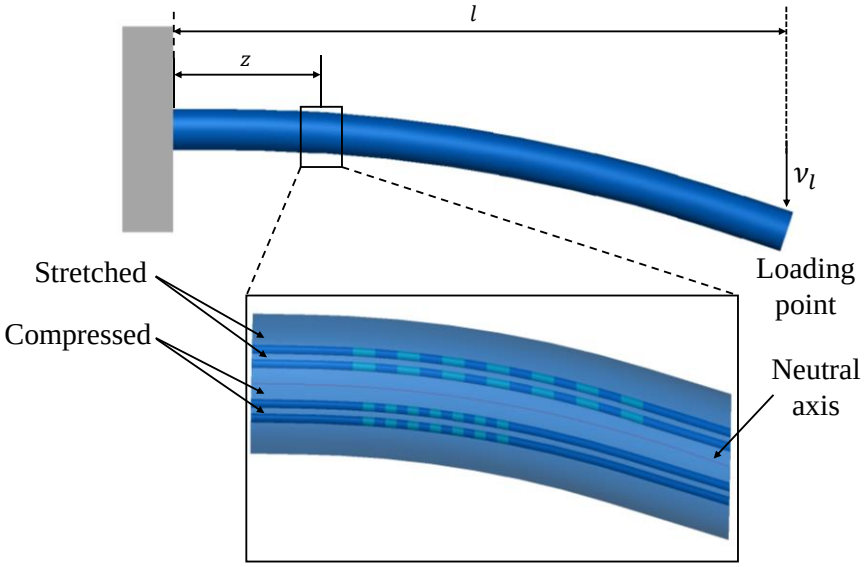

Figure 2-26. MCF with inscribed FBGs cantilever sensor.

Table 2-2. Equations which can be used for the determination of the MCF's curvature with inscribed FBGs.

FBGs' strain sensitivity	$\frac{\Delta\lambda_{reflected}}{\Delta\varepsilon} = 1.2\ pm/\mu\varepsilon$	Equation 2.15
Strain difference between bisection planes separated by distance, d	$\Delta\varepsilon = \varepsilon_{AB} - \varepsilon_{CD} = \frac{y_1}{R} - \frac{y_2}{R} = \frac{d}{R}$	Equation 2.23
Curvature determined from the mechanical properties of materials	$\kappa = \frac{1}{R} = \frac{3\,(l-z)}{l^3}\ v_l$	Equation 2.26

The peak wavelength difference between two FBGs can provide temperature – compensated measurements of the strain induced on the fibre. Moreover, this difference varies linearly with curvature and by deflecting the MCF in two orthogonal directions, calibration can be achieved:

$$\begin{bmatrix}\Delta\lambda_{12}\\ \Delta\lambda_{23}\end{bmatrix} = \begin{bmatrix}c_{12}\\ c_{23}\end{bmatrix} + \begin{bmatrix}p & q\\ r & s\end{bmatrix}\begin{bmatrix}\kappa_x\\ \kappa_y\end{bmatrix} \qquad \text{Equation 2.27}$$

where, p, q, r and s are the calibration parameters for the two directions of deflection.

In conclusion, a MCF curvature sensor with inscribed FBGs and a fixed point can be fabricated, where by monitoring the wavelength peak position of the FBGs the curvature (or the end of the fibre on one plane) can be determined [139]. With this cantilever

geometry, the MCF cannot be twisted during the calibration procedure (as a sensing element). Moreover, considering that the cores of the fibre are not twisted during its fabrication, the calibration procedure can be performed with high accuracy.

2.8. Interrogation of the FBGs inscribed into a MCF

The main difficulty with MCF curvature sensors is the interrogation of the FBGs inscribed into them. Commercially available interrogation systems and most of the fibre components (including lasers and spectrometers) are compatible only with single core fibres. Therefore, an interface which can transfer the optical signal from one core of the MCF to a single core fibre is necessary.

2.8.1. Commercially available fan-out devices

Devices which can guide the light from one core of a MCF fibre to a single-core fibre are commonly called fan-out devices and two different methods of fabrication have been reported. The first is achieved by etching SMFs to a small enough diameter to arrange against the MCF, and aligning them with the MCF cores, in most cases this is achieved by inserting the fibres into a capillary [141]. The second type of fan-out devices is fabricated through 3D waveguide inscription techniques. The 3D inscription of the waveguides into silica glasses can be achieved with femtosecond pulsed lasers and the alignment of the fibres [142]. Figure 2-27 shows the schematic diagrams of both types of fan-out devices. These devices are mandatory for most application which involve MCFs. However, they can be fragile and expensive and may demonstrate sensitivity to their local environment.

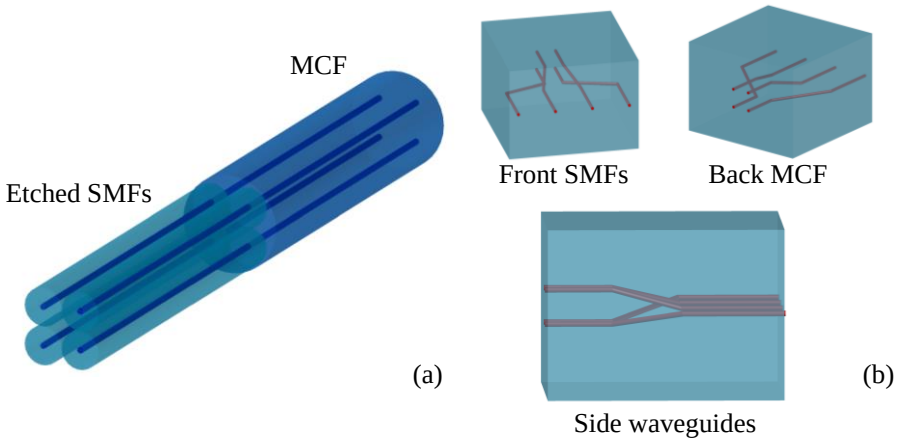

Figure 2-27. Fan-out devices fabricated with (a) etched SMFs and (b) ultrafast laser inscription of optical waveguides (image recreated from [142]).

Finally, photonic lanterns are also reported as an interface between standard fibres (mainly Multimode fibres) and MCFs [143]. In these cases a bundle of the fibres is inserted in capillary with a specific geometry that matches the MCF. Then bundle is tapered down using a drawing towers [144]. These devices are mainly used as mode multiplexers [145, 146]. The photonic lanterns are considered as a good quality interface components, however their fabrication costs are high.

2.8.2. Tapered fibre fan-out device

In this thesis, an alternative fan-out device is fabricated with the MCF itself, by coupling light from all cores of a MCF into one. Therefore, the optical signal from all cores of the MCF can be transmitted through a SMF which is spliced with a single core of the MCF. For applications where the cross talk between the cores of the fibre does not affect the results, this simple fan-out device can become useful.

It has already been demonstrated in literature that light can be coupled from one fibre to another under certain conditions [147]. When two fibres come close to each other, the propagating evanescent field from first can be transferred and guided into the core of the second [148]. This light transfer oscillates between the fibres, along the distance that they are close to each other (the waist). According to the coupling mode theory the power transfer ratio between the fibres depends on the coupling coefficient. This coefficient varies with the separation of the fibres and depends on the wavelength of the light, the refractive indices of the cladding, cores and the surrounding medium, the cladding and cores diameters and finally the waist length [149].

Light transfer can be achieved between more than two optical fibres. David B. Mortimore and John Arkwright determined the power transfer of a 1×7 optical fibre coupler [150]. Moreover, they were able to intensity coupling between cores of a 4×4 fibre coupler with the fibres having the same geometry as the MCF used in this thesis [151]. Figure 2-28 shows the geometry of the fibres with the characteristic parameters which affect the light optical power in each fibre.

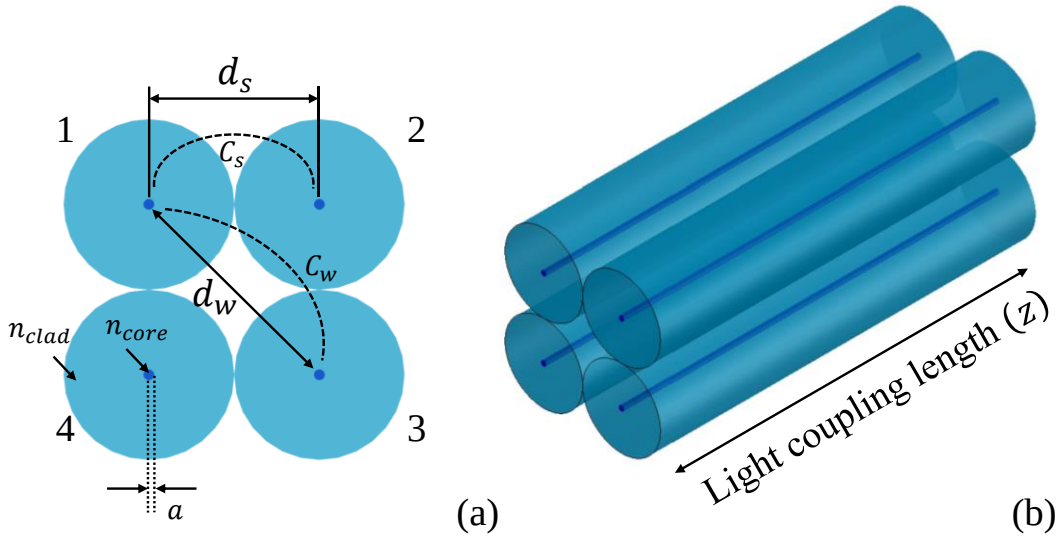

Figure 2-28. The geometry of the 4 × 4 fibre coupler for which the power transfer equations where determined by Mortimore [151], (a) front and (b) side view.

The light power at a distance z in the core of the fibres ($P_1(z)$, $P_2(z)$, $P_3(z)$, $P_4(z)$) is given by the following equations [151]:

$$P_1(z) = \frac{1}{4}[1 + 2\ \cos(2C_s z) \cdot \cos(2C_w z) + \cos^2(2C_s z)]P_1(0) \qquad \text{Equation 2.28}$$

$$P_2(z) = P_4(z) = \frac{1}{4}P_1(0)\sin^2(2C_s z) \qquad \text{Equation 2.29}$$

$$P_3(z) = \frac{1}{4}[1 - 2\ \cos(2C_s z) \cdot \cos(2C_w z) + \cos^2(2C_s z)]P_1(0) \qquad \text{Equation 2.30}$$

where, $P_1(0)$ the initial intensity in fibre 1 is the total input power in the 1 × 4 coupler. In this coupler geometry there are two different coefficients that affect the power transfer between the fibres. The fibres with the shortest distance between them (neighbor fibres, 1-2 and 1-4), are characterized by strong coupling coefficient of light (C_s), while the distant fibres (1-3) exhibit weaker coupling coefficient (C_w). The coupling coefficients can be determined with the following equations [147]:

$$C_s = \frac{\lambda U^2}{2\pi n_{core} r^2 V^2}\left[\frac{K_0(W d_s/r)}{K_1^2(W)}\right] \qquad \text{Equation 2.31}$$

$$C_w = \frac{\lambda U^2}{2\pi n_{core} r^2 V^2}\left[\frac{K_0(W d_w/r)}{K_1^2(W)}\right] \qquad \text{Equation 2.32}$$

where n_{core} and r are the refractive index and the radius of the fibres' cores, while d_s and d_w are the separation between the neighbour and the distant fibres respectively. The oscillation of the power transfer between the fibres is depicted through zeroth and first order of Bessel functions of the second kind, K_0 and K_1. Finally, $V, W\ and\ U$ are the usual modal parameters which can be determined with the following equations [149, 152]:

$$\frac{UJ_1(U)}{J_0(U)} = \frac{WK_1(W)}{K_0(W)} \qquad \text{Equation 2.33}$$

$$U = r(n_{core}^2 k^2 - \beta^2)^{1/2} \qquad \text{Equation 2.34}$$

$$W = r(\beta^2 - n_{clad}^2 k^2)^{1/2} \qquad \text{Equation 2.35}$$

$$k = \frac{2\pi}{\lambda} \qquad \text{Equation 2.36}$$

where, J_0 and J_1 are the zeroth and first order of the Bessel functions of the first kind respectively, n_{clad} is the cladding's refractive index of the fibres, β is the propagation constant of the fibres and k is the wavenumber which can be determined through the Equation 2.36.

Since the geometry of the fibres described above is similar to the MCF structure then the same system can be used for the case of coupling between the cores of the MCF. According to these equations, coupling of light and power transfer from one core to all four cores of a MCF can be achieved under specific circumstances. Since changes on the refractive indices of the cores and cladding cannot be easily achieved after the fabrication of the MCF, changes to the core separation and radii have to be considered. Reduction of the separation and radii can be achieved at the same time by tapering the MCF, albeit with the limitation of keeping the same ratio. Therefore, these equations can be used to model the power transfer between the cores along the waist (coupling length (z)) of the tapered MCF. This theory is considered in Chapter 5.

The fan-out device with tapering approach of the MCF introduces an additional challenge on the fabrication of a MCF curvature sensor with inscribed FBGs. The coupling of light from one core to all four cores of the MCF necessitates the inscription of different λ FBGs into the cores of the fibre. These FBGs need to have reflectance spectra in *different* (i.e. non-overlapping) regions of the spectrum in order the overlap of

the FBGs peaks to be avoided. Therefore, information about the state (stretched or compressed) of each individual core from the FBGs' response can be extracted through one core which can be spliced with an SMF.

2.9. Conclusions

The primary objective of this chapter was to review state of art in various sensors with the focus on optical as well as optical fibre sensors. FBG sensors are a subcategory of optical fibre sensors with numerous applications in various scientific fields. The MCF curvature sensor, which is reviewed in this chapter, is a particular example of these sensors.

The unique structure of the MCF makes it ideal for temperature-compensated measurements of the strain shift applied on the cores of the fibre. Additionally, the core geometry favour the exploitation of mathematical expressions for the calculation of the fibre's curvature. Thus, calibration of the sensor can be easily achieved through the inscribed FBGs' response.

Two different ways of monitoring the FBGs' reflectance spectra are reported in this chapter. The use of commercially available fan-out devices have the advantage that the cross talk between the cores is avoided. Thus, the FBGs spectra can be monitored individually at the same time.

The alternative fan-out device option for the MCF curvature sensor requires coupling of light from one core of the MCF into all four cores. This can be achieved by tapering the MCF, hence the core distances and radii get reduced. Nonetheless, this option necessitates individual inscription of FBGs into the different cores of the MCF. Hence, the overlap between the FBGs' spectra is avoided.

The following chapter is focused on the experimental work done for two different types of optical fibre sensors. The first is a FBG temperature while the second is a FBG attitude sensor. The fabrication as well as their calibration and performance are reported.

2.10. References

[1] M. B. del Rosario, S. J. Redmond, and N. H. Lovell, "Tracking the Evolution of Smartphone Sensing for Monitoring Human Movement," *Sensors (Basel)*, vol. 15, no. 8, pp. 18901-18933, 2015.

[2] S. Patel, H. Park, P. Bonato, L. Chan, and M. Rodgers, "A review of wearable sensors and systems with application in rehabilitation," *Journal of NeuroEngineering and Rehabilitation*, vol. 9, no. 1, p. 21, 2012.

[3] Statista. (Access date: 05.10.2018). Breakdown of the global sensors market in 2015 and 2020, by application Available: www.statista.com/statistics/675448/sensors-market-size-globally-breakdown-by-application/

[4] J. E. Lenz, "A review of magnetic sensors," *in Proc. IEEE*, vol. 78, no. 6, pp. 973-989, 1990.

[5] J. C. Greenwood, "Silicon in mechanical sensors," *Journal of Physics E: Scientific Instruments*, vol. 21, no. 12, pp. 1114-1128, 1988.

[6] A. Nair and C. S. Cai, "Acoustic emission monitoring of bridges: Review and case studies," *Engineering Structures*, vol. 32, no. 6, pp. 1704-1714, 2010.

[7] A. Richter, G. Paschew, S. Klatt, J. Lienig, K. F. Arndt, and H. P. Adler, "Review on Hydrogel-based pH Sensors and Microsensors," *Sensors (Basel)*, vol. 8, no. 1, pp. 561-581, 2008.

[8] Q. Zeng, B. Sun, J. Xu, X. Deng, J. Xu, and Y. Jia, "Development of NiCr/NiSi Thin-Film Thermocouple Sensor for Workpiece Temperature Measurement in Chemical Explosive Material Machining," *Journal of Manufacturing Science and Engineering*, vol. 128, no. 1, pp. 175-179, 2005.

[9] S. Shigematsu, H. Morimura, Y. Tanabe, T. Adachi, and K. Machida, "A single-chip fingerprint sensor and identifier," *IEEE Journal of Solid-State Circuits*, vol. 34, no. 12, pp. 1852-1859, 1999.

[10] P. Werle, F. Slemr, K. Maurer, R. Kormann, R. Mücke, and B. Jänker, "Near- and mid-infrared laser-optical sensors for gas analysis," *Optics and Lasers in Engineering*, vol. 37, no. 2-3, pp. 101-114, 2002.

[11] B. Lee, "Review of the present status of optical fiber sensors," *Optical Fiber Technology*, vol. 9, no. 2, pp. 57-79, 2003.

[12] L. Lu, X. Hu, and Z. Zhu, "Biomimetic sensors and biosensors for qualitative and quantitative analyses of five basic tastes," *TrAC Trends in Analytical Chemistry*, vol. 87, pp. 58-70, 2017.

[13] J. H. Lee, H. E. Jin, M. S. Desai, S. Ren, S. Kim, and S. W. Lee, "Biomimetic sensor design," *Nanoscale*, vol. 7, no. 44, pp. 18379-91, 2015.

[14] C. Ho, A. Robinson, D. Miller, and M. Davis, "Overview of Sensors and Needs for Environmental Monitoring," *Sensors*, vol. 5, no. 1, pp. 4-37, 2005.

[15] L. Su, W. Jia, C. Hou, and Y. Lei, "Microbial biosensors: a review," *Biosensors Bioelectronics*, vol. 26, no. 5, pp. 1788-99, 2011.

[16] J. M. Ko and Y. Q. Ni, "Technology developments in structural health monitoring of large-scale bridges," *Engineering Structures*, vol. 27, no. 12, pp. 1715-1725, 2005.

[17] N. Barbour and G. Schmidt, "Inertial sensor technology trends," *IEEE Sensors Journal*, vol. 1, no. 4, pp. 332-339, 2001.

[18] W. P. Eaton and J. H. Smith, "Micromachined pressure sensors: review and recent developments," *Smart Materials and Structures*, vol. 6, no. 5, pp. 530-539, 1997.

[19] A. Tong, "Improving the accuracy of temperature measurements," *Sensor Review*, vol. 21, no. 3, pp. 193-198, 2001.

[20] R. Narayanaswamy and O. S. Wolfbeis, "Optical Sensors: Industrial Environmental and Diagnostic Applications." *Springer Berlin Heidelberg*, 2010.

[21] D. Rugar, H. J. Mamin, and P. Guethner, "Improved fiber-optic interferometer for atomic force microscopy," *Applied Physics Letters*, vol. 55, no. 25, pp. 2588-2590, 1989.

[22] J. L. Santos and F. Farahi, "Handbook of Optical Sensors." *Taylor & Francis*, 2014.

[23] L. Dziuda, M. Krej, and F. W. Skibniewski, "Fiber Bragg Grating Strain Sensor Incorporated to Monitor Patient Vital Signs During MRI,", *IEEE Sensors Journal*, vol. 13, no. 12, pp. 4986-4991, 2013.

[24] D. T. Angelidis and P. J. Parsons, "Optical micromachined pressure sensor for aerospace applications," *SPIE Optical Engineering* 1992, vol. 31, p. 5.

[25] W. Staszewski, C. Boller, and G. R. Tomlinson, "Health Monitoring of Aerospace Structures: Smart Sensor Technologies and Signal Processing." *Wiley*, 2004.

[26] J. J. Ramsden, Y. P. Sharkan, N. B. Zhitov, and S. O. Korposh, "Sensors for spacecraft cabin environment monitoring," *Acta Astronautica*, vol. 61, no. 7, pp. 664-667, 2007.

[27] J. P. Dakin, "Multiplexed and distributed optical fibre sensor systems," *Journal of Physics E: Scientific Instruments*, vol. 20, no. 8, p. 954, 1987.

[28] X. D. a. H. Y. Tam, "Temperature-insensitive strain sensor with polarization-maintaining photonic crystal fiber based Sagnac interferometer," *Applied Physics Letters*, vol. 90, no. 15, p. 151113, 2007.

[29] G. N. De Brabander, G. Beheim, and J. T. Boyd, "Integrated optical micromachined pressure sensor with spectrally encoded output and temperature compensation," *Applied Optics*, vol. 37, no. 15, pp. 3264-3267, 1998.

[30] V. Singh, H. Juejun, A. M. Agarwal, and L. C. Kimerling, "Integrated Optical Sensors," *IEEE Photonics Journal*, vol. 4, no. 2, pp. 638-641, 2012.

[31] J. Hodgkinson and R. P. Tatam, "Optical gas sensing: a review," *Measurement Science and Technology*, vol. 24, no. 1, p. 012004, 2013.

[32] L. Dae-Sik, L. Duk-Dong, B. Sang-Woo, L. Minho, and K. Youn Tae, "SnO/sub 2/ gas sensing array for combustible and explosive gas leakage recognition," *IEEE Sensors Journal*, vol. 2, no. 3, pp. 140-149, 2002.

[33] M. Chalfie, Y. Tu, G. Euskirchen, W. Ward, and D. Prasher, "Green fluorescent protein as a marker for gene expression," *Science*, vol. 263, no. 5148, pp. 802-805, 1994.

[34] E. Heyduk and T. Heyduk, "Nucleic Acid-Based Fluorescence Sensors for Detecting Proteins," *Analytical Chemistry*, vol. 77, no. 4, pp. 1147-1156, 2005.

[35] X. Peng *et al.*, "Fluorescence ratiometry and fluorescence lifetime imaging: using a single molecular sensor for dual mode imaging of cellular viscosity," *Journal of America Chemistry Society*, vol. 133, no. 17, pp. 6626-35, 2011.

[36] J. Homola, S. S. Yee, and G. Gauglitz, "Surface plasmon resonance sensors: review," *Sensors and Actuators B: Chemical*, vol. 54, no. 1-2, pp. 3-15, 1999.

[37] J. Homola, "Surface Plasmon Resonance Sensors for Detection of Chemical and Biological Species," *Chemical Reviews*, vol. 108, no. 2, pp. 462-493, 2008.

[38] L. Yang, S. S. Saavedra, and N. R. Armstrong, "Sol-gel-based, planar waveguide sensor for gaseous iodine," *Analytical Chemistry*, vol. 68, no. 11, pp. 1834-41, 1996.

[39] K. Tiefenthaler and W. Lukosz, "Sensitivity of grating couplers as integrated-optical chemical sensors," *Journal of the Optical Society of America B*, vol. 6, no. 2, pp. 209-220, 1989.

[40] Z. Gryczynski, O. O. Abugo, and J. R. Lakowicz, "Polarization sensing of fluorophores in tissues for drug compliance monitoring," *Analytical Biochemistry*, vol. 273, no. 2, pp. 204-11, 1999.

[41] J. K. Chu, K. C. Zhao, Q. Zhang, and T. C. Wang, "Construction and performance test of a novel polarization sensor for navigation," *Sensors and Actuators a-Physical*, vol. 148, no. 1, pp. 75-82, 2008.

[42] V. Gruev, R. Perkins, and T. York, "CCD polarization imaging sensor with aluminum nanowire optical filters," *Optics Express*, vol. 18, no. 18, pp. 19087-94, 2010.

[43] I. Pomozi, G. Horváth, and R. Wehner, "How the clear-sky angle of polarization pattern continues underneath clouds: full-sky measurements and implications for animal orientation," *Journal of Experimental Biology*, vol. 204, no. 17, pp. 2933-2942, 2001.

[44] T. Dresel, G. Häusler, and H. Venzke, "Three-dimensional sensing of rough surfaces by coherence radar," *Applied Optics*, vol. 31, no. 7, pp. 919-925, 1992.

[45] L. S. Swenson, "The Ethereal Aether: A History of the Michelson-Morley-Miller Aether-drift Experiments," 1880-1930. *University of Texas Press*, 2013.

[46] B. P. Abbott *et al.*, "Observation of Gravitational Waves from a Binary Black Hole Merger," *Physics Review Letters*, vol. 116, no. 6, p. 061102, 2016.

[47] *Laser Interferometer Gravitational Wave Observatory (LIGO)*.(Access date: 05.10. 2018) Available: www.ligo.caltech.edu/

[48] B. Sepúlveda, J. S. del Río, M. Moreno, F. J. Blanco, K. Mayora, C. Domínguez and L. M. Lechuga, "Optical biosensor microsystems based on the integration of highly sensitive Mach–Zehnder interferometer devices," *Journal of Optics A: Pure and Applied Optics*, vol. 8, no. 7, p. S561, 2006.

[49] A. Ksendzov, M. L. Homer, and A. M. Manfreda, "Integrated optics ring-resonator chemical sensor with polymer transduction layer," *Electronics Letters*, vol. 40, no. 1, pp. 63-65, 2004.

[50] W. M. Macek and D. T. M. Davis, "Rotation Rate Sensing with Traveling-Wave Ring Lasers," *Applied Physics Letters*, vol. 2, no. 3, pp. 67-68, 1963.

[51] V. Vali and R. W. Shorthill, "Fiber ring interferometer," *Applied Optics*, vol. 15, no. 5, pp. 1099-100, 1976.

[52] Y. Qiang, L. Xuyou, and Z. Guangtao, "A kind of hybrid optical structure IFOG," *in Proc. IEEE International Conference on Mechatronics and Automation* pp. 5030-5034, 2009.

[53] K. Industries. Access date: (05.10.2018) Guide to ComparingGyro and IMU Technologies Micro Electro Mechanical Systems and Fiber Optic Gyros Available: web news.kvh.com/LP-WP-Guide-to-Comparing-Gyro--IMU-Technologies_Banner

[54] E. Udd, "An overview of fiber-optic sensors," *Review of Scientific Instruments,* vol. 66, no. 8, pp. 4015-4030, 1995.

[55] A. Hegyi, P. Kiesel, and A. Raghavan, "Time- and Wavelength-Multiplexed Wavelength Shift Detection for High-Resolution, Low-Cost Distributed Fiber-Optic Sensing," *Journal of Lightwave Technology,* vol. 35, no. 19, pp. 4234-4241, 2017.

[56] J. Crisp, "Introduction to Fiber Optics," *Elsevier Science,* 2005.

[57] U. C. Paek and R. B. Runk, "Physical behavior of the neck-down region during furnace drawing of silica fibers," *Journal of Applied Physics,* vol. 49, no. 8, pp. 4417-4422, 1978.

[58] K. Lyytikainen, S. T. Huntington, A. L. G. Carter, P. McNamara, S. Fleming, J. Abramczyk, I. Kaplin, and G. Schötz, "Dopant diffusion during optical fibre drawing," *Optics Express,* vol. 12, no. 6, pp. 972-7, 22 2004.

[59] J. Kirchhof, S. Unger, K. F. Klein, and B. Knappe, "Diffusion behaviour of fluorine in silica glass," *Journal of Non-Crystalline Solids,* vol. 181, no. 3, pp. 266-273, 1995.

[60] M. D. Feit and J. A. Fleck, "Light propagation in graded-index optical fibers," *Applied Optics,* vol. 17, no. 24, pp. 3990-3998, 1978.

[61] G. Cancellieri, "Single-mode Optical Fibres,"*Elsevier* 1991.

[62] J. M. Dudley, G. Genty, and S. Coen, "Supercontinuum generation in photonic crystal fiber," *Reviews of Modern Physics,* vol. 78, no. 4, pp. 1135-1184, 2006.

[63] Fujikura. (2018). *Panda Fiber* (Access date: 05.10.2018). Available: www.fujikura.co.jp/eng/products/optical/opticaldevices/04/2050105_12895.html

[64] R. R. Thomson, R. J. Harris, T. A. Birks, G. Brown, J. Allington-Smith, and J. Bland-Hawthorn, "Ultrafast laser inscription of a 121-waveguide fan-out for astrophotonics," *Optics Letters,* vol. 37, no. 12, pp. 2331-2333, 2012.

[65] K. M. Hilligsøe *et al.*, "Supercontinuum generation in a photonic crystal fiber with two zero dispersion wavelengths," *Optics Express,* vol. 12, no. 6, pp. 1045-1054, 2004.

[66] P. H. Paul and G. Kychakoff, "Fiber-optic evanescent field absorption sensor," *Applied Physics Letters,* vol. 51, no. 1, pp. 12-14, 1987.

[67] R. Correia, S. James, S. W. Lee, S. P. Morgan, and S. Korposh, "Biomedical application of optical fibre sensors," *Journal of Optics,* vol. 20, no. 7, p. 073003, 2018.

[68] A. Leung, P. M. Shankar, and R. Mutharasan, "A review of fiber-optic biosensors," *Sensors and Actuators B: Chemical,* vol. 125, no. 2, pp. 688-703, 2007.

[69] K. Rijal, A. Leung, P. M. Shankar, and R. Mutharasan, "Detection of pathogen Escherichia coli O157:H7 AT 70cells/mL using antibody-immobilized biconical tapered fiber sensors," *Biosensors and Bioelectronics,* vol. 21, no. 6, pp. 871-880, 2005.

[70] X. Fan, I. M. White, S. I. Shopova, H. Zhu, J. D. Suter, and Y. Sun, "Sensitive optical biosensors for unlabeled targets: A review," *Analytica Chimica Acta,* vol. 620, no. 1, pp. 8-26, 2008.

[71] H. Y. Choi, M. J. Kim, and B. H. Lee, "All-fiber Mach-Zehnder type interferometers formed in photonic crystal fiber," *Optics Express,* vol. 15, no. 9, pp. 5711-5720, 2007.

[72] Z. Tian, Z. Tian, S. S. H. Yam, J. Barnes, W. Bock, P. Greig, J. M. Fraser, H. Loock, and R. D. Oleschuk, "Refractive Index Sensing With Mach–Zehnder Interferometer Based on Concatenating Two Single-Mode Fiber Tapers," *IEEE Photonics Technology Letters,* vol. 20, no. 8, pp. 626-628, 2008.

[73] J. Mathew, O. Schneller, D, Polyzos, D. Havermann, R. M. Carter, W. N. MacPherson, D. P. Hand, and R.R. J. Maier., "In-Fiber Fabry–Perot Cavity Sensor for High-Temperature Applications," *Journal of Lightwave Technology,* vol. 33, no. 12, pp. 2419-2425, 2015.

[74] M. J. Gander, W. N. MacPherson, J. S. Barton, R. L. Reuben, J. D. C. Jones, R. Stevens, K. S. Chana, S. J. Anderson, and T. V. Jones, "Embedded micromachined fibre optic Fabry-Perot pressure sensors in aerodynamics applications," in *IEEE SENSORS,* vol. 2, pp. 1707-1712, 2002.

[75] G. Elsa, "Perspectives on stimulated Brillouin scattering," *New Journal of Physics,* vol. 19, no. 1, p. 011003, 2017.

[76] A. Masoudi, M. Belal, and T. P. Newson, "A distributed optical fibre dynamic strain sensor based on phase-OTDR," *Measurement Science and Technology,* vol. 24, no. 8, p. 085204, 2013.

[77] X. Bao and L. Chen, "Recent progress in distributed fiber optic sensors," *Sensors (Basel),* vol. 12, no. 7, pp. 8601-39, 2012.

[78] Institute of Engineering Geodesy and Measurement Systems. *Condition Monitoring of Railway Tracks and Vehicles with Distributed Fiber Optic Sensing*.

[79] Y. I. Rzhavin, "Fiber-Optic Polarization Pressure Sensor," *Measurement Techniques,* journal article vol. 45, no. 7, pp. 738-741, 2002.

[80] H. Y. Fu *et al.*, "Pressure sensor realized with polarization-maintaining photonic crystal fiber-based Sagnac interferometer," *Applied Optics,* vol. 47, no. 15, pp. 2835-2839, 2008.

[81] D. Havermann, J.Mathew, W. N.MacPherson, R. R. J. Maier, and D. P. Hand, "Temperature and Strain Measurements With Fiber Bragg Gratings Embedded in Stainless Steel 316," *Journal of Lightwave Technology,* vol. 33, no. 12, p. 6, 2015.

[82] K. O. Hill, Y. Fujii, D. C. Johnson, and B. S. Kawasaki, "Photosensitivity in optical fiber waveguides: Application to reflection filter fabrication," *Applied Physics Letters,* vol. 32, no. 10, p. 647, 1978.

[83] D. Tosi, "Review and Analysis of Peak Tracking Techniques for Fiber Bragg Grating Sensors," *Sensors (Basel),* vol. 17, no. 10, Oct 17 2017.

[84] T. Erdogan, V. Mizrahi, P. J. Lemaire, and D. Monroe, "Decay of ultraviolet-induced fiber Bragg gratings," *Journal of Applied Physics,* vol. 76, no. 1, pp. 73-80, 1994.

[85] L. Dong, J. Archambault, L. Reekie, S. P. J. Russell, and D. N. Payne, "Single pulse Bragg gratings written during fibre drawing," *Electronics Letters,* vol. 29, no. 17, pp. 1577-1578, 1993.

[86] Y.J. Rao, "In-fibre Bragg grating sensors," *Measurement Science Technology,* vol. 8, p. 21, 1997.

[87] A. G. Simpson, K. Kalli, K. Zhou, L. Zhang, and I. Bennion, "Formation of type IA fibre Bragg gratings in germanosilicate optical fibre," *Electronics Letters,* vol. 40, no. 3, pp. 163-164, 2004.

[88] N. Groothoff and J. Canning, "Enhanced type IIA gratings for high-temperature operation," *Optics Letters,* vol. 29, no. 20, pp. 2360-2362, 2004.

[89] D. Grobnic, C. Hnatovsky, and S. J. Mihailov, "Low loss Type II regenerative Bragg gratings made with ultrafast radiation," *Optics Express,* vol. 24, no. 25, pp. 28704-28712, 2016.

[90] D. B. Hunter and R. A. Minasian, "Microwave optical filters using in-fiber Bragg grating arrays," *IEEE Microwave and Guided Wave Letters,* vol. 6, no. 2, p. 103, 1996.

[91] N. Lizárraga, N. P. Puente, E. I. Chaikina, T. A. Leskova, and E. R. Méndez, "Single-mode Er-doped fiber random laser with distributed Bragg grating feedback," *Optics Express,* vol. 17, no. 2, pp. 395-404, 2009.

[92] A. Othonos, "Fiber Bragg gratings," *Review of Scientific Instruments,* vol. 68, no. 12, pp. 4309-4341, 1997.

[93] A. M. Vengsarkar, P. J. Lemaire, J. B. Judkins, V. Bhatia, T. Erdogan, and J. E. Sipe, "Long-period fiber gratings as band-rejection filters," *Journal of Lightwave Technology,* vol. 14, no. 1, pp. 58-65, 1996.

[94] L. Marques, L. Marques, F.U. Hernandez, S.W. James, S.P. Morgan, M. Clark, R.P. Tatam, S. Korposh, "Highly sensitive optical fibre long period grating biosensor anchored with silica core gold shell nanoparticles," *Biosensors and Bioelectronics,* vol. 75, pp. 222-231, 2016.

[95] B. Mason, G. A. Fish, S. P. DenBaars, and L. A. Coldren, "Widely tunable sampled grating DBR laser with integrated electroabsorption modulator," *IEEE Photonics Technology Letters,* vol. 11, no. 6, pp. 638-640, 1999.

[96] K. O. Hill *et al.,* "Chirped in-fiber Bragg gratings for compensation of optical-fiber dispersion," *Optics Letters,* vol. 19, no. 17, pp. 1314-1316, 1994.

[97] T. Guo, H.-Y. Tam, P. A. Krug, and J. Albert, "Reflective tilted fiber Bragg grating refractometer based on strong cladding to core recoupling," *Optics Express,* vol. 17, no. 7, pp. 5736-5742, 2009.

[98] S. A. Slattery, D. N. Nikogosyan, and G. Brambilla, "Fiber Bragg grating inscription by high-intensity femtosecond UV laser light: comparison with other existing methods of fabrication," *Journal of the Optical Society of America B,* vol. 22, no. 2, pp. 354-361, 2005.

[99] N. Huot, C. Jonin, N. Sanner, E. Baubeau, E. Audouard, and P. Laporte, "High UV average power at 15 kHz by frequency doubling of a copper HyBrID vapor laser in β-barium borate," *Optics Communications,* vol. 211, no. 1-6, pp. 277-282, 2002.

[100] A. Martinez, I. Khrushchev, and I. Bennion, "Thermal annealing of fiber Bragg gratings directly inscribed by an ultrafast infrared laser," *in Proc. Conference on Lasers and Electro-Optics,* vol. 3, pp. 2188-2190, 2005.

[101] P. J. Lemaire, R. M. Atkins, V. Mizrahi, and W. A. Reed, "High pressure H2 loading as a technique for achieving ultrahigh UV photosensitivity and thermal sensitivity in GeO2 doped optical fibres," *Electronics Letters,* vol. 29, no. 13, p. 1191, 1993.

[102] C. L. Liou, L. A. Wang, and M. C. Shih, "Characteristics of hydrogenated fiber Bragg gratings," *Applied Physics A: Materials Science & Processing,* vol. 64, no. 2, pp. 191-197, 1997.

[103] B. S. Kawasaki, K. O. Hill, D. C. Johnson, and Y. Fujii, "Narrow-band Bragg reflectors in optical fibers," *Optics Letters,* vol. 3, no. 2, p. 66, 1978.

[104] K. O. Hill and G. Meltz, "Fiber Bragg Grating Technology Fundamentals and Overview," *Journal of Lightwave Technology,* vol. 15, no. 8, pp. 1263-1276, 17.09.15 1997.

[105] G. Meltz, W. W. Morey, and W. H. Glenn, "Formation of Bragg gratings in optical fibers by a transverse holographic method," *Optics Letters,* vol. 14, no. 15, pp. 823-825, 1989.

[106] B. A. Tahir, J. Ali, and R. A. Rahman, "Fabrication of fiber grating by phase mask and its sensing application,", *Journal of Optoelectronics and Advanced Materials,* vol. 8, no. 4, pp. 1604-1609, 2006.

[107] C. Voigtländer *et al.*, "Ultrashort pulse inscription of tailored fiber Bragg gratings with a phase mask and a deformed wavefront [Invited]," *Optical Materials Express,* vol. 1, no. 4, pp. 633-642, 2011.

[108] G. Rajan, M. Y. M. Noor, E. Ambikairajah, and G. D. Peng, "Inscription of Multiple Bragg Gratings in a Single-Mode Polymer Optical Fiber Using a Single Phase Mask and Its Analysis," *IEEE Sensors Journal,* vol. 14, no. 7, pp. 2384-2388, 2014.

[109] W. Yuan, A. Stefani, and O. Bang, "Tunable Polymer Fiber Bragg Grating (FBG) Inscription: Fabrication of Dual-FBG Temperature Compensated Polymer Optical Fiber Strain Sensors," *IEEE Photonics Technology Letters,* vol. 24, no. 5, pp. 401-403, 2012.

[110] A. Othonos and X. Lee, "Novel and Improved Methods of Writing Bragg Gratings with Phase Masks," *IEEE Photonics Technology Letters,* vol. 7, no. 10, pp. 1183-1185, 1995.

[111] J. D. Prohaska, E. Snitzer, S. Rishton, and V. Boegli, "Magnification of mask fabricated fibre Bragg gratings," *Electronics Letters,* vol. 29, no. 18, pp. 1614-1615, 1993.

[112] N. Sayers, S. Granieri, A. Siahmakoun., "Fabrication of multiple fiber-Bragg gratings on one SMF using a single phase-mask," vol. 5970, pp. 59701J, 2005.

[113] H. Patrick and S. L. Gilbert, "Growth of Bragg gratings produced by continuous-wave ultraviolet light in optical fiber," *Optics Letters,* vol. 18, no. 18, pp. 1484-1486, 1993.

[114] Y. Lai, K. Zhou, K. Sugden, and I. Bennion, "Point-by-point inscription of first-order fiber Bragg grating for C-band applications," *Optics Express,* vol. 15, no. 26, pp. 18318-18325, 2007.

[115] G. D. Marshall, R. J. Williams, N. Jovanovic, M. J. Steel, and M. J. Withford, "Point-by-point written fiber-Bragg gratings and their application in complex grating designs," *Optics Express,* vol. 18, no. 19, pp. 19844-19859, 2010.

[116] A. V. Dostovalov, A. A. Wolf, A. V. Parygin, V. E. Zyubin, and S. A. Babin, "Femtosecond point-by-point inscription of Bragg gratings by drawing a coated fiber through ferrule," *Optics Express,* vol. 24, no. 15, pp. 16232-16237, 2016.

[117] M. A. Davis and A. D. Kersey, "All-fibre Bragg grating strain-sensor demodulation technique using a wavelength division coupler," *Electronics Letters,* vol. 30, no. 1, pp. 75-77, 1994.

[118] G. M. H. Flockhart, R. R. J. Maier, J. S. Barton, W. N. MacPherson, J. D. C. Jones, K. E. Chisholm, L. Zhang, I. Bennion, I. Read, and P. D. Foote, "Quadratic behavior of fiber Bragg grating temperature coefficients," *Applied optics,* vol. 43, no. 13, p. 8, 2004.

[119] G. Rajan, "Optical Fiber Sensors: Advanced Techniques and Applications." *CRC Press,* 2017.

[120] M. M. Werneck, R.C.S.B. Allil, B.A. Ribeiro, and F. V. B. de Nazare, "A Guide to Fiber Bragg Grating Sensors," *Open Science* 2013.

[121] E. Li Enbang Li, J. Xi, J. Xi, J. F. Chicharo, T. Liu, Xi. Li, J. Jiang, L. Li, Y. Wang, Y. Zhang, "The experimental evaluation of FBG sensors for strain measurement of prestressed steel strand," in SPIE *Smart Materials, Nano-, and Micro-Smart Systems*, vol. 5649, p. 7. 2005.

[122] A. T. Alavie, S. E. Karr, A. Othonos, and R. M. Measures, "A multiplexed Bragg grating fiber laser sensor system," *IEEE Photonics Technology Letters,* vol. 5, no. 9, pp. 1112-1114, 1993.

[123] D. Barrera, V. Finazzi, J. Villatoro, S. Sales, and V. Pruneri, "Packaged Optical Sensors Based on Regenerated Fiber Bragg Gratings for High Temperature Applications," *IEEE Sensors Journal,* vol. 12, no. 1, pp. 107-112, 2012.

[124] Z. Zhou and J. P. Ou, "Techniques of temperature compensation for FBG strain sensors used in long-term structural monitoring," *Fundamental Problems of Optoelectronics and Microelectronics II,* vol. 5851, pp. 167-172, 2005.

[125] M. G. Xu, L. Reekie, J. P. Dakin, and J. L. Archambault, "Discrimination between strain and temperature effects using dual-wavelength fibre grating sensors," *Electronics Letters,* vol. 30, no. 13, pp. 1085-1087, 1994.

[126] S. J. Mihailov, "Fiber Bragg Grating Sensors for Harsh Environments," *Sensors,* vol. 12, no. 2, p. 1898, 2012.

[127] I. Garcia, J. Zubia, G. Durana, G. Aldabaldetreku, M. A. Illarramendi, and J. Villatoro, "Optical Fiber Sensors for Aircraft Structural Health Monitoring," *Sensors (Basel),* vol. 15, no. 7, pp. 15494-519, 2015.

[128] C. Wan, W. Hong, J. Liu, Z. Wu, Z. Xu, and S. Li, "Bridge Assessment and Health Monitoring with Distributed Long-Gauge FBG Sensors," *International Journal of Distributed Sensor Networks,* vol. 2013, pp. 1-10, 2013.

[129] T. H. T. Chan *et al.,* "Fiber Bragg grating sensors for structural health monitoring of Tsing Ma bridge: Background and experimental observation," *Engineering Structures,* vol. 28, no. 5, pp. 648-659, 2006.

[130] Y. Wang, J. Gong, D. Y. Wang, B. Dong, W. Bi, and A. Wang, "A Quasi-Distributed Sensing Network With Time-Division-Multiplexed Fiber Bragg Gratings," *IEEE Photonics Technology Letters,* vol. 23, no. 2, pp. 70-72, 2011.

[131] P. Peng-Chun, L. Jia-He, T. Hong-Yih, and C. Sien, "Intensity and wavelength-division multiplexing FBG sensor system using a tunable multiport fiber ring laser," *IEEE Photonics Technology Letters,* vol. 16, no. 1, pp. 230-232, 2004.

[132] Z. Weigang, D. Xiaoyi, Z. Qida, K. Guiyun, and Y. Shuzhong, "FBG-type sensor for simultaneous measurement of force (or displacement) and temperature based on bilateral cantilever beam," *IEEE Photonics Technology Letters,* vol. 13, no. 12, pp. 1340-1342, 2001.

[133] H. J. Patrick, "Self-aligning bipolar bend transducer based on long period grating written in eccentric core fibre," *Electronics Letters,* vol. 36, no. 21, pp. 1763-1764, 2000.

[134] F. M. Araújo, L. A. Ferreira, and J. L. Santos, "Simultaneous determination of curvature, plane of curvature, and temperature by use of a miniaturized sensing head based on fiber Bragg gratings," *Applied Optics,* vol. 41, no. 13, pp. 2401-2407, 2002.

[135] B. J. Wolf, J. A. S. Morton, W. B. N. MacPherson, and S. M. van Netten, "Bio-inspired all-optical artificial neuromast for 2D flow sensing," *Bioinspiration Biomimetics,* vol. 13, no. 2, pp. 1-10, 2018.

[136] Amanda Fender, W. N. MacPherson, R.R. J. Maier, J. S. Barton, D. S. George, R. I. Howden, G. W. Smith, B. J. S. Jones, S. McCulloch, X. Chen, R. Suo, L. Zhang, and I. Bennion, "Two-Axis Temperature-Insensitive Accelerometer Based on Multicore Fiber Bragg Gratings," *IEEE Sensors,* vol. 8, no. 7, p. 7, 2008.

[137] A. Fender; W. N. MacPherson, R. R. J. Maier, J. S. Barton, D. S. George, R. I. Howden, G. W. Smith, B. J. S. Jones, S. McCulloch, X. Chen, R. Suo, L. Zhang, I. Bennion, "Two-axis accelerometer based on multicore fibre Bragg gratings," vol. 6619, pp. 66190Q-4, 2007.

[138] M. Silva-Lopez, "Optical Fibre Sensors for Transverse Strain and Bend Measurement," A dissertation for the degree of Doctor of Philosophy, School of Engineering and Physical Sciences, Heriot-Watt University, 2006.

[139] G. M. H. Flockhart, W. N. MacPherson, J. S. Barton, and J. D. C. Jones, "Two-axis bend measurement with Bragg gratings in multicore optical fiber," *Optics Letters,* vol. 28, no. 6, p. 3, 2003.

[140] P. P. Benham, "Mechanics of engineering materials / P.P. Benham, R.J. Crawford, C.G. Armstrong," *2nd ed. ed. Harlow: Longman,* 1996.

[141] J. Cui, S. Zhu, K. Feng, D. Hong, J. Li, and J. Tan, "Fan-out device for multicore fiber coupling application based on capillary bridge self-assembly fabrication method," *Optical Fiber Technology,* vol. 26, pp. 234-242, 2015.

[142] R. R. Thomson, H. T. Bookey, N. D. Psaila, A. Fender, S. Campbell, W. N. MacPherson, J. S. Barton, D. T. Reid, and A. K. Kar, "Ultrafast-laser inscription of a three dimensional fan-out device for multicore fiber coupling applications," *Optics Express,* vol. 15, no. 18, pp. 11691-11697, 2007.

[143] S. G. Leon-Saval, N. K. Fontaine, and R. Amezcua-Correa, "Photonic lantern as mode multiplexer for multimode optical communications," *Optical Fiber Technology,* vol. 35, pp. 46-55, 2017.

[144] I. Gris-Sánchez, D. M. Haynes, K. Ehrlich, R. Haynes, and T. A. Birks, "Multicore fibre photonic lanterns for precision radial velocity Science," *Monthly Notices of the Royal Astronomical Society,* vol. 475, no. 3, pp. 3065-3075, 2018.

[145] G. M. Saridis, D. Alexandropoulos, G. Zervas, and D. Simeonidou, "Survey and Evaluation of Space Division Multiplexing: From Technologies to Optical Networks," *IEEE Communications Surveys & Tutorials,* vol. 17, no. 4, pp. 2136-2156, 2015.

[146] Z. S. Eznaveh, J. E. Antonio-Lopez, J. C. A. Zacarias, A. Schülzgen, C. M. Okonkwo, and R. A. Correa, "All-fiber few-mode multicore photonic lantern mode multiplexer," *Optics Express,* vol. 25, no. 14, pp. 16701-16707, 2017.

[147] A. W. Snyder, "Coupled-Mode Theory for Optical Fibers," *Journal of the Optical Society of America,* vol. 62, no. 11, pp. 1267-1277, 1972.

[148] M. J. F. DIGONNET and H. J. SHAW, "Analysis of a Tunable Single Mode Optical Fiber Coupler," *IEEE Transaction on microwave theory and techniques,* vol. MTT-30, no. 4, p. 9, 1982.

[149] H. S. Jeong, C. Y. Kim, W. Shin, and T. J. Ahn, "Dual-wavelength first-order optical differentiators based on bidirectional fiber couplers," (in English), *Journal of Optics,* vol. 15, no. 5, 2013.

[150] D. B. Mortimore and J. W. Arkwright, "Theory and fabrication of wavelength flattened 1 x N single-mode couplers," *Applied Optics,* vol. 29, no. 12, pp. 1814-8, 1990.

[151] D. B. Mortimore, "Theory and fabrication of 4 x 4 single-mode fused optical fiber couplers," *Applied Optics,* vol. 29, no. 3, pp. 371-4, 1990.

[152] A. Ankiewicz, A. Snyder, and Z. Xue-Heng, "Coupling between parallel optical fiber cores-Critical examination," *Journal of Lightwave Technology,* vol. 4, no. 9, pp. 1317-1323, 1986.

Chapter 3. Fibre Bragg Grating Temperature and Attitude Sensors

This chapter reports the fabrication and calibration of two different types of sensor which were used in field trials for the Lakshmi project. The first type is a FBG based Temperature sensor while the second is an attitude sensor which consists of three perpendicular to each other individual FBG curvature sensors.

Both types of sensors were mounted on the sensors unit (Figure 3-1) which was used for subsea flow measurements on the Orkney Islands coastline. The temperature sensors serve two purposes: (a) to be used for actual temperature measurements of the sea water and (b) to be used for temperature compensation of the flow and attitude sensors which were mounted on and in the unit respectively. The main purpose of the attitude sensor was to determine the orientation of the deployed sensors unit in the sea.

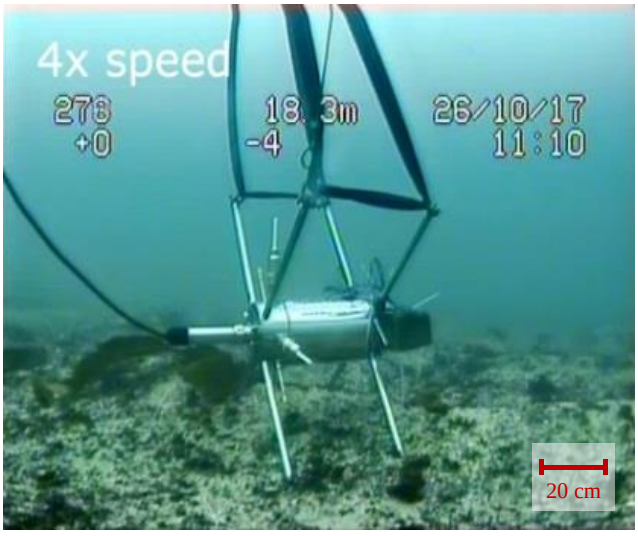

Figure 3-1. Deployed sensors unit at Orkney Islands coastline.

3.1. FBG temperature sensors

The fabrication and calibration of a FBG temperature sensor is a well-established procedure. In the most common cases, the fibre is inserted into a capillary tube or similar structure in order to be strain isolated [1]. The fabricated temperature sensors here, follow the same principle.

3.1.1. Fabrication of FBG temperature sensors

The temperature sensors presented in this chapter were fabricated using a FBG inscribed into a single mode fibre (provided by AtGrating Ltd.). The fibre was inserted into a stainless still capillary tube. Four FBG temperature sensors were fabricated using gratings with nominal central wavelength (λ) of 1517 nm, 1535 nm, 1556 nm and 1575 nm. The primary objective for fabricating these sensors was to measure the local environmental temperature of the sensors unit (see Chapter 1 paragraph 1.4.2). Figure 3-2 (a) and (b) show a schematic diagram as well as an actual image of the FBG temperature sensor. Finally, the fibre was given further protection with external plastic tubing (Figure 3-2 (c)).

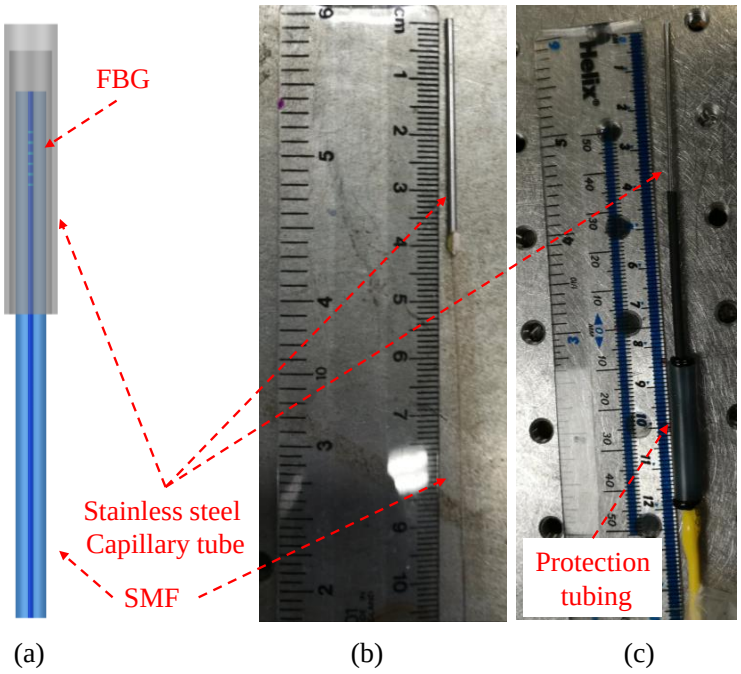

Figure 3-2. FBG temperature sensor (a) schematic diagram, (b) actual sensor and (c) final configuration.

3.1.2. Calibration of the FBG temperature sensors

The sensors unit is designed for subsea measurements; therefore the calibration of the sensors was performed in water over a temperature range of 0 – 20° C. Calibration was achieved with measurements taken from a K-type thermocouple (RS components) using LabVIEW interfaced with a National Instruments data acquisition device (DAQ-6009) [Appendix 1]. The sensors were inserted in water environment at initial temperature ~0° C which reached the room temperature (~22° C) over time. The accuracy of the K-type thermocouple used for these measurements is ±1.5° C, according to the product

datasheet [2]. Measurements on the environmental temperature of the sensors were taken concurrently with the FBG's reflectance peak position response (using an SM130 Micron Optics interrogator). Figure 3-3 shows the calibration graphs for all four temperature sensors.

The response of the FBGs is as expected; an increment of the temperature results in an increase of the reflected reflectance wavelength peak positions. It has been reported in literature that the FBGs wavelength response has a quadratic behaviour over the temperature range of -70° C to 80° C, due to the non-linear behaviour of the thermo-optic coefficient of the silica glass [3]. However, for the range of 0-20° C, a linear approximation can be applied:

$$\lambda = m \cdot T + c \qquad \text{Equation 3.1}$$

Where, λ is the FBGs reflectance wavelength peak position, T is the temperature, m is the gradient and c is the intercept determined from the linear fitting of the calibration graphs.

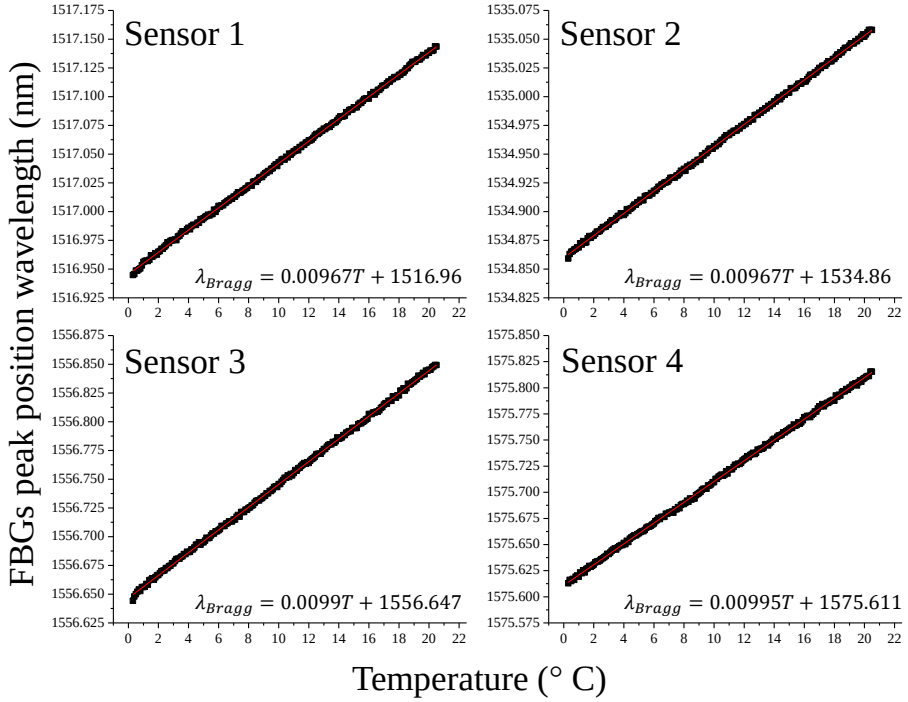

Figure 3-3. Calibration graphs for the four fabricated FBG temperature sensors.

The noise level on the reflectance peak position of the FBGs was recorded over several minutes on a stable temperature, and defined as the half value of the difference between the maximum and minimum value of the wavelength peak position ($(\lambda_{max} - \lambda_{\min})/2$). This level is ±0.003 nm corresponding to ±0.3° C according to Equation 3.1. Hence, with the error introduced from the gradients of the calibration curves (± 1.5° C), it is considered that the FBG temperature sensors can measure with an absolute accuracy of a ~2° C, but resolution of 0.3° C.

The resolution and sensitivity of the temperature sensors reported here are close to a FBG temperature sensor reported in literature [4], in this case the sensor was calibrated with the same probe (K-type thermocouple).

3.2. FBG Based Attitude Sensor

The Attitude sensor presented in this paragraph consists of three different FBG curvature sensors (C1, C2 and C3). Each sensor aims to measure deflection in two planes due to Earth's gravity acting on weights attached to the sensors. The fabrication as well as the calibration of the curvature sensors is reported and the final attitude sensor arrangement is reported.

3.2.1. Fabrication of the FBG curvature sensors

i. Fabrication of the sensor's "Stem"

The fabrication of the three FBG curvature sensors was performed using the experimental set up shown schematically in Figure 3-4. Each individual sensor consisted of four commercially sourced SMFs with inscribed FBGs. The SMFs were positioned in a square arrangement using specially designed fibre holders (plastic discs where the fibres could be thread in a square arrangement). Tension (75 N) was applied to each fibre in order to ensure that they are straight. The four fibres were glued together with an optical adhesive (Norland 68) which was applied at a controlled rate using an automated syringe pump. Curing of the glue applied on the fibres was performed with a ring consisting of UV LEDs (central wavelength λ, 375 nm), Figure 3-5 shows the emission spectrum of the LEDs. Several passes of the UV curing ring along the fibres ensured that a uniform and rigid structure ("stem") was fabricated.

The length of the 'stem' is restricted only by the translation distance of ~15 cm, however in most cases the length was 7 cm. Figure 3-6 shows a cross section of the fibres

stem (taken under the microscope) produced by the set up shown in Figure 3-4. All four FBGs were aligned to each other, hence all four FBGs were positioned at a specific length along the sensor's "stem".

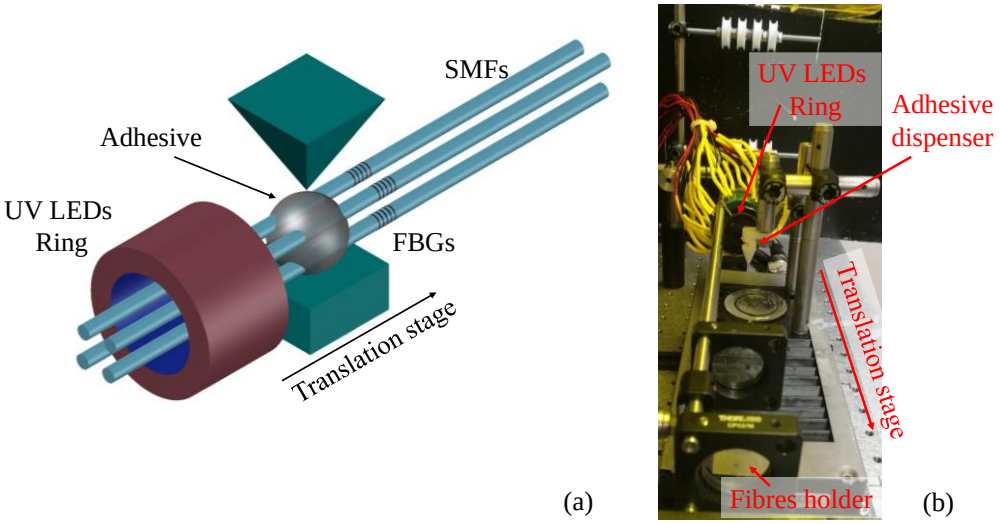

Figure 3-4. (a) Schematic diagram of the experimental set up for the fabrication of the "stem" for the 4-SMFs curvature sensor (b) actual set up.

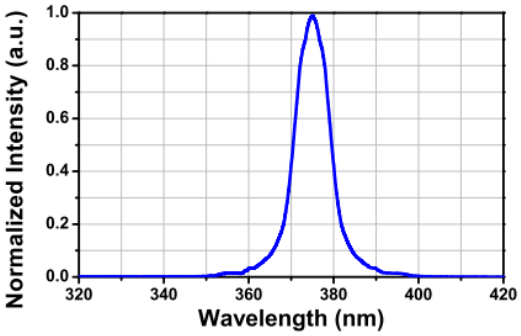

Figure 3-5. Emission spectrum of the LEDs used on the curing proses [5].

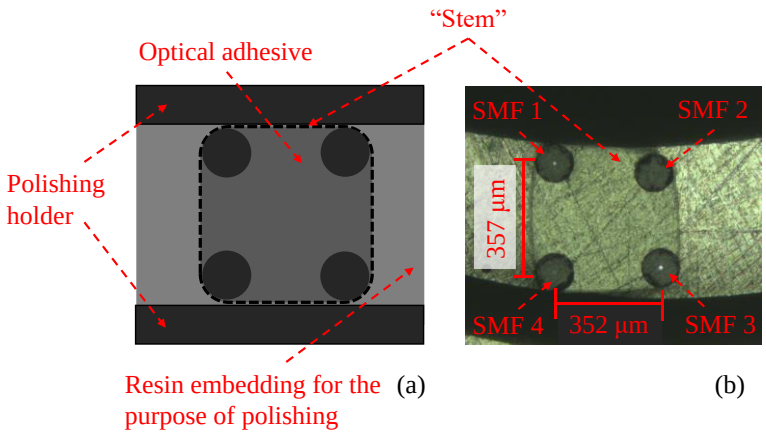

Figure 3-6. (a) Schematic diagram and (b) actual image of the "stem" cross section (the core of the SMFs 1 and 3 are illuminated with white light).

ii. Temperature sensitivity

The FBG curvature sensors used for the fabrication of the attitude sensor are expected to be temperature compensated. The response of the FBGs due to temperature is expected to be affected equally for each individual sensor, since they are all positioned close to each other and their local temperature is the same. Hence, the differential response of the FBG system (wavelength shift) will be only due to strain variation from deflection.

Experiments conducted on strain-isolated curvature sensors produced with the procedure described in section 3.2.1 revealed a drift on the wavelength shift of the FBGs responses. Figure 3-7 shows measurements taken in collaboration with a research associate within our group (Jonathan Morton). The 'stem' sensor (Figure 3-4) was immersed in a water tank and the wavelength peak positions of the four FBGs were monitored alongside the temperature. A maximum of 200 pm drift on the differential response of the FBGs (i.e. FBG1-FBG4) within a temperature range of ~10° C can be spotted.

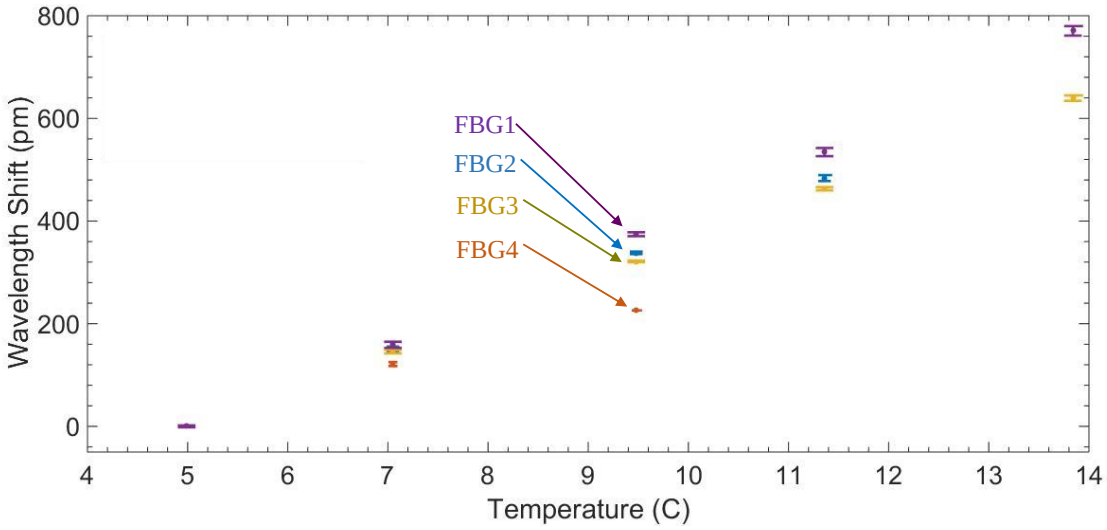

Figure 3-7. The wavelength shifts of the FBGs in the 'stem' was found to vary with respect to the temperature variations (measurements taken in collaboration with Dr. Jonathan Morton).

The un-expected temperature sensitivity of the curvature sensors is considered to be due the dissimilarity of the 'stem' material and structure. The 'stem' consists of optical adhesive and optical fibres. These materials have different thermal expansion coefficients (~10^{-6}/°C for fused silica, ~220×10^{-6}/°C for optical adhesives) which may explain the non-common mode drift. Moreover, a slight misalignment of the FBGs in the sensing element ('stem') during their fabrication can increase this temperature sensitivity.

iii. Cantilever geometry

The cantilever geometry of the sensor was achieved by attaching the sensor stem to a plastic mount (fixed point in Figure 3-8(a)). Figure 3-8 shows a schematic diagram as well as an actual image of an individual curvature sensor which was fabricated for the attitude sensor.

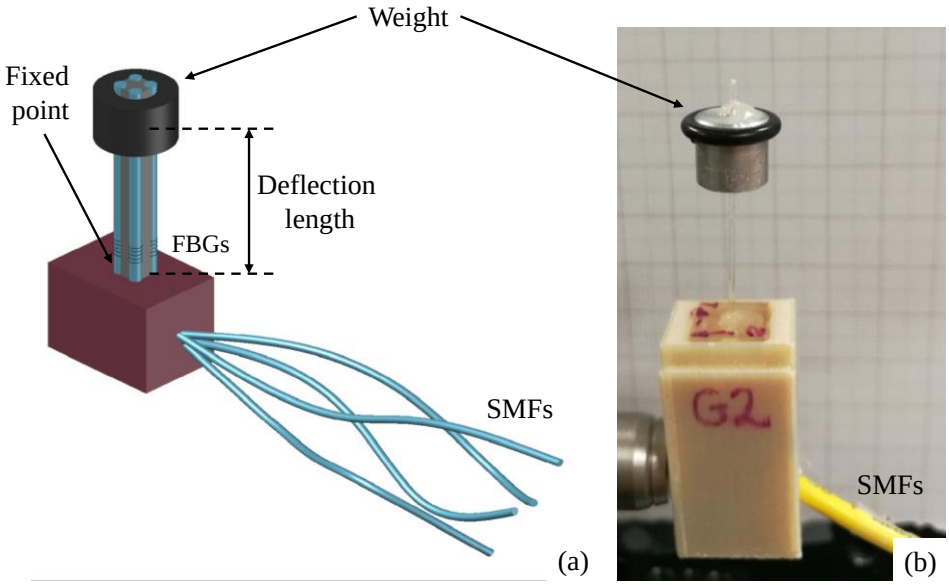

Figure 3-8. (a) Schematic diagram and (b) an actual image of an individual FBG curvature sensor used for the attitude FBG sensor.

The primary objective was to fabricate an attitude sensor with the smallest possible volume, since it had to be inserted into the sensors unit frame. Hence, a study into the deflection of the stem due to various attached weights was performed. The "stem" was mounted on a load cell and deflections were applied at the end of the cantilever. Hence, the load as a function of deflection could be determined and the ideal cantilever length and attached weight were optimised.

It was considered that a maximum of 1.5 nm wavelength shift between two FBGs (the diagonal ($d = \sim 514.324\ \mu m$)) could provide measurements with sufficient accuracy (above the noise levels) on the deflection of the cantilever 'stem'. Figure 3-9 shows the amount of cantilevers deflection for different lengths with various attached weights. This is converted to a deflection of 0.5 mm (v_l) on the 'stem' for the shortest cantilever length ($l = 20\ mm$) using the following equations, (where z is the FBGs distance (e.g. 6mm)):

$$\frac{\Delta\lambda_{reflected}}{\Delta\varepsilon} = 1.2\ pm/\mu\varepsilon \qquad \text{Equation 3.2}$$

$$\Delta\varepsilon = \frac{d}{R} \qquad \text{Equation 3.3}$$

$$\kappa = \frac{1}{R} = \frac{3\,(l-z)}{l^3}\ \nu_l \qquad \text{Equation 3.4}$$

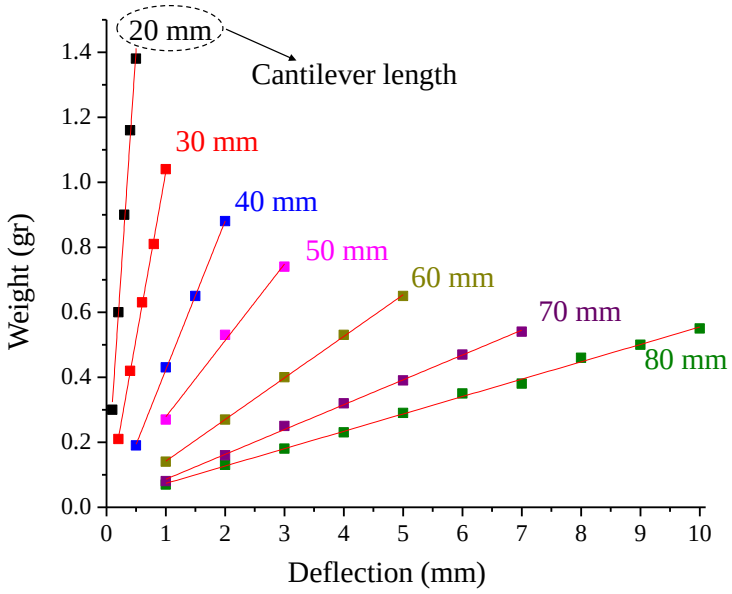

Figure 3-9. Experimental results for the establishment of the ideal weight and length of the curvature sensor.

Additional processing on these data showed that the performance of the cantilever sensor in regards to its stiffness was as expected. The stiffness (s) is defined as the force applied (F) on the cantilever over its displacement (δ), $s = (F/\delta)$.

Figure 3-10 (a) shows the stiffness (gradients of the graphs) calculated for each cantilever 'stem' length produced for the curvature sensors. Moreover, according to beam theory [6], the stiffness of a cantilever (which is deflected at its end) is proportional to the inverse third power of its length ($s \propto \frac{1}{l^3}$). The fitting of these data (Figure 3-11 (b)) showed that the stiffness followed this trend.

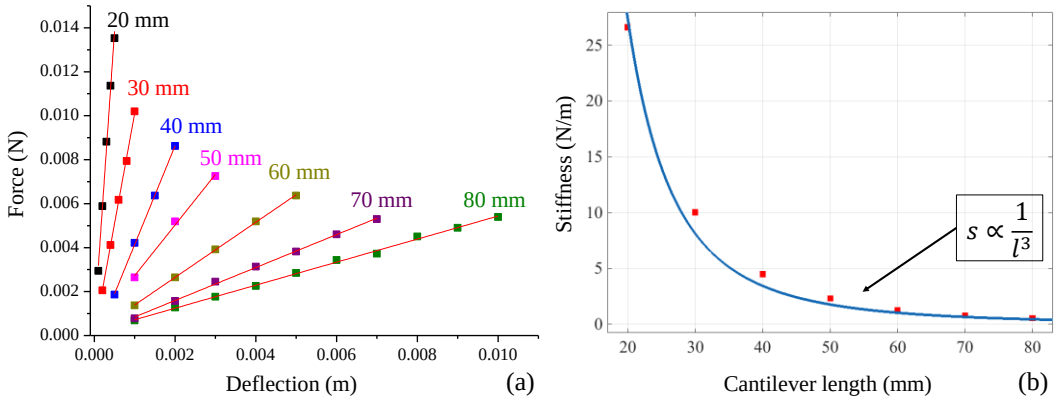

Figure 3-10. (a) Stiffness calculated from the gradients of the force vs the deflection for each case of cantilever length, (b) fitting of the stiffness vs cantilever length.

According to the data produced from these measurements (Figure 3-10) a maximum of 0.5 mm deflection of the cantilever can be achieved with a 1.30 gram weight and 20 mm cantilever length.

iv. Interrogation of the FBGs

The three curvature sensors used for the fabrication of the attitude sensor consist of four FBGs each (twelve FBGs in total for each attitude sensor). In order to monitor all FBGs at the same time a suitable multiplexing scheme is desirable, since the commercial optical interrogator (Micron Optics 130) used for the experiments has four available optical ports. This was achieved with three different wavelength division multiplexers (WDMs), one for each curvature sensor. Figure 3-11 shows a schematic diagram of the multiplexing scheme.

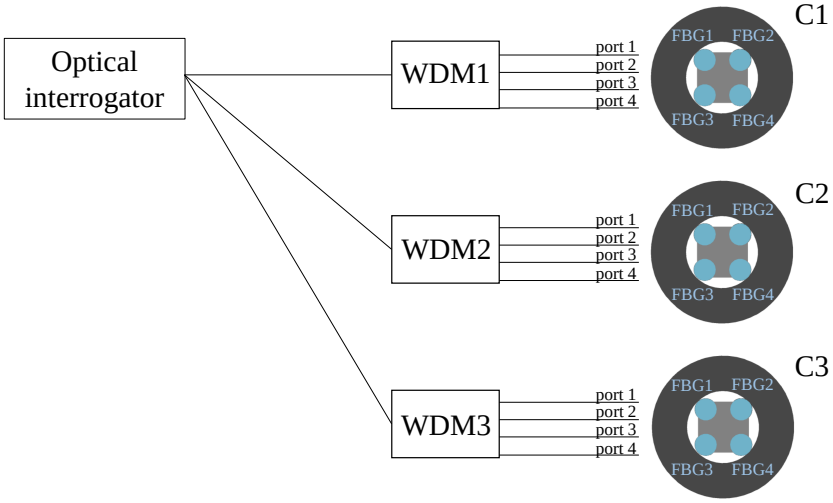

Figure 3-11. Multiplexing scheme of the three curvature sensors for the attitude sensor.

Table 3-1 includes the FBG reflected wavelength peak position for all FBGs used for the three curvature sensors with their measured FWHM (Appendix 2). Moreover, Figure 3-12 shows FBGs reflection spectra after multiplexing monitored with a commercial interrogator (Micron Optics 130). The dashed line is the filtered spectrum which was collected from an optical spectrum analyser (OSA Advantest) from each port of the WDMs used for each sensor.

Table 3-1. FBGs reflected wavelength peak positions and FWHMs for the three curvature sensors.

FBGs	**C1** (nm)		**C2** (nm)		**C3** (nm)	
	λ_{max}	FWHM	λ_{max}	FWHM	λ_{max}	FWHM
1	1532.69	0.2195	1512.87	0.2314	1513.45	0.2163
2	1552.94	0.2075	1527.83	0.2155	1527.67	0.2594
3	1567.71	0.2075	1548.03	0.2115	1548.36	0.2234
4	1585.34	0.1995	1572.27	0.2274	1572.45	0.2051

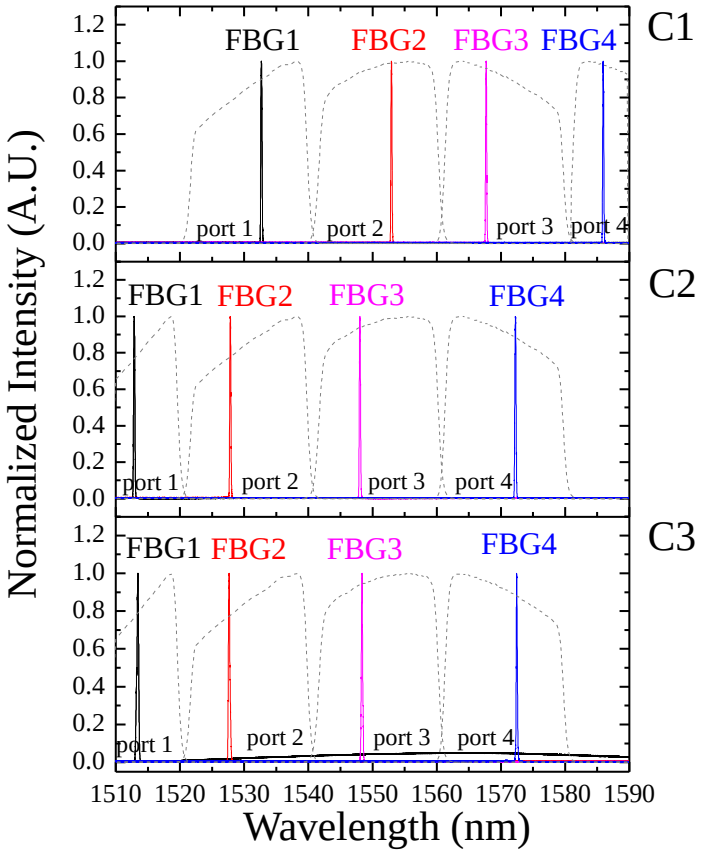

Figure 3-12. Reflection spectra of the multiplexed FBGs for the three curvature sensors used for the attitude sensor, the dashed lines are the filtered spectra which were collected from each port of the WDMs, used for multiplexing of the sensors.

3.2.2. Curvature sensor calibration

A calibration procedure was performed on each individual FBG curvature sensor. The procedure consists of two different steps: (*i*) linear displacement at the end of cantilever (hereafter referred to as linear calibration) of the sensors and (*ii*) rotational displacement of the sensors (hereafter referred to as rotational calibration). Figure 3-13 shows a schematic diagram of the two deflections applied on the sensors. Both parts will be presented in detail for the first FBG curvature sensor (C1). The performance of the other two sensors had similar response and their calibration graphs will be presented at the end of this section.

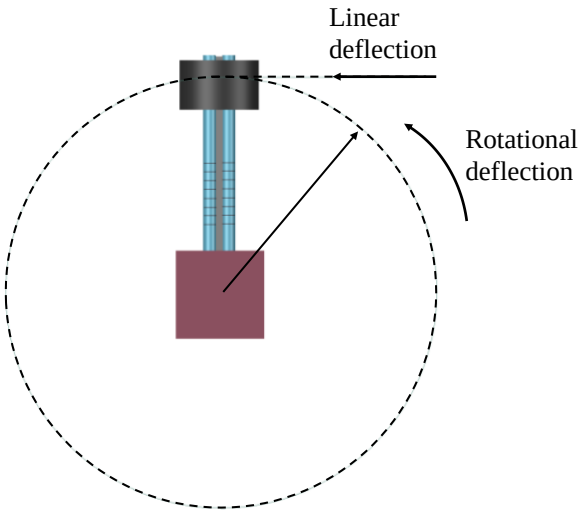

Figure 3-13. Schematic diagram of the rotational deflection of the curvature sensors.

i. Linear Calibration

Linear calibration of the sensors was performed using the equations described in section 2.7.3. The curvature of the cantilever sensor can be determined from beam theory using the material properties [6]:

$$\kappa = \frac{1}{R} = \frac{3\,(l-z)}{l^3}\;\; d \qquad \text{Equation 3.5}$$

where, l is the cantilever length and z is the point along the cantilever where the curvature is determined. For the case where the position z coincides with the actual position of the FBGs, linear calibration of the sensors can be achieved (Figure 3-14). By recording the wavelength peak position of the FBGs upon deflection (d) in two orthogonal directions ($x\ and\ y$) the curvature can be arbitrarily determined according to [7]:

$$\begin{bmatrix} \Delta\lambda_{12} \\ \Delta\lambda_{23} \end{bmatrix} = \begin{bmatrix} c_{12} \\ c_{23} \end{bmatrix} + \begin{bmatrix} p & q \\ r & s \end{bmatrix} \begin{bmatrix} \kappa_x \\ \kappa_y \end{bmatrix} \quad \text{Equation 3.6}$$

where p, q, r, s, c_{12} and c_{23} are the calibration parameters which can be extracted from corresponding experimental measurements, while κ_x and κ_y are the calculated curvatures (Equation 3.6) for the two orthogonal axes.

The distance of the FBGs (z) from the fixed point was 6 mm and their total length was 10 mm. The position of the FBGs along the stem was determined with a localised heat source. The deflection was performed at the weight loading point, therefore the cantilever length (l) was 20 mm. Figure 3-15 shows a schematic 2-D diagram of the side (a) and top view (b) of the sensor. Moreover, the two directions of deflection in regards to the sensor's "stem" cross section are shown in Figure 3-15 (b).

Upon deflection in direction 1, SMFs 2 and 3 are compressed while SMFs 1 and 4 are stretched. Hence, the reflected wavelength peak positions of FBGs 2 and 3 will be decreased, while FBGs 1 and 4 will have the opposite response.

It is noteworthy that upon deflection, a FBG in a cantilever geometry can experience non-uniform strain along its length. This will result on a broadening of the FBG reflectance spectrum and a decrease in the signal. Nonetheless, this does not affect the deflection experiments due to the fact that is systematic for each deflection measurement. Moreover, it has been reported that the FBG sensitivity is affected only in the special cases were the FBG is non-apodized and the strain applied (expressed as a wave) is comparable to the grating length [8].

The response of all four FBGs was monitored for a 2.5 mm total deflection of the sensors with a 0.5 mm increment. The wavelength peak position noise levels are ± 10 pm on each step of deflection. The wavelength peak positions of the FBGs were recorded for 60 seconds at each increment. Figure 3-15 shows their response as well as an average value of the wavelength peak positions at every increment (red marker).

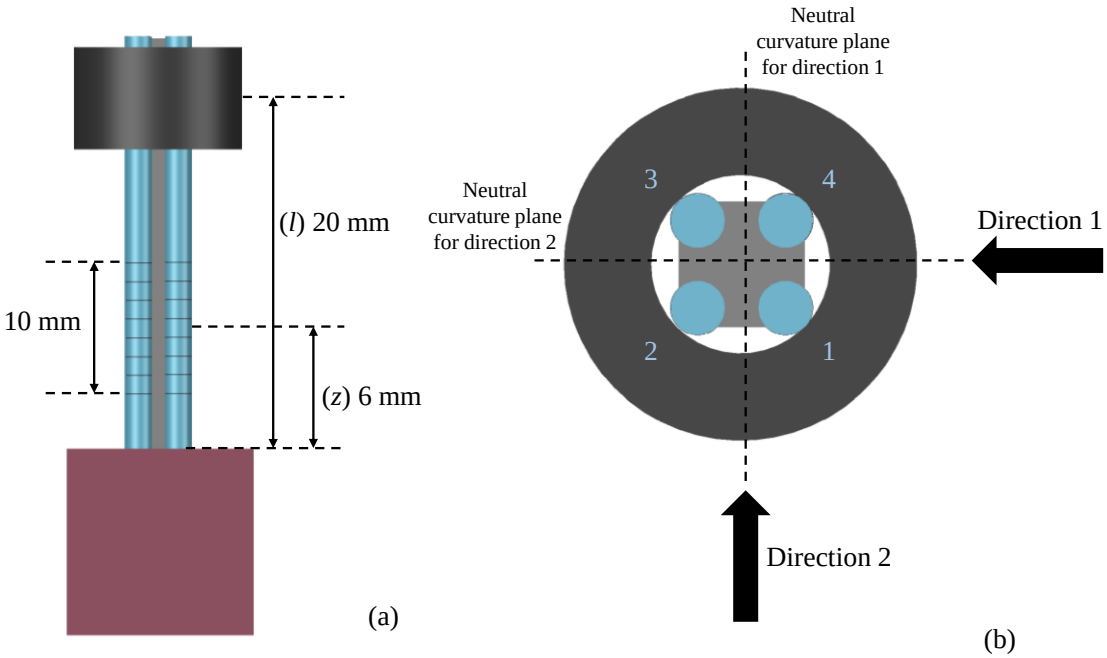

Figure 3-14. A 2-D view of the curvature sensor (a) side view and (b) top view, which show the orientation of the SMFs in regards to the directions of deflection.

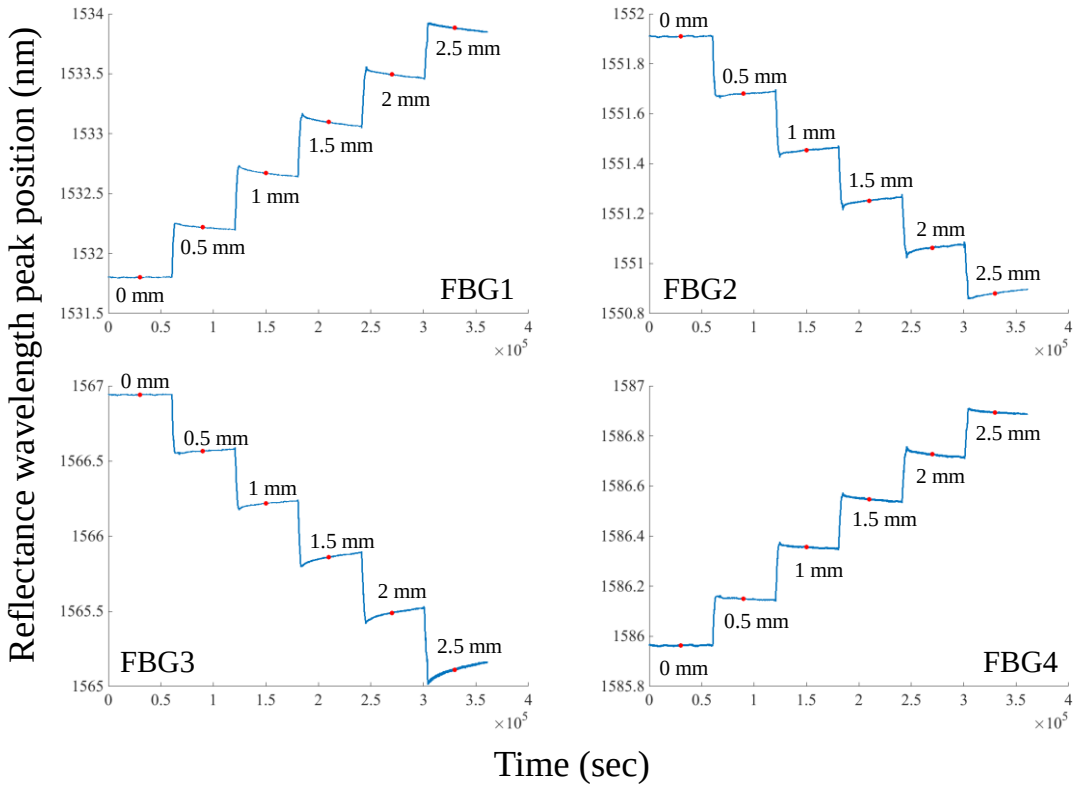

Figure 3-15. Response of all four FBGs upon deflection on Direction 1 for the second curvature sensor (average values – red dots).

The response of the FBGs display a drift mainly at the last three deflection steps (1.5-2.5 mm), with the third FBG of the sensor having the strongest drift. This effect can be

attributed to the deflection procedure, the metal piece which was used for deflecting the sensor drifted to lower deflection lengths during the linear calibration measurements (Figure 3-16). This drift can be calculated out but for this case is not necessary. The same deflection was performed on the same curvature sensor in direction 2. The calibration parameters were extracted using the experimental data according to Equation 3.6.

At least three FBGs are required for the calibration, therefore FBGs 1, 2 and 4 were used (3 omitted due to the highest drift). Figure 3-17 shows the graphs produced using the average values of wavelength peak position shift between FBGs pairs 1-2 and 2-4 *vs* the curvature calculated from Equation 3.5, for the two direction. Finally, Table 3-2 includes all the calculated linear parameters for the second curvature sensor at the two directions of deflection. The same procedure was performed at all FBG curvature sensors (C2 and C3).

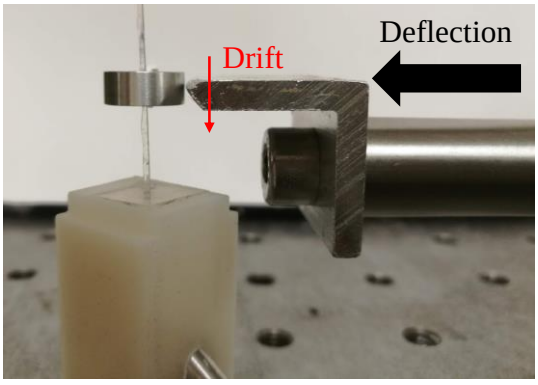

Figure 3-16. Drift produced during the linear calibration procedure.

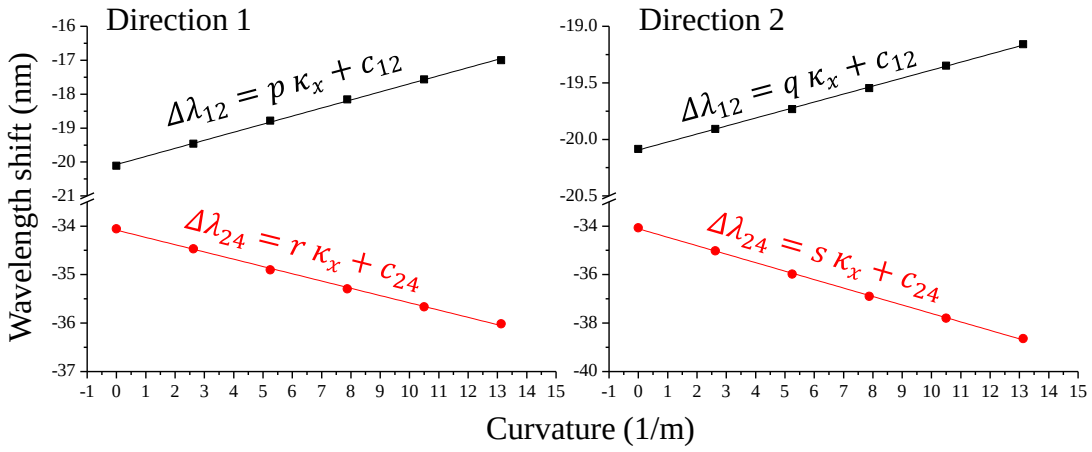

Figure 3-17. Wavelength peak position shift between pairs 1-2 and 2-4 vs the curvature for the first curvature sensor on the two orthogonal directions.

Table 3-2. Linear calibration parameters obtained from the corresponding FBGs pairs from the two directions of deflection.

	c_{12}[pm]	c_{24}[pm]	p[pm·m]	q[pm·m]	r[pm·m]	s[pm·m]
Direction 1	20.07	-34.08	0.238	-	-0.15	-
Direction 2	20.09	-34.11	-	0.0706	-	-0.349

ii. Rotational Calibration

The rotational calibration of the curvature sensors was performed by rotating them through 360° in the directions/axis used for linear calibration. A schematic diagram of the sensor's rotational deflection is shown in Figure 3-13. In this case the deflection of the sensors occurs due to gravity action upon the weight attached to the sensors. The response of the FBGs was recorded for 30 seconds upon rotation with 10° increment. Figure 3-18 shows the response of all four FBGs for the second curvature sensor (C1) upon rotation in direction 1. The FBGs used for curvature sensors C2 and C3 had contiguous response. Moreover, an average value of the wavelength peak positions at each point of rotation was calculated and is marked with red dots on the experimental data.

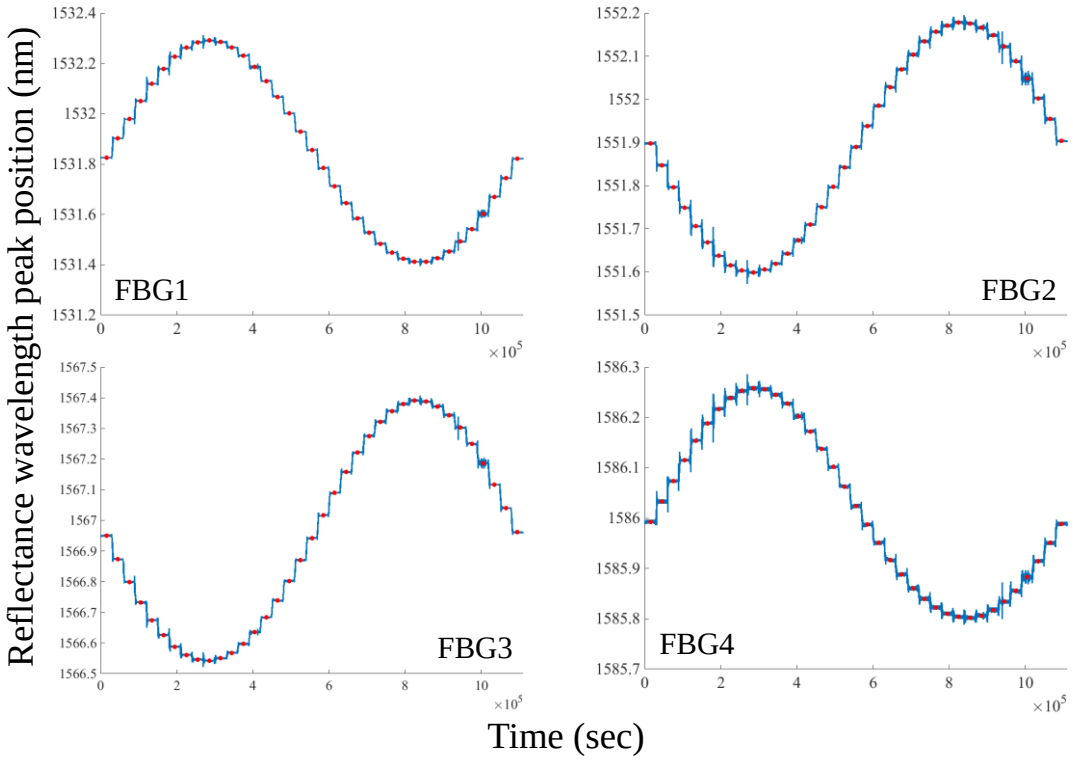

Figure 3-18. Response of all four FBGs upon rotational deflection on Direction 1 for the first curvature sensor (average values – red dots).

By rearranging Equation 3.5 and Equation 3.6, the amount of deflection in the two directions can be calculated by monitoring the FBGs' wavelength peak position response:

$$\kappa_1 = \frac{s}{sp - qr}(\Delta\lambda_{12} - c_{12}) - \frac{q}{sp - qr}(\Delta\lambda_{24} - c_{24}) = \frac{3(l - z)}{l^3} d_1 \qquad \text{Equation 3.7}$$

$$\kappa_2 = \frac{p}{sp - qr}(\Delta\lambda_{24} - c_{24}) - \frac{r}{sp - qr}(\Delta\lambda_{12} - c_{12}) = \frac{3(l - z)}{l^3} d_2 \qquad \text{Equation 3.8}$$

where, d_1 and d_2 are the deflections on directions 1 and 2 respectively. Thus, using FBGs pairs 1-2 and 2-4, the plots of the deflections upon sensor's rotation can be produced. Figure 3-19 shows these graphs for the second curvature sensor for the two directions.

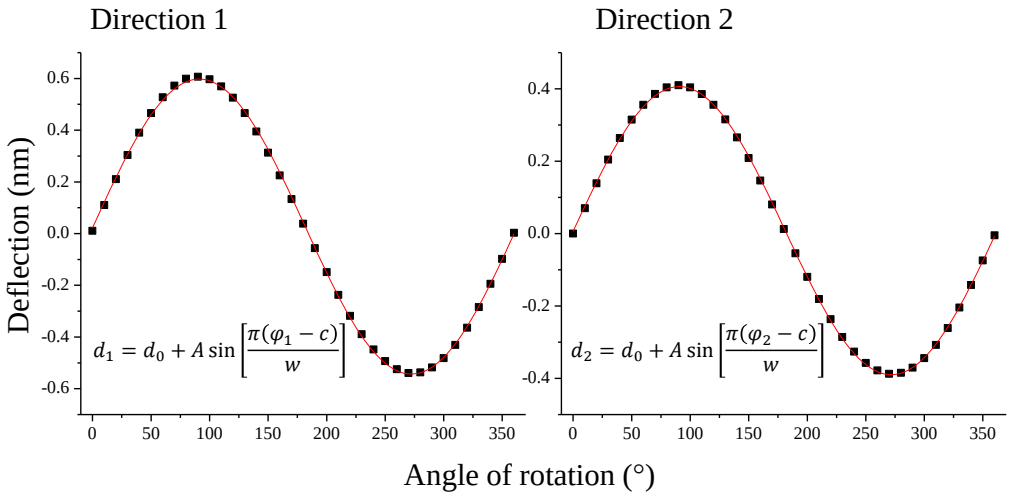

Figure 3-19. Deflection *versus* angle of rotation for the first curvature sensor.

The maximum deflection occurs at the positions where only the vertical component of gravity acts upon the sensor (at 90° and 270°). Hence, the FBGs' wavelength response at these positions have the highest variations in regards to the non-rotated positions (0°, 180° and 360°).

A sinusoidal fitting on the experimental data can provide the angular deflection of the sensor upon the two planes of rotation. Therefore, by monitoring the FBGs wavelength peak position of the curvature sensor, its angular position can be extracted for all cases using the following equation:

$$\varphi_{1/2} = \frac{w}{\pi} sin^{-1} \frac{(d_{1/2} - d_0)}{A} + c \qquad \text{Equation 3.9}$$

Where $\varphi_{1/2}$ are the rotational deflections and $d_{1/2}$ are the linear deflections of the of the curvature sensors on directions 1 and 2 respectively. Moreover, the parameters w and A are the period and the amplitude of the fitted sinusoidal curve respectively, while d_0

and *c* are constants provided from the fittings. Table 3-3 includes the numerical values of these parameters for the second curvature sensor. Rotational calibration of the second and third curvature sensors (C2 and C3) was performed following the same procedure. Their response was similar to the first sensor and their rotational calibration graphs are shown at the next paragraph.

Table 3-3. Rotational calibration parameters for second curvature sensor obtained from the two directions of deflection.

	d_0[°]	w[°]	A[nm]	c[nm]
Direction 1	0.02727	181.18753	0.571	0.478
Direction 2	0.00828	180.96507	0.398	0.241

3.2.3. Calibration graphs for the second and third curvature sensors

The linear and rotational calibration graphs and parameters of curvature sensors C2 and C3 are presented at this section. The response of the FBGs monitored for these sensors were similar to those presented for curvature sensor C1 in both orthogonal directions (Figure 3-15, Figure 3-18).

i. FBG Curvature sensor C2

Figure 3-20 and Figure 3-21 show the linear and rotational calibration graphs respectively on the two directions of deflection for C2.

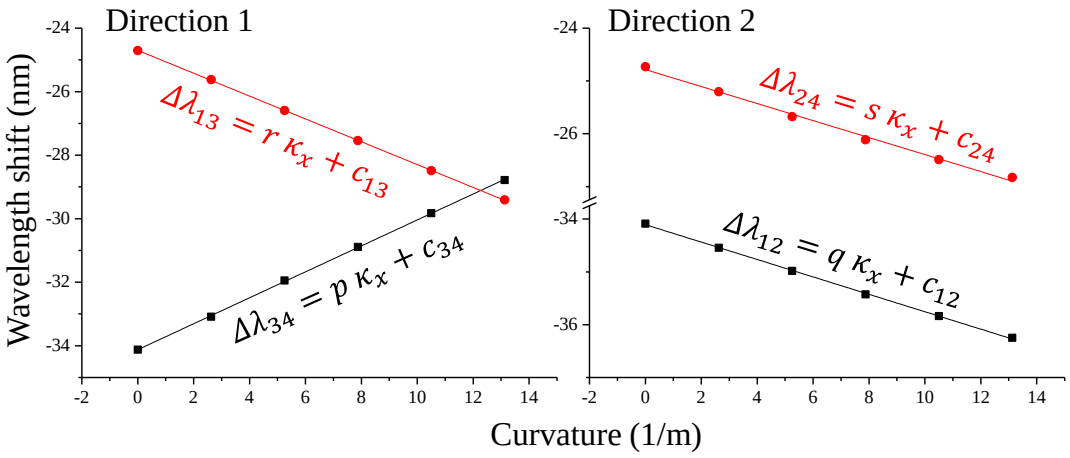

Figure 3-20. Linear calibration graphs for the two orthogonal directions for C2.

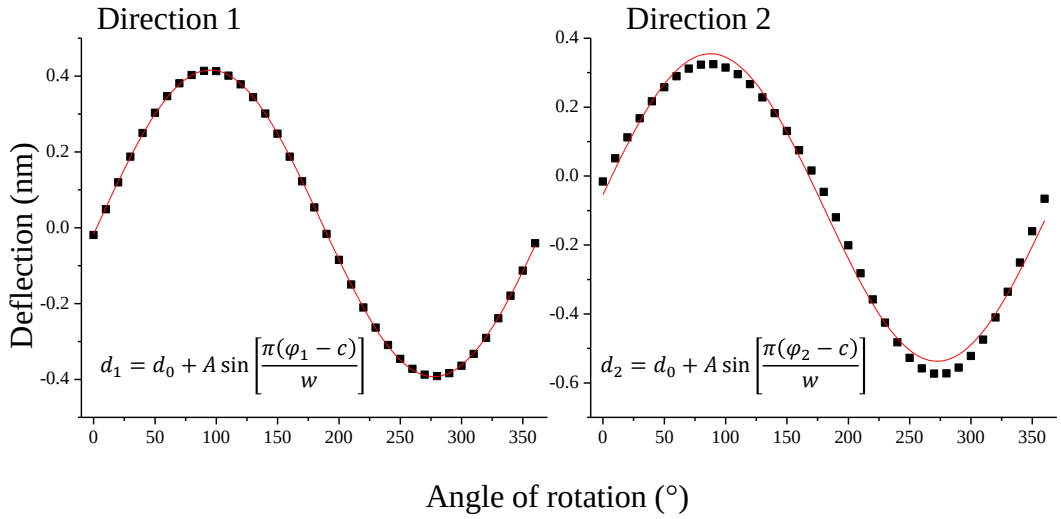

Figure 3-21. Rotational calibration graphs for the two orthogonal directions for C2.

ii. FBG Curvature sensor C3

Similarly to the previous two curvature sensors (C1, C2), the response of the FBGs used on the C3 was monitored under linear and rotational deflection, both are shown in figures 3-22 and 3-23.

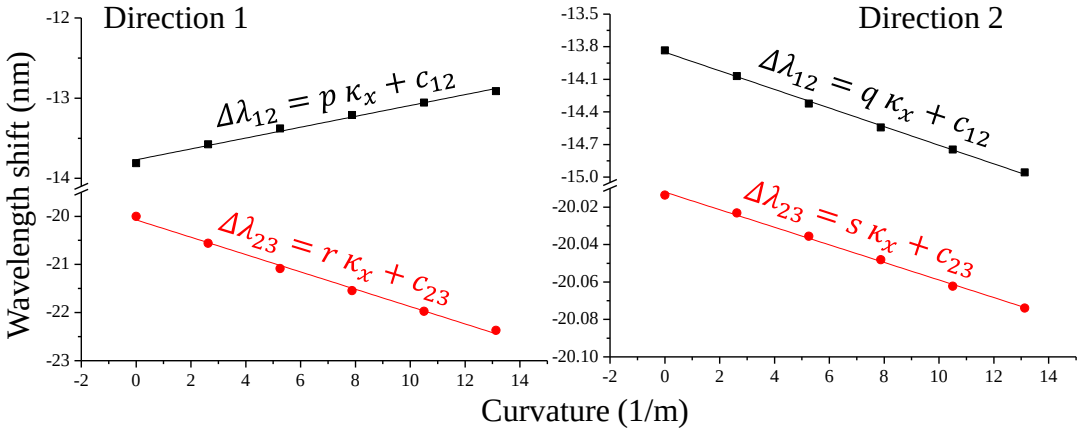

Figure 3-22. Linear calibration graphs for the two orthogonal directions for C3.

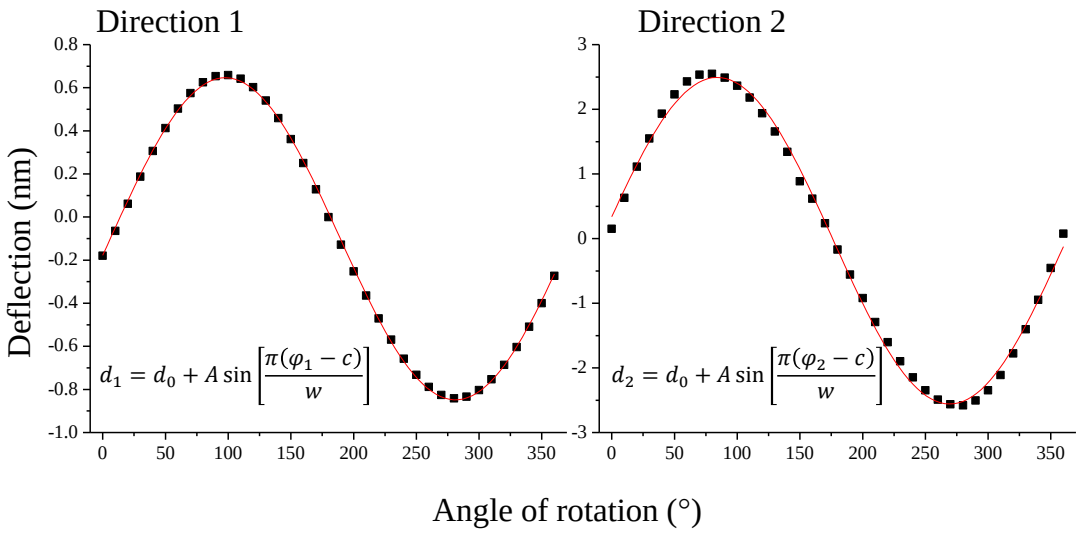

Figure 3-23. Rotational calibration graphs for the two orthogonal directions for C3.

3.2.4. Final configuration of the attitude sensor and performance

Figure 3-24 shows the final arrangement of the FBG attitude sensor ((a) a schematic diagram, (b) actual sensor). The three FBG curvature sensors are positioned at three different points in a metallic platform perpendicular to each other and can provide information about the angular deflection of the platform on two planes. The FBG curvature sensors 1 and 2 (C1 and C2) measure the angular deflections on *yz-plane* and *xz-plane* respectively. Moreover, the third FBG curvature sensor determines whether the platform is in the upright or downwards position.

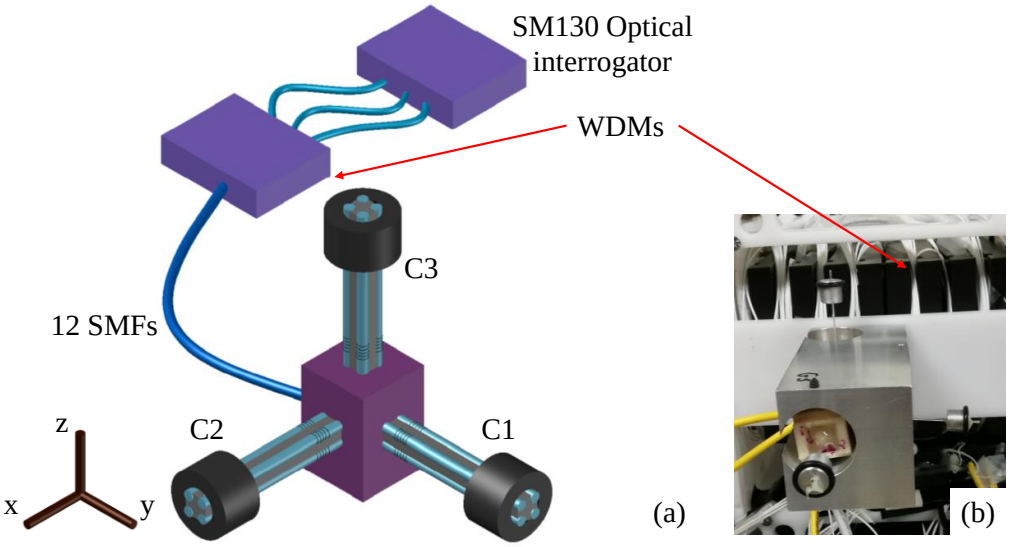

Figure 3-24. Final configuration of the FBG attitude sensor (a) a schematic diagram, (b) actual sensor.

The performance of the attitude sensor was tested by rotating the sensors over 360° in two different directions. The response of the FBGs wavelengths can be converted to angular degrees using the calibration parameters for each curvature sensor and Equation 3.9. Figure 3-25 shows the data collected from the first curvature sensor (C1). Similar response was monitored for the other two curvature sensors (C2, C3).

The initial angular offset (-1.1°, Figure 3-25 (a)) can be attributed to a misalignment of the curvature senor during its repositioning on the rotating platform. The sensor provides reliable measurements within a range of 180° (± 90°) rotation. Therefore, when the sensor exceeds ± 80° measurements on the angular deflection on the same plane can be taken from the subsequent orthogonal sensor. The noise levels of the curvature sensors vary with the highest being close to ± 90° rotation, Figure 3-25 (b) shows that at the 70° the noise is ± 0.75°. While the noise level at 0° is ± 0.2° (Figure 3-25 (d)). Hence, it is considered that the attitude sensor can provide measurements with an accuracy of ± 2°.

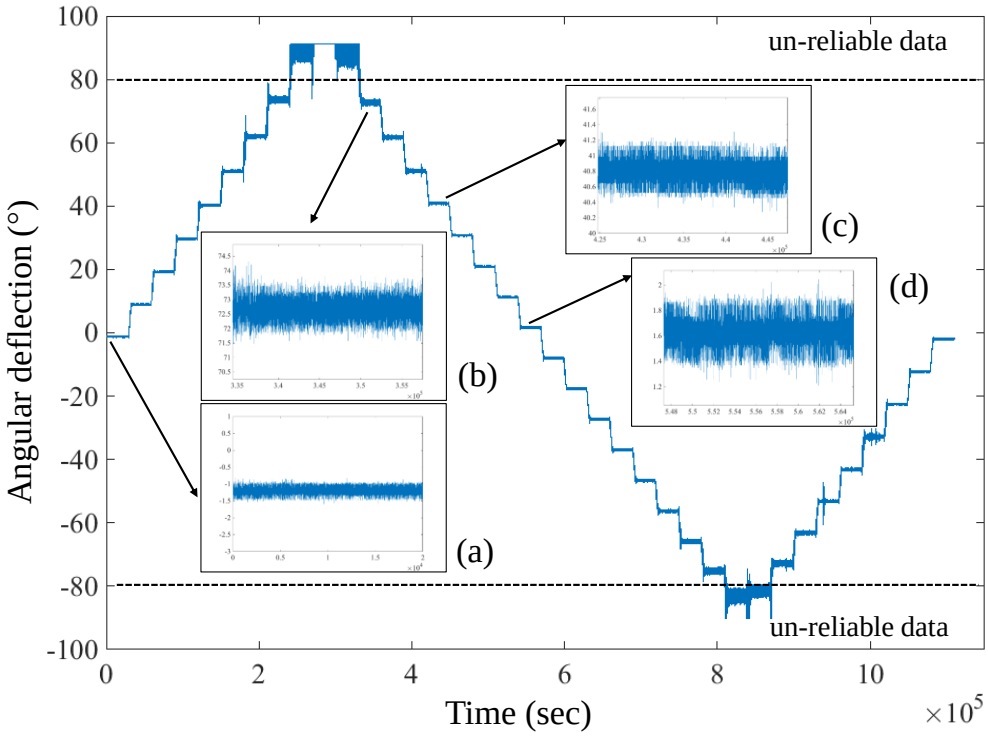

Figure 3-25. Angular deflection of the second curvature sensor extracted from the BFGs response using Equation 3.9 with zoomed in regions which show (a) the initial angular offset -1.1° and resolution at (b) 70° noise levels ± 0.75°, (c) 40° noise levels ± 0.4° and (d) 0° of angular deflection noise levels ± 0.2°.

3.3. Conclusions

This chapter covers the fabrication of two different types of FBG sensors using conventional fibre. The first is a temperature sensor while the second is an attitude sensor. The calibration and performance of both sensors is reported.

Temperature sensors

The FBG temperature sensors, reported here, were fabricated following a well-established technique [1]. Strain isolation of the fibres was performed by enclosing them into stainless steel capillary tubes, and fixing them at one end. The temperature sensitivity of the sensors is considered to have absolute accuracy of ± 2° C and resolution of ± 0.3° C, which is in the requirements for LAkHsMI project.

FBG Curvature sensors

FBG curvature sensors were produced in-house. The equipment allowed for the alignment of four different SMFs containing FBGs in a square structure. Moreover, automated translations of optical adhesive and curing LEDs ensured the rigidity of the sensors. Experiments showed that the curvature sensors were sensitive to environmental temperature variations ~200 pm drift on the differential response of the FBGs. This drift can be compensated using the measurements from the temperature sensors.

Attitude sensor

The FBG attitude sensor consisted of three different FBG curvature sensors, which are positioned at perpendicular planes. The FBG technology for the Attitude sensor was chosen in order to be compatible with the other sensors (i.e. temperature and flow sensors for the sensors unit). Linear and rotational calibration was performed on all three curvature sensors, where MatLab scripts were produced for both cases [Appendix 2]. The calibration procedure require at least three FBGs (two different FBGs pairs). The forth ("redundant") FBG serves two different purposes: (a) It can be used as a spare in case any fibre breakages and (b) it provides the square cross section structure which makes the calibration equations less complicated.

By fixing the sensors at three perpendicular points, the final configuration of the attitude sensor was achieved. This sensor can provide angular deflection measurements on two different planes with a ± 2° accuracy in a total range of 360°.

3.4. References

[1] D. Barrera, V. Finazzi, J. Villatoro, S. Sales, and V. Pruneri, "Packaged Optical Sensors Based on Regenerated Fiber Bragg Gratings for High Temperature Applications," *IEEE Sensors Journal*, vol. 12, no. 1, pp. 107-112, 2012.

[2] *RS Pro Datasheet* (Access date: 05.10.2018) Available: www.uk.rs-online.com/web/p/thermocouples/3630250/

[3] G. M. H. Flockhart, R. R. J. Maier, J. S. Barton, W. N. MacPherson, J. D. C. Jones, K. E. Chisholm, L. Zhang, I. Bennion, I. Read, and Peter D. Foote, "Quadratic behavior of fiber Bragg grating temperature coefficients," *Applied Optics*, vol. 43, no. 13, pp. 2744-2751, 2004.

[4] J. Mandal, S. Pal, S. Tong, K. T. V. Grattan, A. T. Augousti, and S. A. Wade, "Bragg grating-based fiber-optic laser probe for temperature sensing," *IEEE Photonics Technology Letters*, vol. 16, no. 1, pp. 218-220, 2004.

[5] Thorlabs. (Access date: 05.10.2018). *LED370E*. Available: www.thorlabs.com/thorproduct.cfm?partnumber=LED370E

[6] P. P. Benham, "Mechanics of engineering materials", *2nd ed. ed. Harlow: Longman*, 1996.

[7] G. M. H. Flockhart, W. N. MacPherson, J. S. Barton, and J. D. C. Jones, "Two-axis bend measurement with Bragg gratings in multicore optical fiber," *Optics Letters*, vol. 28, no. 6, p. 3, 2003.

[8] R. N. John, I. Read, and W. N. MacPherson, "Design considerations for a fibre Bragg grating interrogation system utilizing an arrayed waveguide grating for dynamic strain measurement," *Measurement Science and Technology*, vol. 24, no. 7, 2013.

Chapter 4. MCF curvature sensor with a silica waveguide fan-out device

This is an experimental chapter which reports the fabrication of a novel optical fibre curvature sensor. This sensor shares the same working principle with the curvature sensors reported in the previous Chapter (specifically the Attitude sensor). However, in this case one Multicore (MCF) is used for fabrication. The cores of the MCF act as strain gauges and when FBGs are inscribed into them, their response can be associated with the curvature of the fibre. The experimental configuration used for the inscription of the FBGs is described and the calibration of the MCF for 2D measurement of the fibre tip is reported. Moreover, the temperature sensitivity of the MCF curvature sensor and interface components is explored. Finally, the differential strain sensitivity of the inscribed FBGs is determined.

4.1. Inscription of Fibre Bragg Gratings in MCF

4.1.1. Experimental set up

Inscription of FBGs was achieved using the phase mask technique 2.5.2 iii. Figure 4-1 shows a schematic diagram of the experimental set up which was commissioned for the FBG inscription. A Copper Vapour (Cu-vapour laser) laser source, emitting at 511 nm and 578 nm was used for the inscription. The Cu-vapour laser, Oxford Lasers (LS 20-50), is a high power (30 W), pulsed (5 ns to 60 ns) laser with 6 mJ maximum pulse energy. A system of a convex and concave lenses (basically a telescope) was used in order to reduce the beam diameter of the laser to ~4 mm. The 511 nm laser emission was frequency doubled using a BBO (Barium - Borate) crystal to provide UV radiation (255.5 nm), suitable for the inscription process. A pellin broca optical prism after the crystal separates the UV beam from the unwanted remaining 511 nm laser emission. A mirror then directs the UV radiation to the cylindrical lens and the phase mask. Finally, the +1 and-1 UV diffraction orders interfere and the fibre is placed in that region. The periodic the UV illumination inscribes the FBG.

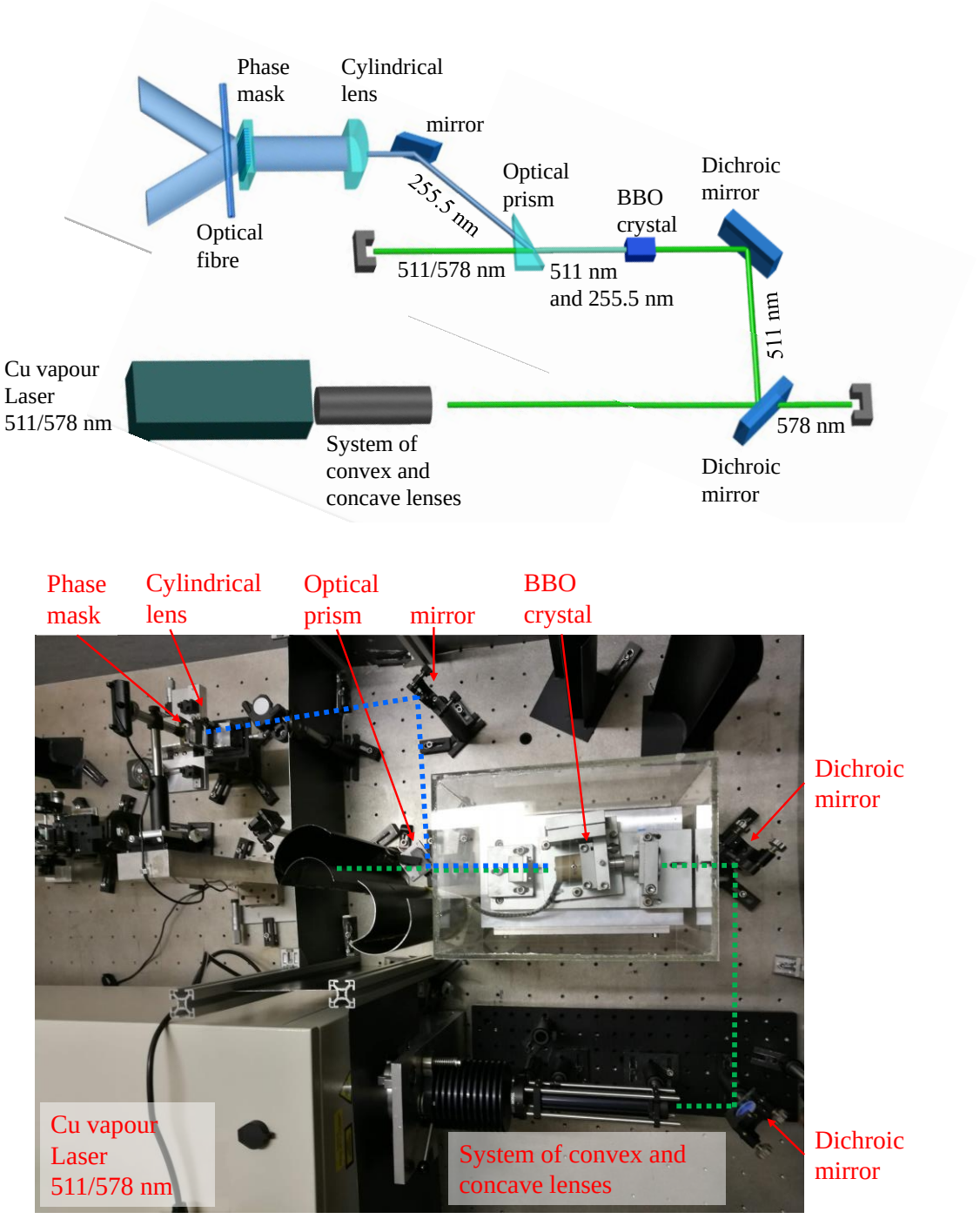

Figure 4-1. Experimental set up for inscription of Fibre Bragg Gratings using a frequency doubled Cu-Vapour laser to produce UV illumination incident on a phase mask (top) schematic diagram (bottom) actual image (the experimental set up originally was built by Dr. Jinesh Mathew and recommissioned by me).

FBGs inscription was achieved using a phase mask (supplied by Coherent) with period $\Lambda_{PM} = 1060.88\,nm$. The expected inscribed Bragg wavelength into a standard SMF, with effective refractive index $n_{eff} \cong 1.445$ [1] can be calculated using Equations 2.5 and 2.2 :

$$\Lambda_{FBG} = \frac{\Lambda_{PM}}{2} = 530.44\ nm \qquad \text{Equation 4.1}$$

$$\lambda_{reflected} = 2n_{eff}\Lambda_{FBG} = 1535.09\ nm \qquad \text{Equation 4.2}$$

4.1.2. Inscribed Fibre Bragg gratings into a single mode fibre

The FBG inscription set up was initially aligned using a SMF. Inscription of FBGs into two different SMF 28 fibres (provided by Corning, doped with Germaium) was performed. The first SMF was loaded into a pressurized hydrogen atmosphere prior to the UV exposure (hydrogenated fibre). This was achieved at room temperature with 20 MPa pressure for a duration of two weeks. The FBGs' reflectance spectra was monitored with a commercial optical interrogator SM 125 (Micron optics) during the fibre inscription process. Reflectance spectra (shown in Figure 4-2 (a)) were recorded every 5 seconds with the reflected peak reaching its highest intensity value after 150 seconds of exposure.

The second SMF was non-hydrogenated and was exposed to the same intensity of UV interference pattern for the same time duration. Figure 4-2 (b) shows the reflectance spectrum of the inscribed FBG and as it is expected, the intensity power of the inscribed FBG is lower in comparison to the hydrogenated fibre. The FBGs inscribed in both the hydrogenated and non-hydrogenated fibres have FWHM of $\sim 0.2\ nm$.

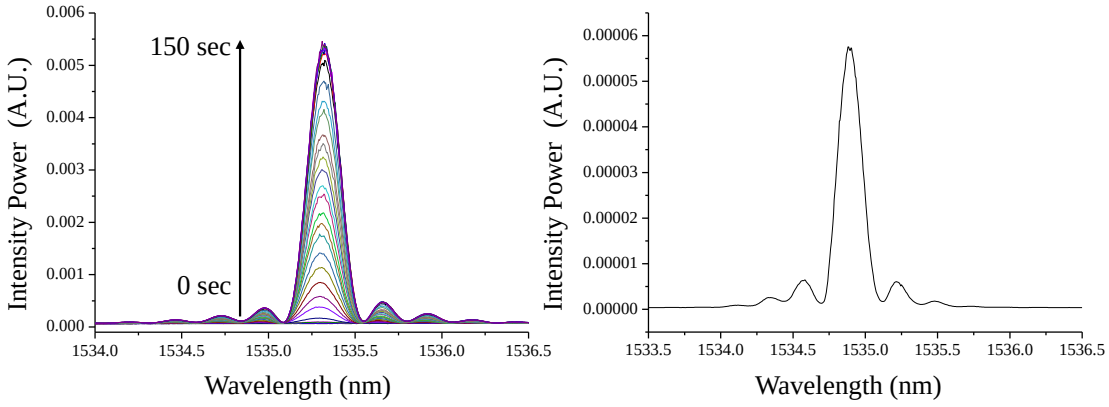

Figure 4-2. (a) FBGs reflectance spectra inscribed in a hydrogenated SMF 28 recorder every 5 seconds during the UV exposure, (b) FBG reflectance spectrum inscribed in a non-hydrogenated SMF 28 (FWHM: 0.21 nm).

The reflectivity of the inscribed Bragg gratings mainly depends upon the photosensitivity of the fibre and the exposure duration. However, the power of the UV beam and the alignment of the optical fibre with respect to the focal position of the

cylindrical lens can affect the final threshold value. Moreover, vibrations on the experimental set up limit the grating's reflectivity or even reduce it during the inscription. This is because the periodic perturbation of the refractive index can be washed out in the presence of vibrations, due to the movement of the interference pattern on the optical fibre. The reflectivity of the FBGs can be determined experimentally through the transmittance or the reflectance spectra.

According to the cut-back technique the recorded reflectance spectra of the inscribed FBG can be correlated with the Fresnel reflection produced from the cleaved end of the fibre to provide a calibrated measure of reflectivity [2]. For a standard SMF, $n_{core} \sim 1.452$, this reflection can be calculated:

$$R = \left|\frac{n_{core} - n_{air}}{n_{core} + n_{air}}\right|^2 \cong 3.8\% \qquad \text{Equation 4.3}$$

Figure 4-3 shows the reflectance spectrum of an inscribed FBG in a non–hydrogenated SMF 28, expressed in both intensity power and reflectivity (~ 4.25%). The background of the inscribed grating is dropped to 0% reflectivity because a refractive index matching gel was applied at the tip of the fibre.

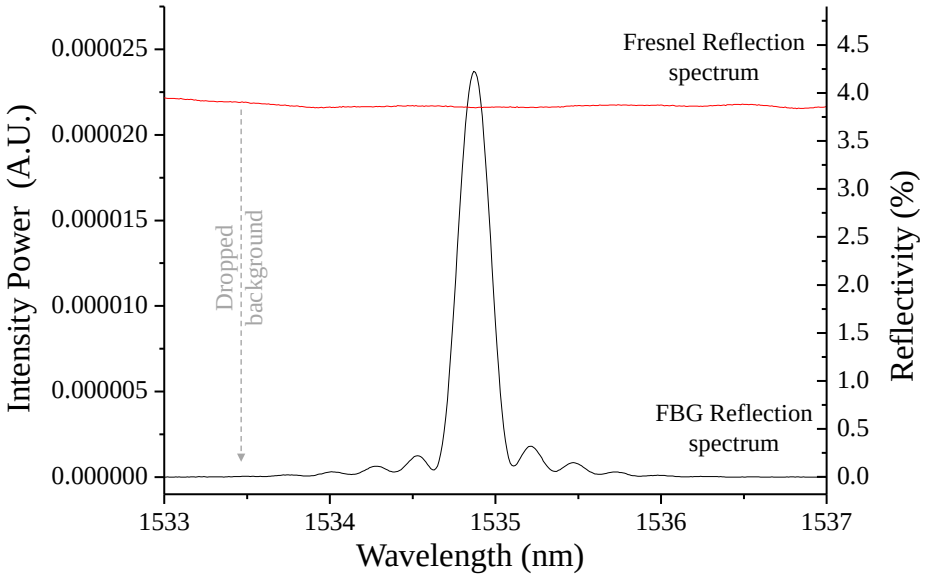

Figure 4-3. FBG inscribed in a non–hydrogenated SMF 28 expressed in terms of intensity power and reflectivity (the background is dropped to zero because index matching gel was applied at the end of the fibre, FWHM: 0.22 nm).

4.2. Fabrication of the MCF curvature sensor

The MCF used for the fabrication of the curvature sensor has four cores positioned in a 50 μm square array. The fibre is designed to operate single-mode at communication wavelengths (~1530-1565). At 50 μm the separation between two adjacent cores is sufficient to eliminate cross talk. The core and cladding radii are 8 μm and 125 μm respectively, while the minimum spacing between core and outer cladding wall is 37 um. Figure 4-4 shows a cross section of the MCF, where the cores are illuminated with white light.

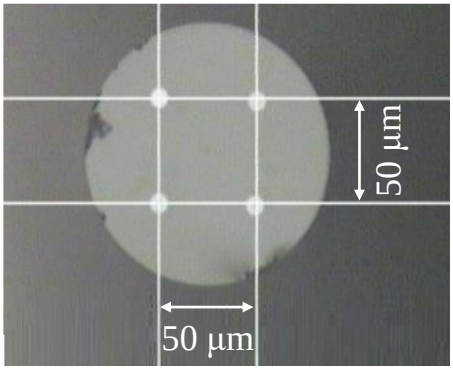

Figure 4-4. Cross section of the Multicore fibre. Cores are illuminated with white light for illustration.

The fabrication procedure of the MCF curvature sensor, presented in this chapter, consists of three separate steps. Initially, a MCF section is spliced onto a fan-out device, thus the optical signal from each core of the MCF is coupled to a conventional SMF. This is required because the reflectance spectra of the FBGs inscribed into the cores of the fibre have to be monitored individually. Secondly, inscription of FBGs into the cores of the MCF fibre section is performed. Finally, the cantilever geometry is produced by fixing the MCF at one specific point (a pivot) relative to the FBGs positions.

4.2.1. Splicing of MCF section to the fan-out device

The fan-out device was designed to couple light from each core of the MCF to a SMF. It was fabricated by ultrafast laser inscription of waveguides into silica glass [3] and was provided by Optoscribe (Livingston, UK). The waveguides arrangement on the left side of the fan-out is identical to the cross section of the MCF. While, on the other side the waveguides are separated and coupled with common SMFs. Figure 4-5 shows a schematic diagram of the device with the fibres attached at each side.

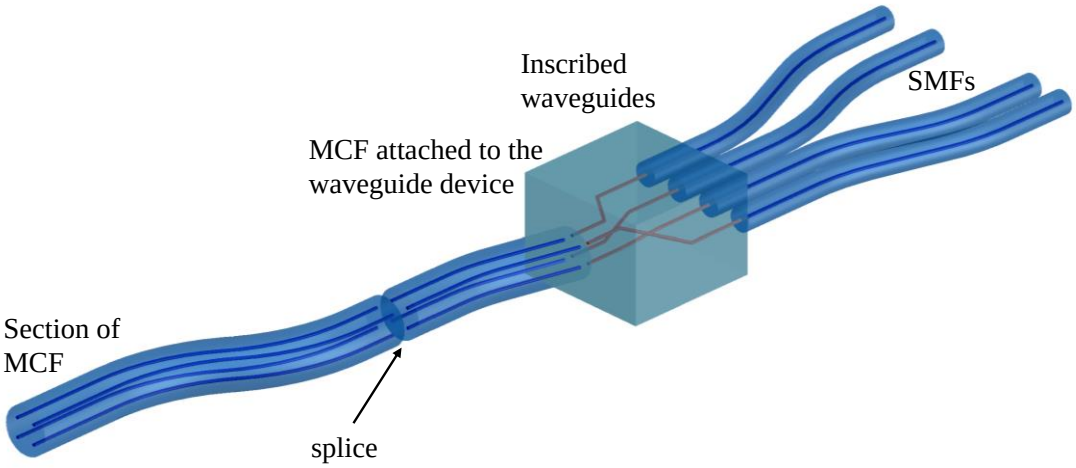

Figure 4-5. Schematic diagram of the 4 core MCF fan-out device with the splice section of the MCF (figure modified from[3]).

The splicing of an additional MCF section onto the fan-out device was achieved with a FSM-100P+ splicer manufactured by Fujikura. This splicer provides end views of the inserted fibres and allows lateral alignment of the fibres in two orthogonal planes (commonly called x and y) as well as rotation (roll) (θ, angle) along the central axis of the fibres. To aid the orientation of the fibres into the splicer light was coupled into one SMF and the MCFs' output was monitored under a microscope in order to optimise coupling into one core only before the splice. After the splice it was expected that by illuminating one SMF of the fan-out device one core of the MCF free end was expected to be illuminated.

Ten splices were produced in order to estimate an average value loss for each core. By monitoring the light power before and after each splicing the losses were measured to be between 1.4 – 2.1 dB for each core. It is known that the optical losses due to lateral offset of the fibre in the splicer can be calculated using the following equation [4]:

$$l_{dB} = 2.17\left(\frac{y}{\omega}\right)^2 \qquad \text{Equation 4.4}$$

where, y is the misalignment of the cores on the two sections of MCF, in this case it can be expressed as $y = rsin\theta \approx r\theta$, for small angles; and ω is the mode field radius and can be calculated using the core radius and the V-number. Measurements on ten different angular offsets showed that the accuracy on the MCFs rotation has to be ±2 μm to ±2.1 μm in order the optical losses to be 1.4 to 2.1 dB respectively. Figure 4-6 shows the

experimental measurements on the splice losses (red fitting line) as well as a theoretical estimation of the losses. This is converted to an angular offset of ±3.2° to ±3.9°.

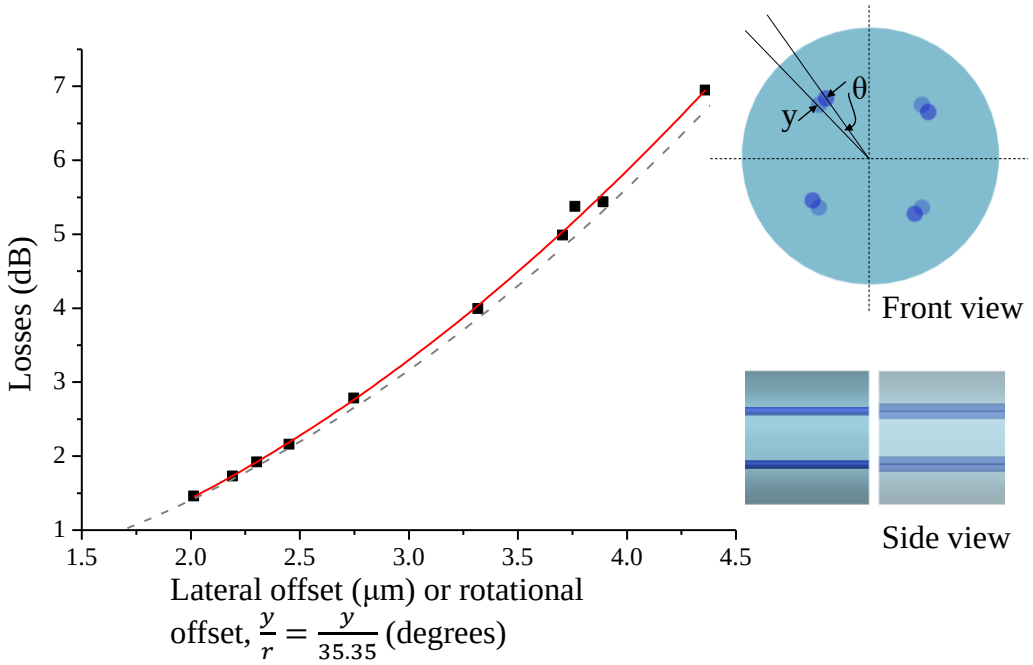

Figure 4-6. Optical losses as a function of the rotational offset between two MCFs during splices (red line) fitted line from the experimental data, (grey dotted line) theoretical model.

4.2.2. Inscription of FBGs into the cores of the MCF

The inscription of the FBGs into MCF section was achieved with the experimental set up described in section 4.1.1. The MCF was placed in the focal position of the cylindrical lens within the UV interference pattern. The MCF was exposed for 120 seconds and all four cores were inscribed with FBGs simultaneously. Figure 4-7 shows the inscribed FBGs reflection spectra in each individual core of the MCF.

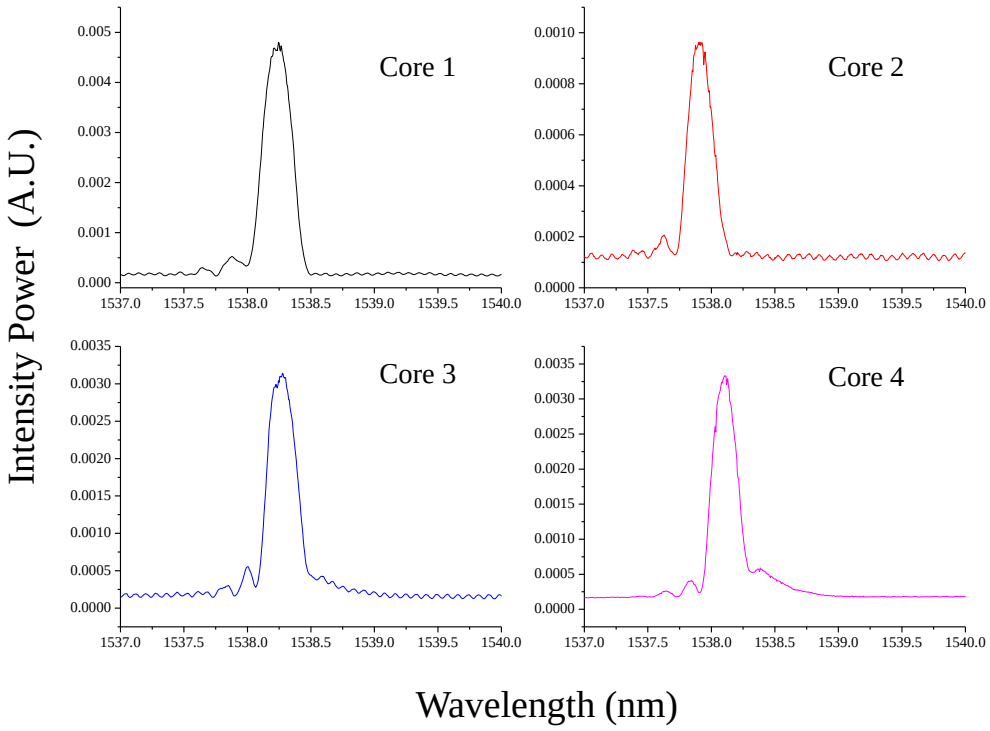

Figure 4-7. FBGs spectra in each individual core of the MCF (FWHM: (core 1) 0.27 nm, (core 2) 0.245 nm, (core 3) 0.265 nm, (core 4) 0.235 nm).

Table 4-1 includes the peak wavelength positions of the FBGs inscribed into the core of the MCF. Since all FBGs were inscribed with a single UV exposure and with the same phase mask it is expected that all have the same peak position. However, small variations in the peak position and reflectivity of the FBGs were observed. The structure of the fibre is the primary reason for these variations [5]. Where one core lies on the focal position of the lens the other three lie outside of it. Therefore, the core in the focal position will have a higher reflectivity FBG as the interference is more intense at this point. Additionally, it has been reported that when a fibre is positioned in an angle with regards to the phase mask, FBGs with different reflectance wavelength can be fabricated [6]. The fibre cladding acts as an additional cylindrical lens, which makes the incident UV beam even narrower or partially distorted. As a result, the cores are exposed with an uneven UV intensity or partially different interference pattern, which therefore results in variations of the peak FBG reflection [7]. Finally there is a possibility that one core is positioned in front of another, therefore a shadowing effect can be produced [8]. However, the variation of the peak positions between the FBGs inscribed into the four cores of the MCF are 0.5 nm about 1500 nm, which is less than 0.05% of the overall wavelength, and well within the detection capabilities of the interrogator.

There are variations of the FBG peak wavelength in comparison with that expected according to the phase mask pitch. The peak position of the inscribed FBG into the standard SMF fibre was around 1535.09 nm, while the average peak positions of the FBGs inscribed into the MCF is 1538.13 nm. This difference can be attributed to slightly different effective refractive index of the MCF (see Equation 4.1 Equation 4.2). A 0.002 variation of the effective refractive index result to a 5 nm shift of the expected FBG reflectance wavelength peak position.

Table 4-1. Wavelength peak position of the inscribed FBGs into each individual core of the MCF.

core	**Wavelength peak position**	
	According to phase mask pitch (nm)	Inscribed FBGs into the MCF (nm)
1	1535.09	1538.24
2		1537.91
3		1538.26
4		1538.1

4.2.3. Cantilever geometry

A cantilever geometry was achieved by fixing the MCF section with the FBGs at one end to a plastic disc using adhesive. High-precision deflection was performed with a metal actuator mounted on a translation stage. An image of the MCF curvature sensor while it is deflected is shown in Figure 4-8 ((a) actual image taken at the lab, (b) schematic diagram). The centre of the FBGs were positioned 15 mm above the fixed point (x) and the deflection was performed 58 mm above from the fixed point (cantilever length). The exact position of the FBGs (± 1 mm) along the MCF cross section was determined with a localised (within a mm) heat source (solder) traveling along the fibre and by observing the response of the FBGs' reflectance spectra.

The cantilever length for this curvature sensor is longer, in comparison to the curvature sensors presented in the third chapter (Attitude sensor). The main reason is that this sensor is not going to be used as an attitude sensor, hence the length is not a restriction on the fabrication.

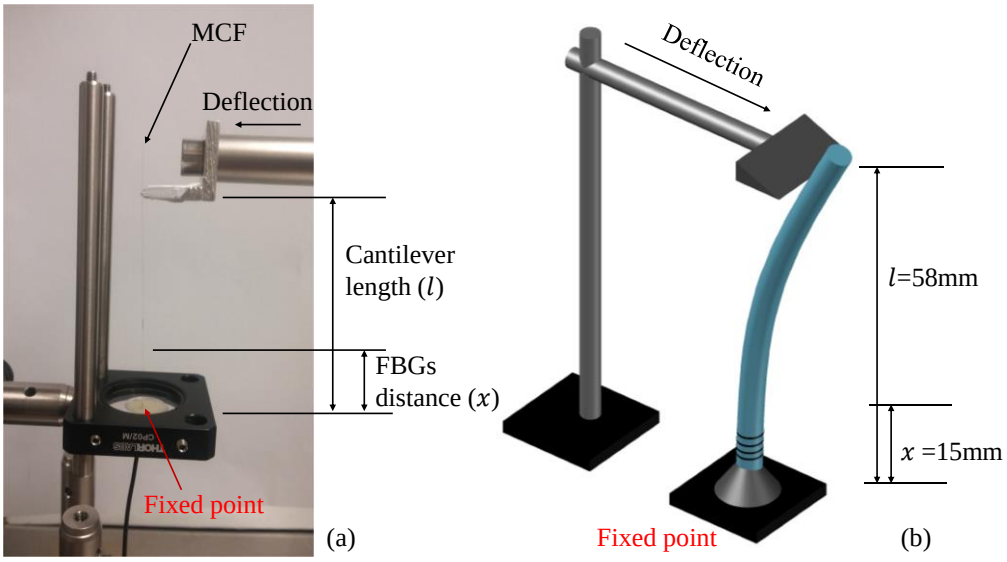

Figure 4-8. Cantilever geometry of the MCF fibre curvature sensor (a) Actual image taken in the lab and (b) schematic diagram of the MCF curvature sensor.

4.3. Response of the FBGs inscribed into the cores of the MCF

4.3.1. MCF curvature sensor

The MCF acts as a curvature sensor by measuring differential strain induced by the bend. Deflection of the MCF was performed in two orthogonal directions. Each direction has a characteristic neutral plane, with two cores that are outside of the plane (with respect to the centre of curvature) being stretched and two cores that are inside of this plane (with respect to the centre of curvature) are being compressed 2.7.2. Figure 4-9 shows an end face view of the MCF with the two directions of deflection. In the first direction of deflection cores 1 and 2 lie in the outer curvature region, hence they are stretched, while cores 3 and 4 are compressed. Similarly, for the second direction of deflection.

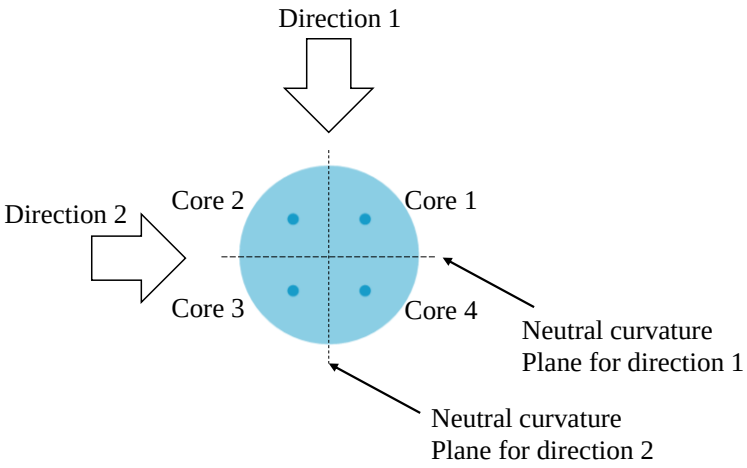

Figure 4-9. The two performed directions of deflection on the MCF.

The overall deflection at the end of the MCF was 5 mm, starting from 0 mm (non-deflected) with 1 mm increments. The response of the inscribed FBGs into each individual core of the MCF was monitored with a commercial interrogator through the SMFs of the fan-out device. The MCF fibre remained at each location for 60 seconds. The response of the FBGs is constant at each deflection step, and no drift was observed (as in the case of the curvature sensors produced for the Attitude sensor) (Figure 4-10).

Figure 4-10 shows the FBGs response upon deflection of the MCF in direction 1. Since cores 1 and 2 are being stretched, the FBGs' peak position inscribed on them is expected to move to a higher wavelength. Conversely, the compressed cores 3 and 4 are expected to demonstrate a shift of their FBGs' reflectance spectra to lower wavelengths (Section 2.6.2). This is in agreement with the data presented in Figure 4-10, for the FBGs inscribed into the four cores of the MCF. Moreover, the noise levels of the FBGs wavelength peak positions at each step of deflection are shown on the graphs with grey font colour numbers. The noise levels were calculated as $(\lambda_{max} - \lambda_{min}/2)$ using Appendix 4.

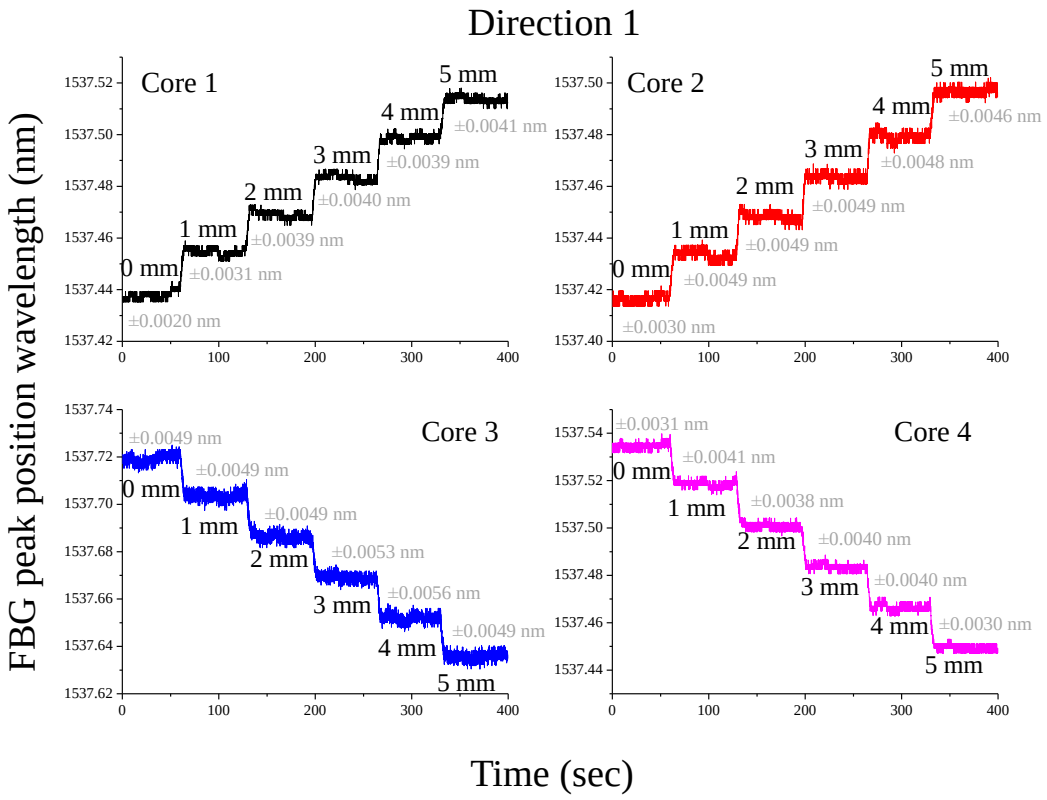

Figure 4-10. Response upon deflection of the FBGs inscribed into each individual core of the MCF in direction 1, cores 1 and 2 are stretched while cores 3 and 4 are being compressed (grey coloured font numbers are the noise levels at each step of deflection).

Similarly, the FBGs' response upon deflection in direction 2 is as expected. Cores 1 and 4 are compressed, hence the peak wavelength of the inscribed FBGs is reduced. Conversely, cores 2 and 3 are stretched, thus the FBGs reflectance peak position increases. The FBGs response of all four inscribed are shown in Figure 4-11.

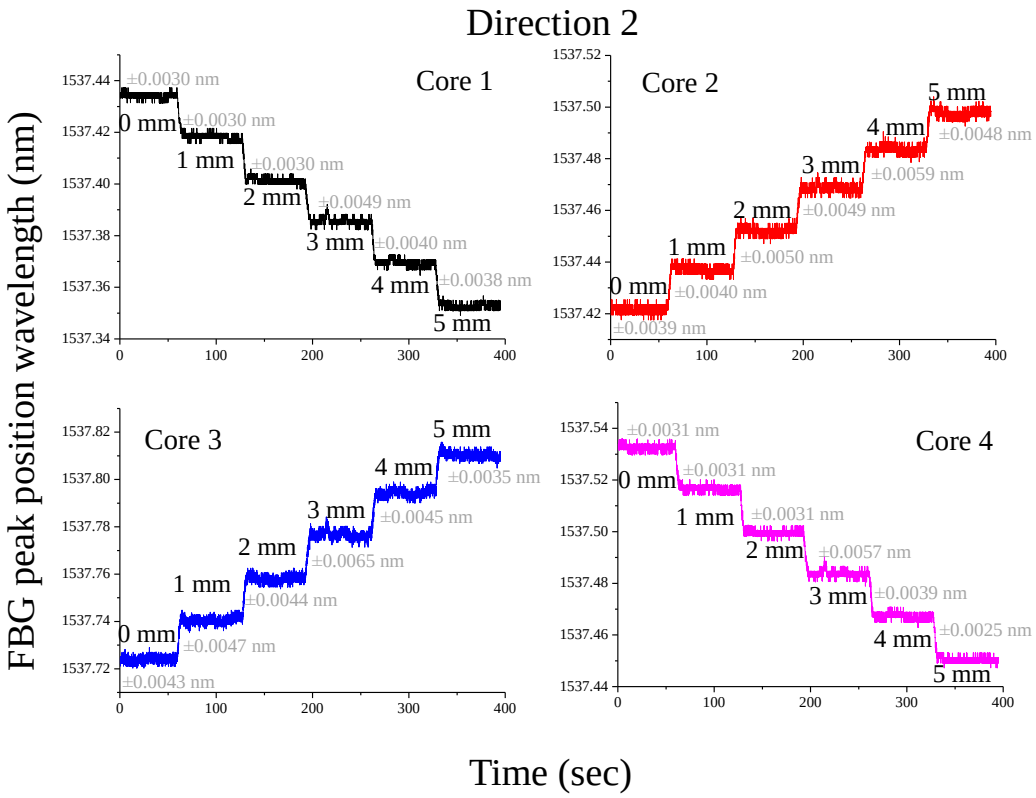

Figure 4-11. Response upon deflection of the FBGs inscribed into each individual core of the MCF in direction 2, cores 2 and 4 are stretched while cores 1 and 4 are being compressed (grey coloured font numbers are the noise levels at each step of deflection).

4.3.2. Calibration of the MCF curvature sensor

The calibration of the MCF curvature sensor necessitates deflection of the fibre in two orthogonal directions (Section 2.7.3). Due to the square array geometry of the fibre, the response of at least three inscribed FBGs (two different core pairs) is required for the calibration of the sensor. Hence, for the MCF sensor described in the previous section, the FBGs inscribed into cores 1, 3 and 4 were used for calibration. The FBG inscribed into core 2 is ignored since it has the lowest reflectance amplitude (Figure 4-7)). The calibration equations for the two pairs are given by [9]:

$$\begin{bmatrix} \Delta\lambda_{14} \\ \Delta\lambda_{43} \end{bmatrix} = \begin{bmatrix} c_{14} \\ c_{43} \end{bmatrix} + \begin{bmatrix} p & q \\ r & s \end{bmatrix} \begin{bmatrix} \kappa_1 \\ \kappa_2 \end{bmatrix} \qquad \text{Equation 4.5}$$

where $\Delta\lambda_{13}$ and $\Delta\lambda_{34}$ are the wavelength shifts of the FBGs reflectance peak positions inscribed into core pairs 1-3 and 4-3. The noise levels of the wavelength shift of the two pairs of FBGs are 0.054 nm and 0.041 nm respectively. An average of the FBGs wavelength peak position for each deflection step was determined through data analysis with MatLab™ (Appendix 5). Moreover, κ_1 and κ_2 is the curvature of the MCF in the two directions of deflections, calculated through Equation 2.26:

$$\kappa = \frac{1}{R} = \frac{3\,(l - x)}{l^3}\ \nu_l \qquad \text{Equation 4.6}$$

where, l is the cantilever length (58 mm), x is the distance of the FBGs from the fixed point (15 mm) and ν_l is the deflection of the fibre (0-5 mm, with 1 mm increment). The position of the FBGs was determined with a localised heat source. Thus the calibration parameters p, q, r, s, c_{13} and c_{34} can be determined from the data presented in Figure 4-12. Where p and r, are the gradients of the FBGs pairs 1-4 and 4-3 versus the curvature, from deflection in direction 1. Likewise, q and s are the gradients of the pairs when the fibre is deflected in direction 2. Finally, c_{13} and c_{34} are the intercepts of the respective response pairs.

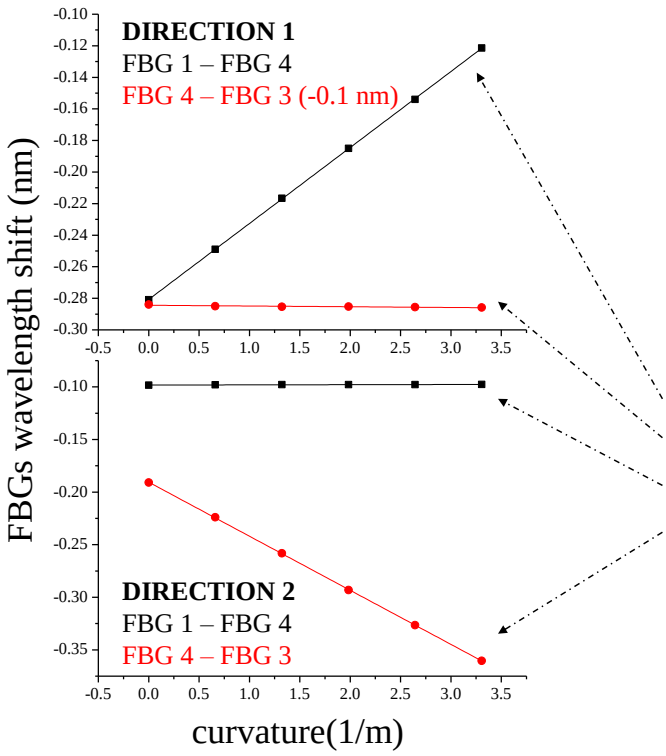

Calibration parameters	
p [nm·m]	0.04814
r [nm·m]	$-4.688\cdot10^{-4}$
q [nm·m]	$1.718\cdot10^{-4}$
s [nm·m]	-0.05142
c_{13} [nm]	-0.379
c_{43} [nm]	0.187

Figure 4-12. Wavelength shift response of the FBGs pairs 1-4 and 4-3 inscribed into the cores of the MCF due to curvature of the fibre and the calibration parameters.

Here the response of the FBGs (wavelength shift) is lower in regards to the curvature sensors produced for the Attitude sensor reported in chapter 3. This is due to different aspects: (a) the distance of the FBGs from the fixed point (15 mm *versus* 6 mm), (b) the cantilever length (58 mm *versus* 10 mm) and (c) the materials stiffness.

4.3.3. Performance of the MCF curvature sensor

The performance of the MCF curvature sensor was studied after calibration. Using the calibration parameters (measured in the previous section, 4.3.2) the position of the fibre tip can be determined. The MCF curvature sensor was forced to move in a circular motion by moving the fibre end using a rotating disc as shown in Figure 4-13. The response of the FBGs inscribed into the cores of MCF was monitored through the fan-out device with the interrogator. The fibre's end position was represented in real time with the use of a LabVIEW script, which included the calibration equations (Equation 4.5). Twenty data points were recorded for each FBG in 1 msec, while the discs speed was 1/4 revolution per minute.

The observed motion of the MCF tip, through the FBGs' response was as expected for several minutes. However, after ~30 minutes the motion drifted to an apparent ellipsoidal motion. It was speculated that this could be a temperature effect since all other experimental parameters (such as mechanical drifts) remained stable. Therefore, further investigation on the performance of the MCF curvature sensor was implemented. A study on the temperature sensitivity of the MCF curvature sensor will be presented in the following paragraphs.

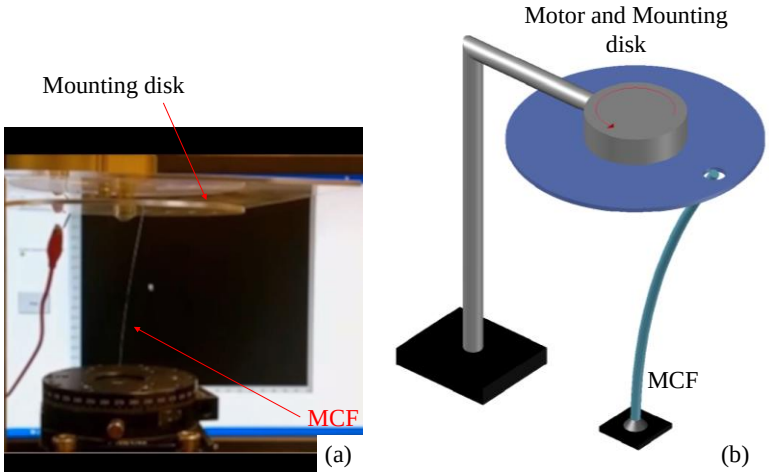

Figure 4-13. Mounting of the MCF curvature sensor for circular motion (a) image taken during the experiment and (b) schematic diagram.

4.4. Temperature sensitivity of the MCF curvature sensor

The strain gauges (cores in the MCF) of the curvature sensor described in the previous paragraphs are positioned close to each other and are surrounded by the same material (the cladding of the MCF). Therefore, it is expected that the FBGs inscribed into the cores of the MCF are equally affected by the local temperature variations. Hence by monitoring the differential strain applied on two FBGs (core pairs), a temperature compensated response is expected [10].

However, the overall system consists from an additional element, which might be affected by temperature variations. The fan–out device is necessary in order to couple light from one core of the MCF to a SMF. This device might be producing an undesirable background, which can affect the resolved reflectance peak position of the inscribed FBGs. In this section, the temperature sensitivity of the MCF curvature sensor will be and interfacing components explored.

4.4.1. Measurements on the circular motion of the MCF curvature sensor

The performance of the MCF curvature sensor was monitored simultaneously with temperature variations of the fan-out device's local environment. The calibration procedure of the sensor (described on section 4.3.2), was performed with the fan-out maintained at a stable temperature of 25.5 °C ± 0.2 °C. The temperature was stabilised using a PID (proportional integral derivative) controller. The circular motion of the MCF was performed with the set up described on section 4.3.3, while the device was at the same temperature. The end position of the MCF can be calculated with equations Equation 4.5 and Equation 4.6, by monitoring the wavelength shifts of FBGs inscribed into cores 1, 3 and 4. Figure 4-14 shows the end position of the MCF on the x-y plane (top view). The radius of the disc generated by the circular motion was 6 mm, which agrees with the calculated value using the FBGs response. The trace of the fibre's tip position in this case is as expected (a constant 6 mm radius circular motion).

Next the response of the FBGs to circular motion over two different temperatures of the fan-out (24.5 °C and 26.5 °C). As before the position of the fibre was calculated with equationsEquation 4.5 andEquation 4.6 with the calibration parameters obtained with the fan-out maintained at 25.5 °C. Figure 4-15 shows the trace motion of the MCF tip position

for a full circle at the different temperatures. The motion of the fibre in these cases diverge from circular, suggesting some temperature sensitivity.

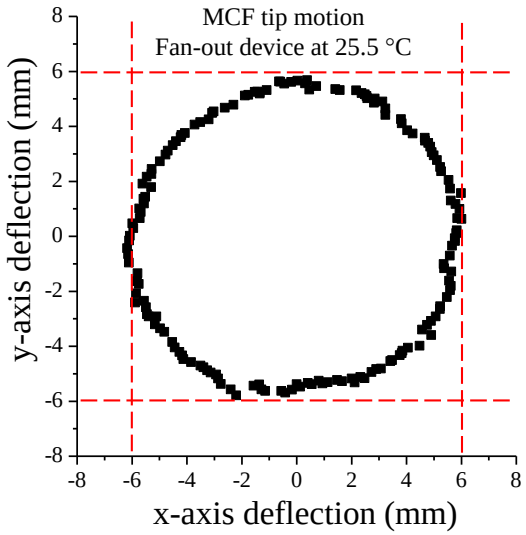

Figure 4-14. Measured circular motion the MCF, through equations Equation 4.5 and Equation 4.6 with the FBGs response inscribed into cores 1, 3 and 4 and using the calibration parameters obtained when the fan-out device maintained at 25.5 °C.

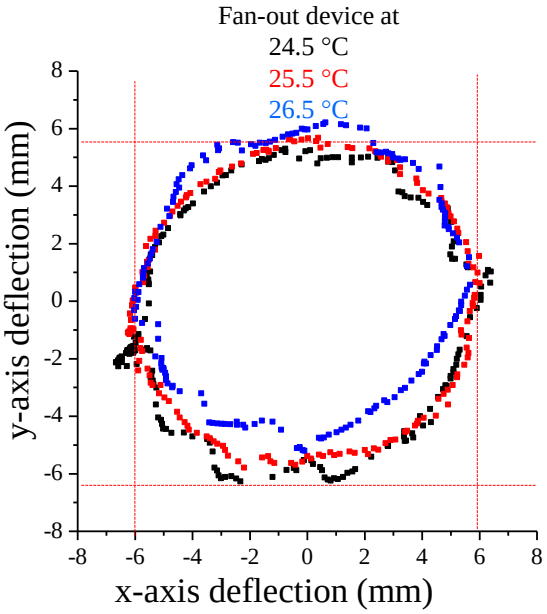

Figure 4-15. Measured motion the MCF tip position, through the response of FBGs inscribed into cores 1, 3 and 4, using the calibration parameters obtained when the fan-out device maintained at 25.5 °C, for different temperatures of the fan-out device.

Finally, the temperature of the fan-out device was 25.5 °C and the trace of the MCF's motion was compared with the initial (Figure 4-14). Figure 4-16 shows the two traces.

Here the circular motion is restored and the calculated data from the FBGs response are comparable with the initial response.

These experiments provide an initial indication that the fan-out device affects the performance of the MCF curvature sensor. However an extended study in each individual element of the system is required to understand the source of this cross-sensitivity. On the following sections the temperature sensitivity of the FBGs and the fan-out device will be explored.

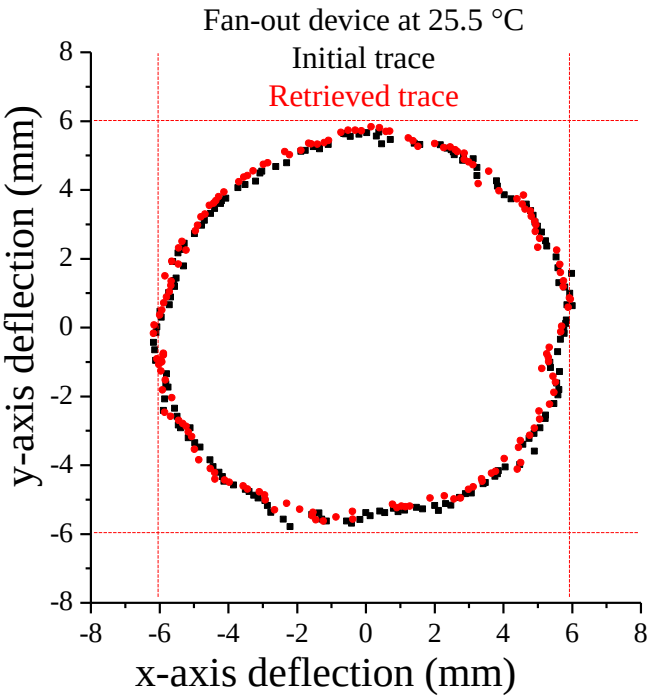

Figure 4-16. MCF tip position trace when the fan-out device is maintained at 25. 5 °C, calculated with the calibration parameters obtained 25.5 °C, the circular motion is restored and the initial trace (black) is comparable to the retrieved (red).

4.4.2. Temperature sensitivity measurements on the individual elements

The temperature sensitivity of the MCF curvature sensor was studied with the experimental set up presented in Figure 4-17. The fan-out device was enclosed in a temperature controlled box using a PID (proportional integral derivative) temperature controller. The tested temperature range (27-29 °C) was restricted by the consideration that the silica waveguide fan-out device has a damage threshold of 30 °C.

The MCF with inscribed FBGs was sandwiched between two metal plates placed on hot plate, this ensured a uniform temperature distribution across the MCF. Moreover, a

groove machined in the metal plate ensured that the FBGs were held strain isolated and their response was affected only by temperature.

The temperatures of the FBGs and the fan-out device was monitored every 10 s, using K-type thermocouples. One thermocouple was positioned close to the FBGs in the metal plates, while the second was positioned close to the fan-out device in the enclosure box. The peak position of the FBGs reflectance spectra was collected for three different cases: (*i*) the fan-out and the FBGs maintained at a stable temperature, (*ii*) the fan-out held at stable temperature while the FBGs experienced temperature variations and (*iii*) FBGs at a stable temperature, while the fan-out device's temperature varied. Graphs which include the FBGs' response with the temperature variations for all three cases will be presented. For each case, the individual FBGs' response inscribed into cores 1, 3 and 4 of the MCF as well as their differential response (core1 – core 3, core 1 – core 4 and core 3 – core 4) will be examined. Ideally the differential response of the FBG for all cases should not be temperature sensitive.

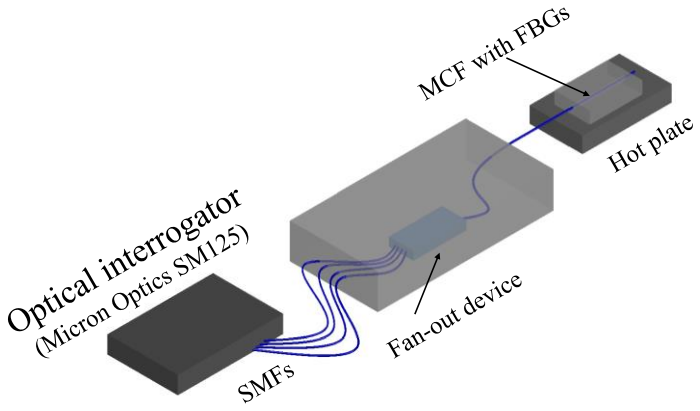

Figure 4-17. Experimental set up for maintaining and varying the fan-out device and FBGs at different temperatures.

i. Fan-out device and FBGs held at a stable temperature

In the first case the fan-out device was held at 27.1 °C ±0.2 °C, while the FBGs at 28 °C ±0.5 °C. Measurements were taken for several hours (~ 5 hours). Figure 4-18 shows the individual FBGs' response for this case. The differential response is shown in Figure 4-19. As it is expected the peak position as well as the wavelength shift of the FBGs, response remain stable over this time. Both figures include the noise levels of the FBGs peak positions and wavelength shifts of the pairs.

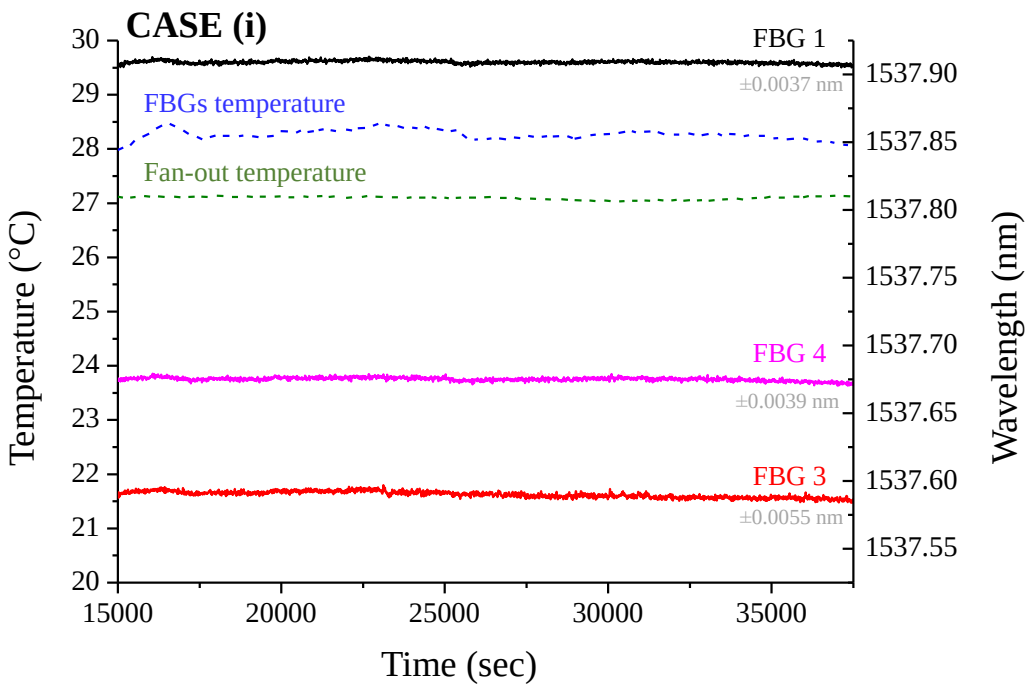

Figure 4-18. Inscribed FBGs' response when the fan-out device was held at 27.1 °C ±0.2 °C and the FBGs at 28 °C ±0.5 °C (grey coloured font numbers are the noise levels).

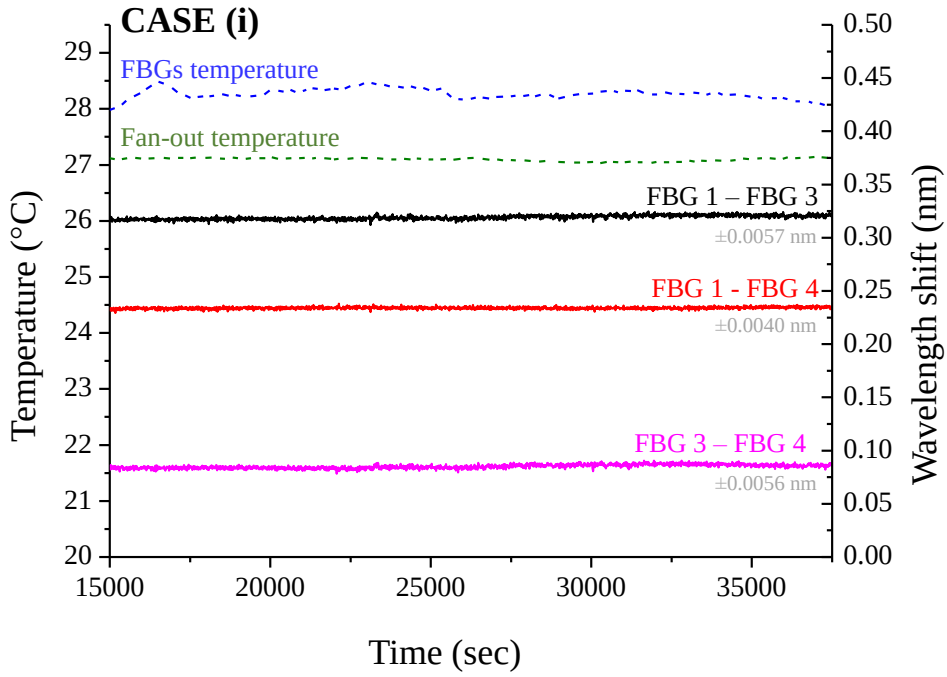

Figure 4-19. Inscribed FBGs' differential response when the fan-out device was held at 27 °C ±0.2 °C and the FBGs at 28 °C ±0.5 °C (grey coloured font numbers are the noise levels).

ii. Fan-out device maintained at stable temperature and the temperature of the FBGs varied

In this case the fan-out device maintained at 27.2 °C ±0.2 °C and the temperature of the FBGs inscribed into the MCF varied from 25 °C to 29 °C with 1 °C increment. The overshoot of the temperature is due to the internal PID of the hot plate, the temperature is considered to be stable after 15000 seconds of each step. The FBGs' peak position was monitored for ~ 1hours by the time that their temperature was stabilized.

Figure 4-20 and Figure 4-21 show that the response of the three individual FBGs follow the temperature variations, as expected. This experiment is presented in two different graphs, due to the time that was required for the fan-out device to be stabilised at 27.2 °C. It is considered that the device is at a stable temperature after the first 3000 seconds, thus conclusions are drawn according to the FBGs response after the first 5000 seconds on the first graph. Figure 4-22 and Figure 4-23 shows the differential response of the FBGs for the same temperature variations. In this case the variations on the FBGs response due to temperature changes are eliminated, as expected. All graphs include the noise levels at each, stable, temperature period.

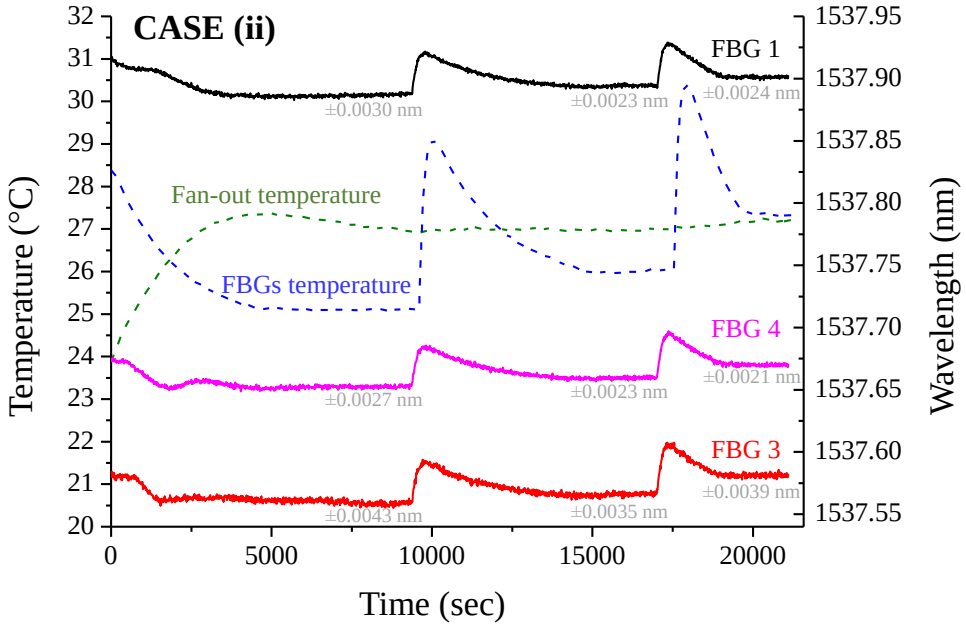

Figure 4-20. Inscribed FBGs' response when the fan-out device was held at 27.2 °C ±0.2 °C and the FBGs temperature varied from 25 °C to 27.5 °C with 1 °C increment, this experiment is presented into two different graphs due to the time that was required for the fan-out device to be stabilised at 27.2 °C (grey coloured font numbers are the noise levels), the first 3000 seconds are not considered for this case since both the FBGs and the fan-out device are in a non-stable temperature.

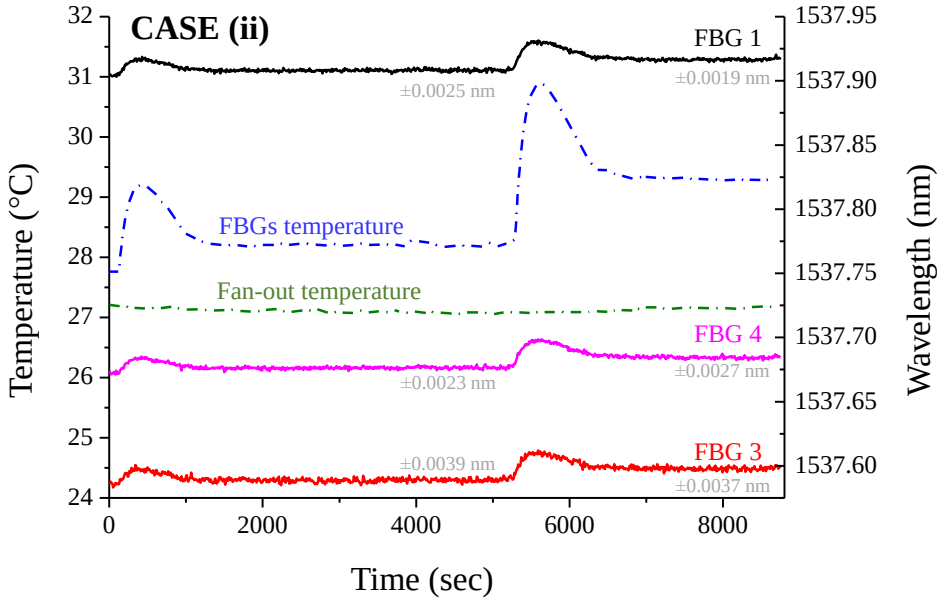

Figure 4-21. Inscribed FBGs' response when the fan-out device was held at 27.2 °C ±0.2 °C and the FBGs temperature varied from 27.5 °C to 29 °C with 1 °C increment, this experiment is presented into two different graphs due to the time that was required for the fan-out device to be stabilised at 27.2 °C (grey coloured font numbers are the noise levels).

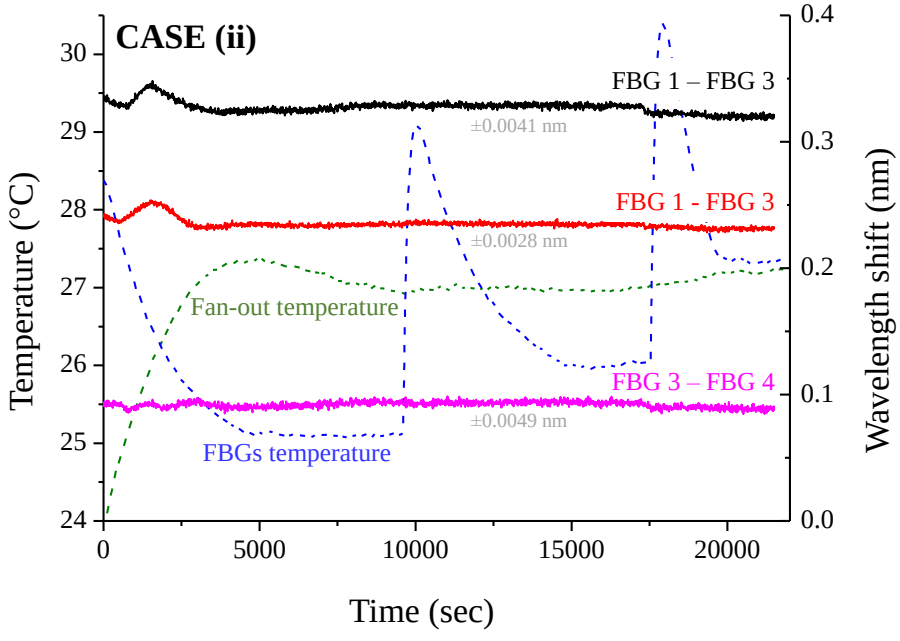

Figure 4-22. Inscribed FBGs' differential response when the fan-out device was held at 27 °C ±0.2 °C and the FBGs temperature varied from 25 °C to 27.5 °C with 1 °C increment. This experiment is presented into two different graphs due to the time that was required for the fan-out device to be stabilised at 27.2 °C (grey coloured font numbers are the noise levels), the first 3000 seconds are not considered for this case since both the FBGs and the fan-out device are in a non-stable temperature.

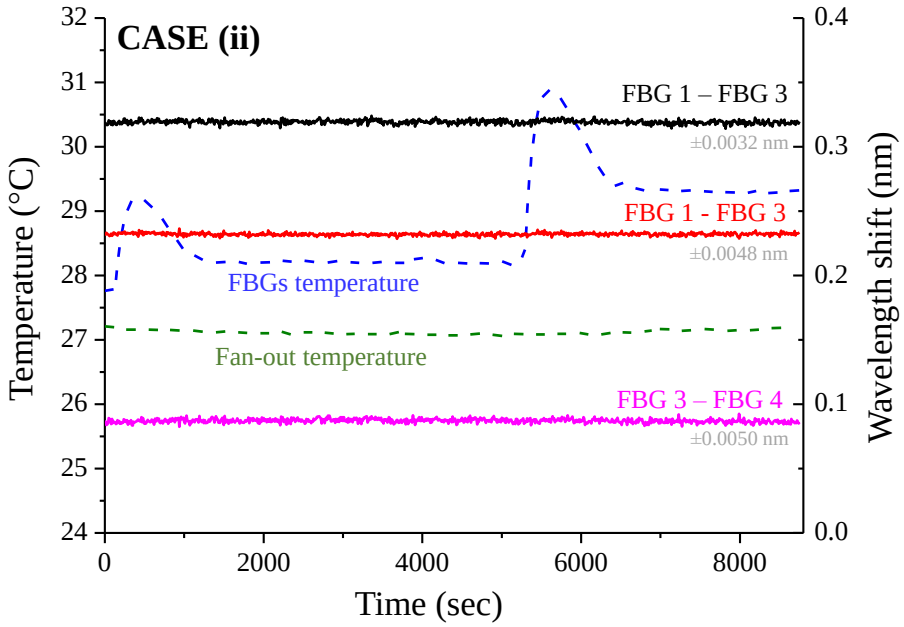

Figure 4-23. Inscribed FBGs' differential response when the fan-out device was held at 27 °C ±0.2 °C and the FBGs temperature varied from 27.5 °C to 29 °C with 1 °C increment. This experiment is presented into two different graphs due to the time that was required for the fan-out device to be stabilised at 27.2 °C (grey coloured font numbers are the noise levels).

iii. The temperature of the fan-out device varied, while the FBGs remained at stable temperature

Finally, the temperature sensitivity of the fan-out device was studied by maintaining the FBGs at a stable temperature (29.4 °C ± 0.2 °C). In this case their differential response should remain stable. The device's temperature varied from 27.2 °C to 28.9 °C with 0.5 °C increment and the FBGs response were recorded for 5000 seconds by the time that the fan-out device was stabilised at a specific temperature. Figure 4-24 shows the response of the inscribed FBGs individually, while Figure 4-25 shows the differential response. In this case, the FBGs' reflectance peaks and more importantly the differential *peak position varies with the fan-out device's temperature changes*. The differential response of FBG pairs 1–3 and 1–4 demonstrate similar response with the device's response (Figure 4-25).

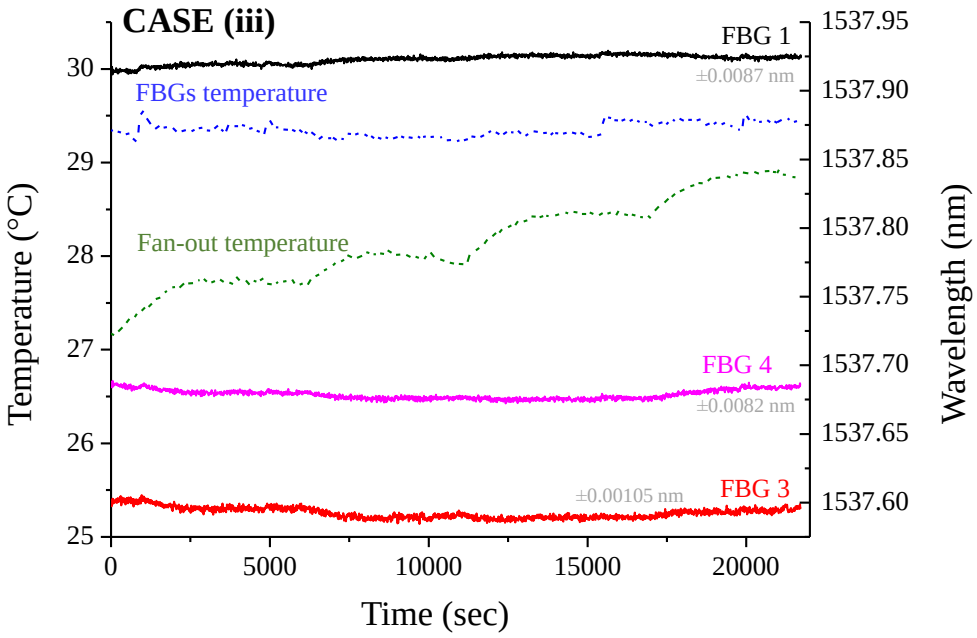

Figure 4-24. Inscribed FBGs' response when the temperature of the fan-out device varied (from 27.2 °C to 28.9 °C with 0.5 °C increment) and the FBGs remained stable (29.4 °C ±0.2 °C) (grey coloured font numbers are the noise levels).

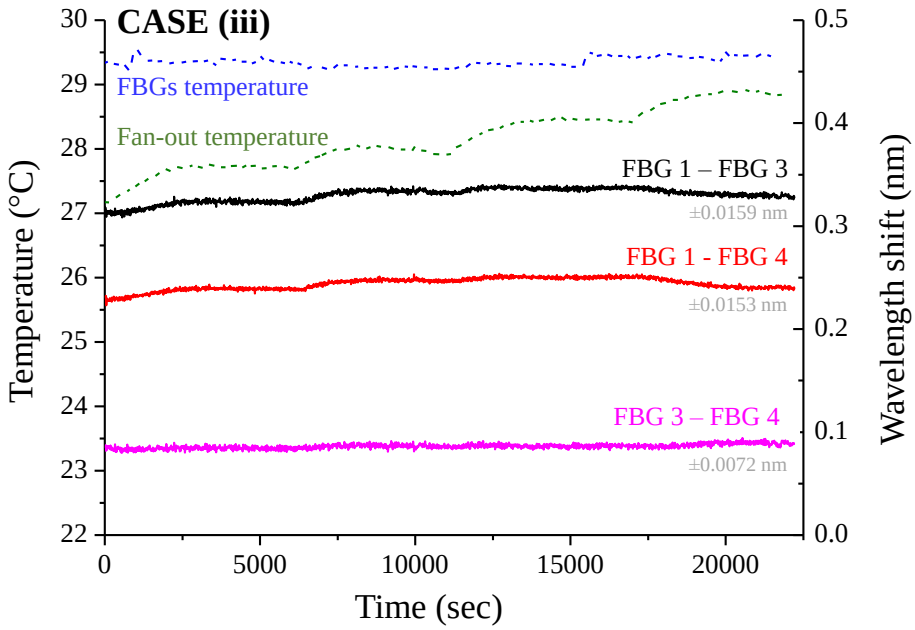

Figure 4-25. Inscribed FBGs' differential response when the temperature of the fan-out device varied (from 27.2 °C to 28.9 °C with 0.5 °C increment) and the FBGs remained stable (29.4 °C ±0.2 °C) (grey coloured font numbers are the noise levels).

The last two cases show that the differential response of the FBGs were immune to temperature changes within the FBGs' local environment. Nevertheless, this response is

affected by temperature variations local to the fan-out device. Figure 4-26 shows two specific regions on the graphs taken in cases (ii) and (iii) for a proper comparison. The differential response of FBGs pair 1-3 remains unaffected with the variation of 2 °C on the FBGs local environment (3500-5550 seconds). This difference varies between ±0.0032 nm, which is in the noise levels of the optical signal for sensor. However, the third case shows that a 0.3 °C temperature variation on the fan-out device's local environment, results to a ±0.0159 nm (which equal to less than a millimetre deflection on the curvature sensor) variation on the differential response of the same FBG pair.

The experiments performed in this section lead to the conclusion that the fan-out device is temperature sensitive and introduces errors in the performance of the MCF curvature sensor system. In the next section a study on the temperature sensitivity of the fan-out device's background spectra will be presented.

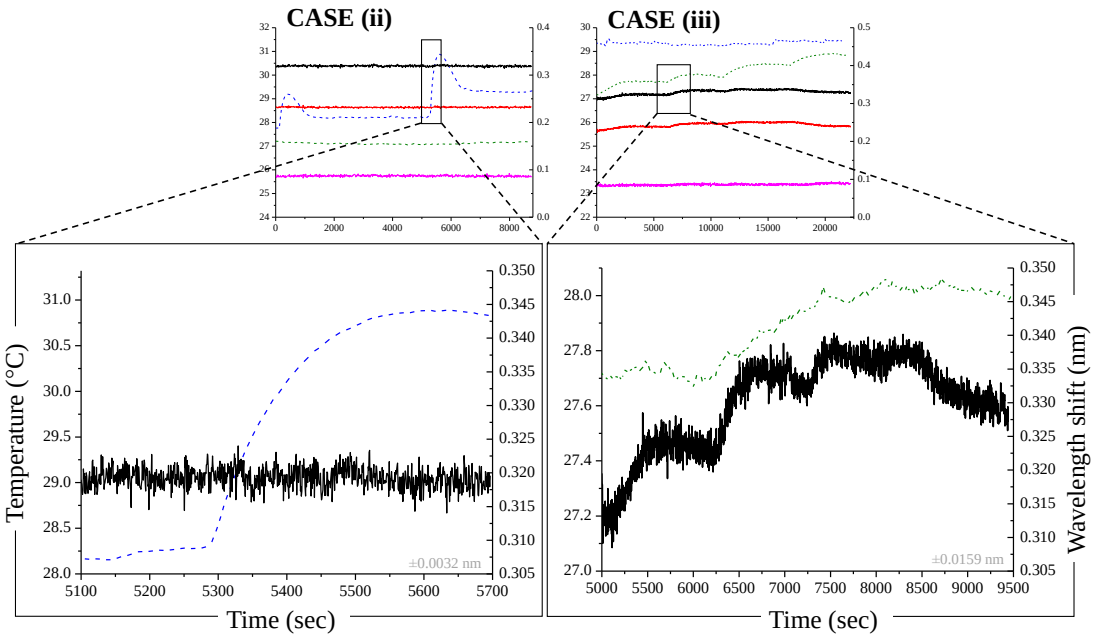

Figure 4-26. Comparison on the differential response of the inscribed FBGS when the temperature of the FBGs varies with the case when the temperature of the fan-out device varies (grey coloured font numbers are the noise levels).

4.5. Background introduced from the fan-out device

In a further study into the fan-out characteristics, the reflectance spectra without the FBGs were monitored. The background reflection spectra produced by the fan-out device affects the resolved peak positions of the inscribed FBGs.

4.5.1. Background spectra monitored through the interrogator

The background spectra of the MCF curvature sensor without the FBGs were monitored using the same interrogator (SM125) used for the previous experiments. The background spectrum for the first core of the MCF is shown in Figure 4-27, where specific regions are highlighted (Figure 4-28). The spectrum was found to have three superimposed sinusoidal patterns, which infer that there are interference effects. Similar sinusoidal patterns were observed at the reflectance spectra of cores 3 and 4. However, in the case of core 2 the sinusoidal patterns 1 and 3, only, were present.

The source of these sinusoidal effects was determined by introducing high attenuation at different points along the MCF and SMF and monitoring the return. The attenuation was achieved by producing a tight bend on the fibres (~1 cm radius). Figure 4-29 shows the spectra at different bending positions of the MCF curvature sensor.

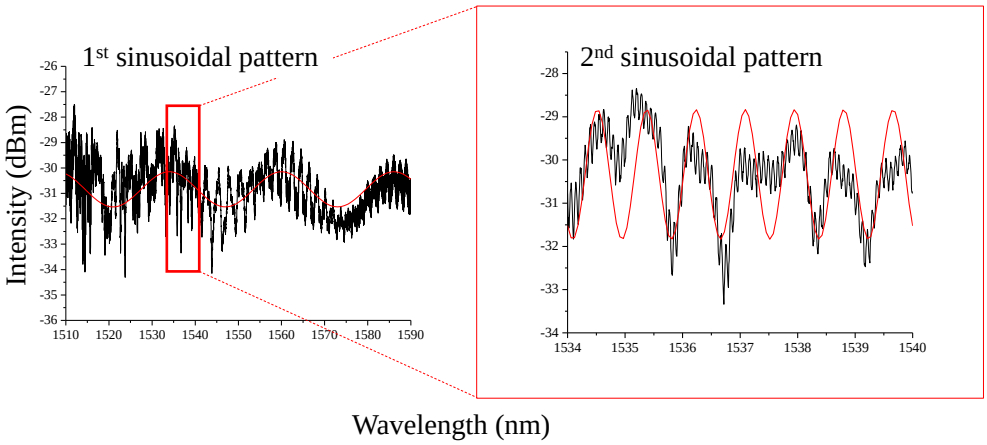

Figure 4-27. Sinusoidal patterns (1 and 2) on the background reflectance spectra produced on the MCF curvature sensor without the FBGs for core 1.

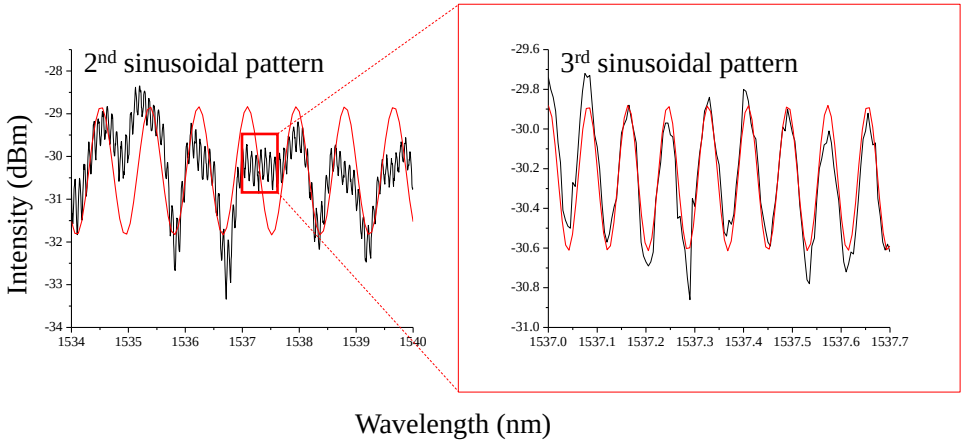

Figure 4-28. Sinusoidal patterns (2 and 3) on the background reflectance spectra produced on the MCF curvature sensor without the FBGs for core 1.

The interface between the interrogator and the SMFs was tested by bending the SMF. In this case all sinusoidal patterns were eliminated, thus this interface does not affect the sensor's performance. However, when attenuation was placed after the fan-out device and before the splicing between the two MCF sections, two interference patterns remained (1st and 3rd). Therefore, it is considered that at least two interference effects are produced by the fan-out device. Finally, the splice was tested by bending the MCF after it. The spectra taken in this case, were similar with the previous (only the 2nd sinusoidal pattern was eliminated). Hence, the splice does not produce any additional interference effect on the MCF curvature sensor. A detailed study on the interference effects produced in the fan-out device will be presented in the following sections.

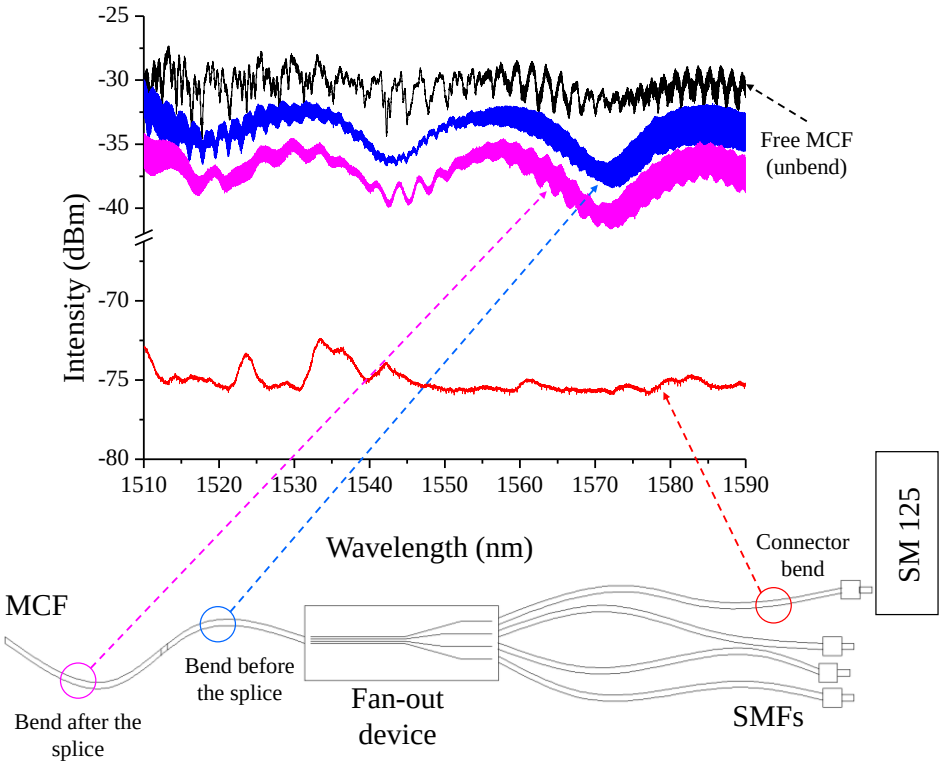

Figure 4-29. Background reflectance spectra of core 1 without the FBGs with high light attenuations (bending) at different positions along the fibres.

4.5.2. Temperature sensitivity of the background reflectance spectra

The same experimental set up (Figure 4-17), was used to study the temperature variations of the background reflectance spectra produced by the fan-out device. Figure 4-30 and Figure 4-31 show the collected spectra from core 1 for two different cases: (*a*) when the fan-out device was maintained at a stable temperature (27.8 °C ± 0.2 °C) where the spectra were monitored for half an hour in total with 5 minutes steps, and (*b*) when

the temperature of the fan-out device varied from 27.5 - 28.8 °C ± 0.2 °C with 0.4 °C increments. In case (*b*) a clear phase shift following the increase of the temperature on the sinusoidal patterns is observed. This is a characteristic behaviour of Fabry-Perot cavities due to temperature variations [11].

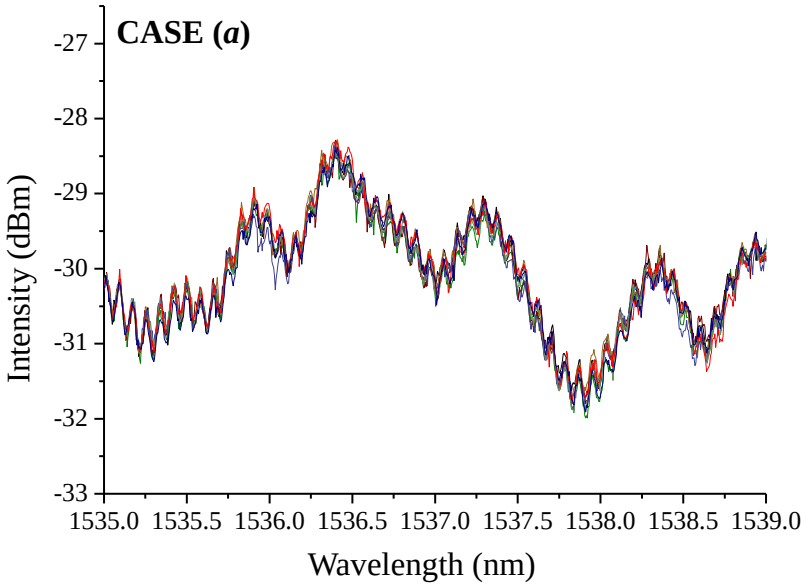

Figure 4-30. Background reflectance spectra on core 1 when the fan-out device remained on stable temperature (27.8 °C ±0.2 °C), the spectra were monitored for half an hour in total, with 5 minutes steps.

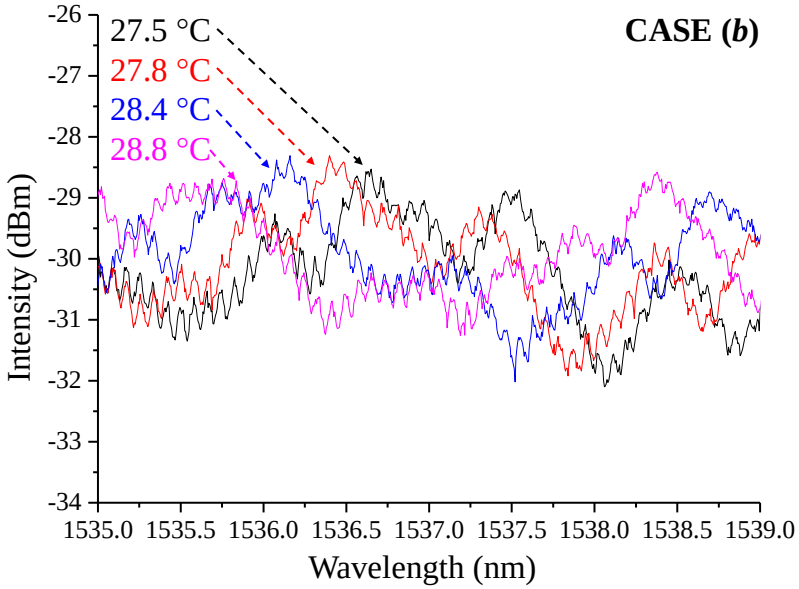

Figure 4-31. Background reflectance spectra on core 1 when the temperature of the fan-out varied from 27.5 - 28.8 °C ±0.2 °C with 0.4 °C increments.

4.5.3. Fabry-Perot optical cavities in the fan-out device

The 1st and the 3rd patterns (see Figure 4-27 and Figure 4-28) remained on the reflectance spectra after bending the MCF after the fan-out device (Figure 4-29). Thus, it is considered that the interference effects are produced due to optical cavities existing in the fan-out device. Nevertheless, the 2nd sinusoidal pattern is eliminated (or shows variation) when the MCF is bent at different positions. Therefore, it is assumed that it is produced from the interference between higher transmission modes.

The fitting process applied on the spectra determined the period (T) of the sinusoidal patterns. The length of an optical Fabry-Perot cavity (l) can be calculated from this period [12]:

$$nl = \frac{\lambda_0^2}{2T\cos\theta} \qquad \text{Equation 4.7}$$

Where, n is the refractive index of the material where the interference occurs (fan-out device), λ_0 is central wavelength of the optical source used (in this case 1550 nm) and θ is the angle of the incident light (in this case $\theta \cong 0$, thus $\cos\theta \approx 1$). A sinusoidal fitting was applied to all four cores for the two cavities related with the fan-out device (1st and 3rd sinusoidal pattern). The calculated optical cavity lengths are shown on Table 4-2.

Table 4-2. Calculated optical Fabry-Perot cavity lengths for all cores of the MCF.

	Optical cavity lengths (nl) (mm)	
	Cavity 1	**Cavity 3**
Core 1	0.0438	14.455
Core 2	0.0494	14.452
Core 3	0.0475	14.441
Core 4	0.0429	14.487
Average	0.0459	14.459

4.6. Low coherence interferometry

A further study to explore the existence of optical cavities in the fan-out device was performed using low coherence interferometry. The formation of an optical cavity requires two separate reflecting surfaces and their position can be determined by looking for positions where a low-coherence interferometer is "balanced" i.e. fringes are observed

and highest visibility relates to the point where path lengths agree [13]. In this section the distance between two reflection interfaces inside the fan-out device will be determined.

4.6.1. Experimental configuration

A schematic diagram of the low coherence experimental is shown in Figure 4-32. The IR broadband light source has central emission wavelength at 1550 nm (λ_0) with short coherence length (~0.053 mm). The emission spectrum of the source recorded by an optical spectrum analyser (OSA) is shown in Figure 4-33. The coherence length can be calculated with the following equation [14]:

$$nl = \frac{2\ ln(2)}{\pi}\frac{\lambda_0^2}{\Delta\lambda} \qquad \text{Equation 4.8}$$

where, $\Delta\lambda$ is the full width at half maximum (FWHM) of the emission spectrum, n is the refractive index of the material in which the light is transmitted. The light is separated into two different optical paths (reference arm and measurement arm) with the use of a beam splitter. The interference between these two paths occurs when they recombine at the photodetector.

Since reflections were believed to be present in the fan-out device, the measurement and the reference arms were configured to have comparable optical lengths $n_{air}l_{act,m} \approx n_{glass}l_{act,r}$ to this position. Where n_{air} and n_{glass} are the refractive indices where the light is transmitted in the two arms and l_{act} is the actual length of the arms.

By moving the two mirrors on the measuring arm with a highly stable velocity the interference between the two signals (reflection from the fan-out device and the end mirror on the measurement arm) could be detected. The interference pattern of He-Ne laser source was monitored concurrently with the interference form the IR source on the same experimental set up to provide an absolute distance measurement. Hence, the optical distance of the IR interference signals could be correlated with the actual optical distance.

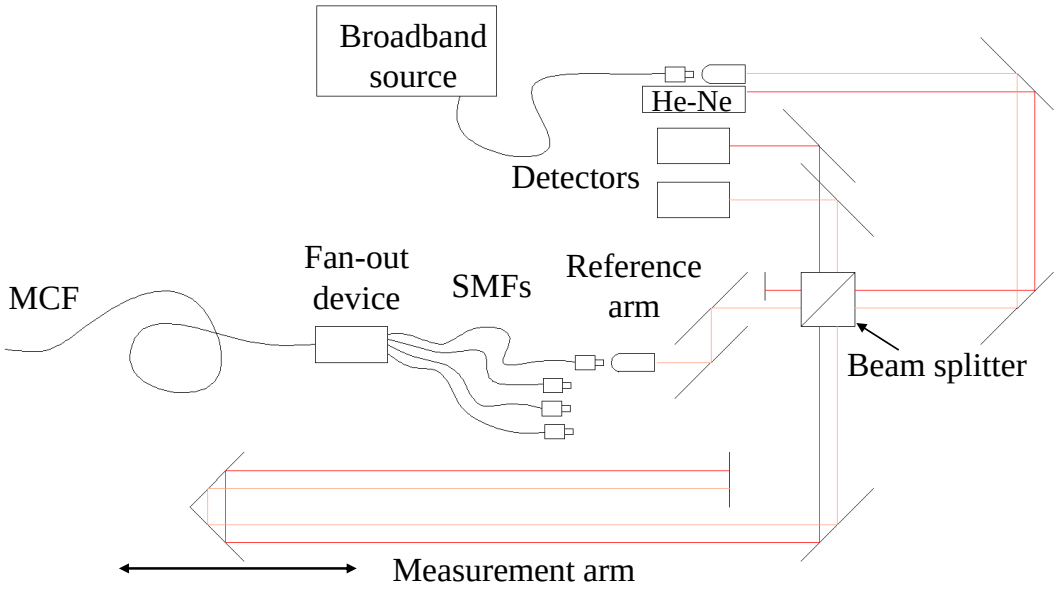

Figure 4-32. Low coherence interferometry experimental set up.

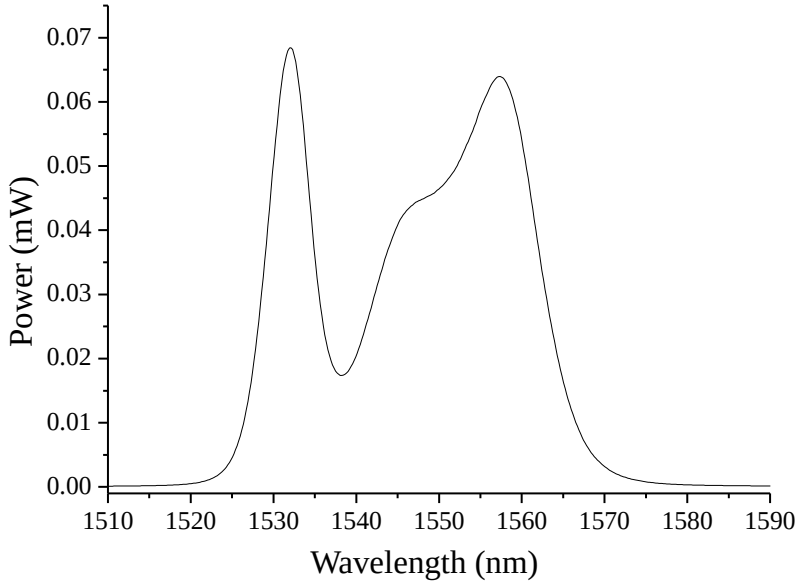

Figure 4-33. Emission spectrum of the IR source used on the low coherence interferometry experiments (FWHM on the wavelength range 1540-1575 nm: 20.092 nm), total optical power 9.04 mW.

4.6.2. Low coherence interferometry experimental results

Two different interference signals could be detected on the IR photodetector due to their interference with the measurement arm. Thus, two different reflecting surfaces were observed to exist in the fan-out device. The optical distance between these surfaces could

be extracted from the interference pattern of the He-Ne laser source as a known calibration. This distance can be expressed [15]:

$$d = \frac{\lambda N}{2} \qquad \text{Equation 4.9}$$

where N is the number of the fringes, and λ is the source's wavelength emission (632.8 nm).

Figure 4-34 shows a typical interference patterns. The optical distance ($n_{air}d$) between the two reflecting surfaces was measured according to Equation 4.9 through a script produced in MatLab™ [Appendix 5].

The measured optical distance between the two different reflecting surfaces, is $\sim$14.5 mm, however the width of the two signals introduces an uncertainty on their exact position, thus an error of ±0.1 mm is considered. Finally, all four SMFs on the fan-out device were tested using the low coherence interferometry experiment set up. The same two reflecting surfaces were detected through all SMFs and the optical distance between them was comparable. Table 4-3 includes the measured optical distances for all four fibres.

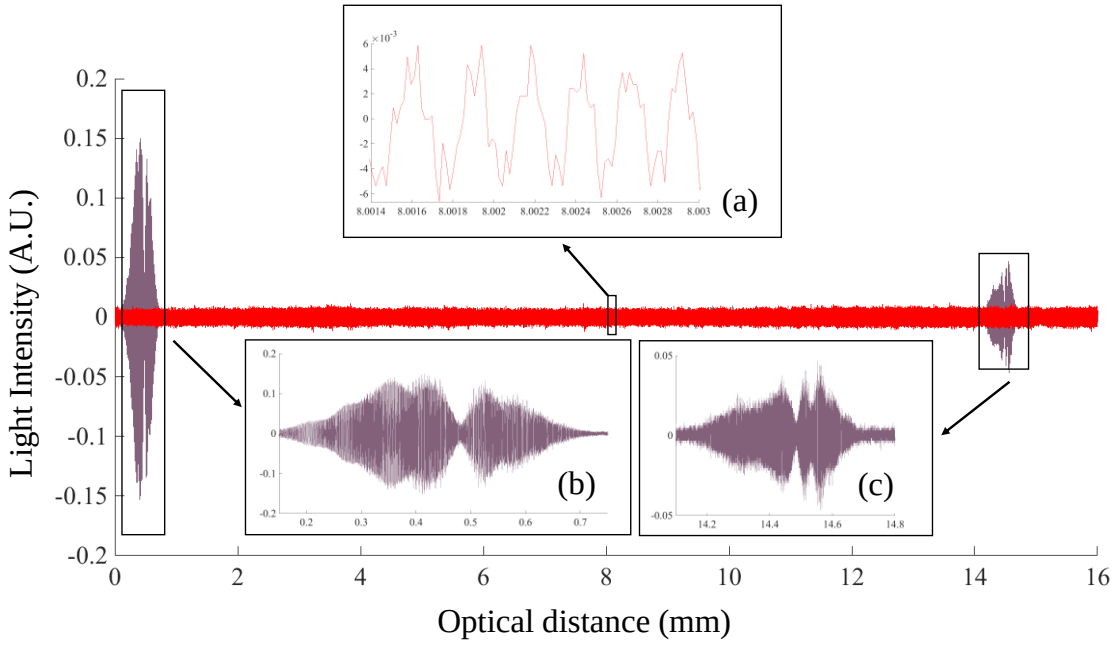

Figure 4-34. Interference patterns produced from the two reflecting surfaces in the fan-out device (a) of the He-Ne laser source (b) of the IR source from the first reflecting surface (c) of the IR source from the second reflecting surface. Both signals were a.c. coupled to remove the d.c. offset.

Table 4-3 Optical distance between the two detected reflecting surfaces in the fan-out device for all four SMFs coupled on the device

	Optical distance (nl) (mm)
SMF1	14.604
SMF2	14.547
SMF3	14.546
SMF4	14.549
Average	14.561

4.7. Comparison on the cavities characterised from the reflection spectra and the low coherence interferometry experiments

Table 4-4 summarizes the optical cavities observed from the two techniques described in paragraphs 4.5.1 and 4.6.2. Two different optical cavities were detected in the fan-out device from the reflection spectra monitored with the interrogator. However, only two reflecting surfaces were identified with the low coherence interferometry experiments, which confirms the existence of only one optical cavity.

Table 4-4. Fabry-Perot optical cavity lengths determined from the sinusoidal fitting on the spectra collected with the interrogator and optical distances between the two reflections determined from the low coherence interferometry experiment for all four cores/SMFs of the fan-out device.

(nl)	**Optical lengths (mm)** from the reflection spectra analysis		**Optical distance (mm)** from low coherence interferometry
	Cavity 1	**Cavity 2**	
Core/SMF 1	0.0438	14.455	14.604
Core/SMF 2	0.0494	14.452	14.547
Core/SMF 3	0.0475	14.441	14.546
Core/SMF 4	0.0429	14.487	14.549
Average	0.0459	14.459	14.561

The optical cavity (cavity 2) that was detected with both techniques is ~14.5 mm in length. The measurements taken from the two techniques for each core/SMF deviate only by 0.7%. Moreover, the length of this optical cavity is comparable to the actual length of the fan-out device. Therefore, it is believed that this optical cavity is formed from the reflecting surfaces at the two ends of the inscribed waveguides in the silica glass (Figure 4-35).

The optical cavity (cavity 1) that was detected only through the reflectance spectra has optical length ~ 0.046 mm. This length is comparable to the IR source's coherence

length used for the low coherence interferometry measurements. The coherence length (~0.053 mm) was calculated using Equation 4.8 and the emission spectrum from the IR source (Figure 4-33). Therefore, the first cavity is close to the experiments resolution and is not detectable. However, it is believed that this length cavity could be formed in the interface between the optical fibres (MCF or SMFs) and the surface of the silica glass where the waveguides are inscribed (Figure 4-35).

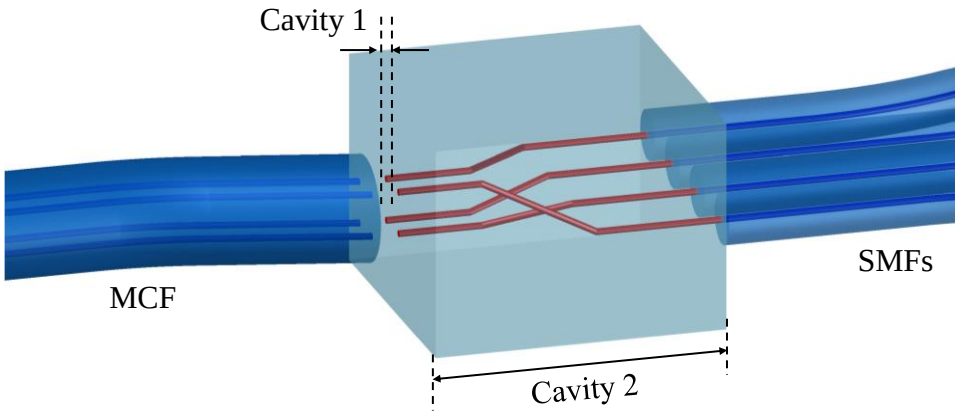

Figure 4-35. Possible positions of the cavities formed in the fan-out device figure recreated according to [3].

4.8. Differential strain sensitivity of the inscribed FBGs

The differential strain sensitivity of the FBGs can be calculated by monitoring their response when the fibre is deflected in the two directions described in section 4.3.1, the inscribed FBGs lie on the two different planes of curvature ((a) and (b)) shown in Figure 4-36. The separation of planes (a) and (b) coincide with the distance between two adjacent cores of the MCF. This distance was measured under a microscope to be 50 ±1 μm (Figure 4-4).

When the MCF is deflected in direction 1, the FBGs inscribed in cores 1 and 4 lie on plane (a), while the FBGs on cores 2 and 3 lie on plane (b). Hence, the separation on the planes of curvature for core pairs 1-4 and 2-3 is zero. The separation on the planes of curvature for core pairs 1-2 and 3-4 is 50 μm. Table 4-5 includes the separation of the curvature planes for all core pairs on the two different directions of deflection.

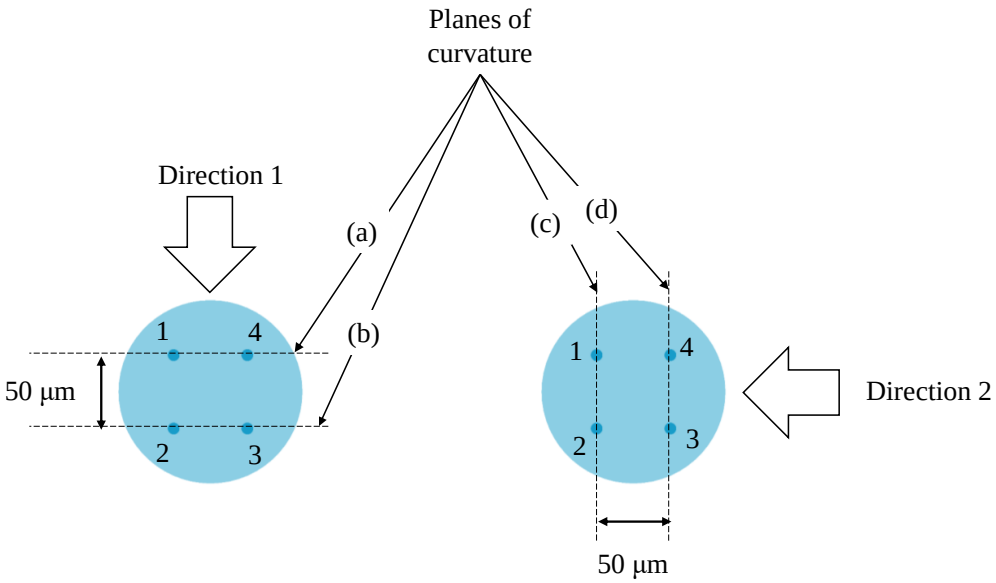

Figure 4-36. A schematic diagram of the planes of curvature where the inscribed FBGs lie.

Table 4-5. Separation of curvature planes when the MCF is deflected on the two directions for all core pairs.

core pairs	direction 1	direction 2
	separation of the planes of curvature (µm)	
core 1-core 2	0	**50**
core 1-core 3	**50**	**50**
core 1-core 4	**50**	0
core 2-core 3	**50**	0
core 2-core 4	**50**	**50**
core 3-core 4	0	**50**

The differential strain sensitivity ($\Delta\lambda_{reflected}/\Delta\varepsilon$, $[pm/\mu\varepsilon]$) of the inscribed FBGs can be determined by monitoring the reflectance wavelength response of the FBGs that lie at separate curvature planes ($d \equiv 50\ \mu m$). According to equations 2.23 and 2.26 the strain shift can be determined:

$$\Delta\varepsilon = \frac{d}{R} \qquad \text{Equation 4.10}$$

$$\kappa = \frac{1}{R} = \frac{3\,(l-x)}{l^3}\ \nu_l \qquad \text{Equation 4.11}$$

where, l is the cantilever length, x is the distance of the FBGs from the fixed point and ν_l is the deflection of the fibre.

4.8.1. Experimental results

Four MCF curvature sensors were fabricated following the procedure described in paragraph 4.2. Calibration deflection experiments on the sensors were performed and the reflectance wavelength peaks of at least three inscribed FBGs were monitored with a commercial SM125 interrogator. Figure 4-37 shows the wavelength shift of the FBGs peak position versus the strain shift measured for the first sensor. The strain shift was calculated using Equation 4.10 and Equation 4.11 for the different deflection increments.

The gradients' absolute value on these experimental data coincide with the FBGs' differential strain sensitivity for the core pairs that lie on separate curvature planes. In Figure 4-37 these core pairs are 1-3 and 3-4 for the first direction, while for the second direction the core pairs on separate curvature planes are 3-1 and 1-4. The absolute value of these gradients is on average 1.14 $pm/\mu\varepsilon$, which is in the expected range. Moreover, the gradients on core pairs 1-4 and 3-4 for the first and second direction of deflection are close to zero as it is expected. In these cases the inscribed FBGs lie on the same plane of curvature, hence ($d \equiv 0\ \mu m$). The same analysis was applied on measurements taken from the linear deflections of all four fabricated MCF curvature sensors. The absolute values of the gradients provided from two different core pairs are for all sensors given in table Table 4-6.

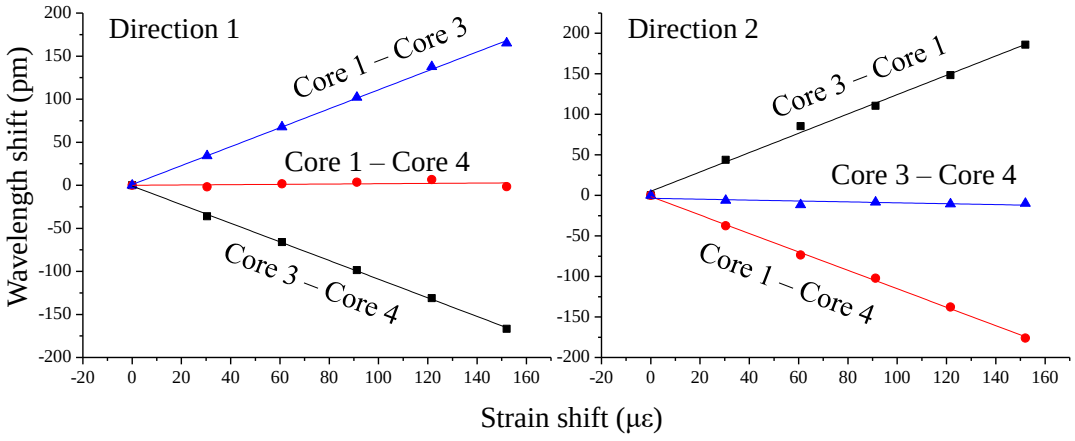

Figure 4-37. Wavelength shift versus strain shift for the calculation of the differential strain sensitivity of the inscribed FBGs.

Table 4-6. Differential strain sensitivity calculated from the FBGs response due to deflection of the MCF in the two specific directions.

Strain sensitivity $[pm/\mu\varepsilon]$	**Direction 1**		**Direction 2**	
	core 1-core 3	**core 3-core 4**	**core 1-core 3**	**core 3-core 4**
sensor 1	**0.94107**	0.03887	0.06753	**0.96546**
sensor 2	**1.02839**	0.00345	0.00939	**0.97226**
sensor 3	**1.0416**	0.00821	0.00964	**1.03184**
sensor 4	**1.19279**	0.05553	0.001815	**1.08219**

An average value of the gradients provided from all four sensors, in the case where the FBGs lie at separate planes of curvature is $\sim 1.032\ [pm/\mu\varepsilon]$ while for the case where the FBGs lie at same planes of curvature is $\sim 0.024\ [pm/\mu\varepsilon]$. Therefore, the differential strain sensitivity of the inscribed FBGs into the MCF is $\frac{\Delta\lambda_{reflected}}{\Delta\varepsilon} \approx 1.032 \pm 0.01\ pm/\mu\varepsilon$. Errors in this value can mainly be attributed to the uncertainty on the exact position of the FBGs in regards to the fixed point along the MCF, (x in Figure 4-8). The uncertainty of the cantilever lengths (l) and the increments of deflection (v_l) introduce negligible errors. Finally, the noise on the wavelength shifts of the inscribed FBGs ($\sim 0.0054\ nm$) used for the calculations can introduce small errors on the calculated strain sensitivity ($\pm 0.16\ pm/\mu\varepsilon$).

4.9. Conclusions

In this chapter the fabrication of a four core MCF curvature sensor is reported. Two different elements constitute the sensor: (a) the FBGs, which monitor the strain variations on the fibre and (b) the fan-out device, which is essential for the interrogation of their response. The fan-out device is an optical component which acts as an interface between the MCF and conventional SMFs. This device is silica glass with inscribed waveguides which transmits light from each individual core of the MCF to a SMF. Splicing an additional MCF section to the MCF attached on the fan-out device was performed for convenience of manufacture. Finally, the inscription of the FBGs on this section was achieved with the phase mask technique.

Due to the unique structure of the MCF (cores in a square array), at least three FBGs are required (two orthogonal pairs of FBGs) for the calibration of the curvature sensor. A two-dimensional representation of the end of the MCF can be produced with the calibration parameters for the sensor. The forced circular motion of the fibre tip was noted

to drift in course of time. This drift lead on exploring the temperature sensitivity of the MCF curvature senor.

The two main elements which constitute the sensor (FBGs and fan-out device) were enclosed into temperature–controlled environments. Experiments on varying the environmental temperature of one component while keeping the other stable were initiated. These experiments indicated that the differential peak position of the FBGs' reflecting wavelength is not affected by the FBGs temperature variations. However, the same wavelength shift was shown to be varying with the temperature changes of the fan-out device's local environment.

Further experiments on the reflectance spectra produced from the fan-out device showed the existence of two different optical cavities with optical lengths ~ 0.0459 mm and ~ 14.459 mm, respectively. Moreover, the existence of the second optical cavity was verified through a low coherence interferometry experiment. The position of two reflecting surfaces was detected and their optical distance was measured to be ~ 14.561 mm. All four cores of the MCF showed the same response in regards to the detected optical cavities in the fan-out. These cavities proved to be temperature sensitive and are believed to introduce an error on the performance of the MCF curvature sensor. This performance is affected for temperature variations (±0.3° C) of the fan-out device higher than.

Finally, the fabrication of four in total MCF curvature sensors was achieved. The differential strain sensitivity of the inscribed FBGs was determined by deflection of these sensors. This value was calculated to be $\frac{\Delta\lambda_{reflected}}{\Delta\varepsilon} \approx 1.032 \pm 0.01\ [pm/\mu\varepsilon]$ which is close to the values reported in literature for conventional FBGs [16].

4.10. References

[1] A. Iadicicco, A. Cusano, A. Cutolo, R. Bernini, and M. Giordano, "Thinned fiber Bragg gratings as high sensitivity refractive index sensor," *IEEE Photonics Technology Letters,* vol. 16, no. 4, pp. 1149-1151, 2004.

[2] G. Huiyong, Z. Yu, T. Jianguan, L. Xiaofu, Y. Haihu, W. Hongqiao, J. Desheng, "Reflectivity measurement of weak fiber Bragg grating (FBG)," *Journal of Wuhan University of Technology-Mater. Sci. Ed.,* journal article vol. 27, no. 6, pp. 1177-1179, 2012.

[3] R. R. Thomson, H. T. Bookey, N. D. Psaila, A. Fender, S. Campbell, W. N. MacPherson, J. S. Barton, D. T. Reid, and A. K. Kar., "Ultrafast-laser inscription of a three dimensional fan-out device for multicore fiber coupling applications," *Optics Express,* vol. 15, no. 18, pp. 11691-11697, 2007.

[4] J. M and M. Y. Jamro, *Optical Fiber Communications: Principles and Practice*. Financial Times/Prentice Hall, 2009, pp. 220-235.

[5] C. G. Askins, T. F. Taunay, G. A. Miller, B. M. Wright, J. R. Peele, L. R. Wasserman, and E. J. Friebele, "Inscription of Fiber Bragg Gratings in Multicore Fiber," p. JWA39, 2007.

[6] A. Othonos and X. Lee, "Novel and Improved Methods of Writing Bragg Gratings with Phase Masks,", *IEEE Photonics Technology Letters,* vol. 7, no. 10, pp. 1183-1185, 1995.

[7] E. Lindley, S. Min, S. Leon-Saval, N. Cvetojevic, J. Lawrence, S. Ellis, and J. Bland-Hawthorn, "Demonstration of uniform multicore fiber Bragg gratings," *Optics Express,* vol. 22, no. 25, pp. 31575-81, 2014.

[8] E. Lindley, S. Min, S. Leon-Saval, N.Cvetojevic, N, Jovanovic. J. Bland-Hawthorn, J. Lawrence, I. Gris-Sanchez, T. Birks, R. Haynes, D. Haynes., "Core-to-core uniformity improvement in multi-core fiber Bragg gratings," vol. 9151, p. 91515F, 2014.

[9] G. M. H. Flockhart, W. N. MacPherson, J. S. Barton, J. D. C. Jones, L. Zhang, and I. Bennion, "Two-axis bend measurement with Bragg gratings in multicore optical fiber," *Optics Letters,* vol. 28, no. 6, p. 387, 2003.

[10] T. Li, Y. Tan, Z. Zhou, and K. Zheng, "A non-contact FBG vibration sensor with double differential temperature compensation," *Optical Review,* journal article vol. 23, no. 1, pp. 26-32, 2016.

[11] J. Mathew, O. Schneller, D. Polyzos, D. Havermann, R. M. Carter, W. N. MacPherson, D. P. Hand, and R. R. J. Maier, "In-Fiber Fabry–Perot Cavity Sensor for High-Temperature Applications," *Journal of Lightwave Technology,* vol. 33, no. 12, pp. 2419-2425, 2015.

[12] Y. O. Barmenkov, D. Zalvidea, S. Torres-Peiró, J. L. Cruz, and M. V. Andrés, "Effective length of short Fabry-Perot cavity formed by uniform fiber Bragg gratings," *Optics Express,* vol. 14, no. 14, pp. 6394-6399, 2006.

[13] S. Kim, J. Na, M. J. Kim, and B. H. Lee, "Simultaneous measurement of refractive index and thickness by combining low-coherence interferometry and confocal optics," *Optics Express,* vol. 16, no. 8, pp. 5516-5526, 2008.

[14] C. K. Hitzenberger, A. Baumgartner, and A. F. Fercher, "Dispersion induced multiple signal peak splitting in partial coherence interferometry," *Optics Communications,* vol. 154, no. 4, pp. 179-185, 1998.

[15] H. A. Deferrari, R. A. Darby, and F. A. Andrews, "Vibrational Displacement and Mode-Shape Measurement by a Laser Interferometer," *The Journal of the Acoustical Society of America,* vol. 42, no. 5, pp. 982-990, 1967.

[16] J. Du and Z. He, "Sensitivity enhanced strain and temperature measurements based on FBG and frequency chirp magnification," *Optics Express,* vol. 21, no. 22, pp. 27111-27118, 2013.

Chapter 5. MCF curvature sensor with tapered fibre fan-out device

Fabrication of MCF curvature sensors with a fibre tapered fan-out device is reported in this chapter. The motivation for fabricating these sensors came from the desire to eliminate the silica inscribed waveguides fan-out device, due to the issued reported in the previous chapter. The challenges arising during the fabrication of these sensors, and their cross-sensitivity to temperature, are discussed. Figure 5-1 shows a schematic diagram and an image of the fabricated MCF curvature sensor with the tapered fan-out device.

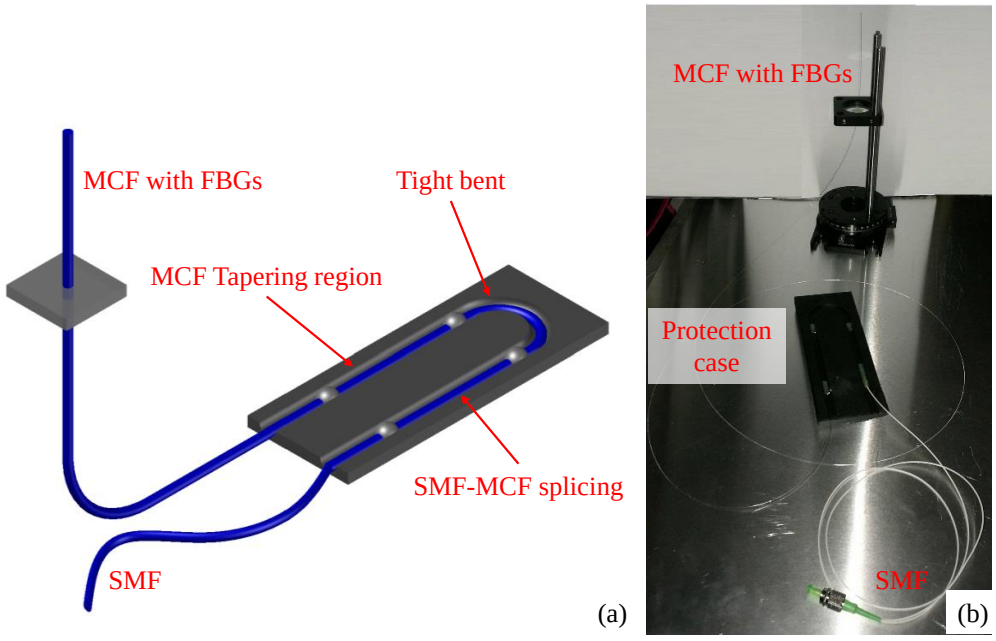

Figure 5-1. (a) Schematic diagram and (b) image of the MCF curvature sensor with the tapered fan-out interconnection.

5.1. Silica waveguides versus tapered MCF fan-out device

In this chapter, an alternative way of addressing FBGs inscribed into the MCF is explored with a desire to eliminate the silica fan-out device. This will both reduce the cost of the sensor system and eliminate the fan-out temperature sensitivity (reported in Chapter 4). The silica waveguide fan-out device was an essential element for the fabrication of the sensors presented in Chapter 4. However, in this Chapter the device is used only during the FBGs inscription in order to monitor the fabrication process. Figure 5-2 (a) includes a schematic diagram of the light transmittance/reflectance path when using a silica waveguides fan-out device.

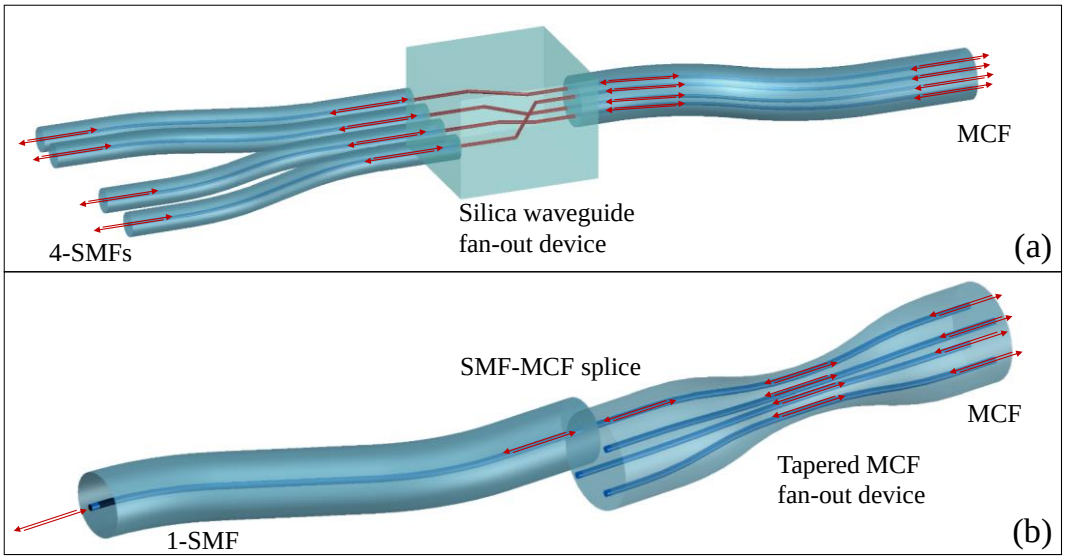

Figure 5-2. Light transmittance/reflectance when using (a) a silica waveguides fan-out device (image recreated according to [1]) and (b) a MCF tapered fan-out device.

The general concept of the MCF tapered fan-out device, Figure 5-2 (b), is based on coupled mode theory. By tapering a section of the MCF it is possible to couple light from one core to all four cores of the MCF. Consequently, by splicing this core to a conventional SMF the reflectance spectrum can be interfaced with a wide range of commercial interrogators or optical spectrum analysers.

5.2. Light coupling between the cores of MCF

This section reports the coupling of light between the four cores of the MCF by tapering the fibre. A mathematical simulation using equations from coupling theory [2] was used in order to predict the required tapering conditions. Experimental results show that coupling of light can be achieved under these conditions (see section 5.2.4). At the end of this section the most suitable tapering parameters for the tapered MCF fan-out device are established and the tapered fan-out device was fabricated according to these.

5.2.1. Theoretical simulation

Coupling of light from one core to all four cores of the MCF can be achieved under specific conditions. These conditions can be met by reducing the distance between the cores of the fibre as well as their radii, according to Mortimore's light coupling analysis [3] (see Chapter 2, section 2.8.2). Both can be achieved by tapering the MCF. A theoretical simulation on the coupling of light from one core to all four cores of the MCF was performed using MatLab™ [Appendix 7]. The primary objective of these simulations

was to predict the most suitable cladding diameter (and hence core-core spacing and core radius) as well as the coupling distance for the best coupling ratio between the four cores.

This model uses equations 2.28-2.36 which are presented in section 2.8.2 and they describe the power transfer from one core of the MCF to all four cores. For the fan-out replacement the simulations considered the reduction of the cladding diameter. Hence, a reduction on the distance between the adjacent (d_s) and distant (d_w) cores of the MCF is achieved. Moreover, by drawing down the cladding diameter, the radii of the four cores (r) are also decreasing with the same proportion (see Figure 5-3). The wavelength of light was assumed to be 1553 nm (the mean FBG reflection wavelength) and the effective refractive index 1.445. In these simulations the initial intensity power is in core 1 of the MCF $P_1(0) = 100$ %. An additional constraint is applied such that the maximum waist length cannot exceed 18 mm: this is due experimental limitations associated with our fibre tapering facility.

Figure 5-4 shows the power coupling predicted from the simulations. As might be expected, coupling of light is absent when the dimensions (d_s, d_w, r) coincide with the actual dimensions of the MCF (without tapering). Moreover, coupling is still absent down to a 100 μm waist diameter. A small portion of light starts to be transferred from core 1 to the remaining three cores in case of 90 - 80 μm waist diameters. However, the light power transfer is less than 10% for an 18 mm coupling length. Finally, a 25:25:25:25 coupling ratio between the four cores of the MCF can be achieved at a 70 μm at ~9 mm, a 60 μm at 5.7 and 17.1 mm and at 50 μm waist diameter at 5.1 and 15.4 mm coupling lengths respectively (see Table 5-1). Therefore, these last three cases are considered suitable for light transfer from one core to all four cores with a desirable coupling ratio. Table 5-1 includes the numerical parameters for all simulations shown in Figure 5-4, as well as the taper lengths where a coupling ratio of a 25:25:25:25 is predicted.

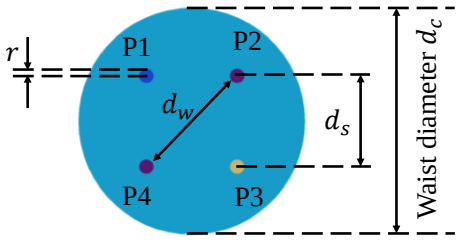

Figure 5-3. Cross section of the MCF with the light coupling parameters.

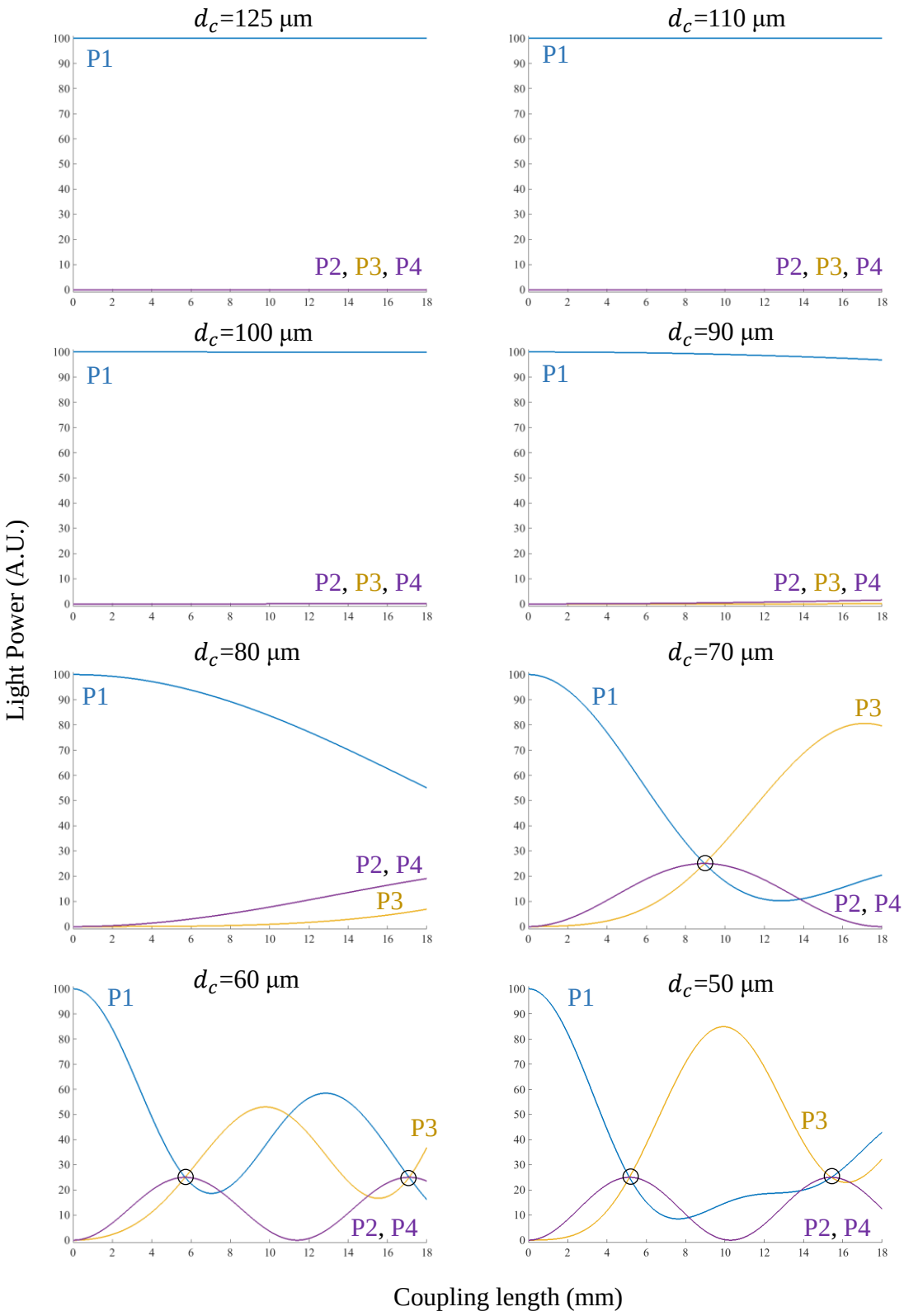

Figure 5-4. Simulations on the light coupling ratios between the cores of the MCF for different waist diameter, with power initially in core 1.

Table 5-1. Numerical parameters used for the light coupling between the cores of the MCF and the coupling lengths were a 25:25:25:25 coupling ratio can be achieved.

waist diameter (μm)	adjacent cores separation (μm)	distant cores separation (μm)	cores radii (μm)	**coupling length 1 (mm)**	**coupling length 2 (mm)**
125	50	71	4	-	-
110	44	62	3.52	-	-
100	40	57	3.2	-	-
90	36	51	2.88	-	-
80	32	45	2.56	-	-
70	28	40	2.24	**9.021**	-
60	24	34	1.92	**5.695**	**17.09**
50	20	28	1.6	**5.113**	**15.42**

Nevertheless, there are two additional aspects to be considered for the tapering of the MCF. These are the experimental instrument limitations and the geometry of the taper. Both are reviewed in the following sections.

5.2.2. Tapering parameters

The MCF tapering was achieved with an arc fusion-splicer (FSM-100P+, Fujikura Ltd.). The splicer includes a function where tapering of the fibre can be achieved. The tapering is achieved with continuous arc while pulling the fibre at a constant velocity (0.2 $\mu m/ms$). The tapering design on the MCF was determined with the splicer's software, where four different parameters could be optimised: (a) The waist length, (b) the waist diameter, (c) the taper down and (d) the taper up lengths. These parameters are shown in a 2-D schematic diagram of the tapered MCF.

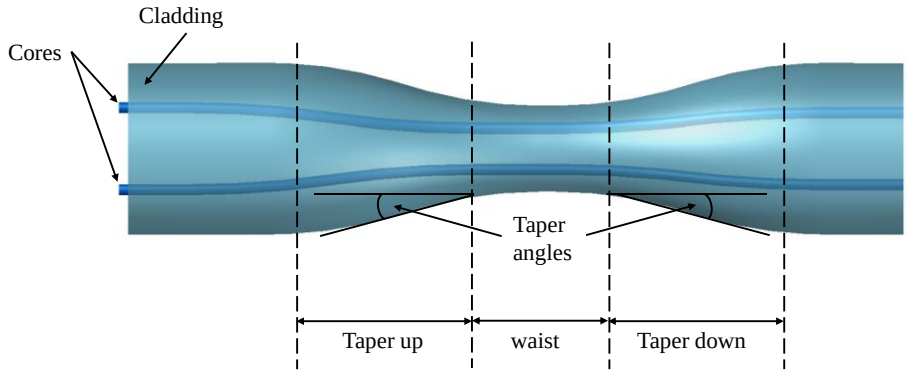

Figure 5-5. A 2-D schematic diagram of the tapered MCF fibre which includes the tapering parameters.

The parameters were chosen considering the splicer's limitations and the theoretical simulation presented in section 5.2. The splicer's motors can travel a total of 18 mm

length. This sets a limit on the waist, taper down and up lengths of the fabrication. The length of the taper up and down regions are critical when considering the losses of the transmitted light. Clearly the geometry of the taper means that the up and down angles are functions of the respective taper lengths and the diameter of the waist. These two lengths set to give the desired angle of the taper. According to literature, this angle determines whether the tapering is in adiabatic, or lossy, [4-6]. For a standard SMF this angle has been reported to be less or equal to 0.35° [7]. When a tapering is in the adiabatic region the coupled light is confined in the cores of the fibre while when it is in the lossy region the majority of the light is coupled on the cladding modes or leaked out of the optical fibre.

The waist diameters of interest are 70, 60 or 50 μm. In addition, two conditions were required to be met: (a) the waist length to coincide with the first 25:25:25:25 coupling ratio length (to within ±0.1 mm) and (b) the total tapering length not to exceed the 17 mm. Table 5-2 includes all possible combinations of these parameters. According to this table the first case (70 μm waist diameter) is eliminated due to the high taper angle. The last two cases are considered to be in the range of all requirements. However, the case of 50 μm waist diameter was chosen due to better taper quality, which is discussed further in the following sections.

Table 5-2. Tapering parameters which were optimised taking into account the splicer's limitations and the coupling simulations.

waist diameter (μm)	coupling length from simulations (mm)	Total tapering length (17 mm)			
		taper down (mm)	waist (mm)	taper up (mm)	taper angles (°)
70	9.021	4	9	4	0.4
60	5.695	5.7	5.6	5.7	0.33
50	5.113	6	5	6	0.35

5.2.3. Experimental MCF tapering

The tapering quality produced with the splicer for the third case (50 μm waist diameter) was explored with two different experiments. The first used the splicer's software while the second used a microscope. Both show that the geometry of the fibre obtained after the tapering procedure was uniform and in good correlation with the original design (see Figure 5-6). Moreover, coupling of light from one core to all four was confirmed for a light source with central emission wavelength at 1550 nm.

i. Measurements produced from the splicer

Measurements on the diameter of the tapered fibre were produced with high accuracy (±2 μm) using the splicer's in built camera and software. After the completion of the tapering procedure (motors pulling/feeding in one direction) and while the fibre is still inserted in the splicer, the motors can follow a reverse motion (motors pulling/feeding in the opposite direction). Hence the cladding diameter can be measured with the splicers camera on two vertical planes (*x* and *y*). Figure 5-6 shows the designed and measured diameters along the total tapering length for the case were the waist diameter is 50 μm.

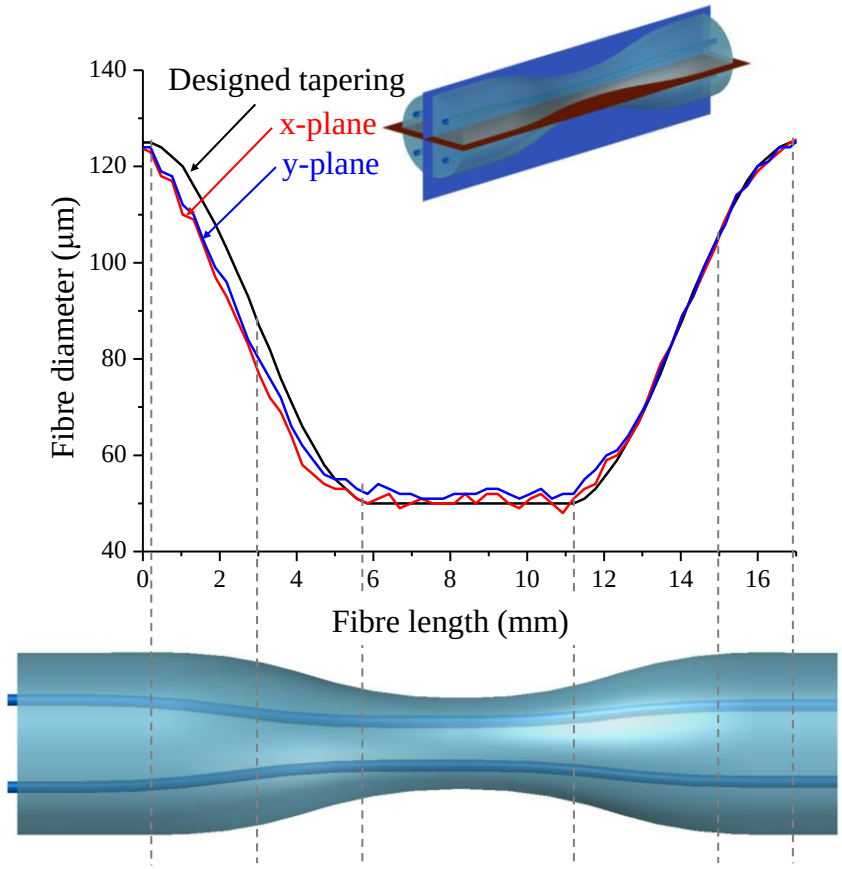

Figure 5-6. Designed tapering and measure profiles on two vertical planes (x and y).

ii. Images taken under a microscope

The tapered piece of the MCF was mounted under a microscope and images were taken in two different cases. In the first case the fibre was lying horizontally and images along the total tapering length were collected (Figure 5-7). While in the second case, the MCF was manually cleaved with a ceramic blade. Thereafter, cross section images of the fibre at the waist region and at a region away from the tapering length (unmodified fibre region for comparison purposes) were taken. Both cross sections were taken in a single

image for comparison reasons. Figure 5-8 shows microscope image as well as schematic diagrams with their dimensions. The accuracy of these measurements were ± 2 µm.

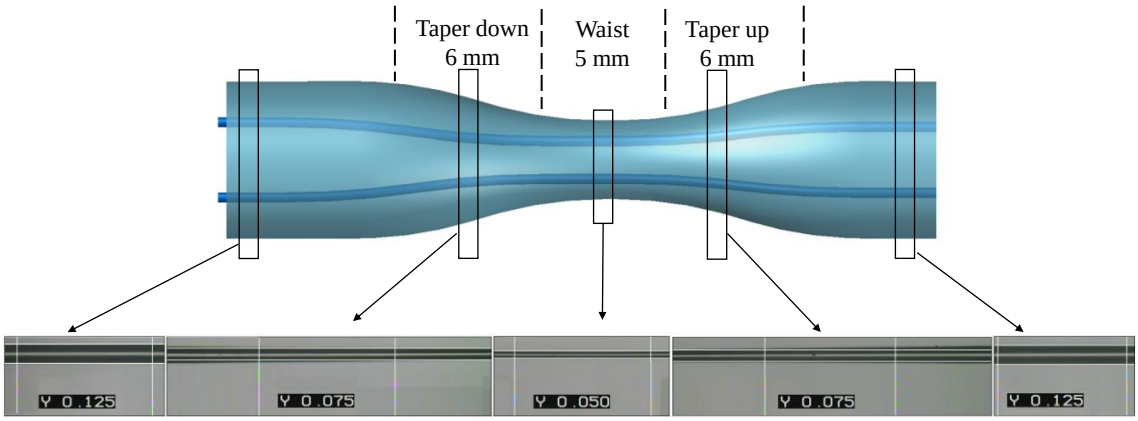

Figure 5-7. Measured profile of the MCF tapering with a microscope (y-measurements shown are expressed in µm).

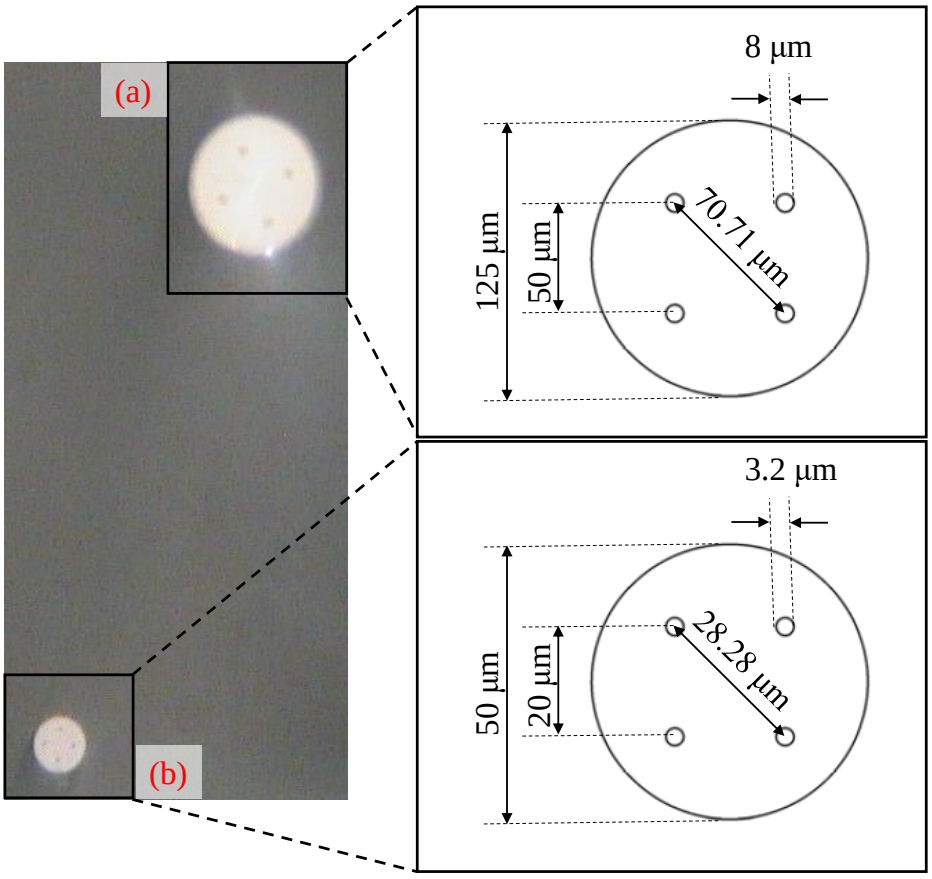

Figure 5-8. MCF cross sections the sections were taken at (a) a non-tapered region and (b) the waist region, both were positioned under the microscope and a single images was taken for comparison.

5.2.4. Experimental coupling of light between the cores of the MCF

The simulations presented in section 5.2, indicate that a 25:25:25:25 coupling ratio of light from one core to all four cores can be achieved at 5.113 mm waist length about a central wavelength of 1553 nm. It should be noted that the simulation considers only the coupling occurring in the waist region (see Figure 5-9). However, coupling of light can start at an earlier point during the tapering down region and may continue through the taper up region. Additionally, the waist length where a specific coupling ratio is achieved depends on the wavelength of the transmitted light, hence for broadband operation will be wavelength dependant (see equations 2.33-2.36). Table 5-3 includes the length where the 25:25:25:25 ratio occurs for wavelengths with ±8 nm separation from the initial wavelength used in the simulations (1553 nm). These wavelengths are of interest for the inscribed FBGs and will be referred in the following paragraphs. According to Table 5-3, the two distant wavelengths (1545 nm and 1561 nm) require a waist length which varies in a range of ± 0.2 mm from the central (1553 nm). Hence, an experimental study were carried out in order to ensure that coupling of light with the tapering parameters reported in 5.2.2 can be achieved.

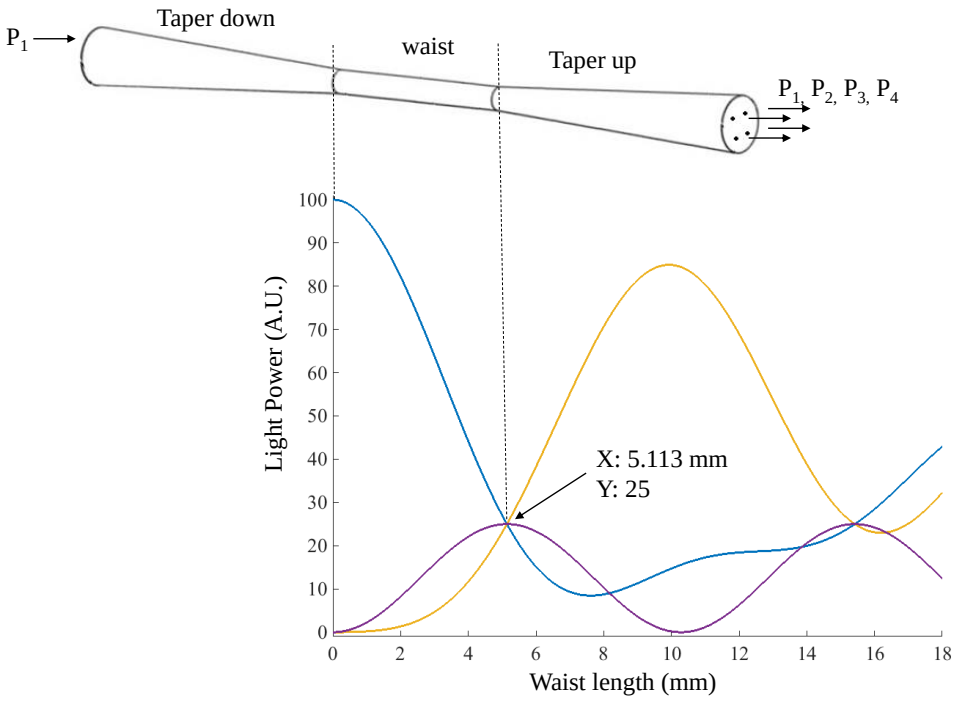

Figure 5-9. Final theoretical simulation on the coupling ratio for the waist length based on 50 μm diameter.

Table 5-3. Waist lengths where a 25:25:25:25 coupling ratio between the four cores of the MCF is achieved for different wavelengths of the transmitted light.

coupling wavelength (nm)	**waist length** (mm)
1545	4.947
1553	5.113
1561	5.155

Two different experiments were conducted in order to observe and measure the power transfer between the cores: Observation was achieved by mounting the MCF under a microscope (*i*), while power measurements were obtained using four photodetectors (*ii*). Both experiments confirmed that, coupling of light between the four cores of the MCF was achieved with the tapering parameters presented in the previous paragraphs. The broadband light source used for these experiments had central wavelength at 1550 nm ± 5 nm.

i. Images taken under a microscope during the tapering procedure

During this experiment one of the cores of the MCF was fusion spliced with a SMF before the tapering procedure. This could be achieved by positioning the MCF into the splicer in a known orientation, using the end view function. Consequently, by moving the SMF along the x or y planes it was possible to align one of the cores of the MCF to the core of the SMF. Figure 5-10 (left) shows a schematic representation of the fibres orientation in the splicer. Figure 5-10 (right) shows a microscope image of the MCF cross section (a) before and (b) after the SMF to MCF splicing. In the first case (a) the cores of the MCF were illuminated with white light in order that their position can be determined. While in the second case (b) red laser light is launched into the SMF demonstrating effective launching into only one core. The cross section confirms that the splicing of one core of the MCF to the SMF has been achieved, since only one core is illuminated with the laser source after the splice.

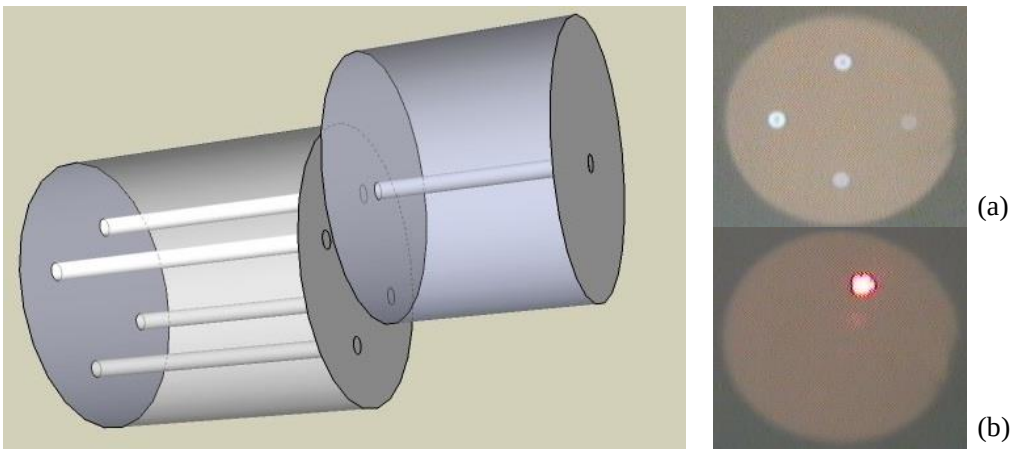

Figure 5-10. LEFT- Schematic diagram of the MCF and SMF orientations in the splicer in order that a core to core fusion splice can be achieved, RIGHT- (a) cross section of the MCF before the splice (cores are illuminated with white light), (b) cross section after the splice (the SMF is illuminated with red laser light), as expected only one core is illuminated.

The tapering of the MCF was performed at a distance (~ 50 cm) from the SMF-MCF splice. During this experiment the free end of the MCF was mounted under a microscope and the SMF fibre was illuminated with a 1550 nm light source. Images of the fibre's cross section were taken during the tapering procedure with a camera operating in the IR region of the optical spectrum. Figure 5-11 shows these images with the first taken before the tapering commenced and the forth being at the end of the procedure. Moreover, images two and three were taken during the procedure where light power transfer between the cores was observed.

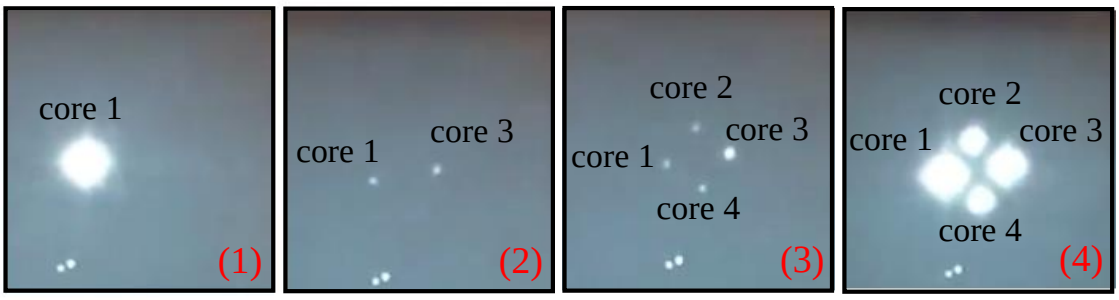

Figure 5-11. Coupling of light (IR, central wavelength 1550 nm) between the four cores of the MCF, (1) before the tapering, (2) and (3) during the tapering process and (4) after the tapering procedure (the two dots on the bottom of each image are produced from the camera in order to establish the position of the recorder image).

ii. Power transfer measured with photodetector

The intensity of the light power transfer from one core of the MCF to the other three was measured with a fan-out device. In this case a section of the MCF was fusion spliced to the silica waveguide fan-out device (paragraph 4.2.1), furthermore the other end of the

MCF was spliced on a SMF (as described earlier). Similarly with the previous case, a 1550 nm light source was coupled to the SMF. The silica waveguide fan-out fibres were connected to photodetectors. Finally, the light intensity measured from the photodetectors was monitored with an oscilloscope during the tapering procedure. Figure 5-12 (a) shows the measured power transfer, while Table 5-4 includes the optical power (in arbitrary units) for the cases before and after tapering and the calculated coupling ratios. However, the measured ratios are not as expected (e.g. 25:25:25:25) this is due to an error of 5 % produced from the losses that are introduced from the fan-out device. Measurements that was done before this experiment showed that the losses of each core/SMF of the silica waveguide fan-out device varied (Insertion losses on: $core\ 1\ = 1.2\ dB$, $core\ 2\ = 1.37\ dB$, $core\ 3\ = 1.93\ dB$ and $core\ 4\ = 1.88\ dB$).

According to Figure 5-12 the total power transfer in all four cores during the 50 -100 seconds drops close to zero. This effect can be attributed to the asymmetry on the shape of the MCF during the tapering process. During the taper fabrication a large angle is produced in the right part of fibre taper (Figure 5-12 (b)). This angle produces high losses [6]. Conversely when the taper up region is being formed (100-120 sec) this taper angle is reducing and the light power recovers.

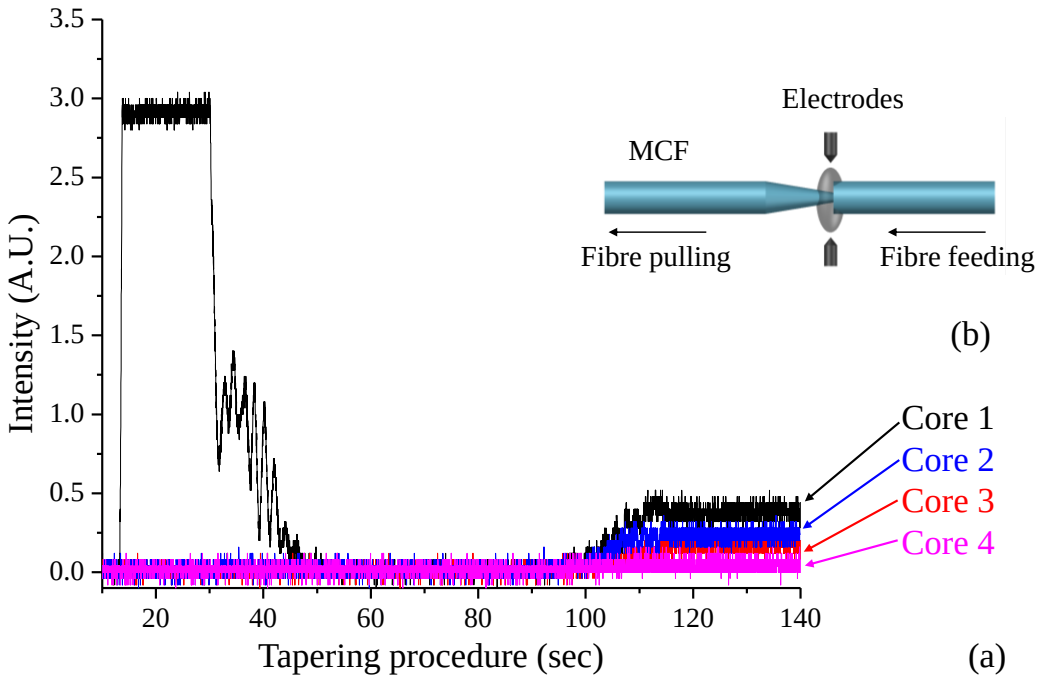

Figure 5-12. (a) Coupling of light from one core of the MCF to all four cores (b) shape of the MCF during the tapering procedure.

Table 5-4. Light intensity before and after the tapering procedure and coupling ratio between the four cores of the MCF.

	Before tapering	**After tapering**	**coupling ratio**
core 1	2.9	0.39	45
core 2	0	0.25	28
core 3	0	0.18	21
core 4	0	0.05	6
Total transmittance: 30%			

5.2.5. Conclusions on the tapering parameters

The section above included a theoretical and an experimental study on coupling of light between the four cores of the MCF. Both show that coupling can be achieved for different tapering parameters. However, it is considered that the most suitable combination of tapering parameters is 6 mm taper down and up lengths and 5 mm waist length. Moreover, for these tapering lengths the most suitable waist diameter is 50 μm. The total duration of the tapering procedure on the MCF depends on the pulling velocity of the fibre. For the chosen velocity of 0.2 μm/ms this duration is 80 seconds. These tapering parameters are used for the fabrication of the MCF curvature sensor with the tapered fibre fan-out device.

5.3. Experimental set up for inscription of individual FBGs

The same experimental set up, described in paragraph 4.1.1 was used for the inscription of FBGs, in order to fabricate the sensors presented in this chapter. However, in this case a mirror after the optical prism intercepted the light in order to guide the UV beam (255.5 nm) to a separate path. On this optical path a bespoke fibre holder was used for individual inscription of FBGs into different cores of the MCF. Individual inscription of FBGs is necessary for the MCF tapered fan-out device Figure 5-2 (b) because the reflectance spectrum of the FBGs in different cores of the MCF has to be in different spectral region in order that overlap be avoided.

5.3.1. Phase masks

Three different phase masks (provided by Ibsen photonics) were used for the individual inscription of FBGs into individual cores of the MCF. The three uniform phase masks were fabricated to generate the +1 and -1 diffraction orders in order the UV interference pattern to be produced.

The phase masks' grating periods (Λ_{FBG}) were chosen based on equations 2.2 and 2.5 for an estimated effective refractive index of the MCF (~1.445):

$$\lambda_{reflected} = 2n_{eff}\Lambda_{FBG} \quad \text{Equation 5.1}$$

$$\Lambda_{FBG} = \frac{\Lambda_{PM}}{2} \quad \text{Equation 5.2}$$

The wavelengths were chosen to avoid overlap of the inscribed FBGs reflectance spectra. For a separation of ~ 8-9 nm FBGs reflectance peak position, the grating pitches (Λ_{FBG}) were calculated to have to differ by ~ 6 nm. Table 5-5 includes the grating pitch of all three phase masks as well are the expected reflectance peak position of the inscribed FBGs into the cores of the MCF.

Table 5-5. Grating pitch and expected reflectance peak position of the inscribed FBGs into the core of the MCF.

phase mask pitch (nm)	**wavelength** (nm)
1066.4	1545
1071.94	1553
1077.47	1561

The phase masks are expensive and fragile optical components. Hence, care needs to be taken to prevent damage. One of the most common causes of damage is during UV exposure. If dust or dirt is on the surface where the UV beam is focused, permanent damage can occur. There are several ways to ensure that this damage is avoided. Frequent cleaning of the phase masks with lens tissues and solvents as well as building the experimental set up in clean rooms are some characteristic solutions.

An experimental technique called Knife edge can determine the focal position of the cylindrical lens prior positioning the phase mask within the FBGs inscription set up. This way the etched surface of the phase mask can be positioned before the focal position of the lens. In this way the UV interference pattern produced from the phase mask is focused in the core of the optical fibre (positioned just after the phase mask). The following section describes the knife edge technique realized on the FBGs inscription set up.

5.3.2. Knife edge technique

The cylindrical lens is an essential optical component to the FBG inscription set up. The main purpose of the lens is to condense/focus the UV beam in one axis. Thus, the UV beam become a plane wave front along the phase mask's etched surface [8]. The focal position of the cylindrical lens was determined with the knife edge technique [9]. Figure 5-13 shows a schematic diagram of the experimental set up used for this technique. A power meter was positioned on the UV beam path after the cylindrical lens. The intensity power of the UV beam was measured by moving the knife edge on the y-axis in different positions along the beam path (z-axis) (Figure 5-14).

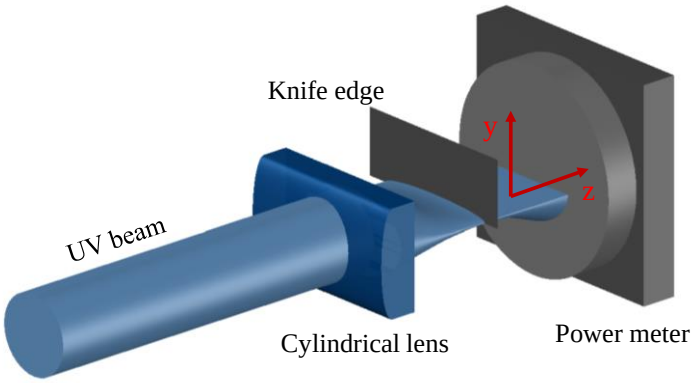

Figure 5-13. Knife edge technique experimental set up, for determination of the focal position of the UV beam.

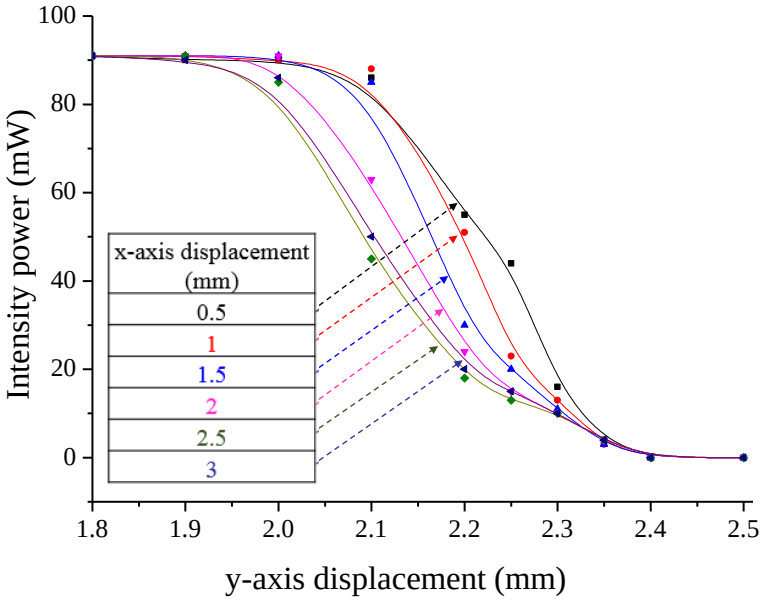

Figure 5-14. Measured intensity power at different positions along the UV beam path.

The beam profile can be represented at each position along the beam path by differentiating the intensity power which was measured at different y-positions [9, 10]. Figure 5-15 (a) shows the differential curve produced from the fitted data taken for the position $x = 2\ mm$. Finally, the full width at half maximum (FWHM) of the curves at different positions along the beam path provide an estimation of the focal position along the UV beam. The measured FWHM for each position along the x-axis and a parabolic fitted curve are shown in Figure 5-15 (b).

The focal position of the UV beam was determined to be at position ~1.75 mm, along the beam path. This is important experimental information, since the position of the phase masks and the fibre holder can be established.

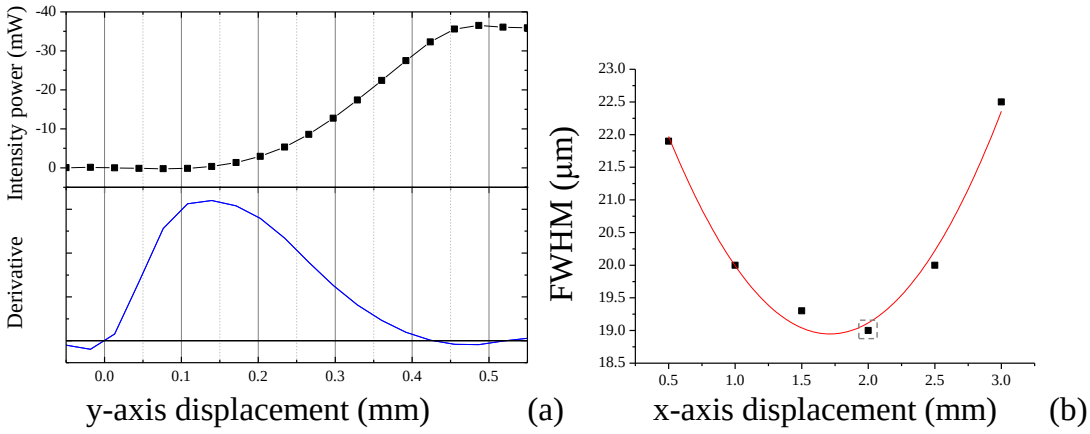

Figure 5-15. (a) Fitted data and differential curve of the measured intensity power at the position x=2 mm (b) measured FWHM for each positions along the x-axis and a fitted curve to determine the focal position of the UV beam, (dashed) the calculated FWHM from the derivative shown in (a).

5.3.3. Fibre holder and orientation of the MCF on the UV beam

Inscription of individual FBGs into discrete cores of the MCF was achieved with a bespoke fibre holder. Appendix [8] includes the designs of the fibre and the phase masks holders that were fabricated. Parts were adapted from commercially available mechanical parts where possible. The fibre holder enabled a 180° controllable rotation of the MCF. Moreover, this holder allowed displacement of the fibre along the x and y planes. Therefore the MCF could be mounted into a specific orientation at a certain position within the UV interference pattern produced by the phase masks. Finally, the cross section of the MCF was monitored with a microscope camera during its rotation and displacement to aid the rotational alignment. Figure 5-16 shows an image of the actual experimental set up and the fibre holder (a), as well as a schematic diagram (b).

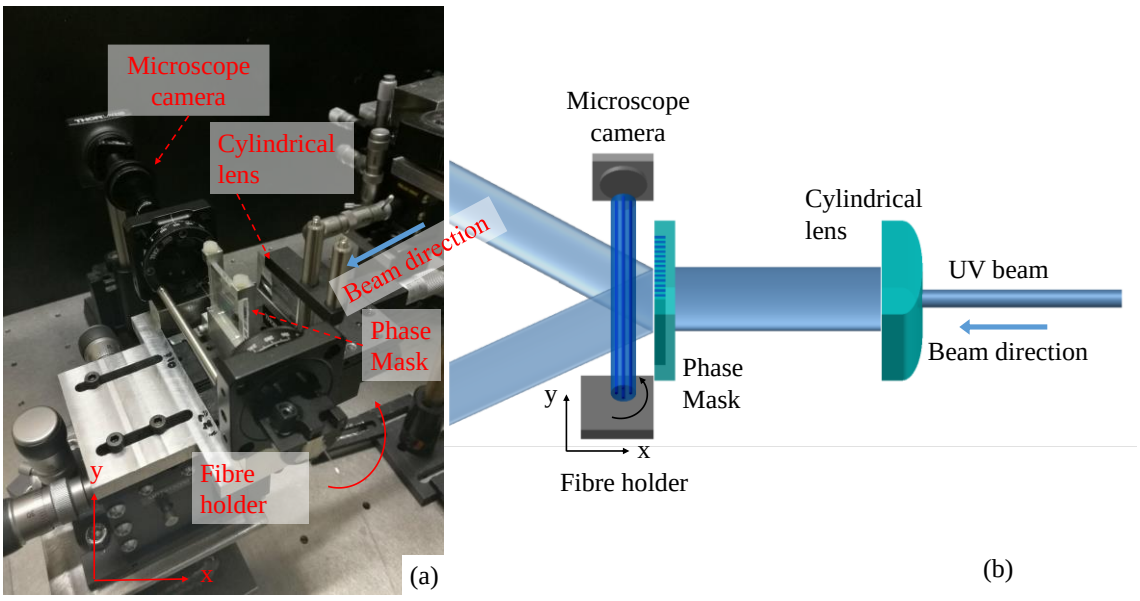

Figure 5-16. Bespoke fibre holder for inscription of individual FBGs (a) actual experimental set up, (b) schematic diagram.

Proper orientation of the MCF with respect to the UV beam is essential for inscription of individual FBGs into the cores of the fibre. This orientation is shown in Figure 5-17 (a), where one core of the MCF is positioned just below the UV interference pattern produced from the phase mask. Consequently, inscription of the FBG in this core can be achieved by adjusting the height (*y-plane*) of the MCF and by bringing it in to the focal position of the cylindrical lens (*x-plane*).

The second FBG can be inscribed by replacing the phase mask and keeping the same orientation of the MCF. In this case the MCF has to be above the UV interference pattern prior to exposure. Therefore, by adjusting again the height (in the opposite direction this time) inscription of a FBG into the opposite core (core 3) can be achieved.

The third FBG can be inscribed into one of the remaining cores (cores 2 or 4) using the final phase mask. In this case a 90° rotation of the fibre is required. Similarly to the previous cases, by adjusting the MCF above or below the UV interference pattern inscription can be achieved. This experimental set up can provide inscription of a fourth different FBG into the final remaining core of the MCF. However, since only three FBGs are required for the fabrication of a MCF curvature sensor, the forth FBG inscription was not carried out.

Figure 5-17 (b) shows an image taken from the microscope camera during the exposure of core 1 into the UV interference pattern. In this case the light emitted from core 1 is due to fluorescence emission associated with the UV exposure.

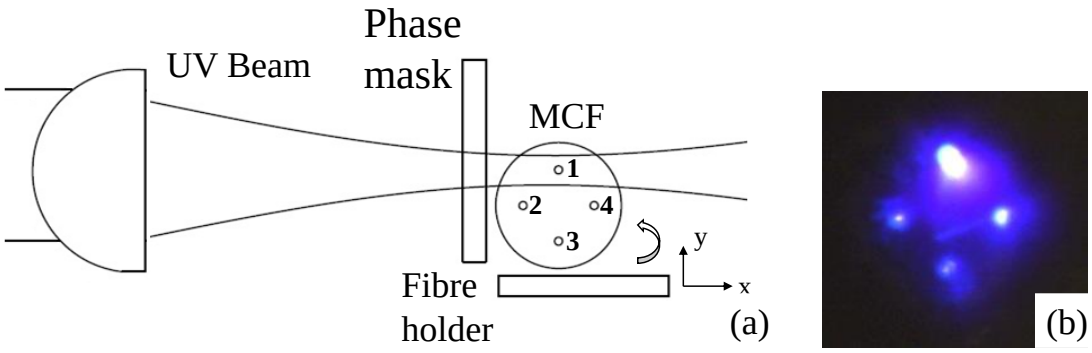

Figure 5-17. (a) Orientation of the MCF during FBG inscription into core 1, (b) Cross section of the MCF taken from the microscope camera (light from one is fluorescence emission associated to the UV exposure).

5.4. Fabrication of a MCF curvature sensor with a fibre tapered fan-out

The fabrication and performance of three different MCF curvature sensors are reported in this section. The first sensor contained two discrete inscribed FBGs, while the second and the third had three discrete inscribed FBGs. Deflection experiments were performed on all three sensors and their response is presented. These are in good agreement with expectations.

5.4.1. First sensor: Two FBGs sensor inscribed in MCF

The MCF curvature sensor presented in this section was fabricated with two discrete FBGs written into two different cores of the MCF. The reflection spectrum was collected through a single SMF spliced onto one core of the MCF and using the taper to couple light from one core to all four. Therefore, interrogation of both FBGs was achieved via a single conventional fibre connecting lead.

i. FBG characteristics

The inscription of the individual Bragg gratings into different cores of the MCF was monitored in real time with the use of a fan-out device. The device aided the fabrication of the FBGs since all MCF cores can be monitored independently and simultaneously.

The first attempt aimed to inscribe the FBGs in two opposite cores of the MCF (cores 2 and 4 in Figure 5-17). This was achieved with the first and third phase masks (presented in 5.3.1). Figure 5-18 shows the inscribed FBGs spectra, the sinusoidal background are interference effects produced from the fan-out device (detailed studies are presented in

chapter 4). Both gratings were inscribed at the same point along the MCF. The wavelength peak position of the FBGs was 1543.7 nm and 1552.25 nm on core 2 and core 4 respectively. Moreover, data in Figure 5-18 shows that cores 1 and 3 are not affected from the inscription.

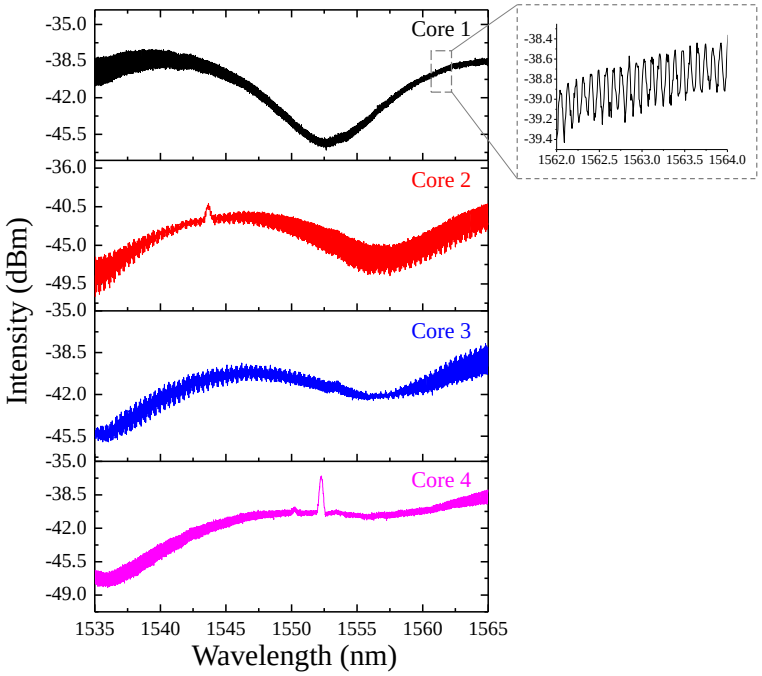

Figure 5-18. Two different FBGs inscribed into cores 2 and 4 of the MCF, fringes presented on these spectra (see zoomed in region) are due to interference effects associated with the silica waveguide fan-out device (detailed studies are presented in chapter 4).

ii. Splicing of the MCF onto a SMF

After fabrication of the FBGs the MCF section was separated from the fan-out device and fusion spliced on an SMF as described in section 5.2.4. In this case an additional effect was observed. One of the two inscribed FBGs is expected to be monitored when one core of the MCF is spliced onto a SMF. However, three reflected wavelengths (Figure 5-19) could be seen on the reflectance spectrum collected from the SMF connected to the interrogator (SM125). One of the peaks was at the expected reflection wavelength of the inscribed FBG into core 4 (1552.24 nm). Nevertheless, the other two peaks (1550.2 nm and 1548.2 nm), are not in the expected range of the FBG reflected wavelengths according to the phase masks grating period (Table 5-5). Moreover, additional ripples were observed on the reflectance spectrum.

These peaks can be considered as FBGs inscribed in the cladding region surrounding the forth core of the MCF [11]. Higher order cladding modes might exist in the transmitted and reflected light. Moreover, since the MCF is relatively short the cladding modes are not naturally attenuated. Coupling to cladding modes may arise due to a misalignment of the cores (MCF-SMF) at the splicing point [12]. One way to ensure that these cladding modes are due to the MCF-SMF splice is by introducing increased cladding mode attenuation along the MCF after the splicing. A cladding mode stripper (tight bend ~ 1 cm, radius) was introduced on the MCF and as it is shown in Figure 5-20 the two peaks are eliminated and the remaining FBG has a reflectance peak wavelength in the expected range, according to the pitch of the phase mask that was used for the inscription (1071.94 nm, Table 5-5). Results presented after this section are obtained with a cladding mode stripper applied to the fibre.

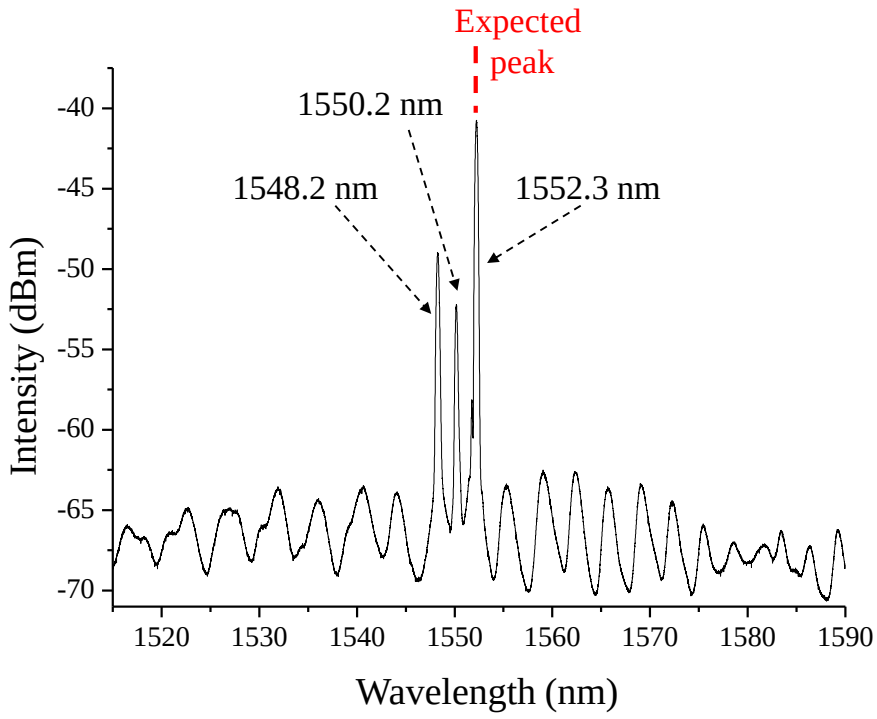

Figure 5-19. Reflectance spectrum monitored with SM 125 interrogator when one core of the MCF is fusion spliced to a SMF.

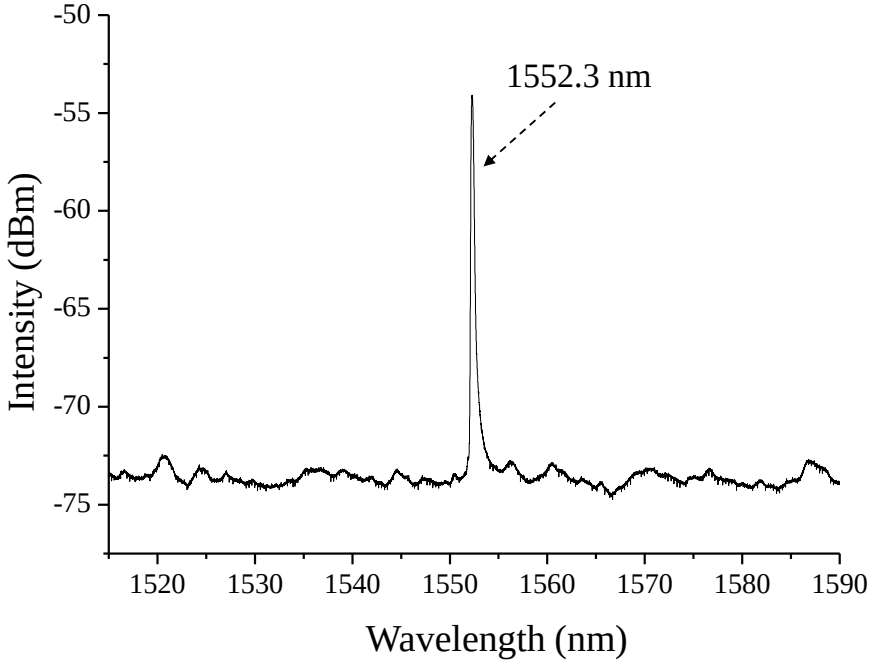

Figure 5-20. Reflectance spectrum monitored with SM 125 interrogator when one core of the MCF is fusion spliced to a SMF and a cladding mode stripper is applied on the MCF (FWHM: 0.27 nm).

iii. Tapering procedure

The reflection spectra of the inscribed FBGs were monitored during the tapering of the MCF (tapering parameters used are determined in 5.2.5), using a commercial SM 125 interrogator connected to the MCF via the SMF. Figure 5-21 shows the spectra recorded every ~1 second with the first one (red) being at 0 seconds and the last one (blue), being at 80 seconds when the tapering procedure has been completed. The two FBGs reflectance spectra inscribed into two different cores of the MCF were observed after the first 60 seconds of the tapering procedure. Additionally, Figure 5-22 shows the reflectance spectrum taken after the completion of the tapering procedure where the two expected peak positions of the inscribed wavelengths can be determined.

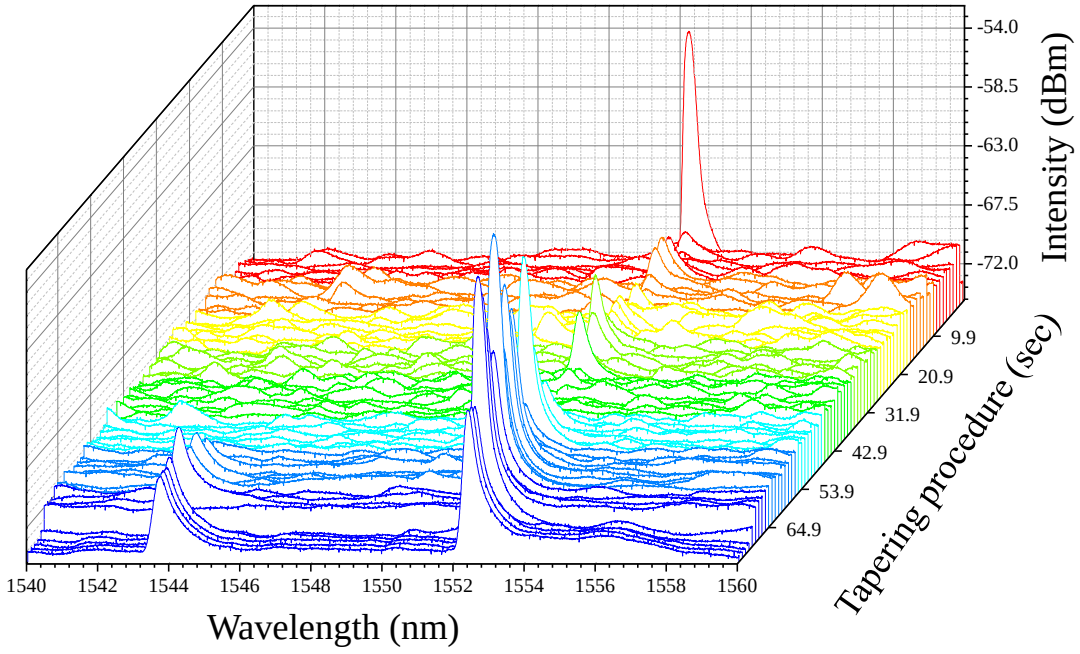

Figure 5-21. Reflectance spectra monitored through the SMF splice on one core of the MCF during the tapering procedure of the MCF.

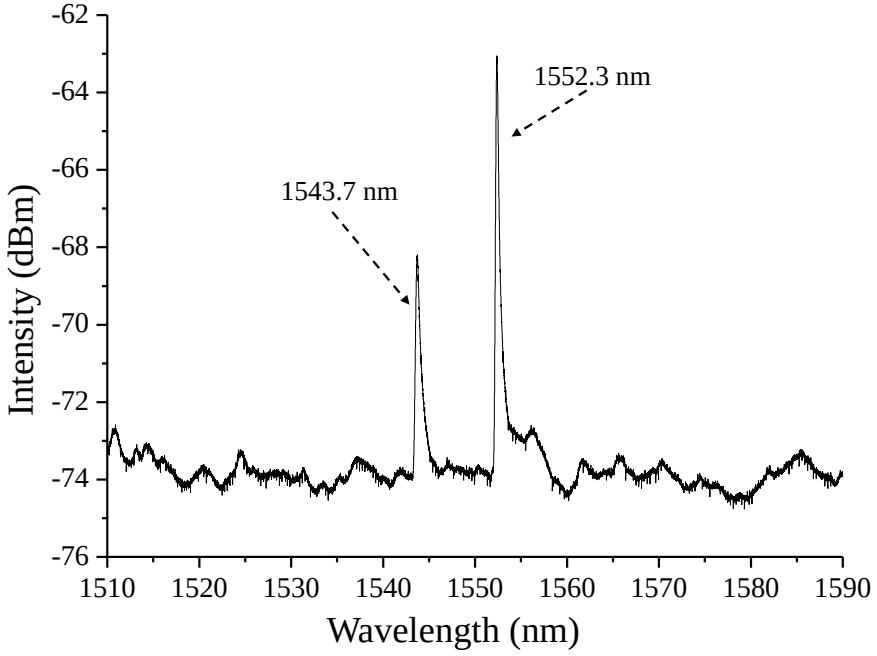

Figure 5-22. Final spectrum after the tapering procedure, the two inscribed FBGs in different cores of the MCF were able to be monitored via a single SMF (FWHM: (first peak) 0.71 nm (second peak) 0.305 nm).

iv. Deflection of the MCF

The final step in the fabrication of this sensor was to fix the MCF at a point in order to form a cantilever geometry. This procedure is presented in section 4.2.3. Once completed, deflection experiments using the MCF could be performed.

The orientation of the MCF in respect to the deflection is shown in Figure 5-23. The response of the two FBGs were monitored as a deflection up to 5 mm was applied to the end of the fibre. The cantilever length was 60 mm and the position of the FBGs was estimated to be 15 ± 1 mm away from the fixed point and determined with a localised heat source. The wavelength peak position of the FBGs spectra was monitored for ~ 60 seconds with 1 mm increment (see Figure 5-24). The reflected peak position of the FBG inscribed into core 2 is increasing upon deflection, since it is being stretched. Whereas, the wavelength peak position of the FBG, inscribed into the compressed core 4, is decreasing, due to compression of this side of fibre.

Figure 5-24 includes the calculated noise at each step of deflection (grey font). The noise determined as the half value of the variant between highest and the lowest value of the reflected wavelength ($(\lambda_{max} - \lambda_{min})/2$) (Appendix [4]). The average value of the noise for the FBG in core two is 0.0133 nm, while for the FBG in core 4 is 0.0057 nm (this is equivalent to 0.08 mm and 0.03 mm actual deflection of the fibre end respectively).

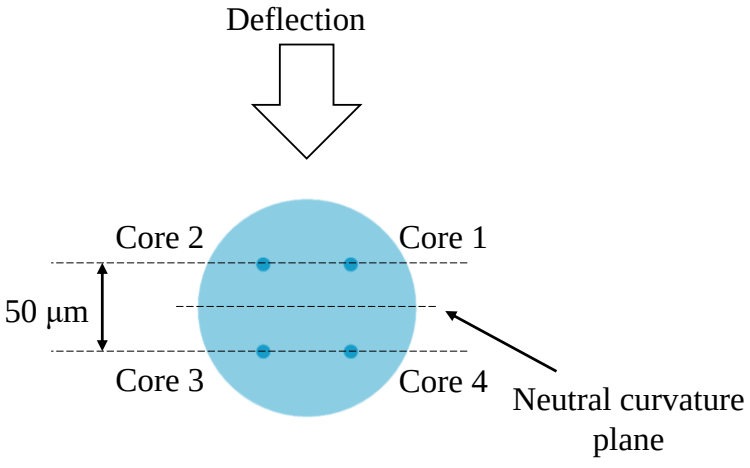

Figure 5-23. Orientation of deflection of the MCF curvature sensor with the fibre tapered fan-out device.

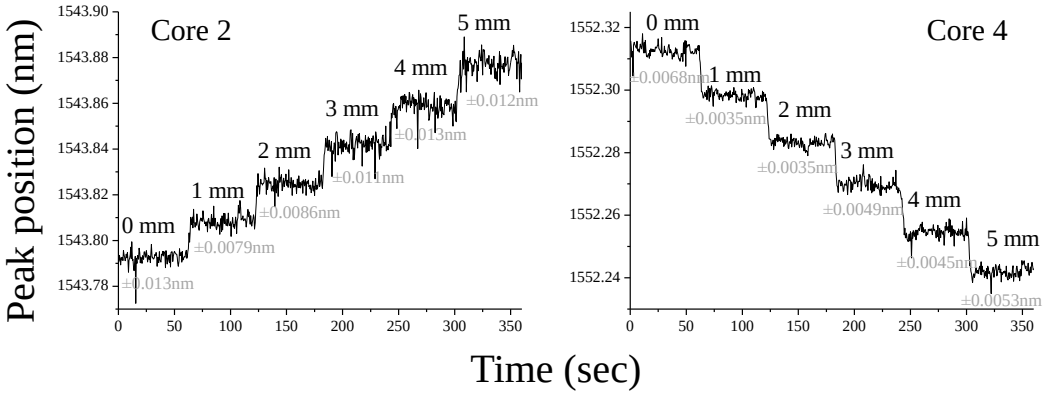

Figure 5-24. Response of the two FBGs inscribed into cores 2 and 4 with different phase masks (grey coloured font numbers are the noise levels determined as the half value of the variant between highest and the lowest value of the reflected wavelength).

Using the following equations (reviewed in Chapter 2, equations 2.15, 2.23 and 2.26), an estimation of the expected wavelength shift for one millimetre of deflection can be calculated for each FBG separately:

$$\frac{\Delta\lambda_{reflected}}{\Delta\varepsilon} = 1.032\ pm/\mu\varepsilon \qquad \text{Equation 5. 3}$$

$$\Delta\varepsilon = \frac{d}{R} \qquad \text{Equation 5. 4}$$

$$\kappa = \frac{1}{R} = \frac{3\,(l-z)}{l^3}\,\nu_l \qquad \text{Equation 5. 5}$$

In this case the distance of the plane where the FBG lies with the neutral plane is d=25 μm, l is the cantilever length (60 mm), z is the distance of the inscribed FBG from the fixed point (15 ± 1 mm), and $\frac{1}{R}$ is the curvature. Hence, the calculated wavelength shift was $\Delta\lambda_{reflected}$ = 0.0161 nm for one millimetre of deflection.

The average value of the wavelength shifts between two steps of deflection with 1 mm separation (0-1 mm, 1-2 mm, 2-3 mm, 3-4 mm and 4-5 mm) calculated for the FBG inscribed in core 2 is 0.01695 nm. While the same value for the inscribed FBG in core 4 is 0.0151 nm. Both values are close to the predicted value from the theory (0.0161 nm).

A separate analysis on these data can be produced by considering the differential wavelength shift of the two inscribed FBGs. An average value of the FBGs reflected peak positions at the different deflection increments was calculated (MatLab™ script,

Appendix [5]) and the wavelength shift between the two FBGs was determined. Using the average value of the FBGs strain sensitivity ($\frac{\Delta\lambda_{reflected}}{\Delta\varepsilon}$) calculated in paragraph 4.8.1 the separation of the planes, in which core 2 and 4 lie was calculated.

According to Equation 5. 5, the gradient of the graph produced from the curvature versus the strain shift coincides with the planes separation (Figure 5-25). The linear fit of this graph has gradient $m = 51.07$ μm, which is close to the actual value (50 μm) of the planes separation on which the cores are lying. Errors can be attributed to slight misalignment of the MCF from that shown in Figure 5-23, as well as uncertainty on the exact position of the inscribed FBGs.

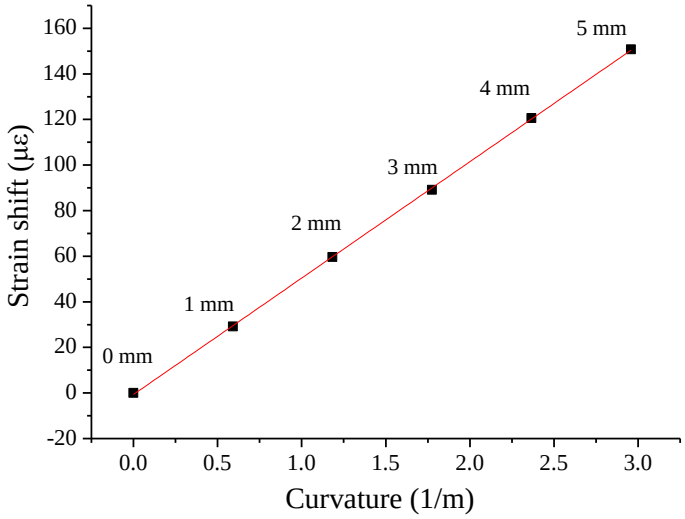

Figure 5-25. Experimental data and best fit for the calculation of the cores separation of the cores using the FBG inscribed into cores 2 and 4 and a MCF tapered fan-out device.

5.4.2. Second sensor: Three FBGs inscribed in MCF

Fabrication of a MCF curvature sensor with three discrete FBGs was achieved. The same procedure described in the previous sections (5.3.3) was followed to realise this. All three FBGs were monitored through the SMF fibre after the tapering procedure along the MCF.

i. Inscription of the FBGs

Inscription of three discrete FBGs was achieved with the three phase masks reported in 5.3.1. The MCF section where the FBGs were inscribed was spliced to a fan-out device. Figure 5-26 shows the FBGs reflection spectra of all four cores of the MCF. Each core

was exposed to the UV interference patterns produced from the phase masks as described in paragraph 5.4.2. The FBGs were inscribed as followed: (a) inscription onto core 1 of the first FBG with reflected wavelength peak position at ~ 1545 nm (first phase mask), (b) inscription of the second FBG into core 2, with reflected wavelength peak position at ~ 1552 nm (second phase mask) and finally (c) the third FBG was inscribed into core 3, with reflected wavelength peak position at ~ 1560 nm.

Reflection spectra were collected through the fan-out device (for all four cores of the MCF) simultaneously to inscription. Similarly, to the previous case, the fringes that present in the background (see insert) of the FBGs reflectance spectra are due to the silica waveguide fan-out device (see chapter 4). Despite the fact that core 4 was not intended to be exposed to any UV interference pattern, one FBG appeared (with reflected wavelength peak position ~ 1545 nm). It is suggested that this FBG might affect the performance of the MCF curvature sensor, hence a detailed study into this will be presented in the following section.

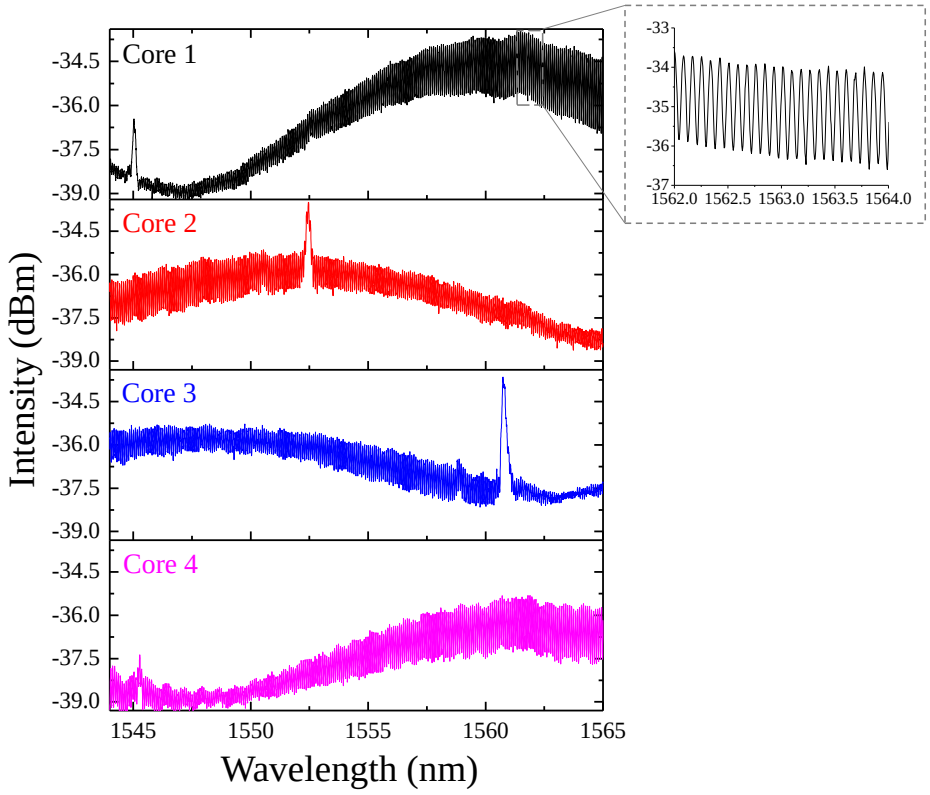

Figure 5-26. FBGs reflectance spectra inscribed individually at each core of the MCF, (zoomed insert) fringes are due to interference effects produced in the silica waveguide fan-out device (see chapter 4).

ii. Analysis on the peak position of the FBGs

The spectra of the two FBGs inscribed into core 1 and 4 are expected to overlap after the tapering procedure. Therefore, the reflectance spectrum of the FBG inscribed at the wavelength ~ 1545 nm will incorporate a component from both core 1 and 4. In this case, the performance of the FBG inscribed into core 1 will be examined, in the presence of the smaller unwanted FBG in core 4.

A study on the FBG reflected wavelength peak positon was developed. In this study, a MatLab™ script [Appendix 9] was produced in order to compare two different cases: (a) the wavelength peak position of the FBG inscribed into core 1 when no other FBG exists ("ideal" case) and (b) the wavelength peak position of the FBG inscribed into core 1 when another FBG exists in the background ("actual" case). In the last case the two FBGs spectra were added together.

The analysis included a Gaussian fit on the actual FBGs reflectance spectra inscribed into core 1 and 4 (see Figure 5-27). Figure 5-27 shows the graph produced from the MatLab™ script for the "ideal" case were only one FBG inscribed into core 1 exists in the wavelength range 1544.5 -1445.5 nm.

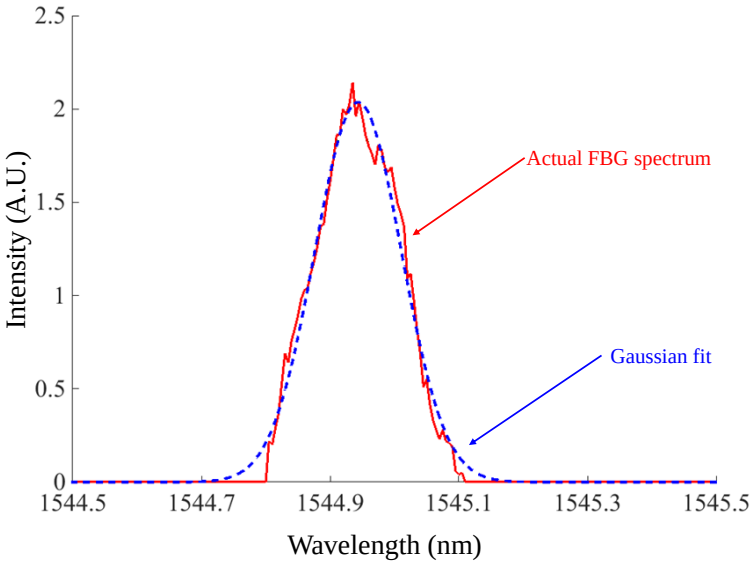

Figure 5-27. FBG Peak position analysis using the Gaussian fitting approach [see Appendix 9].

The same analysis was performed for the actual case were two FBGs exist at the same wavelength range. Moreover, in this case the reflectance spectrum of the FBG inscribed into core 1 was shifted along the wavelength range (1544.5 – 1545.5 nm) with 0.02 nm

increment (see Figure 5-28 (a)). Hence the effect of FBGs spectra overlapping (summed spectrum, FBG inscribed into core 1 summed with the FBG inscribed into core 4) could be studied. The wavelength peak position of the summed spectrum was determined similarly to the previous case with a Gaussian fit. Figure 5-28 (b) shows the Gaussian fittings of the "ideal" case (FBG 1) and the actual (FBG 1 + FBG 4).

Figure 5-28 (b) shows that the two fittings are separated at the overlapping region. Nevertheless, the peak position variations between the "ideal" and "actual" cases are comparable to the system noise. MatLab™ simulations show that the peak position variations is ± 0.0075 nm. Figure 5-29 (a) shows the calculated peak positions of the FBGs inscribed into each individual core (1 and 4), as well as the peak position of the summed spectrum (FBG 1 + FBG 4). Moreover, the wavelength peak position of the FBG inscribed into core 4 was also calculated. This remained at a constant value since no shift on its reflectance spectrum was applied (see Figure 5-29). Finally, the wavelength peak position difference between the "ideal" and "actual" case is shown in Figure 5-29 (b).

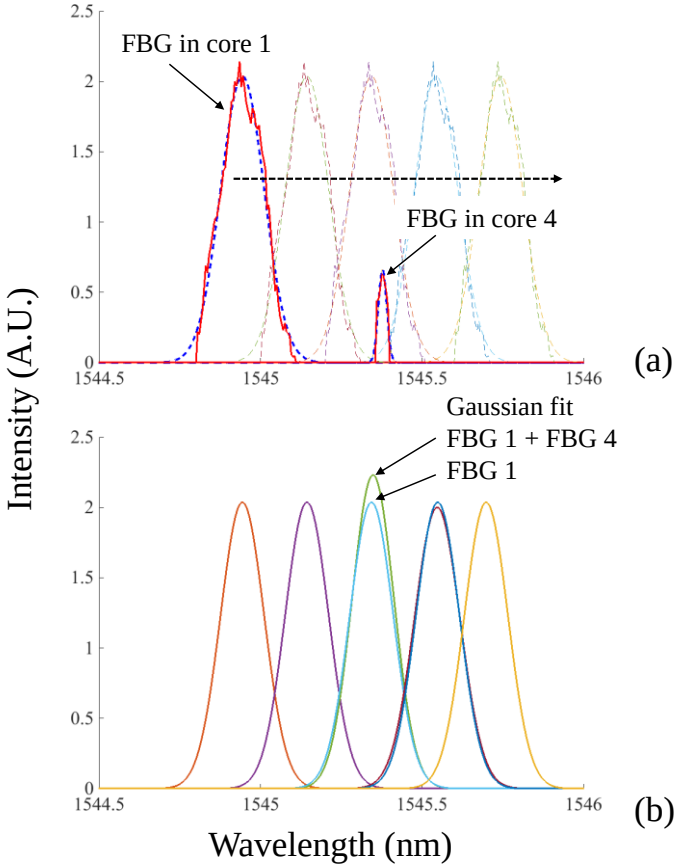

Figure 5-28. (a) FBGs in core 1 and 4 spectra overlapping with the shift of FBG 1 (b) Gaussian fit of the summed spectra (FBG 1 + FBG 4) and ideal case (FBG 1).

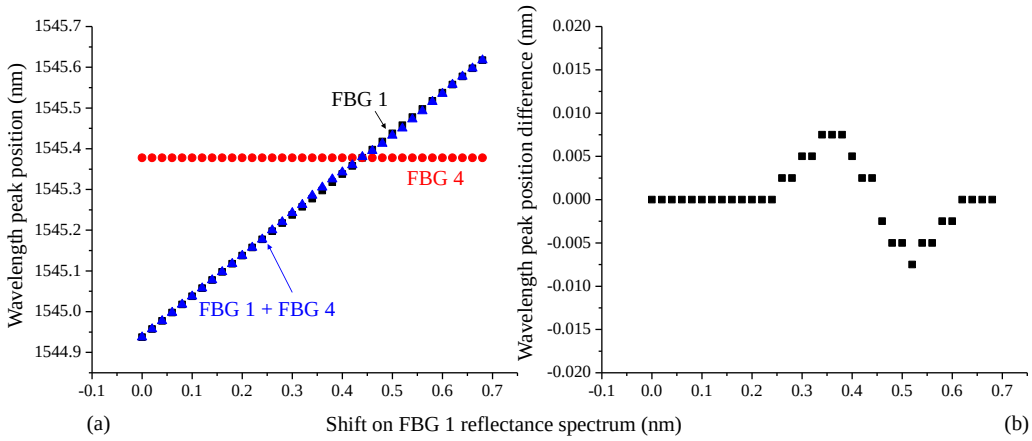

Figure 5-29. (a) Calculated peak positions of the reflectance spectra (FBG1 (square), FBG 4 (circle), FBG 1 + FBG 4 (triangle)) and (b) difference between the wavelength peak positions ("ideal"-"actual" case).

The theoretical and mathematical analysis using the actual spectra of the inscribed FBGs showed that the maximum error that can be introduced in the measurements is ± 0.0075 nm. This is converted to a 0.16 mm of actual deflection of the MCF (Equation 5. 3Equation 5. 4 and Equation 5. 5). Hence, the overlap has minor effect on the results. This is mainly due to the fact that the "unwanted" FBG (inscribed into core 4) has significantly lower reflectivity in comparison to the actual (FBG 1). Therefore it is considered that the performance of the MCF curvature sensor with the FBGs presented in section 5.3.2i will be largely unaffected by this parasitic FBG.

iii. Splicing and tapering procedure

The fabrication of this sensor included a splicing of one core of the MCF with a SMF, similarly to previous cases. The reflectance spectrum collected after the splicing is shown in Figure 5-30 (a). The additional peaks and ripples due to cladding effects are again observed. A cladding mode stripper was applied to the MCF in order to eliminate any transmittance of cladding modes shown in Figure 5-30 (b). Then, the tapering procedure was performed with the parameters described in 5.2.5. Coupling of light between the cores of the MCF was observed and the reflectance spectra of all three FBGs were recorded (Figure 5-31). The spectrum after the tapering procedure is shown in Figure 5-30 (c), where all three expected FBGs are present with additional ripples. Hence, the final spectrum is shown in Figure 5-30(d) with a cladding mode stripper. In this case the ripples are eliminated.

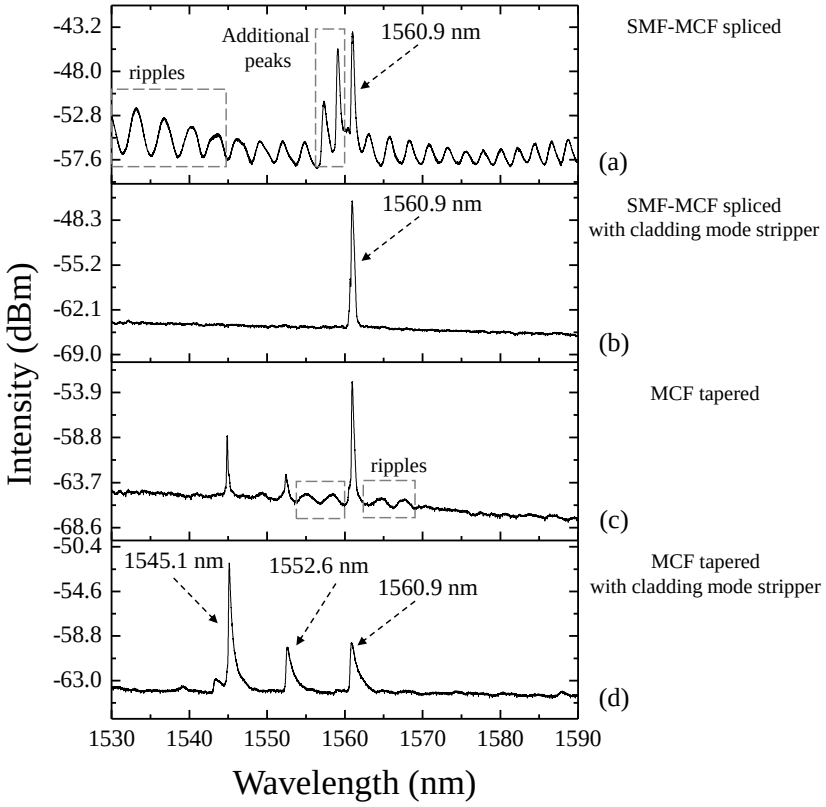

Figure 5-30. FBGs Reflectance spectra collected from the SMF (a) after the SMF-MCF splicing, (b) with the cladding mode stripper, and (c) after MCF tapering (d) with the cladding mode stripper (FWHM: (first peak) 0.235 nm, (second peak) 1.43 nm, (third peak) 1.3 nm).

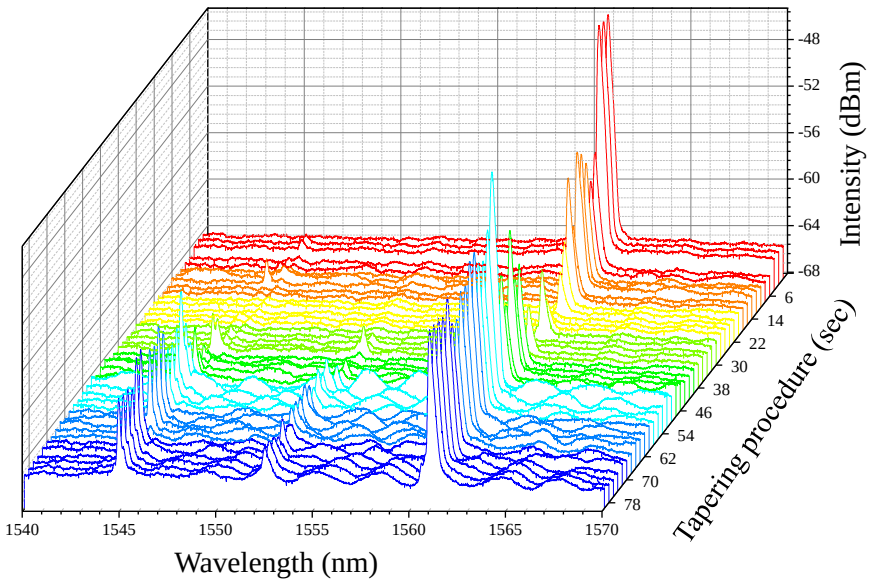

Figure 5-31. Reflectance spectrum collected from the SMF spliced on the MCF during the tapering procedure.

iv. Deflection of the MCF sensor

The fabrication of the MCF cantilever geometry was performed as described in paragraph 4.2.3. Hence, deflection experiments with the MCF curvature sensor could be performed. The peak wavelength positions of the inscribed FBGs into the cores were monitored through the single SMF connected to the interrogator (SM 125). Deflection was performed in two orientations perpendicular to each other to demonstrate 2D operation. Figure 5-32 shows a schematic diagram of the two directions of deflection in regards to the MCF cross section.

Upon deflection in direction 1 (Figure 5-32), the FBGs inscribed into cores 2 and 3 are stretched, hence an increment on the FBGs peak wavelength position is expected. Similarly core 1 is compressed, therefore a decrease on the wavelength peak position this FBG is expected. This is in agreement with the graphs presented in Figure 5-33, where a 5 mm overall deflection of the MCF with 1 mm increment is performed. The reflected wavelength peak positions of the three FBGs was recorded for 60 seconds in each deflection position (0-1 mm). The same deflection was applied upon direction 2 and the three FBGs had the expected response upon deflection on direction 2.

Figure 5-33 also includes the noise levels ($(\lambda_{max} - \lambda_{min})/2$) (Appendix [4])) of the FBG wavelength peak positions for each step of deflection (grey font numbers). These are in average 0.0057 nm for FBG 1, 0.0107 nm for FBG 2 and 0.0055 nm for FBG 3.

The distance of the FBGs from the fixed point for this sensor was $5\ mm\ \pm 1\ mm$ and the cantilever length was $l = 55\ mm$. This means that the expected wavelength shift for each individual FBG upon 1 mm deflection of the MCF is expected to be 0.0233 nm (using equations 5. 3, 5. 4 and 5. 5). This is in agreement with the data presented in Figure 5-33, where the wavelength shift of the individual FBGs for deflection steps with 1 mm difference is in average 0.0218 nm for FBG 1, 0.0237 nm for FBG 2 and 0.0225 nm for FBG3.

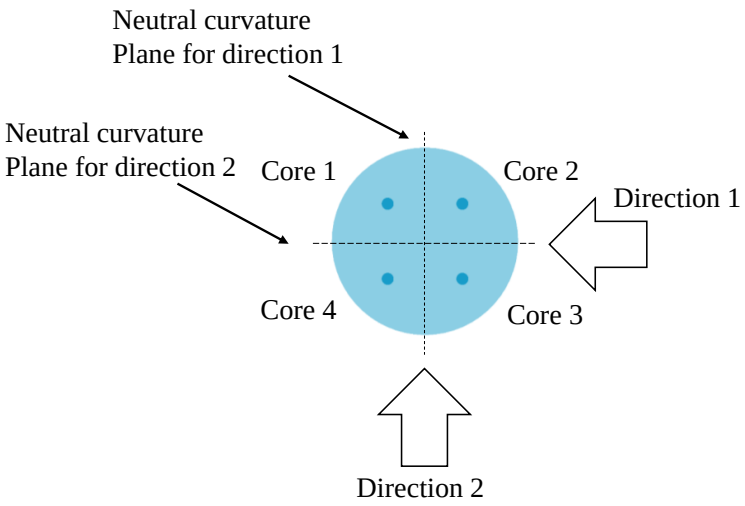

Figure 5-32. The two directions of deflection applied on the MCF.

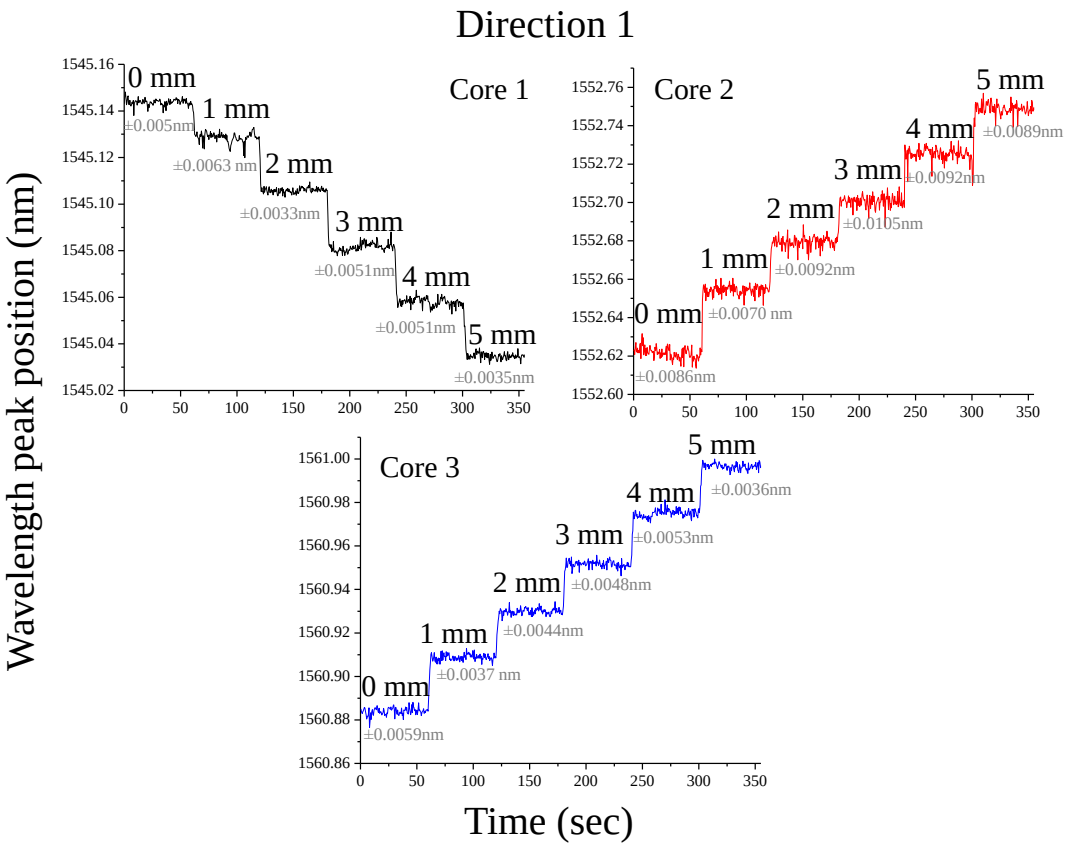

Figure 5-33. FBGs response upon linear deflection in direction 1 (grey coloured font numbers are the noise levels at each step of deflection).

v. FBGs differential strain sensitivity

An average value of the reflected wavelength peak position, at each deflection point, was calculated (similarly to the previous cases) with the MatLab™ script presented in Appendix [5]. The differential strain sensitivity ($\Delta\lambda_{reflected}/\Delta\varepsilon$, $[pm/\mu\varepsilon]$) of the

inscribed FBGs was calculated using their reflected wavelength response upon the two directions of deflection. Hence, the gradients of the graphs produced from the wavelength shift versus the strain shift provide the differential strain sensitivity. Moreover the strain shift can be calculated for each step of deflection according to equations Equation 5. 3,Equation 5. 4 Equation 5. 5.

In the case of deflection upon the two directions shown in Figure 5-32, the actual differential strain sensitivity of the inscribed FBGs can be calculated from the FBGs pairs which lie in separate planes and their distance is $d = 50\ \mu m$ (core separation). Table 5-6 includes the plane separation of all possible FBGs pairs for the two directions.

Figure 5-34 shows the FBGs wavelength shift versus the strain shift upon deflection for the three core pairs presented in Table 5-6. The levels of noise on the wavelength shift between the inscribed FBGs (core pairs) for this sensor are in average ~ 0.015 nm (in actual fibre deflection ±0.03 mm). The calculated gradients are presented in Table 5-7. The gradients of core pairs 2-3 and 1-2 are expected to be zero for directions of deflection 1 and 2 respectively. The difference from the actual gradients can be attributed to the error of the exact position of the FBG from the fixed point (±1 mm) and to a slight rotation of the MCF from the ideal position (Figure 5-32). This is converted to a ± 5 μm error on the plane separation (d) according to equationsEquation 5. 3,Equation 5. 4Equation 5. 5 for the first direction of deflection. While for the second direction of deflection the same error is ± 2.5 μm.

Table 5-6. Planes of curvature separation for the two directions of deflection.

core pairs	Direction 1	Direction 2
	separation of the planes of curvature (μm)	
core 1-core 2	**50**	0
core 1-core 3	**50**	**50**
core 2-core 3	0	**50**

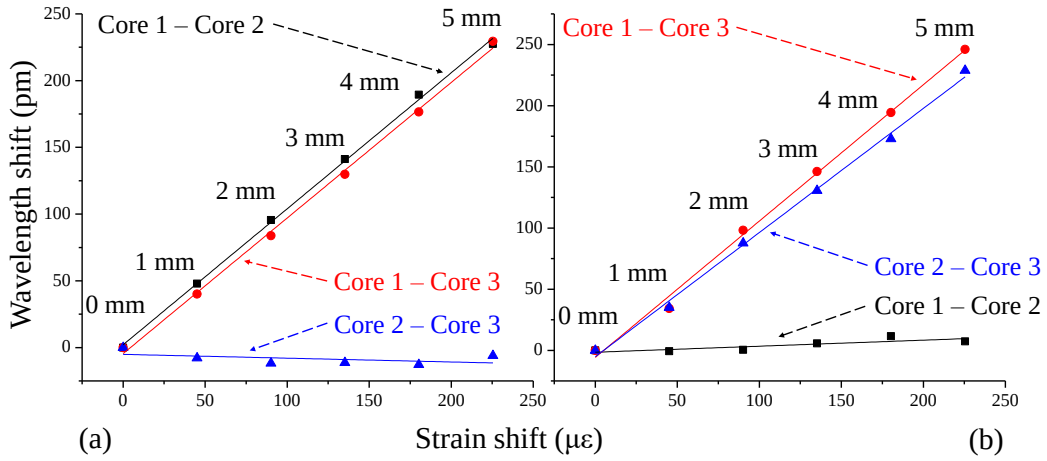

Figure 5-34. Wavelength shift vs strain shift for the calculation of the differential strain sensitivity of the inscribed FBGs (a) for the first orientation (b) for the second orientation.

Table 5-7. Differential strain sensitivity calculated from the FBGs response due to deflection of the MCF in the two specific directions.

	Gradients / Differential strain sensitivity $(\frac{\Delta\lambda_B}{\Delta\varepsilon})$ [pm/μstrain]		
	core 1 - core 2	core 1 - core 3	core 2 - core 3
orientation 1	**1.01882**	**1.01566**	-0.02852
orientation 2	0.04935	**1.11458**	**1.01452**

The average value of the differential strain sensitivity determined from the gradients is 1.041 ± 0.05 $[pm/\mu\varepsilon]$. This value is in the expected range for FBGs operating at a wavelength range around 1550 nm [13, 14]. Additionally, the crosstalk between the two orientations of deflection is less than 5 %.

5.4.3. Third sensor: Three FBGs inscribed in an MCF

The last MCF curvature sensor fabricated had three discrete FBGs inscribed into three different cores of the MCF. This time there was no inscription of any "unwanted" FBG. This was achieved through more careful alignment of the fibre and shorter exposure time.

Figure 5-35 shows the FBGs reflectance spectra inscribed into the three cores monitored through a silica waveguide fan-out device. Subsequently a SMF to MCF splice and taper along the MCF was performed with the same steps presented in the previous sections. This sensor had similar response as previous regarding the ripples and additional peaks presented at the reflectance spectrum. Hence, a cladding mode stripper was applied on the MCF for the following experiments.

Finally, deflection experiments (see Figure 5-32) were performed on the sensor and the response of the FBGs was as expected. Figure 5-36 shows the calculated strains shift versus the curvature. The value of the differential strain sensitivity that was used this time was 1.041 $[pm/\mu\varepsilon]$. This value was calculated using the experimental data from the second sensor. The slope of the FBGs pair (1-3) which lie on two different planes of curvature was measured to be 45.71 μm for the first direction of deflection. While, the corresponding gradient for the second orientation of deflection (Core 1 - Core 2) was measured to be 54.98 μm. This value is close to the actual separation of the cores of the MCF and within the error reported in the previous sensor, which can be attributed to misalignment of the MCF from the ideal case (Figure 5-32). Moreover, the slope between the FBGs pair 1-2 is close to zero as expected.

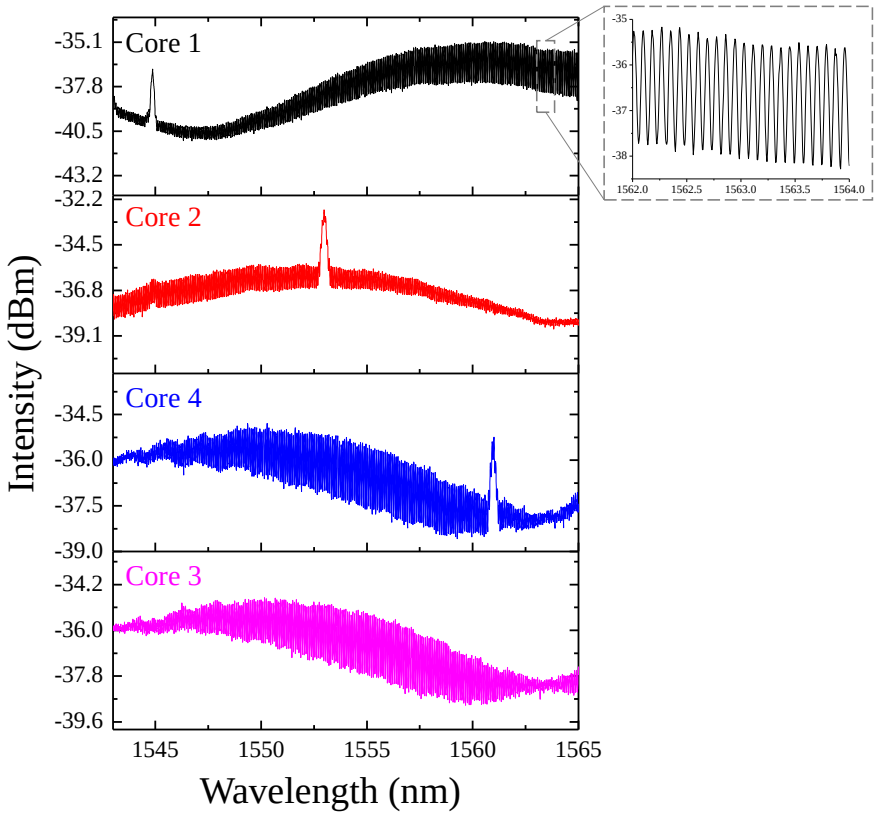

Figure 5-35. Inscribed FBGs reflectance spectra for the third MCF curvature sensor with the fibre tapered fan-out device (zoomed in region) rippled due to the silica waveguide fan-out device.

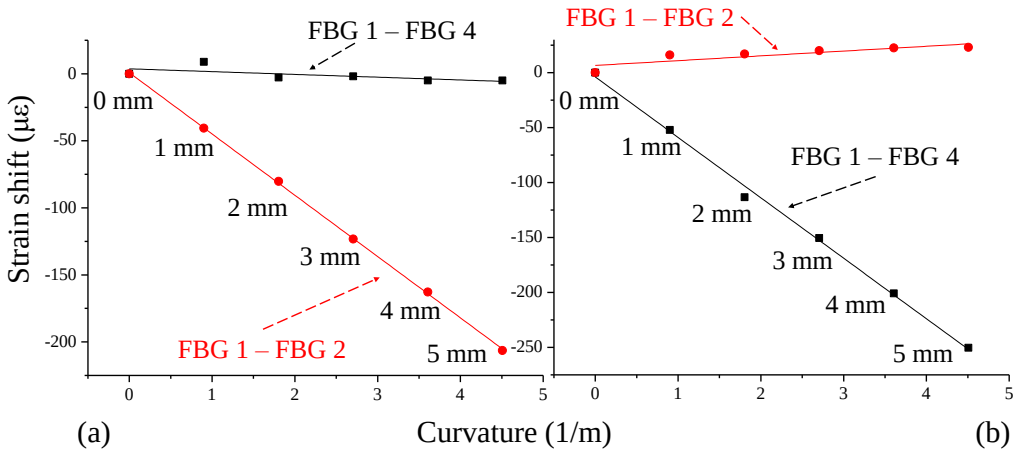

Figure 5-36. Strain shift vs curvature upon deflection on (a) direction 1 and (b) on direction 2 of the third sensor.

5.5. Temperature sensitivity of the MCF curvature sensor with the tapered fibre fan-out device

A study on the temperature sensitivity of the sensor fabrication in section 5.4.3 (Third sensor with three discrete FBGs) was performed. Similarly, to the case of the sensor with the silica waveguides fan-out device (paragraph 4.4.2), the rotation experiment was performed and no variations from the circular motion were noticed over various temperatures. Moreover, the FBGs and the taper region was enclosed in an environment where the temperature could be controlled. The FBGs were inserted in a groove machined in a metallic plate and placed on a hot plate, while the tapering region was enclosed in a box. Figure 5-37 shows a schematic diagram of the experimental setup.

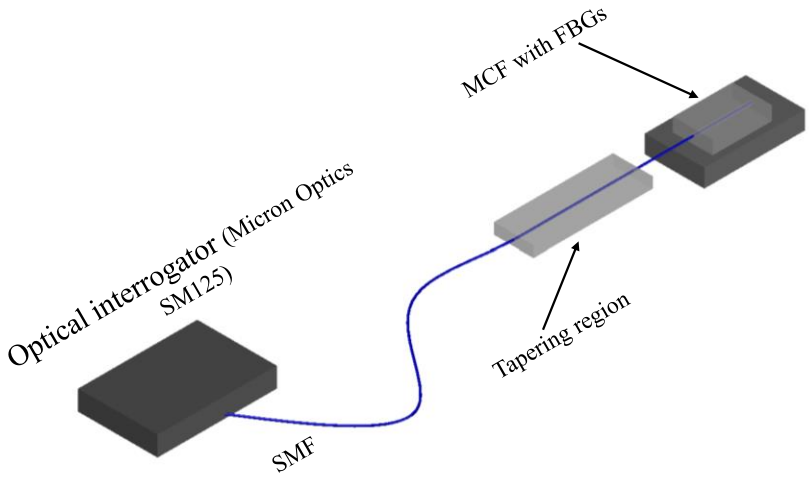

Figure 5-37. Experimental set up used for the temperature sensitivity studied of the MCF curvature sensor.

The local temperature of the tapering region as well as the temperature of the FBGs, were monitored with K – type thermocouples. Measurements of the temperature were recorded every 10 seconds and the study included three different cases: (*i*) both the tapering region and the FBGs maintained at a stable temperature, (*ii*) the FBGs' temperature varied, while the tapering region was held stable and (*iii*) the FBGs maintained at a stable temperature, while the temperature of the tapering region varied. In all cases the wavelength peak positions of the FBGs inscribed into different cores of the MCF was monitored. Moreover, the wavelength shifts between the all possible combination of FBGs pairs (1-2, 1-3 and 2-3) is analysed.

i. Tapering region and FBGs maintained at a stable temperature

In this case the temperature of the tapering region remained at 27 ±0.06 ° C and the FBGs were maintained at 33 ±0.11° C. FiguresFigure **5-38** and Figure **5-39**, show the reflected wavelength peak position of the three FBGs and the shift between them respectively. The response of the FBGs in this case is constant (within the noise) as expected.

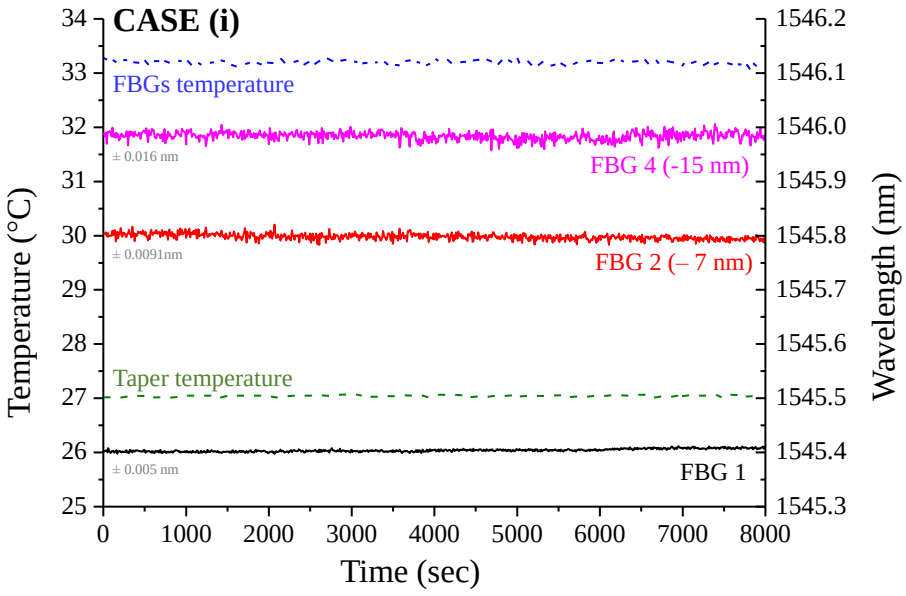

Figure 5-38. FBGs reflectance peak position when both the tapering region and the FBGs maintained at a stable temperature (grey coloured font numbers are the noise levels). FBG 2 and FBG 4 have an -7 nm and -15 nm offset respectively for illustration purposes.

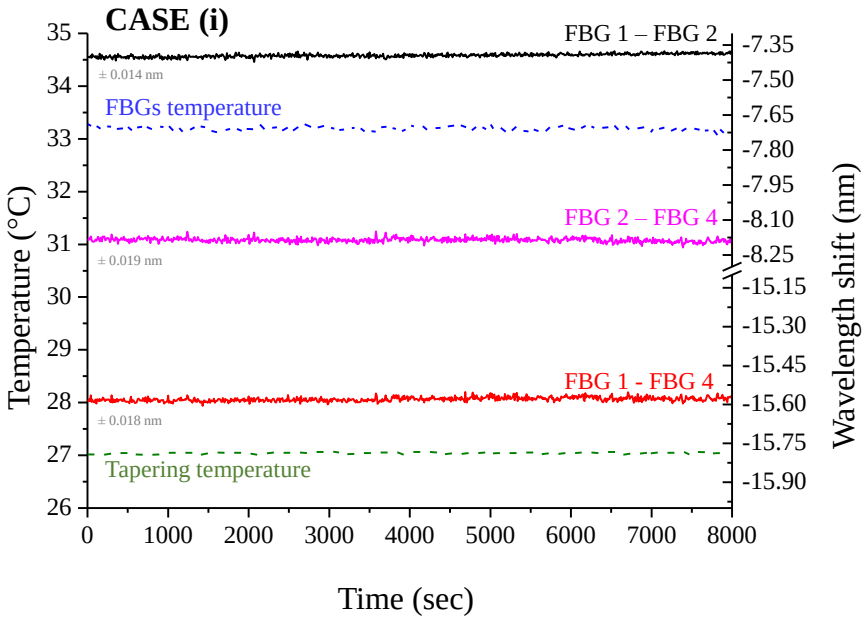

Figure 5-39. Reflectance peak position Wavelength shift between the inscribed FBGs into the three different cored of the MCF when both the tapering region and the FBGs maintained at a stable temperature (grey coloured font numbers are the noise levels).

ii. The temperature of the FBGs varied, while the tapering region maintained a stable temperature

In the second case the tapering region was held stable at 25 ±0.06° C and the temperature of the FBGs varied from 29° C to 37.2° C with a ~ 2° C increment. At each increment the FBGs remained at a stable temperature for ~ 20 seconds. Figure 5-40 shows the response of the individual FBGs upon temperature variations, while Figure 5-41 shows the wavelength shift between them.

The response of the FBGs follow the temperature variations as expected. Their average temperature sensitivity was measured to be 10 pm/°C (according to graphs presented in Figure 5-40), this value is close to the one reported in literature and any errors are attributed to the noise levels of the FBGs wavelength peak position [13]. Moreover, the wavelength shift between the FBGs pairs eliminates the temperature variations upon their response, as expected (noise levels were determined as $(\lambda_{max} - \lambda_{min})/2$) and are written with grey font numbers).

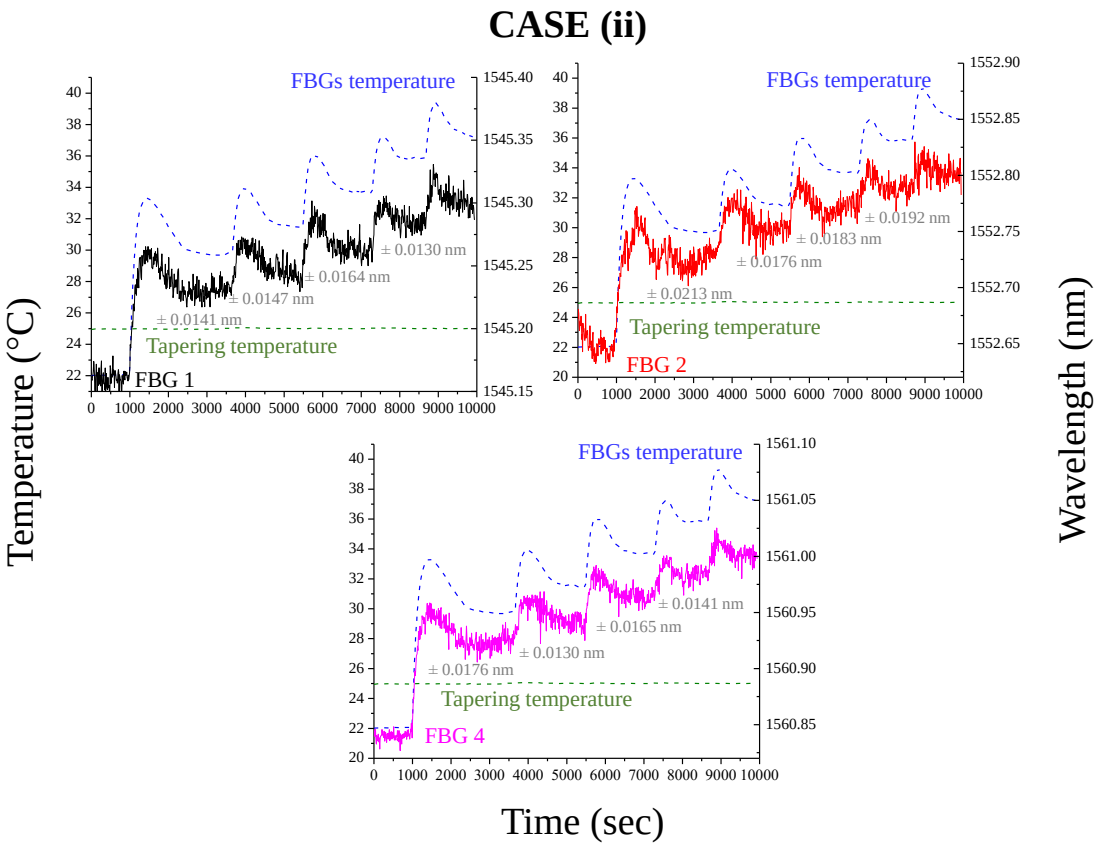

Figure 5-40. FBGs reflectance peak position when the tapering region is maintained at a stable temperature and the FBGs varied from 29° C to 37.2° C with ~ 2° C increment (grey coloured font numbers are the noise levels).

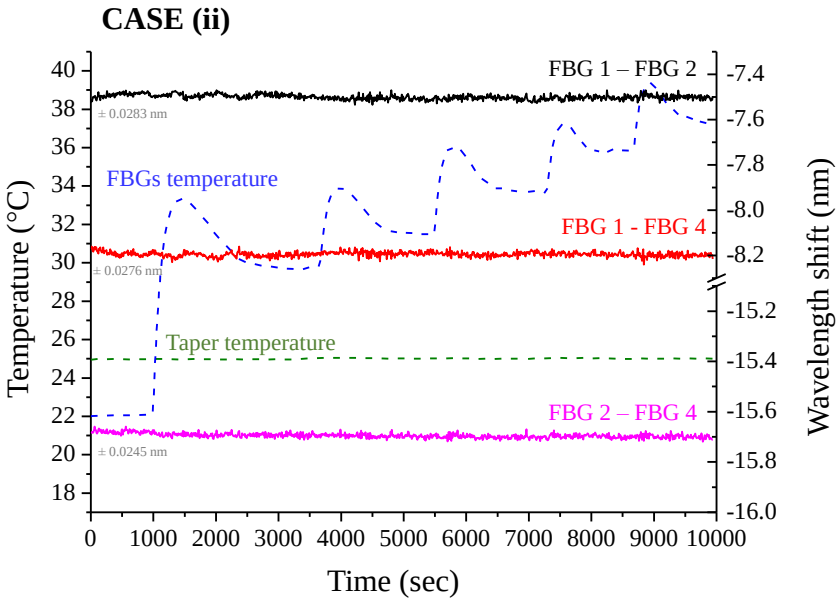

Figure 5-41. Reflectance peak position wavelength shift between the inscribed FBGs into the three different cores of the MCF. The tapering region is maintained at a stable temperature and the FBGs varied from 29° C to 37.2° C with ~ 2° C increment (grey coloured font numbers the noise levels).

Nevertheless, in the first 3000 seconds there are some variations in the wavelength shifts (mainly in the pairs 1-2 and 1-3) which are slightly above the noise level observed (~0.02 nm) for this sensor. These variations are in average ± 0.027 nm and are shown in Figure 5-42. The existence of these variations are considered to be due to non-uniformities on the temperature gradient in the groove were MCF with the FBGs were placed.

In this case the metallic part used to maintain the FBGs at a stable temperature was different with the one used for the sensor presented in chapter 4 (silica glass waveguides fan-out device sensor). This metallic piece had a groove with increased radius and shorter length to avoid damage to the MCF with the inscribed FBGs.

The temperature environment of the FBGs was non-uniform the first 3000 seconds, during initial warm up. However, on the following warming steps (4000 – 10000 seconds), the FBGs wavelength shift was stable within the noise range. Thus it is considered that temperature compensation between them can be achieved.

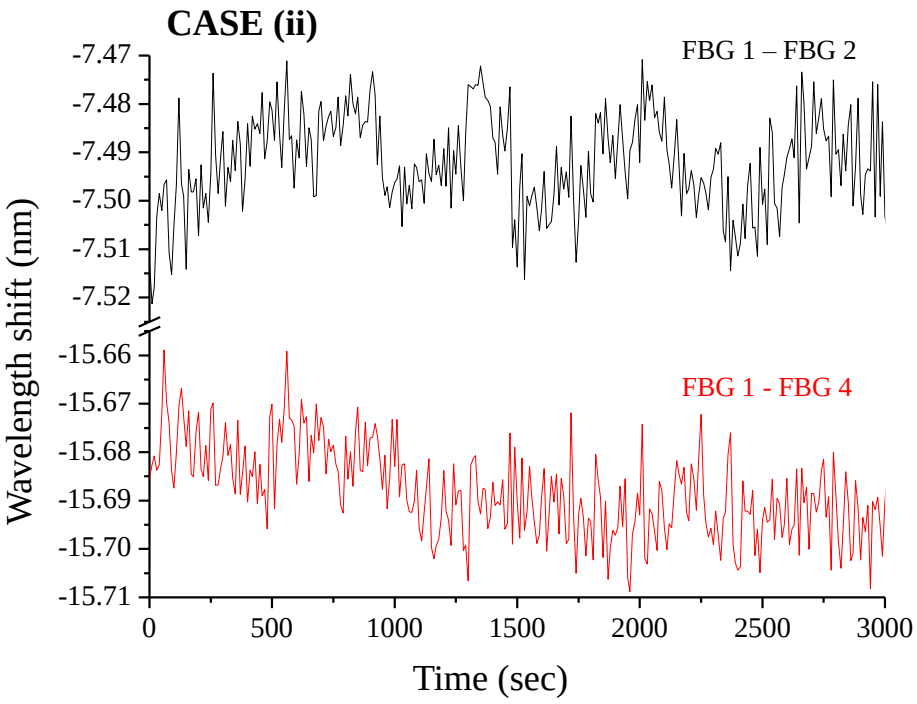

Figure 5-42. Reflectance peak position wavelength shift between the inscribed FBGs into the three different cores of the MCF when the tapering region and the FBGs maintained at a stable temperature and the FBGs varied from 29°C to 37.2°C with ~ 2°C increment for the first 3000 seconds.

iii. FBGs maintained at a stable temperature, while the temperature of the tapering region varied

In the final case the temperature of the tapering region varied from 31° C to 38° C with 2° C increment. This temperature range was chosen under the consideration of having the most stable temperature environment (± 0.06° C) for the taper region using the experimental set up shown in (Figure 5-37). The FBGs temperature maintained a constant 32.4° C± 0.11° C. Figure 5-43 andFigure **5-44** show the response of the three inscribed FBGs and the wavelength shift between the possible FBG pairs respectively. Finally, Figure 5-45 shows a specific region of FBG pairs 1-2 and 1-3.

According to these graphs there is no effect on the MCF curvature sensor upon variations of the temperature in the tapering region. However, it is worth mentioning that a small drift on the FBGs wavelength shifts was observed in this case (mainly for FBG 4). This drift was ~ 0.03 nm for temperature variations of the tapering region above 10° C. This effect can be attributed to the non-uniform local temperature of the inscribed FBGs.

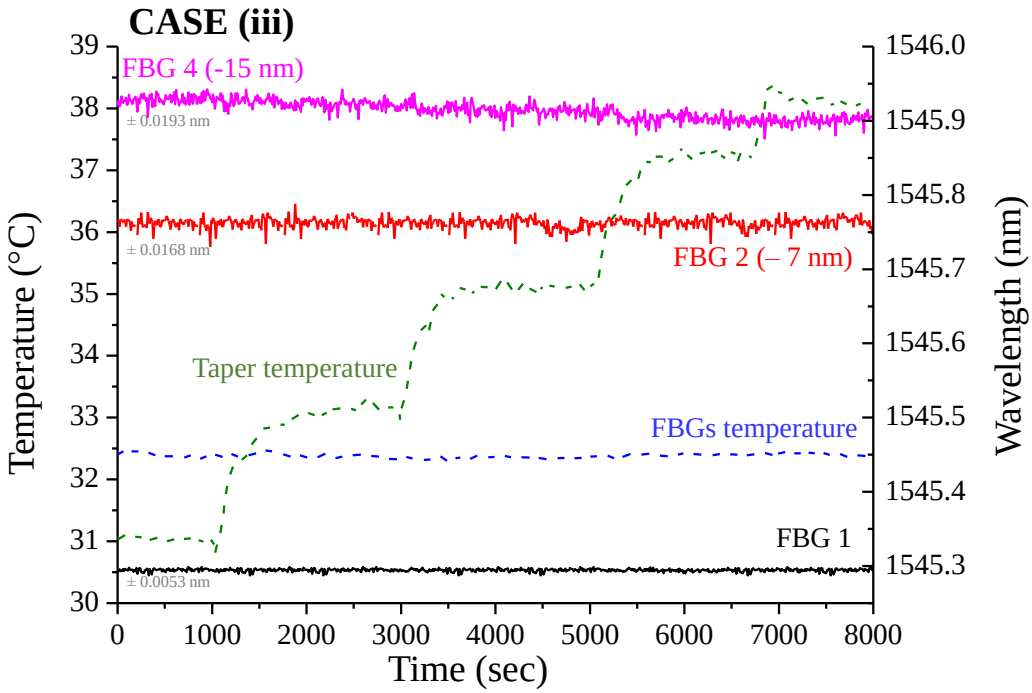

Figure 5-43. FBGs reflectance peak position when the temperature of the tapering region varied from 31° C to 38° C with 2° C increment and the FBGs temperature maintained at 32° C± 0.11° C (grey coloured font numbers the noise levels). FBG 2 and FBG 4 have an offset of an -7 nm and -15 nm respectively for illustration purposes.

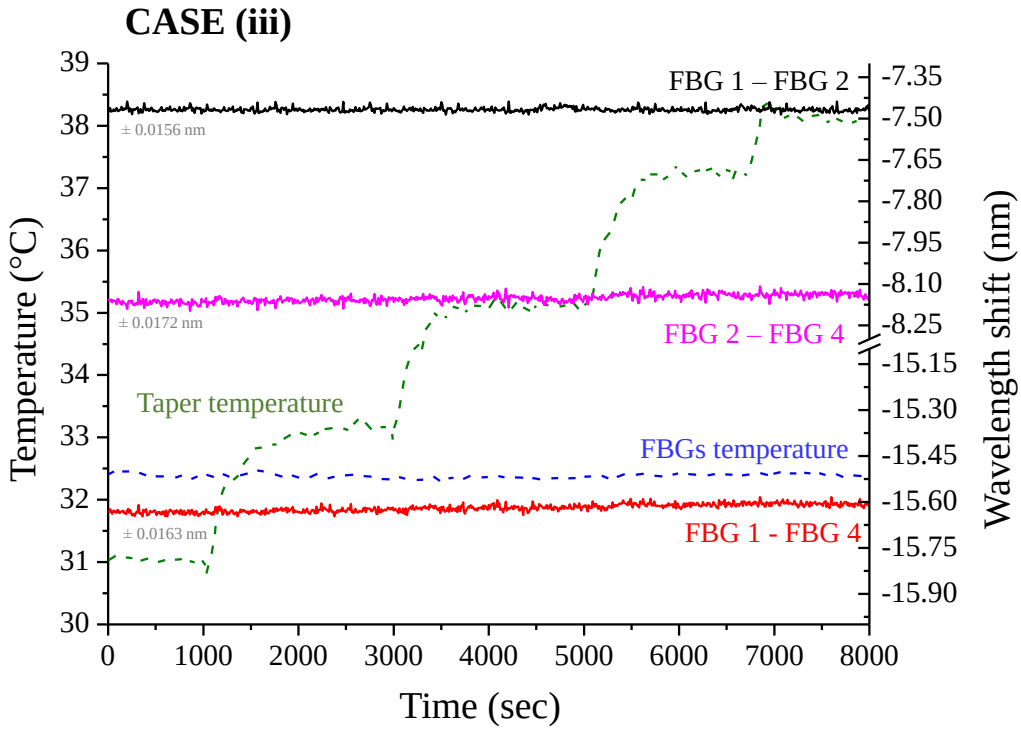

Figure 5-44. Reflectance peak position Wavelength shift between the inscribed FBGs when the temperature of the tapering region varied from 31° C to 38° C with 2° C increment and the FBGs temperature maintained at 32.4° C± 0.11° C.

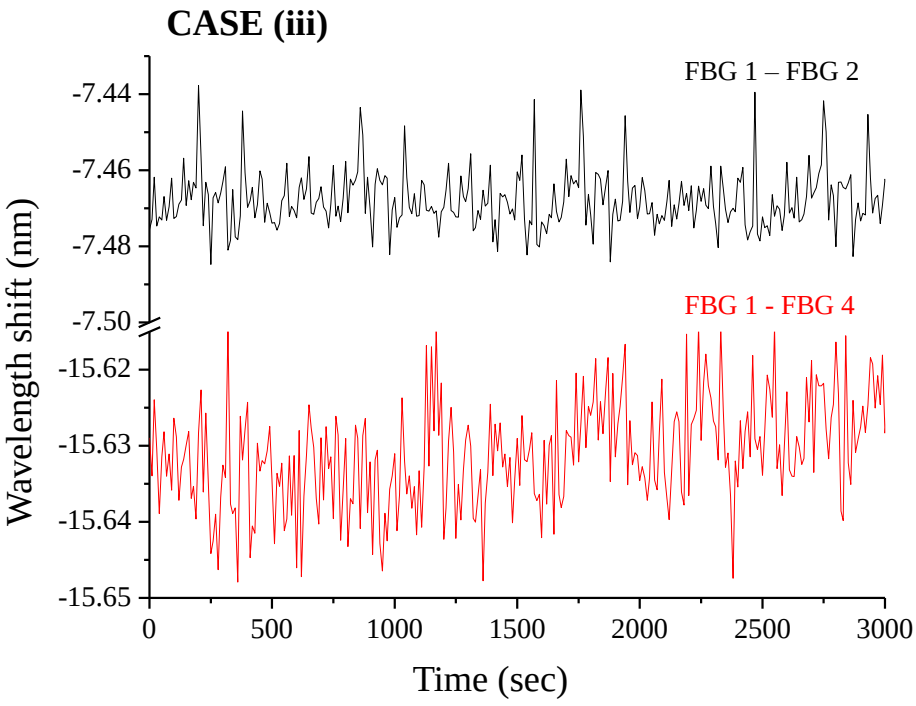

Figure 5-45. Reflectance peak position Wavelength shift between the inscribed FBGs when the temperature of the tapering region varied from 31° C to 38° C with 2° C increment and the FBGs temperature maintained at 32.4° C ± 0.11° C for the first 3000 seconds.

5.6. Conclusions

Fabrication of a MCF curvature sensor with a tapered fibre coupler fan-out device was achieved. This chapter reports a theoretical analysis of the coupling of light from one core to all four cores of the MCF. This was achieved with simulations performed using MatLab^{TM} based on earlier work by Mortimore and Arkwright [3, 15]. Moreover the practical limitations of the experimental instruments were taken into account during this modelling. The model informed the starting point for experimental optimisation.

Coupling of light between the cores of the MCF can be achieved by reducing the fibre's cladding diameter. Therefore, the cores separation as well as their radii can be reduced. The cladding's diameter reduction was achieved by tapering the fibre. Moreover, coupling of light was monitored with several experiments during the tapering procedure. Hence, the tapering parameters were established.

The tapered fibre fan-out approach introduces an additional challenge to the fabrication of the MCF curvature sensor. FBGs on with different reflectance spectrum have to be inscribed, to avoid spectral overlap. Discrete FBGs in 3 cores were inscribed with a bespoke fibre holder. With this holder rotation as well as translation in two planes of the MCF could be controlled. Hence, the correct orientation of the fibre on the UV interference pattern produced from the phase masks could be achieved.

The fabrication of three different MCF curvature sensors is presented in this chapter. The challenges on their fabrication and ways to overcome them are reported. The first challenge includes the fact that the splicing of the SMF with one core of the MCF introduces cladding modes in the transmitted light. These modes were eliminated by producing a tight bend on the MCF after the splicing.

The second challenge arose throughout the FBGs inscription. During the fabrication of the second sensor an "unwanted" FBG was inscribed in one of the cores of the MCF. Peak position threshold analysis showed that the effect of this FBG is minor for the specific reflectivity of the grating.

Finally, studies on the temperature sensitivity of the MCF curvature sensor showed that there is a minor effect on its performance due to temperature variations. A 0.03 nm drift of the wavelength peak positions shifts was observed. Hence, the MCF curvature

sensor is temperature stable and can be used for flow measurements required from LAkHsMI project.

5.7. References

[1] R. R. Thomson, H. T. Bookey, N. D. Psaila, A. Fender, S. Campbell, W. N. MacPherson, J. S. Barton, D. T. Reid, and A. K. Kar "Ultrafast-laser inscription of a three dimensional fan-out device for multicore fiber coupling applications," *Optics Express*, vol. 15, no. 18, pp. 11691-11697, 2007.

[2] A. W. Snyder, "Coupled-Mode Theory for Optical Fibers," *Journal of the Optical Society of America*, vol. 62, no. 11, pp. 1267-1277, 1972.

[3] D. B. Mortimore, "Theory and fabrication of 4 x 4 single-mode fused optical fiber couplers," *Applied Optics*, vol. 29, no. 3, pp. 371-4, 1990.

[4] J. D. Love and W. M. Henry, "Quantifying loss minimisation in single-mode fibre tapers," *Electronics Letters*, vol. 22, no. 17, p. 912, 1986.

[5] J. D. Love, W. M. Henry, W. J. Stewart, R. J. Black, S. Lacroix, and F. Gonthier, "Tapered single-mode fibres and devices. Part 1: Adiabaticity criteria," *IEEE Proceedings J Optoelectronics*, vol. 138, no. 5, p. 343, 1991.

[6] S. Ravets, J. E. Hoffman, P. R. Kordell, J. D. Wong-Campos, S. L. Rolston, and L. A. Orozco, "Intermodal energy transfer in a tapered optical fiber: optimizing transmission," *Journal of the Optical Society of America A*, vol. 30, no. 11, pp. 2361-2371, 2013.

[7] Z. Yu, L. Jin, L. Sun, J. Li, Y. Ran, and B.-O. Guan, "Highly Sensitive Fiber Taper Interferometric Hydrogen Sensors," *IEEE Photonics Journal*, vol. 8, no. 1, pp. 1-9, 2016.

[8] C. Voigtländer, , Ria G. Becker, Jens Thomas, Daniel Richter, Anshuman Singh, Andreas Tünnermann, and Stefan Nolte,"Ultrashort pulse inscription of tailored fiber Bragg gratings with a phase mask and a deformed wavefront [Invited]," *Optical Materials Express*, vol. 1, no. 4, pp. 633-642, 2011.

[9] Y. Suzaki and A. Tachibana, "Measurement of the μm sized radius of Gaussian laser beam using the scanning knife-edge," *Applied Optics*, vol. 14, no. 12, pp. 2809-2810, 1975.

[10] M. A C de Araújo, R. Silva, E. Lima, D. Pereira, and P. De Oliveira, "Measurement of Gaussian laser beam radius using the knife-edge technique: Improvement on data analysis", *Applied Optics*, pp. 393-6, 2009.

[11] T. Yang, X. Qiao, Q. Rong, and W. Bao, "Orientation-Dependent Displacement Sensor Using an Inner Cladding Fiber Bragg Grating," *Sensors*, vol. 16, no. 9, p. 1473, 2016.

[12] C. Gouveia, P. A. S. Jorge, J. M. Baptista, and O. Frazao, "Temperature-Independent Curvature Sensor Using FBG Cladding Modes Based on a Core Misaligned Splice," *IEEE Photonics Technology Letters*, vol. 23, no. 12, pp. 804-806, 2011.

[13] M. M, R. C. S. B. Allil, B. A, and F. V. B. de Nazar, *A Guide to Fiber Bragg Grating Sensors*. 2013.

[14] Enbang Li, Jiangtao Xi Joe F. Chicharo, Tiegen Liu, Xin Li, Junfeng Jiang, Lina Li, Yunxin Wang, Yimo Zhang., "The experimental evaluation of FBG sensors for strain measurement of prestressed steel strand," *in Proc. Smart Materials, Nano-, and Micro-Smart Systems, SPIE* vol. 5649, p. 7, 2005.

[15] D. B. Mortimore and J. W. Arkwright, "Theory and fabrication of wavelength flattened 1 x N single-mode couplers," *Applied Optics*, vol. 29, no. 12, pp. 1814-8, 1990.

Chapter 6. Conclusions and future work

This chapter covers an overview of the sensors produced for the LAkHsMI project and is focused on the work reported in this thesis. In this thesis fabrication and characterisation of optical fibre sensors are reported in detail. The majority of optical fibre LAkHsMI sensors were explored at Chapters 3, 4 and 5 of this PhD thesis. Moreover, this chapter includes a comparison of the optical fibre curvature sensors which were fabricated with the prospect to be used as flow sensors. Finally, potential future work on optimising the overall performance of the sensors is explored.

6.1. General concept of all sensors used on LAkHsMI project

The studies presented in this thesis originate from the E.U. H2020 LAkHsMI project's aims and objectives. The fabrication and performance of different types of sensors were explored for the purposes of LAkHsMI's experimental trials. Figure 6-1 shows an overview of all sensors produced for LAkHsMI project.

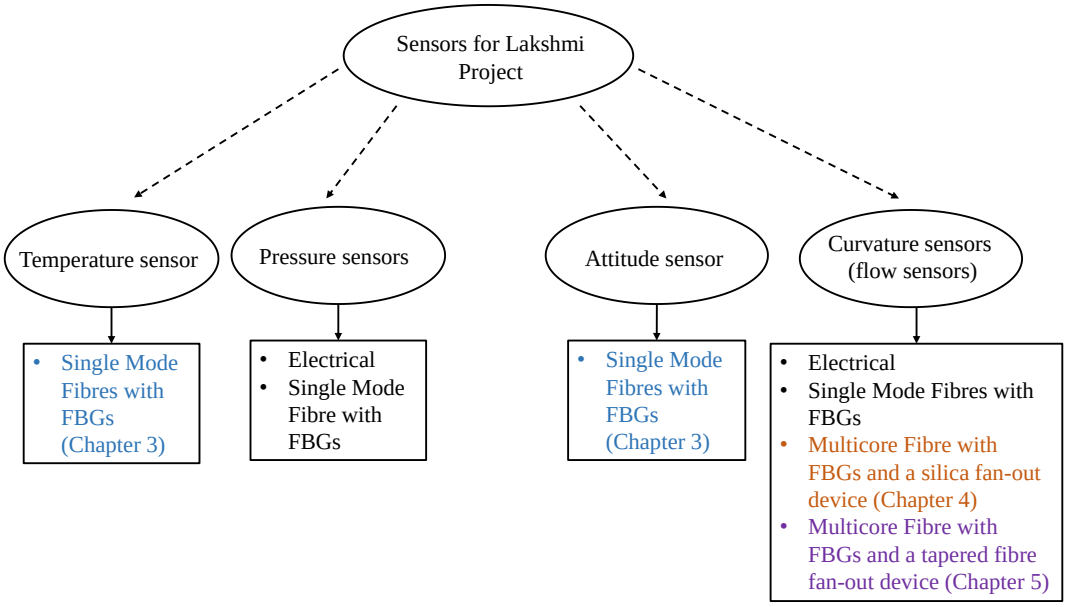

Figure 6-1. Schematic diagram of the sensors produced for LAkHsMI's experimental trials.

As a PhD student at Heriot-Watt University I focused on the fabrication of the optical fibre sensors with my main focus was on the fabrication of the MCF curvature sensor. I worked closely and helped two Research associates (Jonathan Morton, Adrian Dzipalski) who had as primary responsibility for the fabrication of deployable flow sensors. Hence, I was also partially involved on the fabrication and deployment of the flow sensors

produced with SMF FBGs. Figure 6-2 shows schematic diagram of the work (joint and individual) produced during my PhD studies.

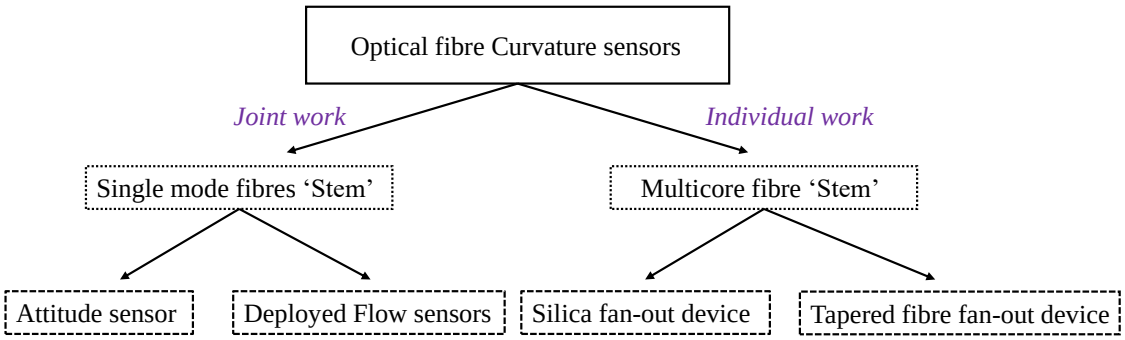

Figure 6-2. Types of curvature sensors that were fabricated for LAkHsMI project.

The flow sensors are essentially curvature sensors which have a typical cantilever geometry. The main difference of the two different types of flow/curvature sensors that were explored is the structure of the sensing element (referred to as the 'stem'). The stem of the first type was fabricated with 4 SMFs while the second was produced with one MCF which contains four cores arranged in a square array. Figure 6-3 shows the cross sections of the two types of sensing stems. The 4 SMFs curvature sensors were actually deployed and used for flow measurements, while the MCF flow sensors were considered as the "next generation" sensors and the work focused on the development of their performance.

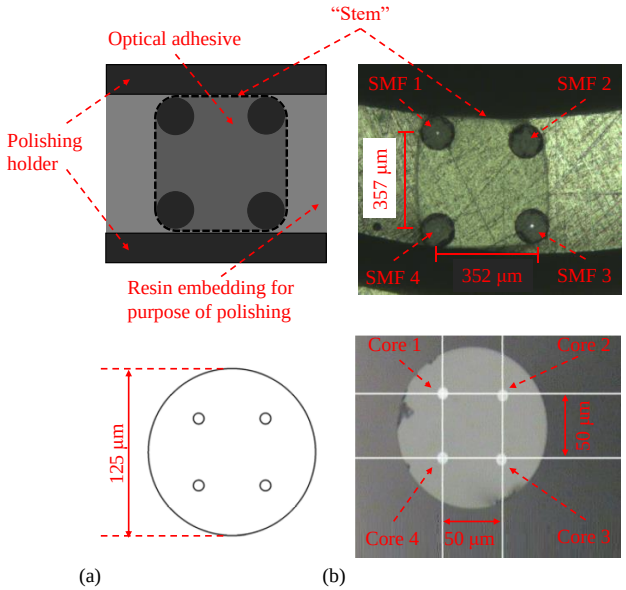

Figure 6-3. 'Stem' sensing elements for both types of curvature sensors produced during LAkHsMI project (a) schematic diagrams, (b) actual cross sections with transmitted illumination of the fibres/cores.

Two different sensors were produced with each sensing element (see Figure 6-2). The four SMFs stem was used for the attitude sensor and as flow sensors on field trials. The MCF curvature sensors were considered as innovative alternatives to flow sensors and two different ways of monitoring the FBGs were studied. The first used a silica waveguide fan-out device, while the second used a tapered fibre fan-out device. Figure 6-2 shows a schematic diagram of all optical fibre curvature sensors that were produced during the LAkHsMI project.

Deployed curvature/flow sensors (4 SMFs sensing element)

This type of curvature sensor uses four SMFs with inscribed FBGs which are bounded together with optical adhesive. The cross section the 'stem' is shown in Figure 6-3 (a), while a side view is shown Figure 6-4. In this case the SMFs act as the strain gauges. The fabrication of the sensor's 'stem' was reported in Chapter 3 for the purposes of producing the Attitude sensor (Figure 6-7). The flow sensors which were used on experimental field trials were fabricated by embedding this stem into protective materials (such as sylgard). Figure 6-5, shows the first four flow sensors that were fabricated and submerged in the sea near Oban (Scotland's Highlands).

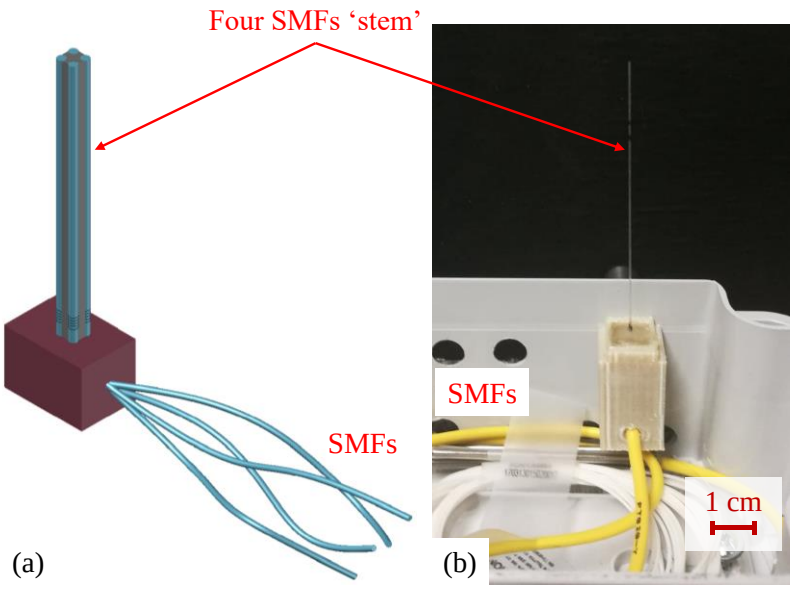

Figure 6-4. Curvature sensor produced from four SMFs glued together (a) schematic diagram and (b) actual sensor.

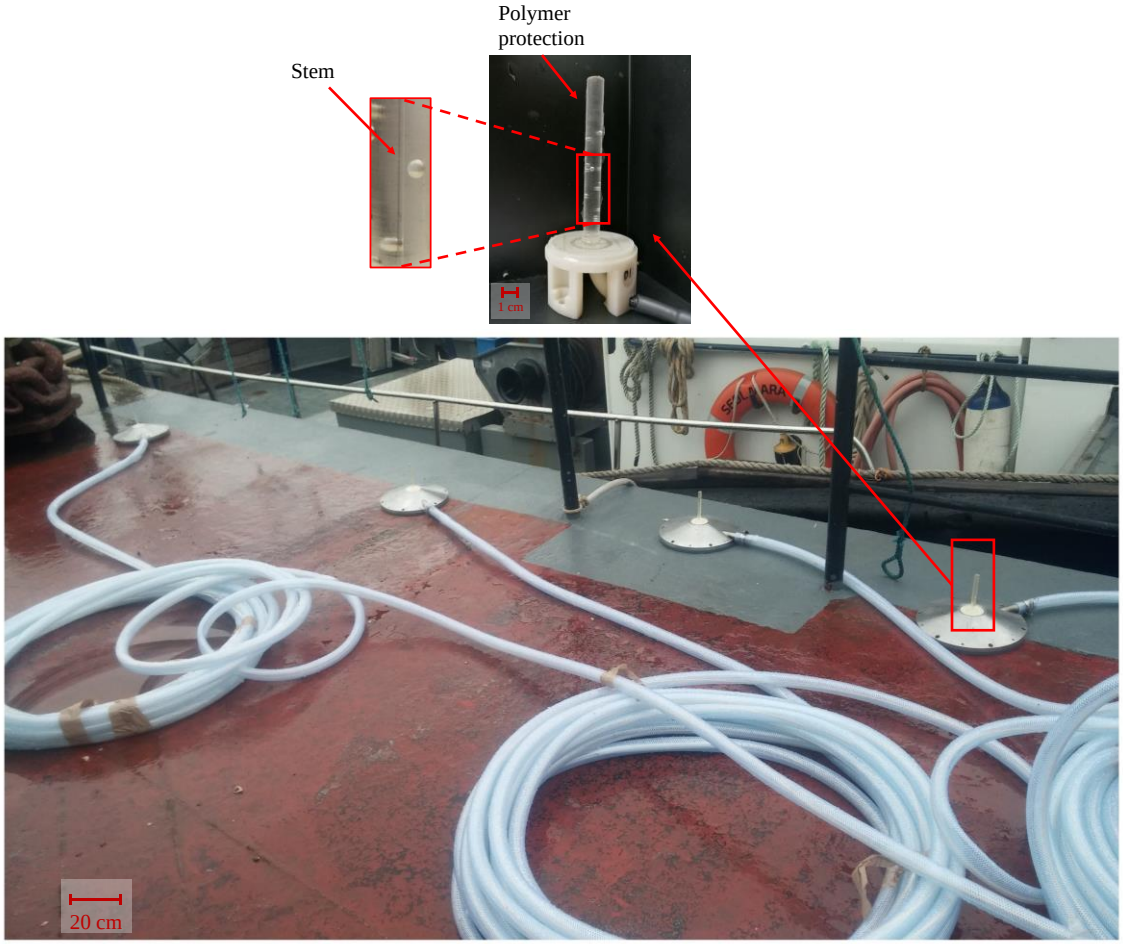

Figure 6-5. Optical fibre flow sensors used for field trials in Oban.

6.2. Individual work

The highlighted optical fibre sensors, in Figure 6-1 are the main focus of this thesis. The temperature sensors, the calibration attitude sensor and the MCF curvature sensors, which could eventually used as flow sensors, are discussed in the three experimental chapters (3, 4 and 5) of the thesis. All of these sensors exploit the properties of inscribed Bragg gratings into the fibres, in order extract information from their environment.

i. Fibre Bragg grating Temperature sensors

The fabrication and calibration of the FBG temperature sensors is a well-established procedure [1]. The fabrication of these sensors was performed through strain isolation, by enclosing the FBGs into rigid tubes with an inner diameter comparable to fibre's cladding diameter (Figure 6-6). Their calibration was achieved by submerging them into water where the temperature was monitored with K-type thermocouples. Their

performance was as expected (with ±2° C error) and they were deployed successfully on field trails in the sensors unit platform (see Chapter 1).

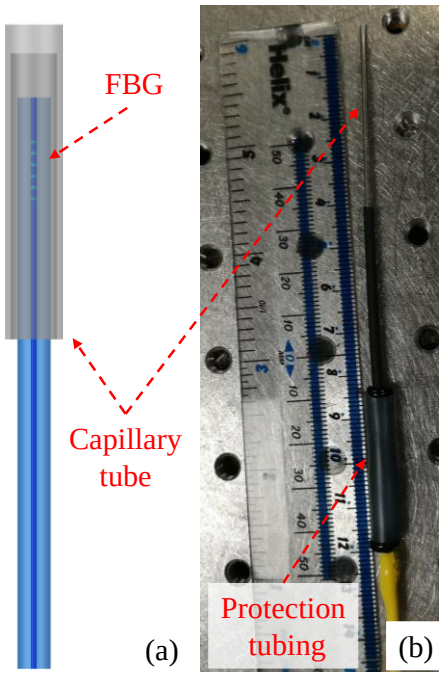

Figure 6-6. FBG temperature sensor used on field trials for Lakshmi project (a) schematic diagram, (b) actual sensor.

ii. Fibre Bragg grating Attitude sensor

The FBG attitude sensor is reported in Chapter 3. The attitude sensor was inspired as a result of needing to know the orientation of the platform onto which the flow sensors were fixed. Optical fibre gyroscopes are well-established and already commercialised for different applications [2]. However, an Attitude sensor compatible to the technology (FBGs) that all-optical fibre LAkHsMI's sensors use (flow and temperature sensors) was desired. Therefore, an innovative FBG Attitude sensor was produced.

The main concept of this sensor was to use Earth's gravity in order that the orientation in two different planes of the platform could be determined. This was achieved by attaching weights on the curvature sensors. Three sensors were fixed perpendicular to each other in the *x*,*y* and *z* axes (Figure 6-7). The calibration procedure of a single curvature sensor is reported in Chapter 3, this procedure required two different types of deflection to be applied on the sensor: (a) a linear calibration deflection and (b) a rotational deflection. The sensor was used for experimental measurements in field trials.

The FBG Attitude sensor performed as expected and deployment with the optical flow and temperature sensors in the sensors unit platform (see Chapter 1) was achieved. The

sensor could provide the orientation of the platform in two different planes with a rotational resolution of ± 2° accuracy.

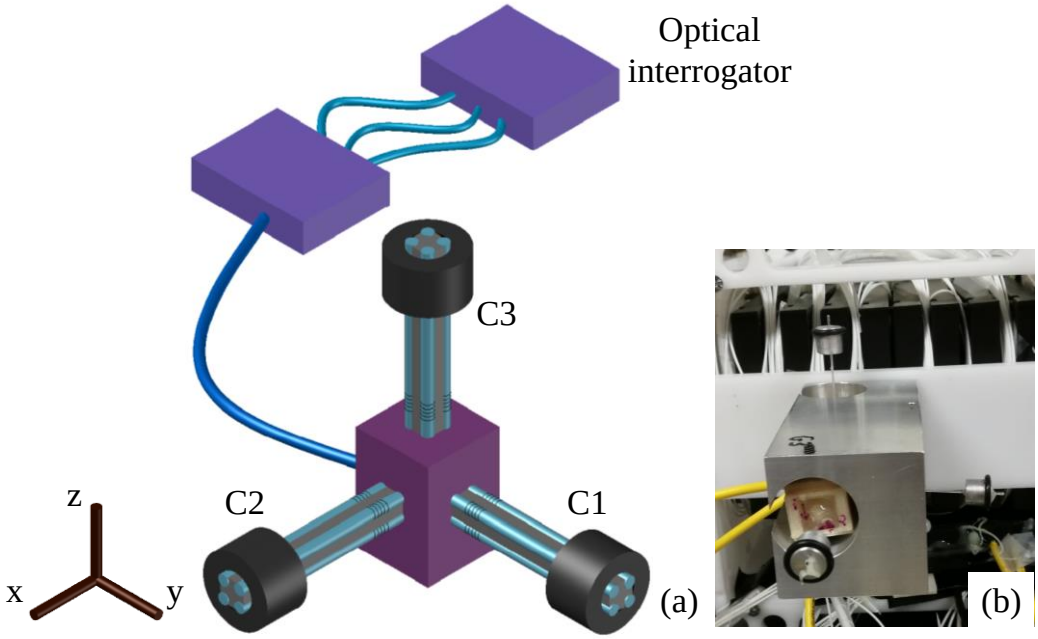

Figure 6-7. Attitude sensor (a) schematic diagram, (b) actual sensor.

iii. Curvature (or potential flow) sensors using a MCF

The curvature sensors that are reported in this thesis can be characterised as strain sensors, where the inscribed FBGs act as strain gauges. Inscription of Bragg gratings into the fibre's cores was performed in house.

The MCF curvature sensor uses the fibre itself as a 'stem' sensing element. In this case, the four optical cores of the fibre act as strain gauges (Figure 6-3). The fabrication and the performance of the MCF curvature sensors was the primary objective of the research presented in this thesis. Experiments show that the sensors can be successfully calibrated using the well-established equations of beam theory [3]. The MCF and the inscribed FBGs were performing as expected and can be used as flow sensors with proper packaging.

The main challenge with using MCF is monitoring of the transmitted or reflected light in each individual core of the fibre. The MCF is not compatible with conventional optical fibre technology. The majority of the experimental instruments (optical interrogators, lasers, or optical spectrum analysers) use standard single core fibres. Therefore, an interface device is required in order to monitor the FBGs reflectance or transmittance spectra using commercial systems. Hence, two MCF curvature sensors were produced

with two different interfaces (see diagram in Figure 6-2). The first uses a silica waveguide fan-out device while the second uses a MCF tapered fan-out device.

MCF Curvature sensor with a silica waveguide fan-out device

The first MCF curvature sensor (Chapter 4) uses a silica waveguide with inscribed waveguides fan-out device [4]. Hence, light can be transmitted from one core of the MCF through the waveguides to a standard SMF. Figure 6-8 shows a schematic diagram as well as an actual image of this type of MCF curvature sensor.

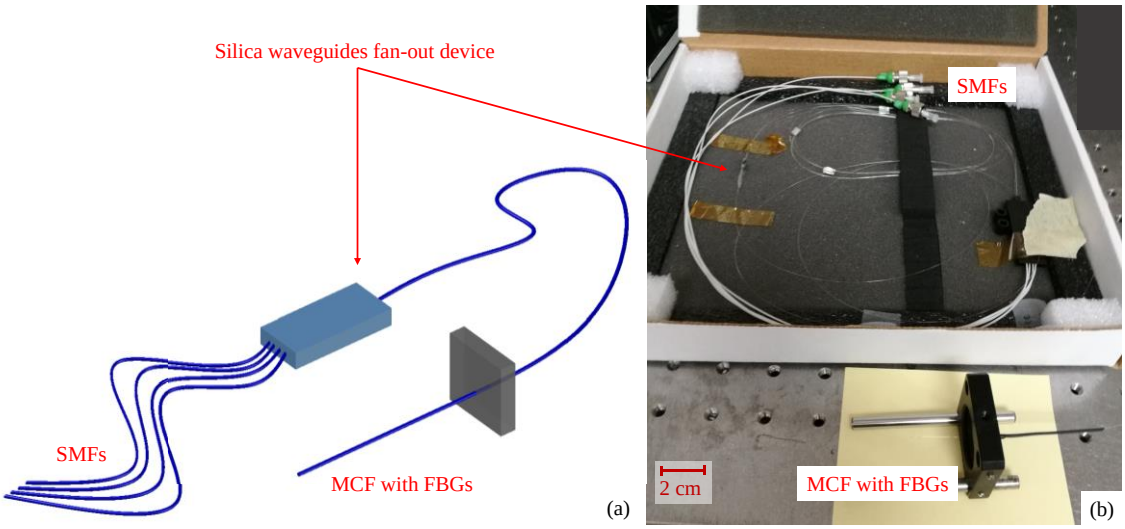

Figure 6-8. MCF curvature sensor with a silica waveguides fan-out device.

The silica waveguide fan-out device that this sensor uses is a fragile and expensive optical interface. Its fabrication is considered complex and requires high accuracy. The waveguides are inscribed using an ultrafast femtosecond laser inscription and precise alignment of the MCF and SMFs with them is required [4]. Moreover, studies on these type of MCF sensors showed that they are temperature sensitive and the effect is attributed to the fan-out (Chapter 4). Hence, an alternative fan-out device was explored.

Curvature sensors produced from a MCF with a tapered fibre fan-out device

The second MCF curvature sensor (Chapter 5) uses a tapered MCF fibre fan-out device. In this case, the transmitted light is coupled from one core of the MCF to all four cores. Hence, the fan-out can be fabricated with less complex techniques (using a splicer with tapering ability) and it can be considered as less fragile and easier to package. Moreover, experiments on the temperature variations of these sensors indicate that they are significantly less sensitive.

This sensor however, requires inscription of FBGs with reflectance spectra in different regions of the overall spectrum of interrogation. In this way spectral overlap is avoided. Individual inscription of FBGs into different cores of the MCF was successfully achieved with a bespoke optical fibre holder. Figure 6-9 shows a schematic diagram as well as an actual image of the MCF curvature sensor with the fibre tapered fan-out device.

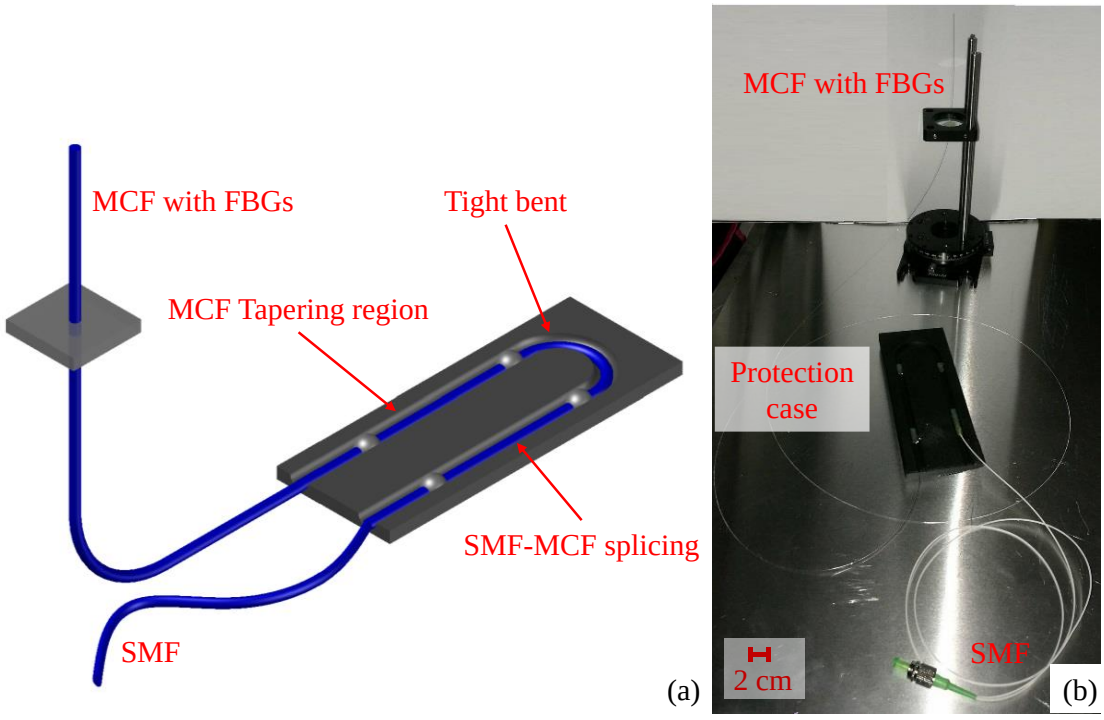

Figure 6-9. MCF curvature sensor with tapered fibre fan-out device (a) schematic diagram and (b) actual image.

6.3. Design Comparison: four SMFs, MCF with waveguide and MCF with tapered fan-out devices

The three curvature sensors at the early stages of their fabrication can be compared to each other under several aspects. In this paragraph the strengths and weaknesses of the "four SMFs" (*first*, Figure 6-4), the "MCF with silica waveguide fan-out device" (*second*, Figure 6-8) and the "MCF with tapered fibre fan-out device" (*third*, Figure 6-9) curvature sensors will be explored. A table which includes all the reported aspects on the comparison of the three sensors, is given at the end of the section (Table 6-1).

6.3.1. Fabrication of the sensors

The fabrication of the *first* sensor can be characterised by low difficulty (Chapter 3). In this case it is considered that inscription of FBGs into the SMFs is not required to be

done in-house since they are commercially available. The most vulnerable fabrication step, is the alignment of the SMFs to each other. The four SMFs have to be aligned in such way that all four inscribed FBGs are positioned at the same point along the 'stem' element. Moreover, the SMFs have to be straight and not twisted (otherwise an error on the calibration procedure is introduced) along the 'stem' element. Both difficulties can be avoided by careful marking and alignment of the fibres. The SMFs can be maintained straight during the fabrication of the 'stem' with pulleys and weights. Translation stages and a syringe pump, as well as stable power LEDs can provide reliable glue deposition and curing.

The procedure can be considered repeatable. However, the cross sections of different 'stems' can vary with 350 ± 10 μm on the separation of the SMFs (Figure 6-3). Moreover, maintance of the fabrication set up is required frequently due to the time depreciation of the optical adhesive and LEDs power. Finally, four in total SMF to SMF splicings are required for the fabrication of one sensor. Therefore, the fabrication can be considered time consuming, but relatively straightforward.

The *second* sensor has a medium difficulty fabrication procedure (Chapter 4). It is considered that the silica fan-out device is commercially provided. In this case the inscription of the FBGs has to be produced "in-house", due to the novelty of the MCF. The phase mask technique used for the inscription is a well-established technique. The main difficulty exists in the alignment of the optics to the fibre. However, after the optimisation of the optics, inscription of FBGs on several fibre sections can be achieved with repeatability and in a small period of time.

The fabrication of this sensor requires only one splicing procedure, MCF to MCF which is attached on the silica fan-out device. A splicer with rotating motors and fibre cross sectional monitoring is required. Cross sectional orientation of the fibres has to be monitored in order to achieve a good quality splice. It is considered that ±3.2° to ±3.9° angular offset can provide a good quality splice.

The *third* sensor has the highest difficulty of fabrication. In this case the inscription of FBGs has to be done selectively into each core of the MCF. Therefore, exchange of phase masks on the FBG inscription set up has to be performed. This introduces different risks during the fabrication of the sensor: (a) the misalignment of the optics and optical fibre on the set-up, (b) inscription of the FBGs at a slightly different point along the MCF

or inscription of an FBG into more than on core and (c) damage of the phase masks during the transaction. The fabrication of this sensor requires a splicing and a tapering procedure. Similarly, to the second sensor a splicer capable of fabricating fibre tapers is required.

All three sensors have in common the cantilever geometry when the fibre is fixed in a holder. The fixed point of the sensors is basically a weak point, since a break of the 'stem' can easily occur on this region. Finally, uncertainties on the exact position of the FBGs in regards to the fixed point can be introduced during this step of sensors fabrication.

6.3.2. Strain Sensitivity

The strain sensitivity of all three curvature sensors is affected by several parameters. The most significant is the rigidity of the stem's material. The *first* sensor has stronger stiffness, since its structure is thicker, in comparison to the *second* and the *third*. Moreover, the stem's structure affects the strain sensitivity according to equation 2.15. The separation (d) of the strain gauges determines the measured strain shift:

$$\Delta\varepsilon = \frac{d}{R} \qquad \text{Equation 6.1}$$

where, $\kappa = \frac{1}{R}$ is the curvature. Thus, the highest the separation that the gauges have, the highest strain difference they experience. Therefore, the *first* sensor is considered to prevail over the *second* and the *third* sensor.

Moreover, the curvature at a point closer to the fixed point of the cantilever geometry is stronger in regards to any other region above this point. Hence according to equations 2.23 and 2.26:

$$\kappa = \frac{1}{R} = \frac{3\,(l-x)}{l^3}\ \ \nu_l \qquad \text{Equation 6.2}$$

where, l is the cantilever length. In the case of the fabricated curvature sensors, the x position coincides with the position of the FBGs along the cantilever. Therefore, by positioning the FBGs closer to the fixed point, sensors with higher strain sensitivity can be produced. All three sensors have design flexibility (by changing the FBGs position) to tune their strain sensitivity using this feature. Hence, in this case none of the three sensors outmatches the others.

Finally, the strain sensitivity of the curvature sensors is strongly related with the FBGs' reflected wavelength peak position difference (Equation 2.15):

$$\Delta\lambda_{reflected} \cong c\frac{d}{R} \qquad \text{Equation 6.3}$$

Sensors with the lowest noise on the wavelength difference are more sensitive. The noise of the wavelength peak positions is related to the interrogation's system specifications. It depends on the peak position and threshold analysis of the reflectance spectrum of the inscribed FBGs. Moreover, it is affected by the FBGs strength and their spectral width. The noise levels of all three sensors are comparable, with the *second* having the lowest (± 7.5 pm).

6.3.3. Temperature Sensitivity

The structure of all three sensors suggests that they will be temperature compensated. When the wavelength peak positions *shifts* of *FBGs pairs* are monitored the temperature effect upon the individual FBGs is expected to be eliminated. The general concept is that the FBGs lie close to each other and are surrounded by the same material. Hence, all FBGs experience the same variations due to local environment temperature changes. However, all three sensors displayed drifts on their FBGs differential response due to temperature changes while strain isolated.

The *first* sensor displayed 200 pm drift on the differential response of the FBGs within a temperature range of ~10° C. The graph reporting this drift is given in the third Chapter of this thesis (Figure 3-7). This drift can be attributed to slight misalignment of the FBGs embedded into the 'stem' structure. Moreover, in this case the optical adhesive (surrounded material) is a separate material to the strain gauges (optical fibres, silica glass). Thus, this 'stem' has variable overall thermal expansion coefficient.

The *second* sensor is expected to be even less temperature sensitive. In this case, the 'stem' is only one fibre, therefore the cladding material is the same with the strain gauges' material (cores of the fibre, silica glass). However, temperature effects upon its expected performance were reported [5]. In this case the FBGs were not affected by their local environment temperature. Nevertheless, their differential response was affected by the environmental temperature of the silica fan-out device. A drift on the FBGs differential response of 460 pm over 10 ° C temperature variations was reported. These effects were

due to cavities that were found in the silica fan-out device. An extensive study on these effects is reported in Chapter 4.

Finally, the *third* sensor has the silica fan-out device replaced to a MCF tapered fan-out device. Therefore, the temperature effects due to cavities are expected to be eliminated and the differential response of the FBGs is expected to display no drift. However, a 30 pm drift on this response was mentioned in Chapter 5. This drift is significantly lower than the previous sensors. It is considered to occur due to uncertainties in the experimental set up or slight differentiation of the position were all three FBGs were inscribed.

6.3.4. Packaging and Robustness for field trials

Two of the most significant criteria for choosing the most suitable sensor for field trials during the Lakshmi project was their ease of deployment and their robustness. The sensors were aimed to be used for benthic flow measurements. Hence, small volume sensors which can be embedded into stronger materials are more suitable. Moreover, less complicated optically designed sensors are easier to package, handle and modify during field trials.

The simple design of the *first* sensor makes it the most suitable for field trials. For simultaneous interrogation of an array of the FBGs this sensor requires Wavelength division multiplexers (WDMs), which can increase the overall volume of each sensor. However, the first sensor is considered robust and easy to handle.

The *second* sensor has the most complicated design. The silica fan-out device requires a protective box where it can be enclosed. Moreover, the curvature sensor requires WDM for simultaneous interrogation of FBGs. Hence, this sensor has overall big volume and is considered as fragile and difficult to handle.

The *third* sensor has the lowest designed volume. The WDM in this case is replaced to the tapered region of the MCF. It can be considered fragile due to the low diameter of the sensor at the tapered region. However, proper packaging (with a tapering case, Figure 6-9) can provide good robustness. Therefore, it is considered this sensor has potential to be easy to handle.

6.3.5. Scalability

Two different parameters have to be considered in order the sensors' scalability to be speculated. Their costs of fabrication and their optical losses of the transmitted light. The fabrication of *first* sensor can be considered as the most cost effective sensor. Moreover, this sensor has low optical losses. In this case, only the insertion losses of the WDMs have to be explored. Hence the *first* sensor is the most suitable for the scaled up trial experiments of LAkHsMI project.

The *second* sensor has the highest cost of fabrication due to the novelty on the MCF structure (not a standard SMF). Additionally, the silica waveguide fan-out device is an additional optical component which have to be fabricated with high precision. Moreover, it requires specialised experimental equipment (splicer) for the fabrication. This sensor has increased optical losses due to the interface of the silica fan-out device.

The *third* sensor has lower costs of fabrication in regards to the second sensor, due to the elimination of the silica fan-out device. However, this sensor has increased optical losses due to the tapering procedure. In the overall scheme this sensor can reach the first's sensors potentials or even overcome them by optimising its optical losses.

Finally, the time endurance of the sensors can be considered as a parameter that affects their scalability. The *first* sensor is considered to have the quickest corrosion over time. The different materials (optical adhesive and optical fibres) with which the 'stem' is fabricated have weaker bonds in comparison to the MCF 'stem'. The *second* sensor is more prone to corrosion in regards to the *third,* due to the silica waveguide fan-out device. The device has a specific temperature range it can operate and over this range it is possible to be damaged. Hence, it is considered that the *third* sensor has the strongest endurance over time.

Table 6-1. Comparison of all three fabricated curvature sensors for Lakshmi project.

low	
medium	
high	

		Curvature sensors		
		first sensor	**second sensor**	**third sensor**
Fabrication	Difficulty	4 SMF-SMF splices	1 MCF-MCF splice/ FBGs inscription	1 MCF-SMF splice/ FBGs individual inscription
	Time consuming	~8hours/sensor	~4hours/sensor	~8hours/sensor
Strain sensitivity	Materials stiffness	Optical adhesive	Silica glass	Silica glass
	Structure	50µm core separation	350µm SMF to SMF separation	50µm core separation
	Noise levels	± 10 pm	± 7.5 pm	± 10 pm
Temperature sensitivity (10° C)		200pm drift	450pm drift	30pm drift
Packaging	Fragility	5 weak points	3 weak points and fan-out device	3 weak points and tapering region
	Designed volume	4 SMFs	4 SMFs and fan-out device	1 SMF and tapering region
Scalability	Cost	Off the shelf supplies	Novel MCF and fan-out device	Novel MCF
	Optical losses	4 Splices	1 Splice and fan-out device	1 Splice and tapering region
	Corrosion over time	2 different materials (optical fibres and adhesive)	1 Material but 2 different component (optical fibre and fan-out device)	1 Material (optical fibre)

6.4. Future work

The primary objective of LAkHsMI project is to provide flow sensors which can be used in harsh benthic environments. The development in a short and long term of the optical fibre sensors for Lakshmi project will be discussed here. The focus will be on the FBG *Attitude* sensor (Figure 6-7) and the curvature sensors which will be referred as *first* (Figure 6-4), *second* (Figure 6-8) and *third* (Figure 6-9), similarly to the previous section.

Short-term developments

The *Attitude* sensor has the expected performance. However, improvements on its accuracy (± 2°) of measurements should be considered. This can be achieved with automated linear and rotational calibration procedures.

Progress on the *first* sensor should be towards improving the temperature sensitivity which can be reduced by producing an automated means of aligning the SMFs in the

fabrication set up. It has been shown that three FBGs are required for a two dimensional measurement of the cantilever curvature [6]. Hence, the additional FBG can be calibrated in order to measure and compensate the wavelength shifts produced on the three FBGs (which measure the curvature) due to temperature

The temperature sensitivity of the *second* sensor has been determined to be due to the silica waveguide fan-out device. Therefore, an enclosure which will maintain the device at a stable temperature is required. Moreover, the same enclosure can operate as an external protection for the fragile fan-out waveguide device.

The *third* sensor has the highest potential. Different techniques or improvements on the existing FBG inscription can be explored. The exploration of different cylindrical lenses or addition of lenses on the phase mask technique can be performed with the goal of individual FBG fabrication. Moreover, the point-by-point FBG inscription [7] can eliminate the risks of inscribing FBGs into more than one core. Additionally, studies on optimising the SMF to MCF splicing procedure can be explored. Finally, the ideal tapering parameters can be investigated with end goal to minimise the optical losses of the sensor. A commercially available 1×4 bidirectional coupler has insertion losses of ~7-8 dB at central wavelength 1550 nm [8].

Long-term developments

Several optical fibre gyroscope sensors have been reported in literature with the majority of them using the Sagnac effect [2]. Hence the FBG *Attitude* sensor can be replaced with these well established and accurate sensors. However, progress on combing the FBG interrogation technology (used for the flow sensors) with the interference spectroscopy (used for the attitude sensor) has to be derived.

Further studies on the *first* (four SMFs) curvature sensor could be focused on its packaging and decrease of volume. The packaging can be mainly improved at the "weak" points (splicing and the fixed point), using different fibre protection techniques such as the UV curing protection sleeves of bare fibres. Moreover, other techniques and schemes of FBGs multiplexing, such as Time Division Multiplexing (TDM) can be explored. Finally, different optical adhesives for the fabrication of the 'stem' sensing element can be studied. Thus the most suitable adhesive needs to be determined in regards to ageing, strain and temperature sensitivity.

Regarding the progress on the MCF curvature sensors (*second* and *third*), fabrication of a different interface between MCF to SMF devices can be considered. An interesting example is to cut the MCF in longitudinal and perpendicular planes. This can be achieved using short pulse lasers with laser machining techniques [9]. After the cutting each core remains in one quartile of the cross section of the MCF. Consequently, each quartile with one core of the MCF can be spliced on a SMF.

An alternative example can be the inscription of waveguides similar to the ones that the *second* senor uses but placed in the MCF itself. The waveguides will intersect with one specific core of the MCF. Then the light will be transmitted through a SMF spliced on this core. In this case inscription of different FBGs into the four cores of the MCF is required.

Different optical fibres sensing techniques can be explored for the fabrication of the curvature or flow sensors. Recently researchers have focused on MCFs with twisted cores for shape sensing [10]. Moreover, distributed Brillouin optical fibre sensors are extensively explored for flow sensing [11]. In this case, the deployment requires well established and simple techniques, similar to electrical cables.

Finally, according to their working principles the curvature sensors which were reported here can be used for alternative applications. Examples include the anemometers or accelerometers. In this case the sensors can be used for measurements of the wind velocity for the purposes of building wind farms.

6.5. Conclusions

This chapter includes an overall review of the sensors produced for LAkHsMI project. The fabricated optical fibre curvature sensors, which can be used as flow sensors, were compared to each other. Each sensor displays different strengths and weaknesses. However, the *first* sensor was the one used for field trails due to the simplicity of its fabrication and scalability.

Nevertheless, the *third* sensor can be characterised as the “next generation” flow sensor for LAkHsMI project. This sensor has potential lowest possible volume and has the lowest temperature sensitivity. Moreover, other optical components (such as WDMs and couplers) are eliminated due its working principles. The two main drawbacks of this

sensor is complexity of the fabrication and the optical losses. Both can be improved with further study.

6.6. References

[1] D. Barrera, V. Finazzi, J. Villatoro, S. Sales, and V. Pruneri, "Packaged Optical Sensors Based on Regenerated Fiber Bragg Gratings for High Temperature Applications," *IEEE Sensors Journal*, vol. 12, no. 1, pp. 107-112, 2012.

[2] V. M. N. Passaro, A. Cuccovillo, L. Vaiani, M. Carlo, and C. E. Campanella, "Gyroscope Technology and Applications: A Review in the Industrial Perspective," *Sensors (Basel)*, vol. 17, no. 10, Oct 7 2017.

[3] G. M. H. Flockhart, W. N. MacPherson, J. S. Barton, and J. D. C. Jones, "Two-axis bend measurement with Bragg gratings in multicore optical fiber," *Optics Letters*, vol. 28, no. 6, p. 3, 2003.

[4] R. R. Thomson, H. T. Bookey, N. D. Psaila, A. Fender, S. Campbell, W. N. MacPherson, J. S. Barton, D. T. Reid, and A. K. Kar, "Ultrafast-laser inscription of a three dimensional fan-out device for multicore fiber coupling applications," *Optics Express*, vol. 15, no. 18, pp. 11691-11697, 2007.

[5] N. Papachristou, J. Morton, R. M. Carter, R. R. J. Maier, and W. N. MacPherson, "Temperature effects upon a multicore optical fibre curvature sensor,", in Proc. IEEE sensors, Glasgow, pp. 1-3, 2017.

[6] G. M. H. Flockhart, W. N. MacPherson, J. S. Barton, J. D. C. Jones, L. Zhang, and I. Bennion, "Two-axis bend measurement with Bragg gratings in multicore optical fiber," *Optics Letters*, vol. 28, no. 6, p. 387, 2003.

[7] G. D. Marshall, R. J. Williams, N. Jovanovic, M. J. Steel, and M. J. Withford, "Point-by-point written fiber-Bragg gratings and their application in complex grating designs," *Optics Express*, vol. 18, no. 19, pp. 19844-19859, 2010.

[8] L. components. (2018). *Compact fiberoptic coupler/splitter 1x4*. (Access date: 05.10 .2018) Available: www.lasercomponents.com/de-en/product/singlemode-couplers-couplers-pm/

[9] S. Nikumb S. Nikumba, Q. Chena , C. Lia , H. Reshefa , H.Y. Zhengb , H. Qiub , D. Low, "Precision glass machining, drilling and profile cutting by short pulse lasers," *Thin Solid Films*, vol. 477, no. 1, pp. 216-221, 2005.

[10] M. Amanzadeh, S. M. Aminossadati, M. S. Kizil, and A. D. Rakić, "Recent developments in fibre optic shape sensing," *Measurement*, vol. 128, pp. 119-137, 2018.

[11] X.-F. Zhao, L. Li, Q. Ba, and J.P. Ou, "Scour monitoring system of subsea pipeline using distributed Brillouin optical sensors based on active thermometry," *Optics & Laser Technology*, vol. 44, no. 7, pp. 2125-2129, 2012.

APPENDIXES:

[1] LabVIEW script for automated temperature measurements from K-type thermocouples:

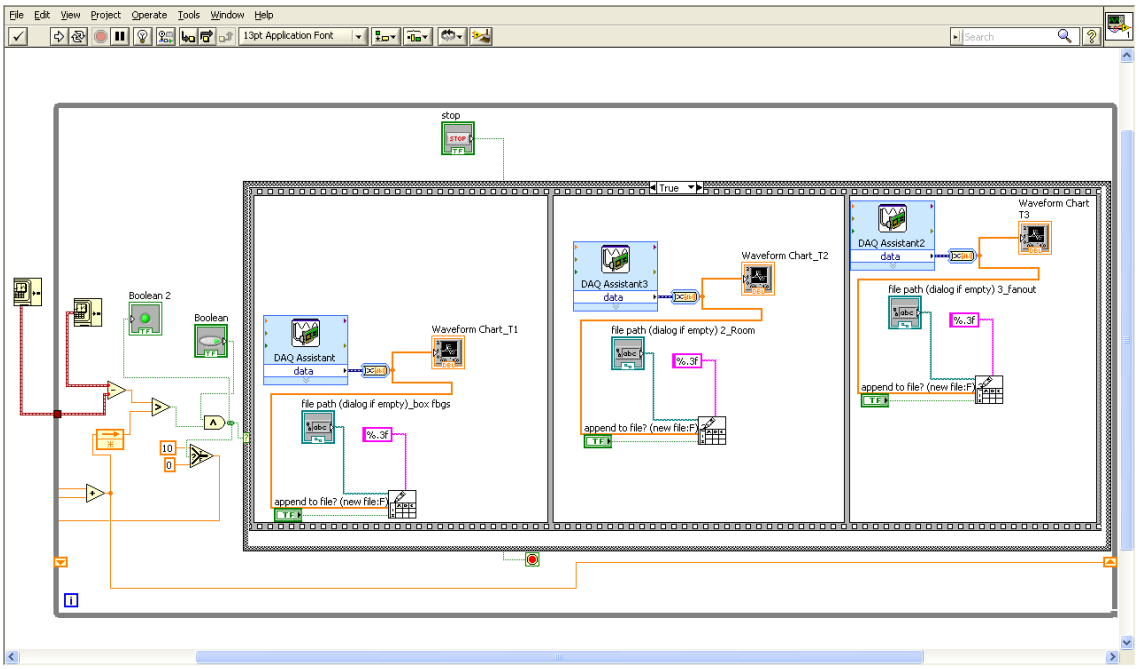

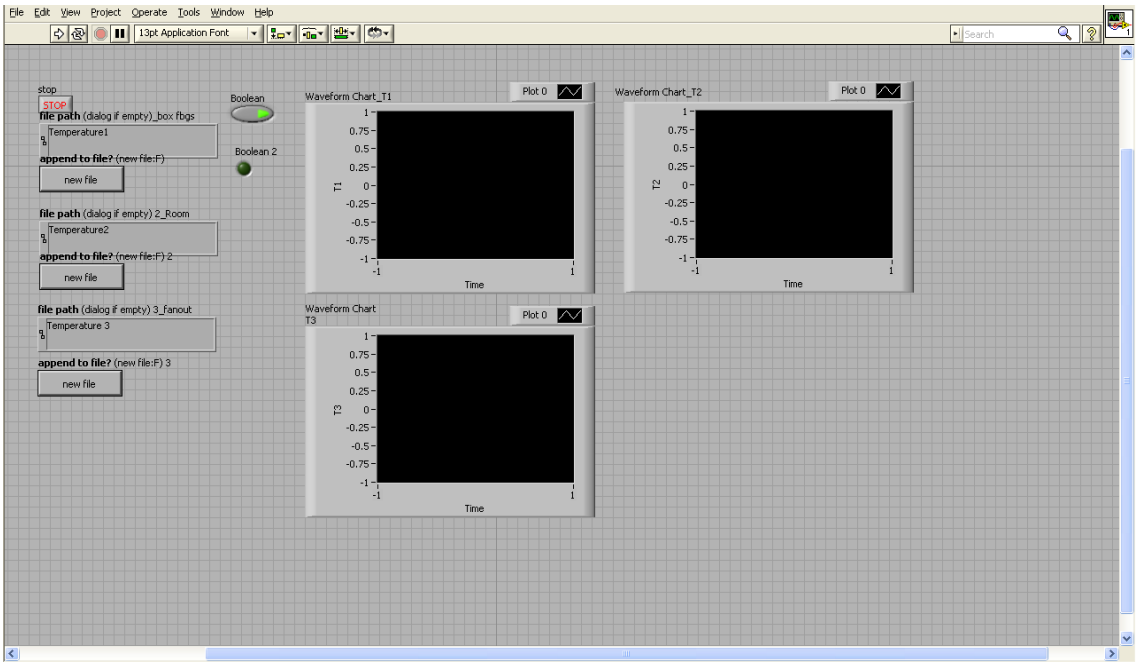

[2] Calculation of the FWHM:

```
plot(spec(:,1),spec(:,2))
[M0,N0]=max(spec(:,2));
lmax=spec(N0,1);
athalf=M0/2; % athalf=M0-3 (for the dBm scale)
k=0
for i=1:1:20039
    if spec(i,2)>=athalf && k==0
    firsty=spec(i,2);
    firstpoint=spec(i,1);
    k=1
    end
    if spec(i,2)<=athalf && k==1
    secondy=spec(i,2);
    secondpoint=spec(i,1);
    k=2
    end
end
FWHM=secondpoint-firstpoint
```

[3] MatLab™ scripts for the calibration of the FBG curvature sensors for the Attitude:

- Linear calibration:

```
%YOU HAVE TO GIVE ME TABLES: DIRECTION1 AND DIRECTION2 SO I CAN MOVE ON
%IF YOU WANT ME TO CALCULATE CORRECTLY DEFLECT LINEARLY YOUR SENSOR
%DO A 0.5mm DEFLECTION
%STAY THERE FOR 1 MINUTE
%SAMPLE EVERY 1 msec
[m,n]=size(Direction1);
for i=1:1:m;
    x(i,1)=i;
end;
for FBG=1:1:4
sum=0;
k=1;
l=0;
t=10000;
for n=50001:60000:m
for v=t:1:n
    sum=Direction1(v,FBG)+sum;
    l=l+1;
end
    average(k,FBG)=sum/l;
    l=0;
    k=k+1;
    sum=0;
    t=t+60000;
end
end
x2(1,1)=30000;
x2(2,1)=90000;
x2(3,1)=150000;
x2(4,1)=210000;
x2(5,1)=270000;
x2(6,1)=330000;
```

```
%CHECK IF EVERYTHING IS OK (WITH MY AVERAGING)!!! and decide which two
core
%pairs i am using
for FBG=1:1:4
    figure(FBG)
    hold on
    plot(x,Direction1(:,FBG))
    scatter(x2,average(:,FBG))
end
%TELL ME MY CORE PAIRS ((1,2)=1 (1,3)=2 (1,4)=3, (2,3)=4, (2,4)=5,
(3,4)=6)
corepair1=1;
corepair2=5;
wavelengthshift(:,1)=average(:,1)-average(:,2); %CORE PAIR 1,2
wavelengthshift(:,2)=average(:,1)-average(:,3); %CORE PAIR 1,3
wavelengthshift(:,3)=average(:,1)-average(:,4); %CORE PAIR 1,4
wavelengthshift(:,4)=average(:,2)-average(:,3); %CORE PAIR 2,3
wavelengthshift(:,5)=average(:,2)-average(:,4); %CORE PAIR 2,4
wavelengthshift(:,6)=average(:,3)-average(:,4); %CORE PAIR 3,4
%calculate my curvature
%FBGs distance (z)
z=6;
%Cantilever length (l)
l=20;
for o=1:1:6;
    W=(o-1)*0.5;
    c(o,:)=(((3*(l-z)*W)/(l^3))*1000)/1000000000;
end;

%for mydata=1:1:6
    %figure(mydata)
    %scatter(c(:,1),wavelengthshift(:,mydata))
%end

ft = fittype( 'poly1' );
[fitresult, gof] = fit( c, wavelengthshift(:,corepair1), ft );
coeffvals = coeffvalues(fitresult);
c12=coeffvals(1,2);
p=coeffvals(1,1);
ft = fittype( 'poly1' );
[fitresult, gof] = fit( c, wavelengthshift(:,corepair2), ft );
coeffvals = coeffvalues(fitresult);
c23=coeffvals(1,2);
r=coeffvals(1,1);
%-----------------------SECOND DIRECTION-----------------------------
[m2,n2]=size(Direction2);
for i=1:1:m2;
    x3(i,1)=i;
end;
for FBG=1:1:4
sum2=0;
k=1;
l=0;
t=10000;
%gia ena lepto metrisi, me 1 msec, vima 0.5mm
for n=50001:60000:m2
for v=t:1:n
    sum2=Direction2(v,FBG)+sum2;
    l=l+1;
end
    average2(k,FBG)=sum2/l;
```

```
    l=0;
    k=k+1;
    sum2=0;
    t=t+60000;
end
end
%CHECK IF EVERYTHING IS OK (WITH MY AVERAGING)!!! and decide which two
core
%pairs i am using
for FBG=5:1:8
    FBG2=FBG-4;
    figure(FBG)
    hold on
    plot(x3,Direction2(:,FBG2))
    scatter(x2,average2(:,FBG2))
end
wavelengthshift2(:,1)=average2(:,1)-average2(:,2); %CORE PAIR 1,2
wavelengthshift2(:,2)=average2(:,1)-average2(:,3); %CORE PAIR 1,3
wavelengthshift2(:,3)=average2(:,1)-average2(:,4); %CORE PAIR 1,4
wavelengthshift2(:,4)=average2(:,2)-average2(:,3); %CORE PAIR 2,3
wavelengthshift2(:,5)=average2(:,2)-average2(:,4); %CORE PAIR 2,4
wavelengthshift2(:,6)=average2(:,3)-average2(:,4); %CORE PAIR 3,4

ft = fittype( 'poly1' );
[fitresult, gof] = fit( c, wavelengthshift2(:,corepair1), ft );
coeffvals = coeffvalues(fitresult);
c12_2=coeffvals(1,2);
q=coeffvals(1,1);
ft = fittype( 'poly1' );
[fitresult, gof] = fit( c, wavelengthshift2(:,corepair2), ft );
coeffvals = coeffvalues(fitresult);
c23_2=coeffvals(1,2);
s=coeffvals(1,1);

linearcalibrationparametersD1(1,1)=c12;
linearcalibrationparametersD1(2,1)=p;
linearcalibrationparametersD1(3,1)=c23;
linearcalibrationparametersD1(4,1)=r;

linearcalibrationparametersD2(1,1)=c12_2;
linearcalibrationparametersD2(2,1)=q;
linearcalibrationparametersD2(3,1)=c23_2;
linearcalibrationparametersD2(4,1)=s;

%SAVE THE RESULTS THAT I GAVE YOU linearcalibrationparametersD1 AND
%linearcalibrationparametersD2
%CREATE A 4x2 TABLE WHICH YOU WILL HAVE TO IMPORT IT TO THE rotational
%calibretiongyronew script
%THANK YOU :D
```

- Rotational Calibration:

```
%YOU HAVE TO GIVE ME TABLES: ROTATION1 AND LINEARCALIBRATIONPARAMETERS
%IF YOU WANT ME TO CALCULATE CORRECTLY ROTATE 360 YOUR SENSOR
%DO A 10 DEGREES ROTATION
%STAY THERE FOR 30 SECONDS
%SAMPLE EVERY 1 msec
%USE THE SAME CORE PAIRS WITH THE LINEAR CALIBRATION
[m,n]=size(rotation1);
k=1;
```

```
for i=1:1:m;
  x(k,1)=k;
  k=k+1;
end

for FBG=1:1:4
sum=0;
k=1;
l=0;
t=10000;

%gia 30 sec metrisi, me 1 msec, vima 10 moires
for n=25001:30000:1110000;
for v=t:1:n;
    sum=rotation1(v,FBG)+sum;
    l=l+1;
end
    average(k,FBG)=sum/l;
    l=0;
    k=k+1;
    sum=0;
    t=t+30000;
end
end
g=15000;

for i=1:1:37;

    x2(i,1)=g;
    g=g+30000;
end
for FBG=1:1:4
    figure(FBG)
    hold on
    plot(x,rotation1(:,FBG))
    scatter(x2,average(:,FBG))
end
%TELL ME MY CORE PAIRS ((1,2)=1 (1,3)=2 (1,4)=3, (2,3)=4, (2,4)=5,
(3,4)=6)
corepair1=1;
corepair2=5;
wavelengthshift(:,1)=average(:,1)-average(:,2); %CORE PAIR 1,2
wavelengthshift(:,2)=average(:,1)-average(:,3); %CORE PAIR 1,3
wavelengthshift(:,3)=average(:,1)-average(:,4); %CORE PAIR 1,4
wavelengthshift(:,4)=average(:,2)-average(:,3); %CORE PAIR 2,3
wavelengthshift(:,5)=average(:,2)-average(:,4); %CORE PAIR 2,4
wavelengthshift(:,6)=average(:,3)-average(:,4); %CORE PAIR 3,4
%FBGs distance (z)
z=6;
%Cantilever length (l)
l=20;
%MYBIGK in nm
MYBIGK=((3*(l-z))/(l^3))*(10^(-12));
%MYBIGA I need the linear calibration parameters for the same core pairs
p=linearclibrationparameters(2,1);
r=linearclibrationparameters(4,1);
q=linearclibrationparameters(2,2);
s=linearclibrationparameters(4,2);
MYBIGA=1/((s*p)-(q*r));
```

```
c12=(linearclibrationparameters(1,1)+linearclibrationparameters(1,2))/
2;
c23=(linearclibrationparameters(3,1)+linearclibrationparameters(3,2))/
2;
Deflection1(:,1)=((s*MYBIGA)*(wavelengthshift(:,corepair1)-c12)-
(q*MYBIGA)*(wavelengthshift(:,corepair2)-c23))/MYBIGK;
%Deflection1 IN mm
Deflection1(:,1)=Deflection1(:,1)/1000000;
%-------------------------------------ROTATION2-----------------------
------
[m,n]=size(rotation2);
k=1;
for i=1:1:m;
  x3(k,1)=k;
  k=k+1;
end

for FBG=1:1:4
sum=0;
k=1;
l=0;
t=10000;

%gia 30 sec metrisi, me 1 msec, vima 10 moires
for n=25001:30000:1110000;
for v=t:1:n;
    sum=rotation2(v,FBG)+sum;
    l=l+1;
end
    average2(k,FBG)=sum/l;
    l=0;
    k=k+1;
    sum=0;
    t=t+30000;
end
end
g=15000;

for i=1:1:37;

    x2(i,1)=g;
    g=g+30000;
end
for l=5:1:8
    FBG=l-4;
    figure(l)
    hold on
    plot(x3,rotation2(:,FBG))
    scatter(x2,average2(:,FBG))
end
%TELL ME MY CORE PAIRS ((1,2)=1 (1,3)=2 (1,4)=3, (2,3)=4, (2,4)=5,
(3,4)=6)
corepair1=1;
corepair2=5;
wavelengthshift2(:,1)=average2(:,1)-average2(:,2); %CORE PAIR 1,2
wavelengthshift2(:,2)=average2(:,1)-average2(:,3); %CORE PAIR 1,3
wavelengthshift2(:,3)=average2(:,1)-average2(:,4); %CORE PAIR 1,4
wavelengthshift2(:,4)=average2(:,2)-average2(:,3); %CORE PAIR 2,3
wavelengthshift2(:,5)=average2(:,2)-average2(:,4); %CORE PAIR 2,4
wavelengthshift2(:,6)=average2(:,3)-average2(:,4); %CORE PAIR 3,4
```

```
Deflection2(:,1)=((p*MYBIGA)*(wavelengthshift2(:,corepair2)-c23)-
(r*MYBIGA)*(wavelengthshift2(:,corepair1)-c12))/MYBIGK;
%Deflection1 IN mm
Deflection2(:,1)=Deflection2(:,1)/1000000;
%-----------------------------------------------------------------
-----

%I AM DONE WITH THE CALIBRATION
%YOU HAVE TO TAKE TABLES DEFLECTION1/2 AND USE ORIGIN FOR SINUSOIDAL
%FITTING
%GOOD LUCK WITH YOUR RESULTS! :D
```

[4] MatLab™ script for noise determination:

```
[m,n]=size(Direction1);
for i=1:1:m;
    x(i,1)=i;
end;

zero(:,1)=Direction1(1:100,1);
M0=max(zero(:,1));
N0=min(zero(:,1));
average0=(M0-N0)/2;
x0(:,1)=x(1:100,1);

one(:,1)=Direction1(134:243,1);
M1=max(one(:,1));
N1=min(one(:,1));
average1=(M1-N1)/2;
x1(:,1)=x(134:243,1);

two(:,1)=Direction1(249:364,1);
M2=max(two(:,1));
N2=min(two(:,1));
average2=(M2-N2)/2;
x2(:,1)=x(249:364,1);

three(:,1)=Direction1(373:478,1);
M3=max(three(:,1));
N3=min(three(:,1));
average3=(M3-N3)/2;
x3(:,1)=x(373:478,1);

four(:,1)=Direction1(505:602,1);
M4=max(four(:,1));
N4=min(four(:,1));
average4=(M4-N4)/2;
x4(:,1)=x(505:602,1);

five(:,1)=Direction1(617:716,1);
M5=max(five(:,1));
N5=min(five(:,1));
average5=(M5-N5)/2;
x5(:,1)=x(617:716,1);

hold on
plot(x,Direction1(:,1))
plot(x0,zero(:,1))
```

```
plot(x1,one(:,1))
plot(x2,two(:,1))
plot(x3,three(:,1))
plot(x4,four(:,1))
plot(x5,five(:,1))

averageofallnoises=(average0+average1+average2+average3+average4+avera
ge5)/5
```

[5] MatLab™ scripts on averaging the wavelength peak positions for the MCF curvature sensors:

```
[m,n]=size(Direction1);
for i=1:1:m;
    x(i,1)=i;
end;
for FBG=1:1:4;
    sum=0;
    %initial time range
    l=200;
    j=500;
    b=0;

    for k=1:1:6
        for t=l:1:j
        sum=Direction1(t,FBG)+sum;
        b=b+1;
        end
    average(k,FBG)=sum/b;
    %time range
    l=l+1300;
    j=j+1300;
    sum=0;
    b=0;
    end
end
    x2(1,1)=600;
    x2(2,1)=1700;
    x2(3,1)=3400;
    x2(4,1)=4700;
    x2(5,1)=6000;
    x2(6,1)=7300;
for FBG=1:1:3;
    figure(FBG)
    hold on
    plot(x,Direction1(:,FBG));
    scatter(x2,average(:,FBG));
end
```

[6] MatLab™ scripts on determining the distance between the two reflection peaks using the He-Ne interference pattern, using measurements taken from the low coherence experiment:

```
x=AU(:,1);
y1=IRinterference(:,2);
y2=HeNeinterference(:,3);
```

```
hold on
l=1000000;
plot(x(1:l/2),y1(1:l/2))
plot(x(l/2:l,1),y1(l/2:l,1))
plot(x,y2)
M=max(y1(1:l/2,1));
[M,firstmaxposition]=max(y1(1:l/2,1));
N=max(y1(l/2:l));
[N,secondmaxposition]=max(y1(l/2:l));
secondmaxposition=secondmaxposition+l/2-1;
l=1;
m=0;
REDpeaks=0;
%Measures how many He-Ne peaks exists between the reflection signals
for l=firstmaxposition:1:secondmaxposition
if any(y2(l,1)>0.0037);
    m=1;
end
if (m==1) && any(y2(l,1)<-0.0037);
    REDpeaks=1+REDpeaks;
    m=0;
end
l=l+1;
end
%Translates the peaks to actual distance
distanceinnm=(REDpeaks*632.8)/2;
distanceinmm=distanceinnm*(10^(-6))
```

[7] Light coupling from one core to all four cores of the MCF:

- Actual script:

```
close all
clear all
% refractive indeces
nclad=1.45;
ncladsquare=nclad^2;
ncore=1.4542;
ncoresquare=ncore^2;
% l= wavelenght
l=1.553;
% k=wavenumber
k=(2*pi)/l;
% a= core RADIUS,if I change the core radius at this
% programme I have to change it MYFUN as well
waistdiameter=50
a=((waistdiameter*8)/125)/2;
% I call a function "myfun" from an other matlab script
%this function is a sytsem of functions for modal parameters and an
%equation that includes bessel equations.
fun=@myfun
%i am asking to solve the system and i give some initial values [1,1,1]
in order
%matlab to solve them.
%The answers are on a matrix [x(1) x(2) x(3)].
x= fsolve(fun,[1,1,1]);
u=real(x(1));
w=real(x(2));
b=real(x(3));
Vsquare=u^2+w^2;
```

```
V=Vsquare^(1/2);
% I have all i need to calculate the coefficient u,w,v,a and I need to
give
% the distances of the cores
ds=(50*waistdiameter)/125;
dw=(2^(1/2))*ds;
e=(l/(2*pi*ncore))*(u^2/(a^2*Vsquare));
fs=(besselk(0,w*ds/a))/(besselk(1,w))^2;
fw=(besselk(0,w*dw/a))/(besselk(1,w))^2;
%I multiply the coupling coefficient by 1000 because I calculate it in
1/um
%I want to have it in 1/mm.
Cw=(e*fw)*1000;
Cs=(e*fs)*1000;
%Then the power at each fiber core will be dependent on the distance z
and i
%have to create graphs for that.
syms z
Pzero=100;
Pone=(1/4)*Pzero*(1+2*cos(2*Cs*z)*cos(2*Cw*z)+(cos(2*Cs*z))^2);
Ptwo=(1/4)*Pzero*((sin(2*Cs*z))^2);
Pthree=(1/4)*Pzero*(1-2*cos(2*Cs*z)*cos(2*Cw*z)+(cos(2*Cs*z))^2);
Pfour=(1/4)*Pzero*((sin(2*Cs*z))^2);
hold on
ezplot(Pone,[0,18])
ezplot(Ptwo,[0,18])
ezplot(Pthree,[0,18])
ezplot(Pfour,[0,18])

%The two cores have the same power coupling since they are at the same
%distance colour purple the diagonal one is yellow.
%--------------------------------------------------------------------
```

- Script of the function used in the actual script:

```
function F = myfun(x)
u=x(1); w=x(2); b=x(3);
l=1.553;
a=1.6;
k=(2*pi)/l;
nclad=1.45;
ncore=1.4542;
F(1)=u*besselk(0,w)*besselj(1,u)-w*besselk(1,w)*besselj(0,u);
F(2)=a*sqrt(ncore^2*k^2-b^2)-u;
F(3)=a*sqrt(b^2-nclad^2*k^2)-w;
end
```

[8] Mechanical designs of the fibre and phase masks holders:

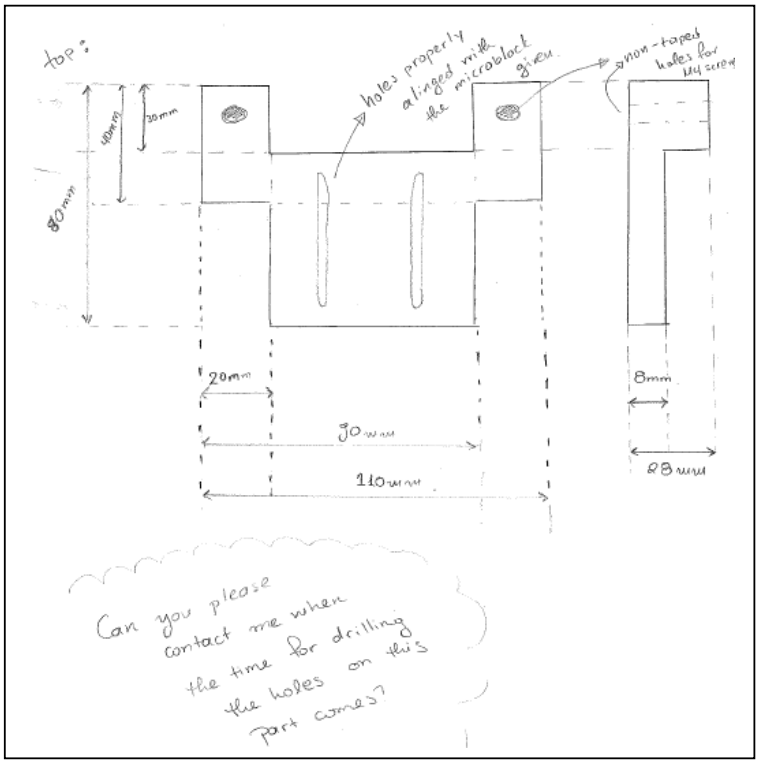

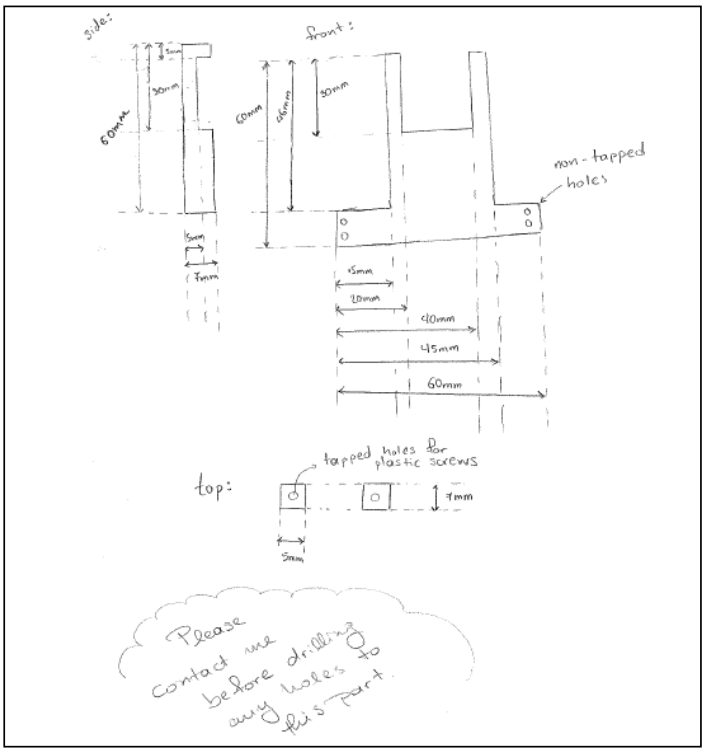

[9] MatLab™ scripts for the threshold analysis to determine the effect of the "unwanted" FBG:

- Determination of the reflected wavelength peak position using a Gaussian fit:

```
filename = 'myspectra';
str = [filename,'= initial;'];
eval(str);

%wavelength axis
x=myspectra(:,1);
[m,n]=size(myspectra);

for p=2:1:18
%choise of the threshold
threshold=p*0.08;
myspectra(:,4)=myspectra(:,2)+myspectra(:,3);
for d=2:1:4
absolutespectra(:,d)=myspectra(:,d)-myspectra(1,d);
fitresult=fit(x,absolutespectra(:,d),fittype( 'gauss1' ));
for k=1:1:m
    fitdata(k,d)=fitresult(x(k));
    [maxvalue,maxindex]=max(fitdata(:,d));
    boundary(1,d)=maxvalue*threshold;
end
end
for k=2:1:4
for i=1:1:m
    thresholdline(i,k)=boundary(1,k);
end
end

for e=2:1:4
subspectrum(:,e)=fitdata(:,e)-thresholdline(:,e);
end
for t=2:1:4
%find my first intercept
for i=m:-1:1;
   if subspectrum(i,t)>0;
       firstwavelength=x(i,1);
   end;
end;
%find my second intercept
for i=1:1:m;
   if subspectrum(i,t)>0;
       lastwavelength=x(i,1);

   end;
end;
%find the reflected wavelength peak position
peakposition(p,t)=(firstwavelength+lastwavelength)/2;
end

end
```

```
hold on
plot(x,fitdata(:,2))
plot(x,fitdata(:,3))
plot(x,thresholdline(:,2))
plot(x,thresholdline(:,3))
plot(x,absolutespectra(:,2))
plot(x,absolutespectra(:,3))
plot(x,fitdata(:,2))
plot(x,fitdata(:,4))
plot(x,fitdata(:,2))
```

- Shift of the FBG spectrum which was inscribed into core 1:

```
%Everytime i run it i move my spectrum 0.005nm

filename = 'myspectra';
str = [filename,'= initial;'];
eval(str);
[m,n]=size(initial);
initial2(m,1)=0;
initial2(:,1)=-38.6;

for i=1:1:m;
initial2(i+1,1)=initial(i,2);
end;
for i=1:1:m;
initial(i,2)=initial2(i,1);
end;
```

LIST OF TABLES

LIST OF FIGURES